UNIVERSITY OF CALIFORNIA SAN DIEGO

A Mechanics-based Virtual Model of NEES-UCSD Shake Table: Theoretical Development and Experimental Validation

A dissertation submitted in partial satisfaction of the requirements for the degree

Doctor of Philosophy

in

Structural Engineering

by

Ozgur Ozcelik

Committee in charge:

Professor Joel P. Conte, Chair
Professor J. Enrique Luco, Co-chair
Professor Miroslav Krstic
Professor Bhaskar Rao
Professor José I. Restrepo

2008

The Dissertation of Ozgur Ozcelik is approved, and it is acceptable in quality and form for publication on microfilm and electronically:

_____

_____

_____

_____
Co-Chair

_____
Chair

University of California, San Diego

2008

To my grandparents, Huruhan, Suna, Mustafa and Mehmet Ali,
my parents Yadigar and Kemal
and my sister Ozge

I have always imagined that the paradise will be
a kind of library...

Jorge Luis Borges

TABLE OF CONTENTS

ACKNOWLEDGEMENTS

The research for this dissertation was performed at the University of California, San Diego under the direction and supervision of Professor Joel P. Conte and Professor J. Enrique Luco. I would like to give to them my most sincere gratitudes. Their guidance in my research has been always inspirational and most helpful. Through out my Ph.D. studies, they were not only my “Ph.D. advisors” but also teachers and supports in life matters. Their place in my live will be forever felt.

I would like to give my special thanks to my doctoral committee members, Professor Miroslav Krstic, Professor Bhaskar Rao, and Professor José I. Restrepo who have always been willing to dedicate their time during the critical periods of my research studies.

The experimental work at San Diego owes much to Tomaso Trombetti, James Batti, Kenny Kenzel, Robert Beckley, Donald Morris, Laurance Berman, and Dan Radulescu. I would also like to give my thanks to people at MTS System Corporation Allen Clark, Brad Thoen, Marty Gram, Terry Nelson, Steve Pickford, and Joe Albright for their continuing support in providing important information.

Another thanks go to Mr. Quan Gu for his support and time in implementing the client-server technique. Also, I would like to give my bests to my research group, fellow students and friends Babak Moaveni, Maurizio Gobbato, Xianfei He, André Barbosa, Michele Barbato, Gabriel Acero, Yuyi Zhang, Marios Panagiotou, Andreas Stavridis, Ivan Bartoli, Antonio Di Cesare, Andrea Belleri, Salvatore Salamone,

Houman Ghajari, Pino Palermo, Hyunjung Young, Geert Lombaert and many others who have made my stay here in San Diego more enjoyable.

A very special thanks go to Professor Serap Kahraman and Professor Turkay Baran from the Civil Engineering Department in Dokuz Eylul University, Izmir who have been incredibly helpful and caring in all aspects of my life. Their support in finding a four-year research scholarship in abroad will always be greatly appreciated.

My American family in Saint Louis, Biehle family, they have been a life inspiration to me always; they have made me feel at home during the first years of my stay here. I have learnt and will learn from them greatly.

My family deserves a very special thanks for going through with me all the highs and lows of my time here in San Diego and for resisting to be away from me for the last six years. Last but not least, I am most grateful to Ms. Carmen Amaddeo who has been a life companion to me for the last two years; we have together passed through one of the most challenging periods of our lives, I can easily say that without her my experience here would be incomplete; her help in putting this thesis in its final format is also greatly appreciated.

This work was supported by a Grant from the National Science Foundation through the George E. Brown Jr. NEES program Grant No. CMS-0217293, by the Englekirk Center Board of Directors, and by NEESinc through a NEES facility enhancement project. Four year research scholarship provided by the Higher Education Council of Turkiye through Dokuz Eylul University is gratefully acknowledged.

Chapter 3 is a reprint of the material accepted for publication in Earthquake Engineering and Structural Dynamics (2008), Ozcelik, O., Luco, J.E., Conte, J.P., Trombetti, T., and Restrepo, J.I. The dissertation author was the first author of this paper.

Chapter 4 is a reprint of the material accepted for publication in the Journal of Engineering Mechanics (2008), Ozcelik, O., Luco, J.E., and Conte, J.P. The dissertation author was the first author of this paper.

VITA

1999	Bachelor of Civil Engineering, Dokuz Eylul University, Izmir, Turkey
2000-2002	Master of Science on Structural Engineering, Dokuz Eylul University, Izmir, Turkey.
2001 – 2002	Teaching Assistant. Department of Civil Engineering, Dokuz Eylul University, Izmir, Turkey
2002 - 2008	Graduate Research Assistant, Department of Structural Engineering, University of California at San Diego
2003 - 2007	Teaching Assistant. Department of Structural Engineering, University of California at San Diego, Fall Quarters
2008	Doctor of Philosophy, University of California, San Diego

PUBLICATIONS

Ozcelik, O., Luco, E.J., Conte, J.P., Trombetti, T.L., and Restrepo, J.I. (2008). "Experimental characterization, modeling and identification of the UCSD-NEES shake table mechanical system." Earthquake Engineering and Structural Dynamics, Volume 37(2), pp. 243-264, doi: 10.1002/eqe.754.

Ozcelik, O., Luco, E.J., and Conte, J.P. (2008). "Identification of the Mechanical Subsystem of the NEES-UCSD Shake Table by a Least-Square Approach." ASCE Journal of Engineering Mechanics, Volume 134(1), pp. 23-34, doi: 10.1061/(ASCE)0733-9399(2008)134:1(23).

Luco, J.E., Ozcelik, O., and Conte, J.P. (2008). "Acceleration Tracking Performance of NEES-UCSD Shake Table." *ASCE Journal of Structural Engineering*, September, under review.

FIELDS OF STUDY

Major Field: Civil Engineering (Structural Engineering)

Studies in Experimental Structural Dynamics

ABSTRACT OF THE DISSERTATION

A Mechanics-based Virtual Model

of NEES-UCSD Shake Table:

Theoretical Development and Experimental Validation

by

Ozgur Ozcelik

Doctor of Philosophy in Structural Engineering

University of California, San Diego, 2008

Professor Joel P. Conte, Chair

Professor J. Enrique Luco, Co-chair

Large servo-hydraulic shaking table systems are essential tools in experimental earthquake engineering. They provide effective ways to subject structural components, substructures, or entire structural systems to dynamic excitations similar to those induced by real earthquakes. A typical shake table system includes mechanical, hydraulic, and electronic components.

The main objective of this study is to develop a comprehensive mechanics-based virtual model for the large NEES-UCSD shake table under bare and loaded table conditions. The shake table model developed in this study includes a virtual replica of the actual controller, four servovalve models, two single-ended actuators, two effective accumulators, a two-dimensional mechanical subsystem model, and linear/nonlinear specimens modelled using the finite element analysis framework OpenSees. OpenSees is integrated to the rest of the simulation model in Matlab-Simulink® using a client-server technique developed within this work. Test-simulation correlation studies show that the virtual system model developed is capable of reproducing the nonlinear dynamic response behaviour of the NEES-UCSD shake table.

An extensive set of shake table tests using harmonic and earthquake acceleration records as reference/commanded signals were performed on the NEES-UCSD table to assess its signal reproduction fidelity after tuning the table controller and using an iterative time-history matching technique. These tests were designed to quantify the effects of the amplitude of the signal used for tuning the table on the signal reproduction fidelity. It was found that the level of fidelity in signal reproduction achieved for a specific amplitude of the commanded signal under the corresponding optimum tuning of the table cannot be maintained when reproducing the same signal at different amplitudes. This is a clear indication that shake tables are highly nonlinear systems and the current state-of-the-art controller and tuning techniques fall short of compensating accurately for these inherent system nonlinearities.

The mechanics-based virtual system model developed is extremely useful for: (i) understanding the underlying coupled nonlinear dynamics of a large shake table system; (ii) investigating the most significant sources of signal distortion; (iii) offline tuning of the actual table either by using only the virtual replica of the existing controller or by combining it with simulation-based iterative time history matching techniques; (iv) investigating shake table - linear/nonlinear specimen interaction problem; and (v) future more advanced control algorithm developments.

INTRODUCTION

Large servo-hydraulic shaking table systems are essential tools in experimental earthquake engineering. They provide effective ways to subject structural components, substructures, or entire structural systems to dynamic excitations similar to those induced by real earthquakes. The typical shake table system includes a variety of mechanical (platen, yaw/pitch/roll restraining systems, vertical and lateral bearings, reaction block, foundation, and linear/nonlinear specimen), hydraulic (pumps, hydraulic lines, accumulator bank, distributed accumulators along hydraulic line, servovalves, and actuators), and electronic (controller, various types of transducers, signal conditioning units, data acquisition system) components.

The main objective of a shaking table system is to reproduce acceleration time history records within a reasonable accuracy therefore subject structural systems to real time input excitations thereof retaining realistic inertial and damping effects. However, reproduction of a prescribed acceleration time history record (e.g., earthquake accelerations) with such systems remains to be imperfect (Rinawi and Clough, 1991; Kusner et al., 1992; Clark 1992; Crewe, 1998; Conte and Trombetti, 2000; Crewe and Sewern, 2001; Trombetti and Conte, 2002). Within the Network for Earthquake Engineering and Simulation Consortium (NEES) major shake table facilities have been added to the shake table inventory of the Unites States (e.g., NEES at Buffalo, NEES at Reno, and NEES at San Diego). These large facilities are

currently used to investigate aspects of structural and geotechnical seismic behavior that cannot be readily extrapolated from testing at smaller scales, or under quasi-static or pseudo-dynamic conditions. With the recent advancements of experimental test methods, numerical simulation tools, and high-speed communication networks researchers are able to conduct also geographically distributed tests using these state-of-the-art testing facilities. Geographically distributed testing combines the capabilities of two or more sites to conduct tests on structural systems that could not be performed at one site due to limited site capacity (Takahashi and Fenves, 2005). New testing facilities and their innovative usages bring new challenges to the field of shake table testing. One of these challenges is in high-fidelity control of shake table systems.

Dynamic tests with shake tables require the table platform to follow a reference signal (e.g., displacement or acceleration). Controller is the electronic device (analog or digital) that supplies the appropriate command to the servovalve(s) in order to drive the table along the correct trajectory (i.e., path). Shake table control systems are usually based on linear control algorithms in which it is assumed that the plant can be modeled as a set of linear differential equations and the dynamic parameters of the plant are known and fixed during experiments (Stoten and Gomez, 2001). Linear controllers can be tuned with high degree of precision when the plant has known parameters and behaves linearly. On the other hand, linear controllers are not well suited for non-linear regimes and do not respond as expected if the plant parameters change or have been wrongly estimated (Gomez, 1999). Earlier works on the

performance characterization of shake tables reveal that shake tables are highly nonlinear devices that the table response is a function of the input amplitude level in which it operates (Clark, 1983; Kusner et al., 1992; Clark, 1992; Zhao et al., 2005). Some of the major sources of nonlinearities in shake table systems are servovalve(s), nonlinear viscous and friction dissipative sources, total system leakage including servovalve(s) and actuator(s), changes in volumes of actuator chambers, and system pressure fluctuations.

As large shake table facilities become available (e.g., NEES-UCSD shake table in U.S.A and NIED E-Defense table in Japan etc.), testing full scale specimens on shake tables is now more and more frequent. In large scale shake table tests, often the specimen is more massive than the table and can exhibit nonlinear behavior under the reproduced table motion and its characteristics can change suddenly especially if a collapse situation occurs. For such test conditions, one of the most significant problems arises from the fact that the dynamics of the specimen is as relevant to the dynamic model of the overall system as the table itself (Clark, 1984; Crewe, 1998; Gomez 1999; Stoten and Gomez, 2001). Nonlinear table/specimen interaction as well as other sources of nonlinearities further complicates the accurate control of shake tables with linear controllers.

Adjusting control parameters to optimize the response of the shake table system is called tuning. Ideally, a tuned shake table system would have a transfer function between the reference and achieved signals (total table transfer function) characterized by unit gain and zero phase shift across the entire operating frequency

range under loaded (i.e., with a specimen) table conditions. With linear controllers, due to the reasons explained above, it is not possible to achieve such total transfer functions. To remedy the inaccuracies in linear controller tuning, prior to the actual test usually an offline or an online (iterative) time history matching technique is employed. A simple offline approach for compensating the controller deficiencies is to apply a pre-filter (e.g., inverse total table transfer function estimated prior to the test) once to the reference signal which results in a modified reference signal (i.e., drive signal) accounting for the dynamics of the system (Hwang et al., 1987; Twitchell and Symans, 2003). Inverse transfer function is estimated using white noise while the specimen is mounted on the table to take into account the table/specimen interaction. One very important drawback in offline approach is that when the transfer function is estimated, if the amplitude of white noise is too high the specimen on the table may be damaged; on the other hand if the amplitude of white noise is too low then nonlinearities in amplitude scaling of the drive signal may mean that the transfer function estimated from low level amplitude white noise is not representative of the actual system performance with large amplitude earthquake signals. In online (iterative) time history matching technique, command signal is repeatedly modified by addition of a fraction of the pre-filtered error between the actual and desired table motion. The error is pre-filtered by the inverse of the total table transfer function and it can be the initial estimation or an updated one from the last iteration (Crewe, 1998). The iteration process is repeated until the errors fall within a desired level. Online time history matching techniques can deal with the repeatable nonlinearities such as

servovalve nonlinearities. Both in offline and online techniques, extreme care has to be given to the specimen for not prematurely damaging it.

A recent test study done by Luco et al. (2008) on the NEES-UCSD shake table investigates the effect of amplitude scaling in tuning of shake tables under bare table conditions. The tests were designed to quantify the effect that the tuning amplitude has on the level of signal fidelity. For these tests, first the table response was optimized, as much as possible, by adjusting the gains of the linear controller. This step was followed by an online time history matching technique applied to a scaled down or scaled up versions of the intended acceleration motions. Drive inputs obtained at the end of the iteration process were scaled up or down according to several test amplitudes and the resulting motions were reproduced on the table. A number of comparisons and measures were used to evaluate the signal reproduction capability of the shake table which included direct comparisons of the acceleration time histories, peak accelerations, constant ductility response spectra for the achieved and intended platen accelerations, and relative root mean square error value to offer a cumulative measure in signal reproduction. Based on these different comparisons, it was concluded with certainty that a signal fidelity level achieved for a specific amplitude by a certain tuning cannot be maintained at a different amplitude. Especially, difficulties encountered with tuning at low amplitudes and testing at much higher amplitudes indicate the need for an accurate virtual tuning of the table based on a detailed mechanics-based model of the complete system and, eventually, for a more advanced controller. It should be noted here that for a loaded table conditions, tuning

at low amplitudes and testing at higher amplitudes is the only option since the specimen can not be sacrificed during table tuning. Offline and/or online time history matching techniques are not the solution to achieve high fidelity in signal reproduction for loaded table conditions.

The complex dynamics of large shaking table systems emanate from multiple dynamic interactions and nonlinearities among various system components (Dyke et al., 1995; Conte and Trombetti, 2000; Trombetti and Conte, 2002; Ozcelik et al., 2008(1); Ozcelik et al., 2008(2)). In the literature, we find a limited number of studies focusing on modeling and simulation of complete servo-hydraulic testing systems (Hwang et al., 1987; Rinawi and Clough, 1991; Clark, 1992; Dyke et al., 1995; Dimig et al., 1999; Conte and Trombetti, 2000; Williams et al., 2001; Twitchell and Symans, 2003; Thoen and Laplace, 2004; Zhao et al., 2005; Zhao et al., 2006). Dyke et al. (1995) developed a linear model for a servovalve/actuator system attached to a linear shear type structure for investigating the role of control-structure interaction; the analytical model also includes a displacement controller and force feedback loop. Conte and Trombetti (2000) developed a linear analytical model of a small-to-medium size shake table system accounting for servovalve time delay, actuator dynamics, oil leakage through the actuator seals, foundation flexibility, and linear elastic multi-degree-of-freedom (MDOF) specimen dynamics. Williams et al. (2001) have developed a realistic numerical model of a dynamic structural testing system, which includes a nonlinear model of the servovalve actuator system, servovalve leakage, controller, and the specimen modeled as a linear elastic single-degree-of-freedom

(SDOF) system. Thoen and Laplace (2004) presented a comprehensive numerical model of a medium size shake table for off-line tuning purposes; their model includes the real-time controller software, servovalve spool dynamics, a nonlinear servovalve-actuator model, an accumulator model, a linear payload model, a nonlinear friction model, and foundation dynamics. Recently, Zhao et al. (2005) presented a numerical model for the effective force testing system in which a detailed nonlinear servovalve model is used where two independent sources of servovalve flow nonlinearities were taken into account; leakage within the servovalve and inside the actuator chambers is modeled as an effective total system leakage and is found to be equivalent to damping of actuator dynamics.

Overview of the NEES-UCSD LHPOST. NEES-UCSD Large Performance Outdoor Shake Table (LHPOST) located at a site 15 km away from the main campus of the University of California at San Diego ($32^{\circ}53'37''N$ and$117^{\circ}06'32''W$), is a unique outdoor experimental facility that enables next generation seismic tests to be conducted on very large structural and soil-foundation-structure interaction systems. A three-dimensional rendering of the overall shake table system is shown in Figure I.1(a). The LHPOST consists of a moving steel platen (7.6m wide by 12.2m long); a reinforced concrete reaction block; two servo-controlled dynamic actuators with a force capacity in tension/compression of 2.6MN and 4.2MN, respectively; a platen sliding system (6 pressure balanced vertical bearings with a force capacity of 9.4MN each and a stroke of ±0.013m); an overturning moment restraint system (a pre-stressing system consisting of two Nitrogen-filled hold-down struts with a hold-down

force capacity of 3.1MN each); a yaw restraint system (two pairs of slaved pressure balanced bearings along the length of the platen); a real-time multi-variable controller, and a hydraulic power supply system. The technical specifications of the LHPOST include a stroke of ±0.75m, a peak horizontal velocity of 1.8m/s, a peak horizontal acceleration of 4.2g for bare table conditions and 1.28g for a rigid payload of 400tons, a horizontal force capacity of 6.8MN, an overturning moment capacity of 50MN-m, and a vertical payload capacity of 2000tons where the peak platen acceleration reduces to 0.3g. The frequency bandwidth is 0-20Hz. Other detailed specifications of the NEES-UCSD LHPOST can be found elsewhere (Conte et al., 2004; Van Den Einde et al., 2004).

Figure I.1(b) shows the detailed schematic representation of the major components of LHPOST and the way they interact with each other. There are two pumps in the system providing hydraulic power to various parts of the table. Pump 1 supplies hydraulic power to the servovalves, vertical and yaw bearings (not shown in schematics) by providing 720lit/min flow at 21.0MPa (190gpm at 3000psi) pressure. Hydraulic line carrying the flow from Pump 1 is indicated as PP which stands for pilot pressure. Pump 2 charges the accumulator bank; flow provided by this pump is 416lit/min at 21.0MPa (114gpm at 5000psi) pressure. 9500 liter capacity accumulator bank charged up to 35.0MPa provides the high flow needed to simulate transient earthquake signals. Blow-down valve converts the high pressure oil from the accumulator bank to a system pressure of 21.0MPa for controlling the actuators. Hydraulic supply line carrying the regulated oil is indicated as P which stands for

main pressure. Also shown Figure I.1(b) are the small in-line accumulators each with capacity of 95 liters and charged up to 13.8MPa (2000psi) pressure. There are two actuators on the West and East sides of the table platen. Each actuator has two high performance servovalves attached on them (therefore there are total of four servovalves on the system). Close-coupled (C.C.) accumulators are attached to the actuators and they are 57 liters each and are also charged up to 13.8MPa (2000psi) pressure. Low-pressure return flow is collected in the surge tank. Actuators drive the table platen which slides on the low friction vertical bearings, pre-charged hold-down struts pull the platen down with constant vertical forces in order to restrain the pitch motion of the platen. Forces generated by the system are reacted by the foundation block and surrounding soil. Controller on the system sends control signal computed using the reference and feedback signals to the servovalves in order to move the platen along a desired path.

The reaction block and the surrounding soil are shown in Figure I.1(b) as parts of the shake table system. Large forces that the actuators of LHPOST exert on the reaction block and surrounding soil suggests the need to determine the induced ground motion in the vicinity of the table in order to evaluate the effects that any motion of the block itself would have on the control of the shake table. In order to study dynamic soil-foundation interaction effects, an extensive forced vibration test study using eccentric mass shakers has been carried out on the foundation block of LHPOST prior to the construction of the shake table. Forces exerted by the shakers are normalized to the maximum force (6.8MN) that actuators can exert on the foundation. Results of this

study reveal that the foundation block essentially translates as a rigid body along East-West (EW) direction with slight out-of-plane deformation of the East and West end walls; the block also bends in addition to rocking about the North-South (NS) axis. The frequency response of the EW motion peaks at 10 Hz with amplification factor of 1.3; vertical frequency response indicates that the amplitudes of the vertical displacements increase with horizontal distance to the NS axis of rotation at least for frequencies below 15 Hz. Experimentally obtained frequency response curves indicate that the maximum scaled horizontal and vertical displacements for the maximum theoretical harmonic actuator force of 6.8MN amplitude at 10 Hz frequency would be 0.26mm and 0.17mm, respectively. These displacements are sufficiently small to have no effect on the control of the shake table which relies on the assumption that the relative displacement of the platen with respect to the reaction block represents the absolute displacement of the platen (Luco et al., 2008).

The main objective of this study is to develop a comprehensive mechanics-based model of the large NEES-UCSD shake table for bare and loaded table conditions. The model includes the virtual replica of the controller, four servovalve models including servovalve spool dynamics and two independent servovalve flow nonlinearities, two single-ended actuators with variable internal volumes, two accumulators modelling the average supply pressure drop, two-dimensional mechanical subsystem model extended from the previously identified one-dimensional mechanical subsystem model which includes the effects of effective mass of the platen, nitrogen-filled hold-down struts, and various viscous and Coulomb dissipative

mechanisms, and finally linear/nonlinear specimens modelled using a generic finite element analysis software. Based on the forced vibration test results of the foundation block, the soil-foundation compliance effects will be ignored in the virtual model by assuming them to be rigid. This mechanics-based virtual model will be extremely useful for: (i) understanding the underlying coupled nonlinear dynamics of a large shake table system therefore providing insight into the sources of various signal distortions; (ii) off-line tuning of the actual table; (iii) future advanced control algorithm developments; and (iv) investigating shake table-linear/nonlinear specimen interaction problem.

LIST OF FIGURES

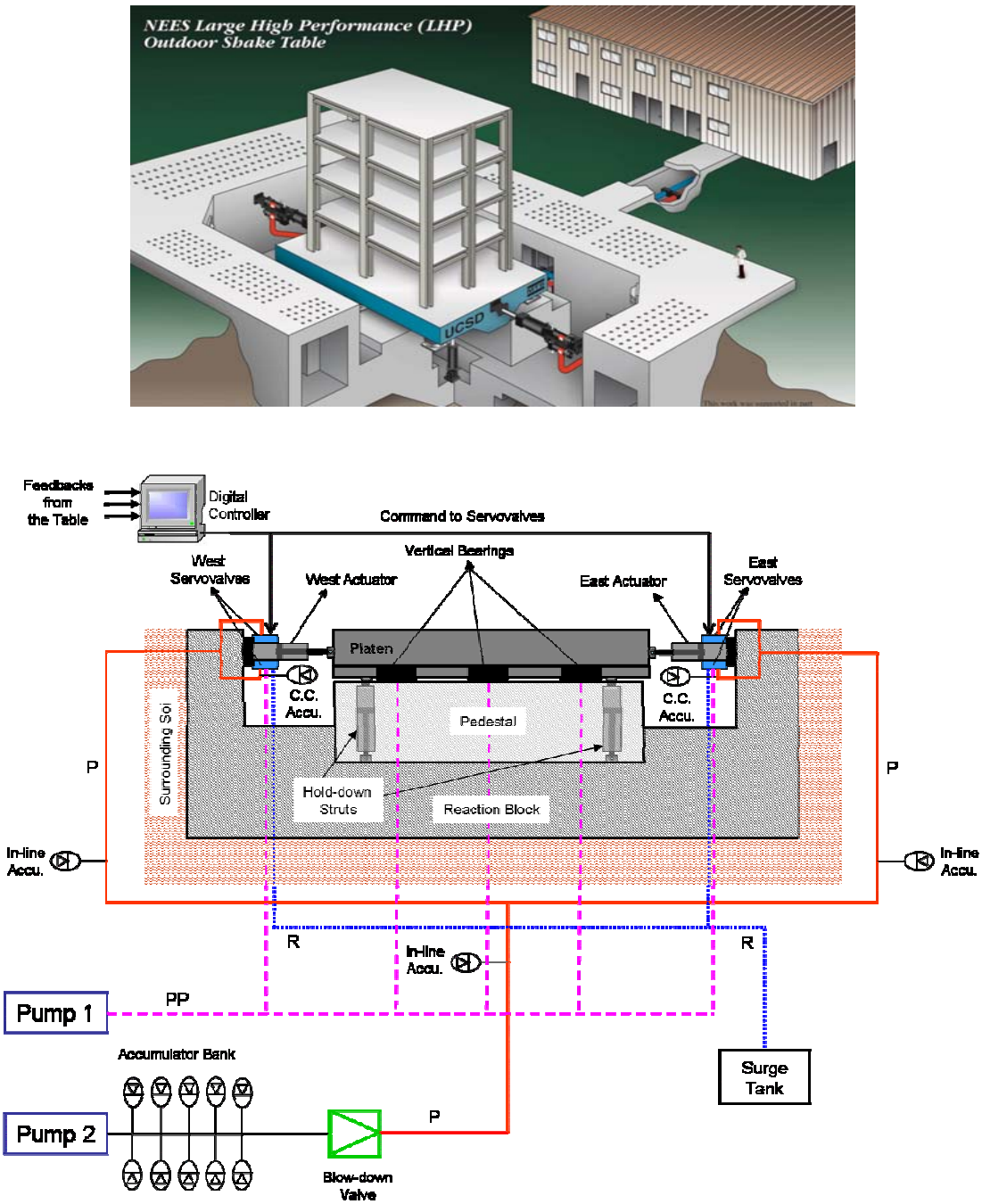

Figure I.1: (a) 3D rendering of the NEES-UCSD shake table; (b) schematics of the overall hydraulic, mechanical, and electronic components.

REFERENCES

Clark, A., Dynamic Characteristics of Large Multiple Degree of Freedom Shaking Tables. *Proc. 10th World Conf. on Earthquake Engineering*, Madrid, Spain, 2823-2828, 1992.

Clark, A.J. and Cross, D.J. (1984). "The effect of specimen resonances on accurate control of multiple defree-of-freedom servo-hydraulic shaking tables." *Proc. 8th World Conference on Earthquake Engineering*, San Francisco, California, U.S.A.

Clark, A.J. (1983). "Sinusoidal and Random Motion Analysis of Mass Loaded Actuators and Valves." *Proc. National. Conference Fluid Power*, Vol. 37: 168-171.

Crewe, A. J., Severn, R. T., The European Collaborative Program on Evaluating the Performance of Shaking Tables. *Phil. Trans. R. Soc. Lond. A*, 359, 1671-1696, 2001.

Crewe, A. J. (1998). "The characterization and optimization of earthquake shaking table performance." Ph.D. Thesis, University of Bristol.

Conte, J.P., and Trombetti, T.L., Linear Dynamic Modeling of a Uni-axial Servo-Hydraulic Shaking Table System. *Earthquake Engineering and Structural Dynamics*, 29(9), 1375-1404, 2000.

Conte, J.P., Luco, J.E., Restrepo, J., Seible, F., and Van Den Einde, L., (2004). "UCSD-NEES Large High Performance Outdoor Shake Table.' *17th ASCE Engineering Mechanics Conference*, Newark, U.S.A, June 13-16, 2004.

Dyke, S. J., Spencer, B. J., Quast, P., and Sain, M. K. (1995). "Role of control-structure interaction in protective system design." *J. Eng. Mech., 121(2), 322-338.*

Dimig, J., Shield, C., French, C., Bailey, F., and Clark, A. (1999). "Effective force testing: a method of seismic simulation for structural testing." *J. Struct. Eng.*, 125(9), 1028-1037.

Gomez, G.E. (1999). "Application of the MCS algorithm to the control system of the Bristol shaking table." Ph.D. Thesis, University of Bristol.

Hwang, J. S., Chang, K. C., and Lee, G. C., The System Characteristics and Performance of a Shaking Table. *NCEER Report No. 87-0004, National Center for Earthquake Engineering Research, State University of New York at Buffalo*, NY, 1987.

Kusner, D. A., Rood, J. D., and Burton, G. W., Signal Reproduction Fidelity of Servohydraulic Testing Equipment. *Proc. 10th World Conference on Earthquake Engineering*, Rotterdam, 2683-2688, 1992.

Luco, J.E., Conte, J.P., Ozcelik, O. (2008). "Experimental study of the dynamic interaction between the foundation of the NEES-UCSD shake table and surrounding soil." *Under preparation for submission to Soil Dynamics and Earthquake Engineering.*

Luco, J.E., Ozcelik, O., and Conte, J.P. (2008). "Acceleration tracking performance of the NEES-UCSD shake table." *J. Struct. Eng.*, under review.

Rinawi, A. M., and Clough, R. W., Shaking Table-Structure Interaction. EERC Report No. 91/13, Earthquake Engineering Research Center, University of California at Berkeley, CA, 1991.

Thoen, B. K., and Laplace, P. N., Offline Tuning of Shaking Tables. Proc. 13th World *Conf. on Earthquake Engineering*, Vancouver, B.C., Canada, Aug. 1-6, 2004, Paper No. 960.

Thoen, B. K., 469D Seismic Digital Control Software. MTS Corporation, 2004.

Ozcelik, O., Luco, E. J., Conte, J. P., Trombetti, T. L., and Restrepo, J. I. (2008(1)). "Experimental characterization, modeling and identification of the UCSD-NEES shake table mechanical system." *Earthquake Eng. Struct. Dyn.*, 37:243-264.

Ozcelik, O., Luco, E.J., and Conte, J.P. (2008(2)). "Identification of the mechanical mubsystem of the NEES-UCSD shake table by a least-square approach." ASCE *J. Eng. Mech.*, 134(1), 23-34, doi: 10.1061/(ASCE)0733-9399(2008)134:1(23)

Stoten, D.P., Gomez, E. (2001). "Adaptive control of shaking tables using minimal control synthesis algorithm." *Phil. Trans. R. Soc. Lond. A*, 359, 1697-1723.

Takahashi, Y., Fenves, G.L. (2005). "Software framework for distributed experimental-computational simulation of structural systems." *Earthquake Eng. Struct. Dyn.*, 35:267-291.

Trombetti, T.L., and Conte, J.P., Shaking Table Dynamics: Results from a Test Analysis Comparison Study. *Journal of Earthquake Engineering,* 6(4), 513-551, 2002.

Twitchell, B. S., and Symans, M. D., Analytical Modeling, System Identification, and Tracking Performance of Uniaxial Seismic Simulators. *Journal of Engineering Mechanics*, 129(12), 2003.

Van Den Einde, L., Restrepo, J., Conte, J. P., Luco, E., Seible, F., Filiatrault, A., Clark, A., Johnson, A., Gram, M., Kusner, D., and Thoen, B., Development of the George E. Brown Jr. Network for Earthquake Engineering Simulation (NEES) Large High Performance Outdoor Shake Table at the University of California, San Diego. *Proc. of 13-th World Conference on Earthquake Engineering*, Vancouver, BC Canada, August 1-6, 2004, Paper No. 3281.

Williams, D. M., Williams, M. S., and Blakeborough, A., Numerical Modeling of a Servohydraulic Testing System for Structures. *Journal of Engineering Mechanics, ASCE*, 127(8), 816-827, 2001.

Zhao, J., Shield, C., French, C., Posbergh, T., Nonlinear System Modeling and Velocity Feedback Compensation for Effective Force Testing. *Journal of Engineering Mechanics*, 131(3), 244-253, 2005.

Zhao, J., French, C., Shield, C., and Posbergh, T. (2006). "Comparison of Tests of a Nonlinear Structure Using a Shake Table and EFT Method." *J. Struct. Eng.*, 132(9), 1473-1481.

CHAPTER 1

THREE-VARIABLE CONTROLLER (TVC)

1.1. Three-Variable Controller (TVC) Transfer Functions

In this section, transfer functions for the constitutive parts of the Three-Variable Controller (TVC) will be given.

1.1.1. Three-Variable Controller

The controller of the LHPOST is the digital MTS Three Variable Controller (TVC). It is known in control theory as a state variable controller. It has additional special features to compensate for linear and nonlinear system distortions for both harmonic and broadband command signals (e.g., amplitude/phase control, adaptive harmonic cancellation, adaptive inverse control, on-line iteration, and notch filters).

The three state variables controlled by the TVC are displacement, velocity, and acceleration. The controller can be set to run under displacement, velocity or acceleration control mode. Depending on the control mode only one state variable becomes the primary control variable while others serving only as compensation (feed-forward and/or feedback) signals to improve damping and stability of the system. The transfer functions between all the inputs and outputs of the TVC are provided by the MTS Systems Corporation (Thoen, 2004).

A block diagram of the TVC is given in Figure 1.1. The reference generator takes the reference signal, which represents the desired displacement, velocity, or acceleration depending on the control mode, and creates the reference states u_{ref}, $\dot{u}_{ref}$, $\ddot{u}_{ref}$, and $\dddot{u}_{ref}$ (i.e., jerk reference signal), which are used as feedforward signals in the controller. The feedback states u_{fbk}, $\dot{u}_{fbk}$, and $\ddot{u}_{fbk}$ are generated by the feedback generator which combines displacement and acceleration sensors (feedback signals), each with their respective bandwidth limitations to create wideband estimates of the feedback states.

The reference and feedback states are weighted by the reference and feedback gains, respectively, shown in the figure. It should be noted here that the displacement feedback gain is the only non-zero feedback gain. Therefore, it can be said that the TVC is simply a displacement controller with sophisticated reference (feed-forward) gains (Thoen, 2004). The high-pass filter applied on the force feedback signal (equivalent to the delta-pressure signal multiplied by the actuator effective piston area) removes static and low frequency components from the force feedback, prior to input it into the TVC to damp the oil column resonance. Five notch filters are also incorporated in the controller to compensate for resonances and anti-resonances. Each notch filter frequency response is defined by three parameters: the center frequency, 3dB bandwidth, and notch depth (Thoen, 2004). Note the presence of scale factors to convert input signals denominated in engineering units to volts. This way physically different unit signals can be blended together in some what consistent way. Another important reason for using volts scaling is so that the controller gains have units of

volts per volt so that if the units of the controller are changed, the controller need not be retuned. The scale factors are $10/D_{\max}$, $10/V_{\max}$, $10/A_{\max}$, and $10/F_{\max}$ which are applied to displacement, velocity, acceleration, and force input signals, respectively. Quantities D_{MAX}, V_{MAX}, and A_{MAX} are the calibrated engineering unit maximums corresponding to 10 volts output of the conditioners. Note that the scale factor applied to acceleration is also applied to jerk (Thoen, 2004).

Three Variable Controller shown in Figure 1.1, can be represented in a more compact form by the transfer function view of its constitutive parts. The representation shown in Figure 1.2 will facilitate the derivations of these transfer functions

The transfer functions of the constitutive parts of TVC, (i.e., G_R, G_D, G_V, G_A, and G_F) can not be given here in this study due to proprietary reasons. In the following sections, some details about these parts will be presented.

1.1.2. Reference Generator G_R

The Reference Generator takes the reference signal, which represents desired displacement, velocity, or acceleration depending on control mode, and creates the reference states u_{ref}, $\dot{u}_{ref}$, $\ddot{u}_{ref}$, and $\dddot{u}_{ref}$, which are used as feed-forward signals in the controller.

Note that signals of physical dimensions of displacement, velocity, and acceleration are blended together (Figure 1.1). In order for this to occur correctly, the signals must first be converted into a consistent, *canonical* set of units, namely, units consisting only of displacement units and time. For example, if displacement units are inches, then canonical velocity units are inches/sec and canonical acceleration units

are inches/sec/sec. The canonical factors D_{canon}, V_{canon} and A_{canon} convert user units to canonical units. The displacement canonical factor D_{canon} is always unity. V_{canon} and A_{canon} are often non-unity depending on user velocity and acceleration units. Note that the canonical factor applied to acceleration is also applied to jerk (Thoen, 2004). The parameters of the Reference Generator are high-pass cut-in frequency: f_{HP}; low-pass cut-off frequency: f_{LP}; and damping coefficient: ζ (always set to 0.707).

1.1.3. Feedback Generator

In a typical shaking table configuration, measured displacement and an LVDT and accelerometer generate acceleration data for each axis of the machine. Often LVDT data is valid over the low-medium frequency range (typically, 0-15 Hz), but above this range the data is unusable, due to the combined effects of mechanism backlash and the problem of resolving small amplitude signals with finite accuracy analogue-to-digital conversion. On the other hand, accelerometer signals are accurate in the medium-high frequency range (i.e. typically up to ~50 Hz) (Stoten et al., 2001). Therefore the problem is to determine a suitable combination of displacement and accelerometer signals to cover the entire frequency range of operation. The technique used to do this is called the composite filtering.

The Feedback Generator in TVC combines displacement and acceleration sensors, each with their respective bandwidth limitations, to create wideband estimates of the feedback states (i.e. improved estimates of the states) u_{fbk}, $\dot{u}_{fbk}$, and $\ddot{u}_{fbk}$. The improvements are intended to provide estimates of unmeasured data (e.g. velocity),

and to obtain more consistent estimates of measured data over a wider frequency range. It should be noted that the Feedback Generator is considered as a part of the plant, not the controller (Thoen, 2004).

The fundamental assumptions behind the synthesis method (i.e. composite filtering) can be summarized as follows (Stoten et al., 2001)

i. the acceleration signal $\ddot{u}_{raw}$ can have a non-zero mean,

ii. the acceleration signal must be integrated twice, with the effects of the bias removed after a suitably short transient period,

iii. the signal from (ii) is filtered by the high-pass component of the complementary filter,

iv. the displacement signal is filtered by the low-pass component of the complementary filter,

v. both filter components must be proper and of minimal order, and

vi. the gain and phase of the resulting composite filter are unity and zero.

The general configuration of the groups of filters is shown in Figure 1.3, where $G_h'(s)$ is the high-pass complement, and $G_l'(s)$ is the low-pass complement and $y_{fc}, (f = \{d, v, a\})$, is the required composite signal. In series with each complementary filter, there are auxiliary filters (i.e. integrators or differentiators). The number of integrators or differentiators is dependent upon the composite signal to be generated (Table 1.1).

From (iv), it is required that

$$G_h'(s) + G_l'(s) = 1 \tag{1.1}$$

1.1.4. ad2d: Composite Filter for Displacement

For the ad2d composite filter, below given high-pass and low-pass complementary filters are used

$$G_h'(s) = \frac{s^3}{s^3 + a_2 s^2 + a_1 s + a_0} \quad G_l'(s) = \frac{a_2 s^2 + a_1 s + a_0}{s^3 + a_2 s^2 + a_1 s + a_0} \tag{1.2}$$

From (1.2), it is clear that (1.1) is satisfied. The coefficients of the high and low pass filters given in (1.2) can be calculated as

$$a_0 = a^3; a_1 = 2a^2; a_2 = 2a \tag{1.3}$$

where a is the cross-over frequency in rad/s, and it is the same for both of the complementary filters. a determines the range where below that value LVDTs work better, and above accelerometers. Figure 1.4 shows the bode plots of complementary high-pass and low-pass filters for two different values of a.

From Table 1.1, $nh = -2$ and $nl = 0$ for the ad2d filter, therefore the composite filters $G_h(s)$ and $G_l(s)$ take the following forms

$$G_h(s) = \frac{s}{s^3 + a_2 s^2 + a_1 s + a_0} \tag{1.4}$$

$$G_l(s) = \frac{a_2 s^2 + a_1 s + a_0}{s^3 + a_2 s^2 + a_1 s + a_0} \tag{1.5}$$

The estimated u_{fbk} by the composite filtering technique summarized above can be written as

$$u_{xfbk}(s) = G_h(s)\ddot{u}^{raw}_{xfbk}(s) \cdot \frac{A_{canon}}{D_{canon}} + G_l(s)u^{raw}_{xfbk}(s) \tag{1.6}$$

As for the Reference Generator, continuous time integration operator, $1/s$, is approximated with backward Euler discrete time integration. Similar expressions as given in (1.6) can be derived for estimating the velocity and accelerations feedback states (Stoten et al., 2001)

1.1.5. Force Feedback Low-pass Filter

The force feedback low-pass filter removes high frequency components from the force feedback (equivalent to the delta-pressure signal multiplied by the actuator piston area. This filter is a second-order Butterworth low-pass in which the cutoff frequency is determined by the 3dB frequency.

In the real controller the cut-in frequency of this filter is set always to 1000 Hz. It is effect on the acquired force signal is negligible; therefore TVC model presented here will not include this filter. In the real-time software 469D, the low-pass force filter has been recently removed.

1.1.6. Force Feedback High-pass Filter

The force feedback high-pass filter removes static and low frequency components from the force feedback (equivalent to the delta-pressure signal multiplied by the actuator piston area), prior to being input to the TVC as a feedback signal to increase the damping of the oil column resonance. This filter is a second-order Butterworth

1.1.7. Reset Integrator

The reset integrator removes DC offsets between displacement reference and displacement feedback. Its transfer function is given as follows

1.1.8. Notch Filters

The notch filters are used to suppress resonances and boost anti-resonances, there are total of five notch filters in TVC. The parameters of each notch filter are: center frequency f_0, 3dB bandwidth b_w, and notch depth $depth$. The effect of these parameters on the notch filter frequency response is shown below schematically. Note that the notch depth can be set to positive or negative.

Each notch is implemented as an all-pass filter $A(z)$ with the filter input and output weighted and summed as follows

$$G_{NOT}^{i}(z) = w_0^i \left[\frac{w_1^i}{w_0^i} A_i(z) + 1 \right], \; i = 1, 2, \ldots, 5$$
$$w_0^i = 1 + depth/2, \; w_1^i = -depth/2 \tag{1.7}$$

It is important here to revisit some of the properties of all-pass filters. The frequency response $A(e^{j\omega})$ of an all-pass filter exhibits unit magnitude at all frequencies

$$\left| A(e^{j\omega}) \right|^2 = 1 \text{ for all } \omega \tag{1.8}$$

The transfer function of such a filter has all poles and zeros occurring in conjugate reciprocal pairs, and takes the form given below

$$A(z) = \prod_{k=1}^{M} \frac{\gamma_k^* - z^{-1}}{1 - \gamma_k z^{-1}} \tag{1.9}$$

For stability reasons γ_k must satisfy $|\gamma_k| < 1$ condition for all k to place all poles inside the unit circle. An alternative form of (1.9) by using the fact that the poles and zeros of a all-pass filter occur in complex conjugate pairs

$$A(z) = \frac{z^{-M} D(z^{-1})}{D(z)} \tag{1.10}$$

Therefore, the numerator polynomial is obtained from the denominator polynomial by reversing the order of the coefficients. As an example,

$$A(z) = \frac{a_2 + a_1 z^{-1} + z^{-2}}{1 + a_1 z^{-1} + a_2 z^{-2}} \tag{1.11}$$

In this case, the numerator and denominator polynomials are said to form a mirror-image pair. When the coefficients of all-pass filter are not real, then the numerator and denominator coefficients form a Hermitian mirror-image pairs. The (Hermitian) mirror-image symmetry relation between the numerator and denominator polynomials of an all-pass transfer function can be exploited to obtain a computationally efficient filter realization with minimum number of multipliers (Regalia et al., 1988).

From (1.8), setting $A(z) = Y(z)/U(z)$ reveals that

$$\left|Y(e^{j\omega})\right|^2 = \left|U(e^{j\omega})\right|^2 \text{ for all } \omega \tag{1.12}$$

By integrating both sides from $\omega = -\pi$ to π and applying Parseval's relation, the following expression can be found

$$\sum_{n=-\infty}^{\infty} |y(n)|^2 = \sum_{n=-\infty}^{\infty} |u(n)|^2 \tag{1.13}$$

The interpretation of expression given in (1.13) is that the output energy and input energy of an all-pass filter is equal to each other therefore all-pass filter is *lossless*.

Another useful property of interest is the change in phase for real coefficient all-pass filter over the frequency range $\omega \in [0, \pi]$. An M^{th} order real all-pass function satisfies the property given below (Regalia et al., 1988)

$$\int_0^{\pi} \tau(\omega) d\omega = M\pi \tag{1.14}$$

where $\tau(\omega)$ is the group delay function of an all-pass filter and defined as

$$\tau(\omega) = -\frac{d}{d\omega}[\arg\ A(e^{j\omega})] \tag{1.15}$$

The interpretation of (1.14) is that the change in phase of the all-pass function as ω goes from 0 to π is $-M\pi$ radians.

$$\begin{gathered} k_1 = -\cos(2\pi fT) \\ k_2 = \frac{1-\tan(\pi \cdot bw \cdot T)}{1+\tan(\pi \cdot bw \cdot T)} \\ a_1 = k_1(1+k_2) \\ a_2 = k_2 \\ A(z) = \frac{a_2 + a_1 z^{-1} + z^{-2}}{1 + a_1 z^{-1} + a_2 z^{-2}} \\ w_0 = 1 + depth/2 \\ w_1 = -depth/2 \\ G_{NOT}(z) = \frac{(w_0 + w_1 a_2) + (w_0 + w_1) a_1 z^{-1} + (w_1 + w_0 a_2) z^{-2}}{1 + a_1 z^{-1} + a_2 z^{-2}} \end{gathered} \tag{1.16}$$

The transfer function given in (1.16) is directly used in the real-time controller, but since everything else is in the simulation model of the TVC is in continuous form, the transfer function $G_{NOT}(z)$ is transformed to continuous time and implemented in that format in the simulation model by bilinear approximation (Tustin) to the derivative.

The way the notch filters are implemented in TVC allows the independent tuning ("orthogonal" tuning, Regalia et al., 1988) of the notch frequency f_0 (i.e. center frequency), bandwidth b_w, and the depth *depth*. Figure 1.6 through Figure 1.8 illustrates the orthogonal tuning property of the notch filters in TVC.

1.1.9. TVC Transfer Functions

G_R, G_D, G_V, G_A, and G_F are the transfer functions of the constituent parts of TVC. Details of these constituent parts are given below, again note that the feedback generator is not considered as a part of TVC but as a part of the plant, i.e. belong to the plant, not specifically to the TVC. By referring to Figure 1.1, and referring to the feed-forward and feed-back gains given shown in Figure 1.2 the following expressions can be written (Thoen, 2004)

$$G_{COM}(s) = k_M G_{INT}(s) \prod_{i=1}^{5} G_{NOT}^{i}(s) \tag{1.17}$$

$$\begin{aligned} G_R(s) = G_{COM}(s) \cdot [k_{PF} G_{RD}(s) \cdot \frac{10}{D_{\max}} + k_{VF} G_{RV}(s) \cdot \frac{10}{V_{\max}} + \\ + k_{AF} G_{RA}(s) \cdot \frac{10}{A_{\max}} + k_{JF} G_{RJ}(s) \cdot \frac{10}{A_{\max}}] \end{aligned} \tag{1.18}$$

$$G_D(s) = -k_P G_{COM}(s) \cdot \frac{10}{D_{\max}} \tag{1.19}$$

$$G_V(s) = -k_V G_{COM}(s) \cdot \frac{10}{V_{\max}} \tag{1.20}$$

$$G_A(s) = -k_A G_{COM}(s) \cdot \frac{10}{A_{\max}} \tag{1.21}$$

$$G_F(s) = k_{DP} G_{COM}(s) G_{DP}(s) \cdot \frac{10}{F_{\max}} \tag{1.22}$$

1.1.10. Closed-Loop Transfer Function

The closed-loop transfer function of the plant can be derived by using Figure 1.9. Note that the feed-back generator is considered to be the part of the plant. The transfer function of the closed loop system can be computed from the transfer functions of the individual components derived above. It is useful to first derive the open-loop transfer function (from the signal *out* to *purple arrow* in Figure 1.9). This is easily done by block diagram algebra as follows

$$G_{OL} = -(G_D H_D + G_V H_V + G_A H_A + G_F H_F) \tag{1.23}$$

When the shaking table is in the displacement mode, i.e. the reference signal is displacement, the closed loop transfer function becomes

$$\frac{u_{xfbk}}{R} = \frac{G_R H_D}{1 + G_{OL}} \tag{1.24}$$

In velocity mode, i.e. the reference signal is velocity, closed-loop transfer function takes the following form

$$\frac{\dot{u}_{xfbk}}{R} = \frac{G_R H_V}{1 + G_{OL}} \tag{1.25}$$

In acceleration mode, i.e. the reference signal is acceleration, closed-loop transfer function would be

$$\frac{\ddot{u}_{xfbk}}{R} = \frac{G_R H_A}{1 + G_{OL}} \tag{1.26}$$

LIST OF TABLES

Table 1.1: Auxiliary filter indices for acceleration and displacement measurements.

Composite Signal, y_{fc}	*nh*	*nl*
y_{dc}	-2	0
y_{vc}	-1	+1
y_{ac}	0	+2

LIST OF FIGURES

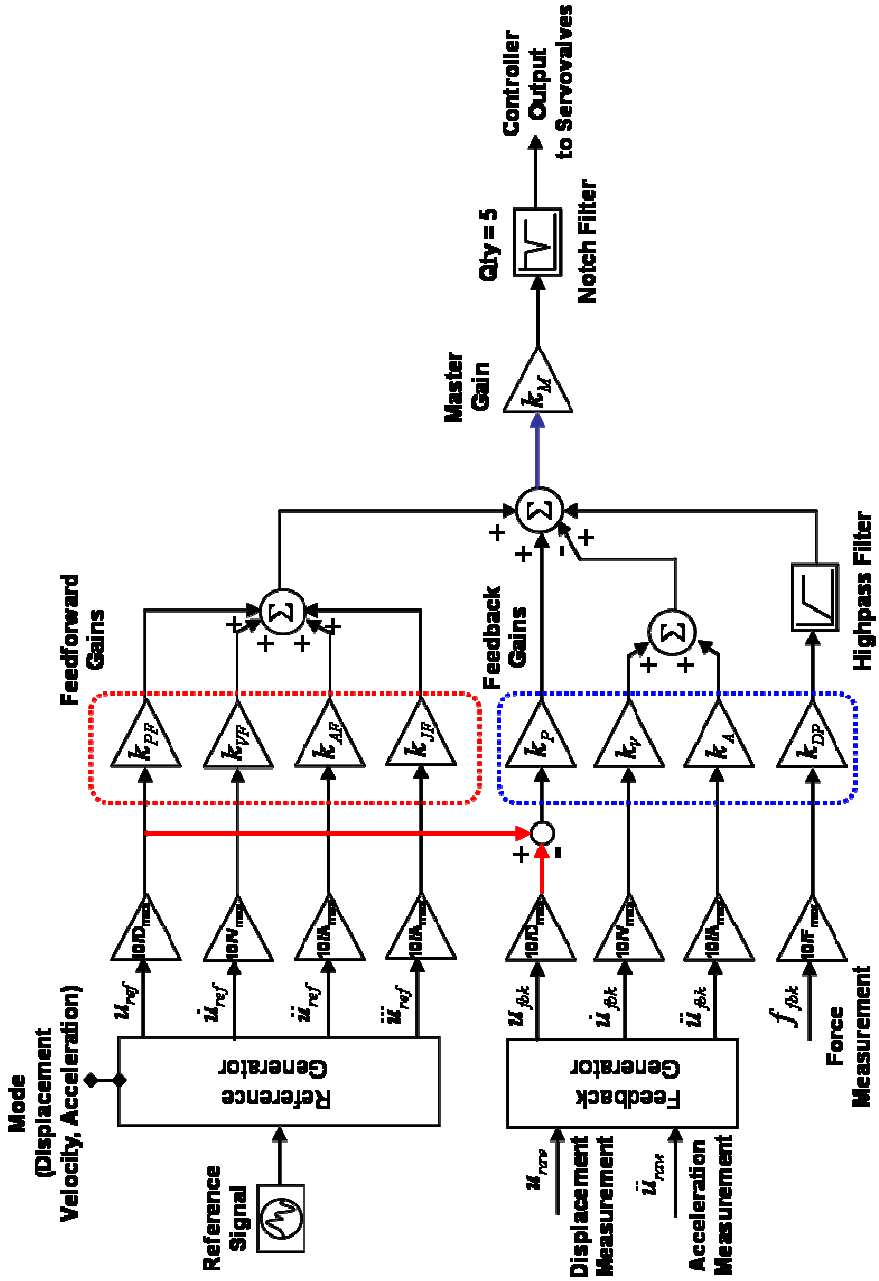

Figure 1.1: Constitutive parts of Three Variable Controller.

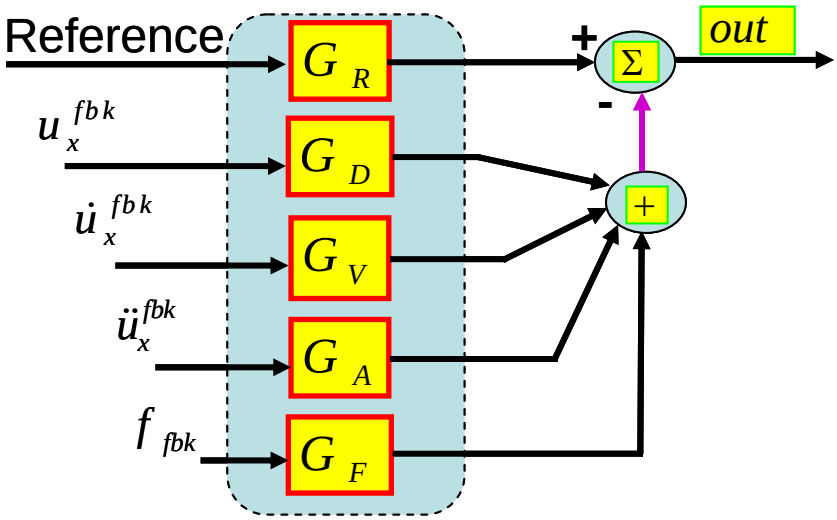

Figure 1.2: Transfer function view of Three Variable Controller.

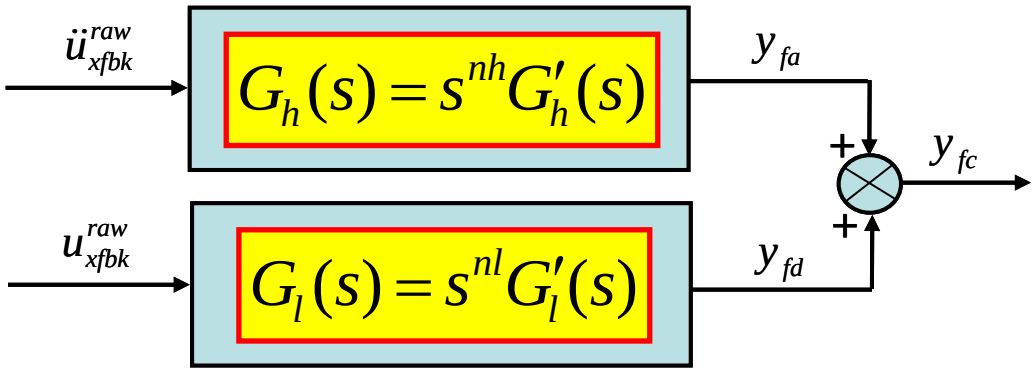

Figure 1.3: Feedback Generator in transfer function view.

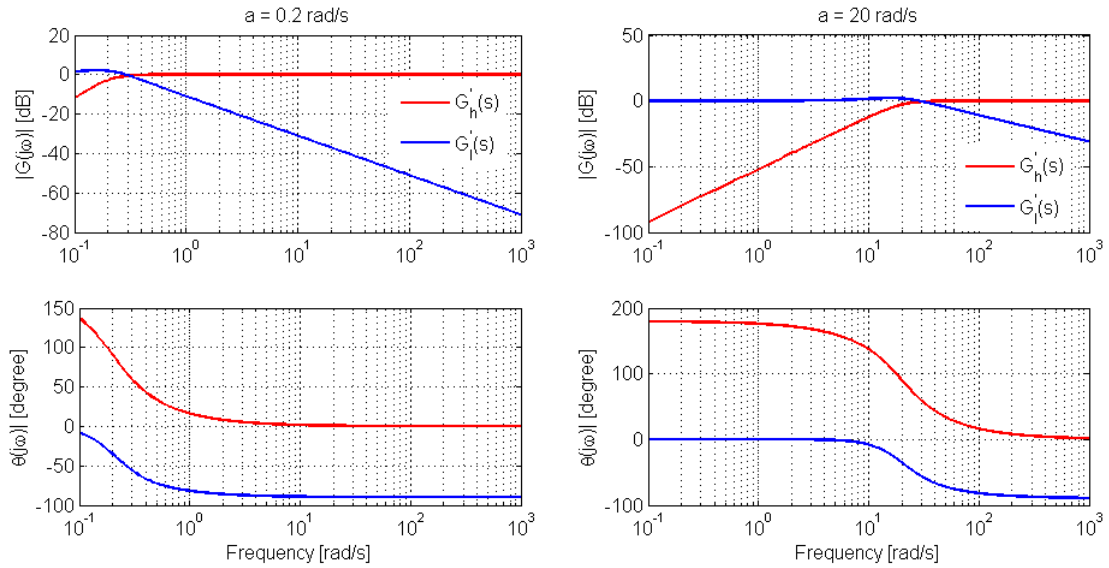

Figure 1.4: Bode plots of the complementary filters for two different values of cross-over frequency a.

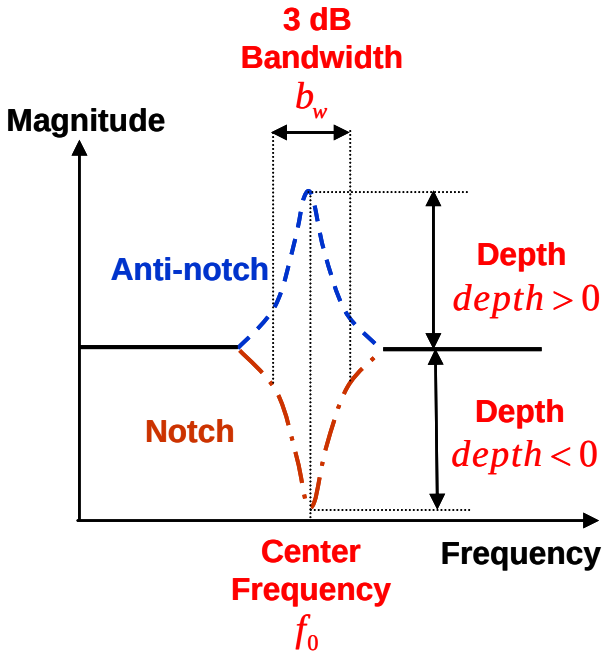

Figure 1.5: Effect of notch filter parameters on the frequency response of notch filters.

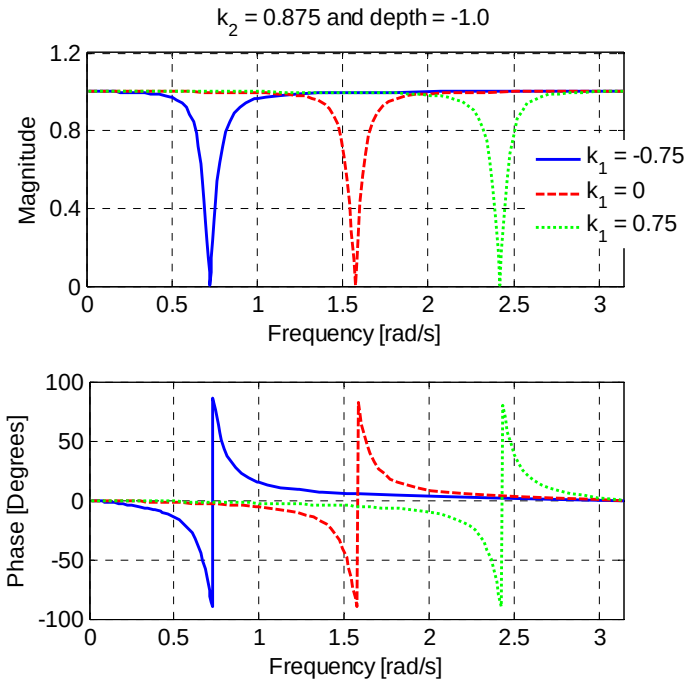

Figure 1.6: Effect of tuning parameter k_1, related to the center frequency f_0.

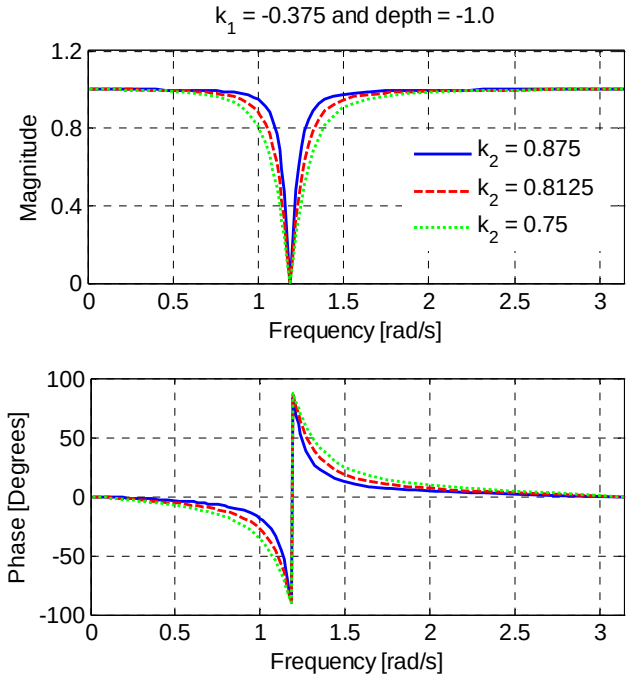

Figure 1.7: Effect of tuning parameter k_2, related to bandwidth b_w

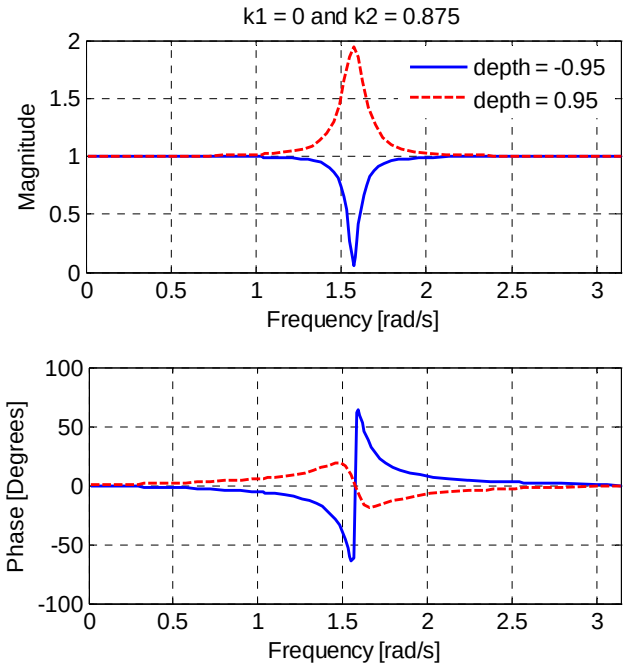

Figure 1.8: Effect of tuning parameter k_3, related to depth *depth.*

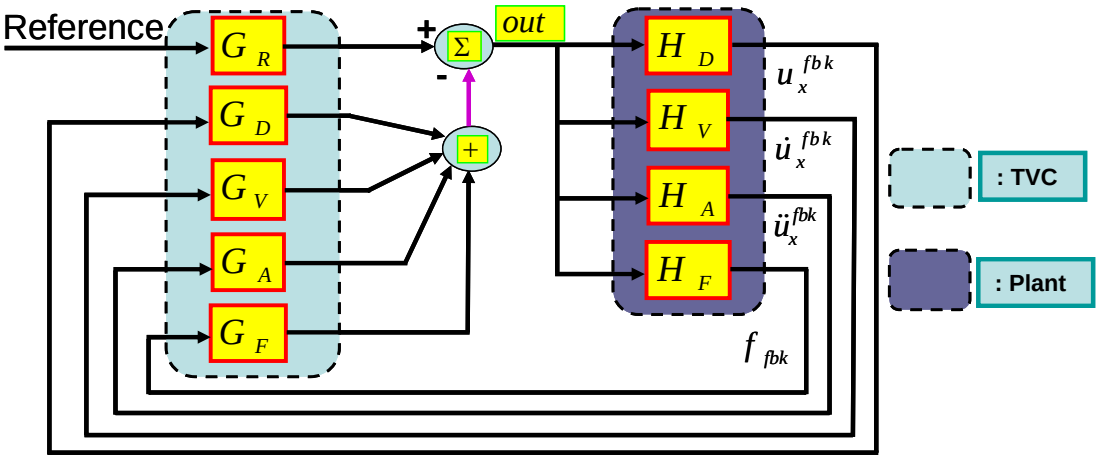

Figure 1.9: TVC and the plant.

REFERENCES

Thoen, B. K., 469D Seismic Digital Control Software. MTS Corporation, 2004.

Stoten, D., Magonette, G., Severn, R.T., and Bairrao, R., Developments in the Automatic Control of Experimental Facilities. *Report No. 9 European Consortium of Earthquake Shaking Tables*, Lisboa, 2001.

Regalia, P.A., Mitra, S.K., and Vaidyanathan, P.P. (1988). "The digital all-pass filter: a versatile signal processing building block." *Proceedings of the IEEE*, Vol. 76(1):19-37.

CHAPTER 2

SERVOHYDRAULIC SYSTEM EQUATIONS

2.1. General Servovalve Analysis

The servovalve model shown in Figure 2.1 is classified in the literature as a four-way, three-land flow-control valve. The quantity $x_v(t)$ is the displacement of the fourth stage spool of servovalve, and positive direction of the spool displacement is also shown in the figure.

The flow coefficient is defined as

$$\bar{K}_v = C_d \cdot \sqrt{2/\rho} \tag{2.1}$$

where C_d is the discharge coefficient and ρ is the mass density of the fluid. Since we are interested only in steady-state characteristics, the compressibility flows are zero and the continuity equations for the two valve chambers are

$$q_L = q_A = q_{SA} - q_{AR} \tag{2.2}$$

and

$$q_L = q_B = q_{SB} - q_{BR} \tag{2.3}$$

here q_L is the flow through the load (going in and out of actuator chambers) and therefore called the load flow. Assuming that the leakage flows are zero, when $x_v > 0$ $q_A = q_{SA}$ and $q_B = -q_{BR}$, and when $x_v < 0$ $q_A = -q_{AR}$ and $q_B = q_{SB}$. Here positive flow indicates that flow is going into the actuator, and negative flow indicates that flow is coming out of the actuator.

The load pressure or pressure drop across the load is defined as

$$P_L = P_A - P_B \tag{2.4}$$

Notice that depending on the servovalve main spool displacement, P_L can be positive or negative; a negative load pressure, P_L, indicates that the actuator piston is moving along the negative direction. Notice that negative and positive directions of the actuator are dictated by the positive and negative sign convention of the servovalve main spool.

Based on the orifice equation for potential flows, also called the square root orifice law, or Bernoulli's equation, the flow through each orifice can be written as

$$q_{SA} = \bar{K}_v A_{SA}(x_v)\sqrt{P_S - P_A} \tag{2.5}$$

$$q_{AR} = \bar{K}_v A_{AR}(x_v)\sqrt{P_A - P_R} \tag{2.6}$$

$$q_{SB} = \bar{K}_v A_{SB}(x_v)\sqrt{P_S - P_B} \tag{2.7}$$

$$q_{BR} = \bar{K}_v A_{BR}(x_v)\sqrt{P_B - P_R} \tag{2.8}$$

Most orifice flows occur at high Reynolds numbers. Flows at high Reynolds number are called turbulent flows, while flows at low Reynolds number are called laminar flows. The relationship between pressure drop and flow changes depending on the flow regime. For example, in laminar flow regimes flow becomes linearly proportional with pressure drop, not with the square-root of the pressure drop (Merritt, 1967).

The orifice areas depend on valve geometry and four equations are required to define the areas $A_{SA}, A_{BR}, A_{SB}, A_{AR}$ as a function of spool displacement.

$$\begin{aligned} A_{SA} &= A_{SA}\left(x_v\right) \quad A_{BR} = A_{BR}\left(x_v\right) \quad x_v > 0 \\ A_{SB} &= A_{SB}\left(-x_v\right) \quad A_{AR} = A_{AR}\left(-x_v\right) \quad x_v < 0 \end{aligned} \tag{2.9}$$

Thus eleven equations are necessary to define load flow as a function of valve opening and and load pressure

$$Q_L = Q_L\left(x_v, P_L\right) \tag{2.10}$$

The plot of (2.10) is known as “pressure-flow curves”. In the vast majority of cases the servovalve orifices are “matched” and “symmetrical”, although this is not the case for LHPOST valves, it is still very important to understand the flow characteristics of matched and symmetric valves.

Matched orifices require that

$$\begin{aligned} A_{SA} &= A_{BR} \\ A_{SB} &= A_{AR} \end{aligned} \tag{2.11}$$

and symmetrical orifices require

$$A_{SA}(x_v) = A_{SB}(-x_v)$$
$$A_{BR}(x_v) = A_{AR}(-x_v) \tag{2.12}$$

Based on the matched and symmetric nature of the orifices, all the areas can be defined with a single area A_v. It should be noted that during the manufacturing process, great care is taken to ensure that the orifice areas are matched and symmetrical, otherwise valves will exhibit peculiar valve coefficients near neutral (Merritt, 1967).

If the orifices are both matched and symmetrical, flows will exhibit the following property

$$q_{SA} = q_{BR} \tag{2.13}$$

$$q_{SB} = q_{AR} \tag{2.14}$$

this translates into $q_A = q_B$ assuming that the leakage flows are negligible. Substitute (2.5), (2.8) and (2.11)a into (2.13) and assuming that P_R is zero will yield the following

$$P_S = P_A + P_B \tag{2.15}$$

Notice that equation (2.14) will yield the same result. If equations (2.4) and (2.15) are solved for P_A and P_B, the following expressions can be found

$$P_A = \frac{P_S + P_L}{2} \tag{2.16}$$

$$P_B = \frac{P_S - P_L}{2} \tag{2.17}$$

For a matched and symmetrical valve with no load, i.e. P_L = 0, the pressure in each actuator chamber will be the same. As load is applied, the pressure in one chamber will increase as the other will decrease the same amount. Thus, the pressure drop across the orifices (AS) and (BR) will be the same and total pressure drop across the valve will be P_L; this verifies (2.13). Similarly (2.14) can be verified, use $P_L = P_A - P_B < 0$ and (2.15), then solve for P_A and P_B. Note that the equal pressure drop property across the orifices for a matched and symmetric valve is a property that is sought after also for non-matched/non-symmetric orifices.

2.1.1. Load Flow Equation

Now we can derive the load flow equation for an ideal critical center valve with matched and symmetrical orifices based on the above observations. Ideal critical center valve is defined as the orifice edges are perfectly square with no rounding and that there is no radial clearance between the spool and the sleeve. Since the geometry is assumed to be ideal, we can assume that the leakage flows q_{AR} and q_{SB} are zero for x_v>0, and q_{BR} and q_{SA} are zero for x_v<0. Based on this simplification, we can write the following equation by substituting (2.16) and (2.5) into (2.2)

$$q_L = q_{SA} - q_{AR} = q_{SA} = \hat{K}_v A_v(x_v)\sqrt{P_S - P_L} \quad x_v > 0 \tag{2.18}$$

Notice that $\hat{K}_v = \bar{K}_v / \sqrt{2}$ in (2.18), and $q_{AR} = 0$. For the negative spool displacement q_{AR} becomes the return flow from the corresponding actuator chamber to the return line, and again assuming that the leakage flows are zero, we can obtain the load flow

equation for the negative spool displacement, substitute (2.16) and (2.6) into (2.2) (assuming that P_R is equal to zero)

$$q_L = q_{SA} - q_{AR} = -q_{AR} = -\hat{K}_v A_v(x_v)\sqrt{P_S + P_L} \quad \text{for } x_v < 0 \tag{2.19}$$

Equations (2.18) and (2.19) are the pressure - flow equations for an ideal critical center valve with matched and symmetrical orifices. These two equations can be combined into one equation as follows

$$q_L = \hat{K}_v A_v(x_v)\frac{x_v}{|x_v|}\sqrt{P_s - \frac{x_v}{|x_v|}P_L}\ ,\ |x_v| < x_v^{\max} \tag{2.20}$$

Equation (2.20) can further be elaborated for deriving an expression showing a relationship between actuator force, actuator piston velocity (proportional to the flow) and servovalve spool displacement.

At this point assume that rectangular ports are used for the orifices; this way derivations become more tractable. For the rectangular orifice area, we can write

$$A(x_v) = wx_v \tag{2.21}$$

where w is the constant area gradient of the servovalve orifices and x_v is the spool displacement. With a constant area gradient, (2.20) can be written as

$$q_L = \hat{K}_v wx_v\sqrt{P_s - \frac{x_v}{|x_v|}P_L}\ ,\ |x_v| < x_v^{\max} \tag{2.22}$$

$$q_L = \hat{K}_v wx_v^{\max}\frac{x_v}{x_v^{\max}}\sqrt{P_s - \frac{x_v}{|x_v|}P_L} \tag{2.23}$$

$$q_L = \hat{K}_v w x_v^{\max} \sqrt{P_s} \frac{x_v}{x_v^{\max}} \sqrt{1 - \frac{x_v}{|x_v|} \frac{P_L}{P_s}} \tag{2.24}$$

Note that the maximum load flow occurs when there is a full pressure drop (P_s) across the servovalve and the orifice area is fully open. This flow can be written as

$$q_{\max} = \hat{K}_v \cdot w \cdot x_v^{\max} \cdot \sqrt{P_s} = \hat{K}_v \cdot A_v^{\max} \cdot \sqrt{P_s} \tag{2.25}$$

where $A_v^{\max}$ is the maximum orifice area. By using (2.25), (2.24) can be written as

$$q_L = q_{\max} \cdot \frac{x_v}{x_v^{\max}} \sqrt{1 - \frac{x_v}{|x_v|} \frac{P_L}{P_s}} \tag{2.26}$$

$$\frac{q_L}{q_{\max}} = \frac{x_v}{x_v^{\max}} \sqrt{1 - \frac{x_v}{|x_v|} \frac{P_L}{P_s}} \tag{2.27}$$

Equation (2.27) is the dimensionless relationship between the load flow and the load pressure. Load pressure, P_L , can be written from (2.27) as

$$P_L = \frac{|x_v|}{x_v} \cdot P_s \left[1 - \left(\frac{q_L / q_{\max}}{x_v / x_v^{\max}} \right)^2 \right] \tag{2.28}$$

Multiply both sides of (2.28) by the actuator area

$$P_L \cdot A_{act}^{eq} = \frac{|x_v|}{x_v} \cdot \left(P_s \cdot A_{act}^{eq} \right) \cdot \left[1 - \left(\frac{q_L / q_{\max}}{x_v / x_v^{\max}} \right)^2 \right] \tag{2.29}$$

$$\frac{F_{act}}{F_{act}^{\max}} = \frac{|x_v|}{x_v} \cdot \left[1 - \left(\frac{q_L / q_{\max}}{x_v / x_v^{\max}} \right)^2 \right] \tag{2.30}$$

$$\frac{F_{act}}{F_{act}^{\max}} = \frac{|x_v|}{x_v} \cdot \left[1 - \left(\frac{\left(V_{act} \cdot A_{act}^{eq}\right) / \left(V_{act}^{\max} \cdot A_{act}^{eq}\right)}{x_v / x_v^{\max}} \right)^2 \right] \tag{2.31}$$

$$\frac{F_{act}}{F_{act}^{\max}} = \frac{|x_v|}{x_v} \cdot \left[1 - \left(\frac{V_{act} / V_{act}^{\max}}{x_v / x_v^{\max}} \right)^2 \right] \tag{2.32}$$

Where F_{act} and V_{act} are the instantaneous actuator force and piston velocity, respectively. In order to emphasize the dimensionless character of (2.32), a set of new parameters are introduced: $F_0 = \frac{F_{act}}{F_{act}^{\max}}$: dimensionless actuator force; $V_0 = \frac{V_{act}}{V_{act}^{\max}}$: dimensionless velocity of the actuator piston; $\overline{x}_v = \frac{x_v}{x_v^{\max}}$: dimensionless servovalve spool displacement. By using the dimensionless parameters, (2.32) can be written in the following form

$$F_0 = \frac{|V_0|}{V_0} \cdot \left[1 - \left(\frac{V_0}{\overline{x}_v} \right)^2 \right], \quad |\overline{x}_v| < 1 \tag{2.33}$$

Equation (2.33) expresses the actuator force as a function of actuator piston velocity and servovalve spool displacement in a dimensionless way. It is called as the servo-hydraulic system equation. It should be emphasized that (2.33) is a direct result of the square root orifice law (or Bernoulli's equation).

Figure 2.2 is the plot of (2.33) for different normalized spool displacements. These curves can be interpreted as the phase plane capacity for motion of the actuator servovalve combination. It is interesting to note that in the second and fourth

quadrants it is possible to obtain a normalized velocity greater that unity although the effective supply pressure remains constant. In these quadrants the servovalve is acting as a throttling device for taking energy from the load (Clark, 1983).

In quadrants I and III the actuator velocity reaches to its maximum value actuator force reaches to zero, and when the actuator force reaches its maximum the actuator velocity reaches to zero. Two observations can be made from Figure 2.2: (i) nonlinearity of flow (proportional to the piston velocity) - load pressure relation increases with increasing load pressure, and (ii) non-linearity between piston velocity and actuator force is also a function of spool opening.

Equation (2.33) can be rearranged to give an expression for spool displacement as

$$\bar{x}_v = \frac{V_o}{\sqrt{1 - \frac{V_o}{|V_o|} F_o}} \tag{2.34}$$

Again note that (2.34) is a direct result of Bernoulli's equation. In order to investigate the effect of Bernoulli's equation on the spool movement, it is assumed that a harmonic motion is reproduced by the servovalve-actuator combination given as

$$\begin{aligned} V_0 &= \bar{V}_0 \cos(\theta) \\ F_0 &= \bar{F}_0 \cos(\theta) \end{aligned} \tag{2.35}$$

Two amplitude sets are considered for the velocity and force amplitudes as $\bar{V}_0 = 0.8,\ \bar{F}_0 = 0.8$ and $\bar{V}_0 = 0.6,\ \bar{F}_0 = 1.0$. The plot of spool motion, (2.34), versus cycle position θ for the harmonic motions given in (2.35) with the specified

amplitudes are shown in Figure 2.3. Note the skewed and anti-symmetric distortion caused by the Bernoulli's equation, and the "switching" at zero velocity (or maximum force) of the servovalve spool opening. Another way to look at the pressure switching phenomenon can be possible through superimposing the plots of (2.35) on the phase plane.

The harmonic motion shown as an ellipse given in dark green line passes through the peak force and the harmonic motion shown as a circle with light green line forces spool displacement to pass beyond the 80% opening curve (shown as dashed purple line). It is documented in Clark (1983) that a possible safe design can be made from two conditions: (i) keep the required force less than or equal to 95% of the maximum, and (ii) keep the required spool opening to less than or equal to 80%. The harmonic motions given in (2.35) violate the given safe design criterion which shows itself as extreme motion of the spool motion at zero velocity.

2.2. Servovalves on LHPOST and Minimum Waveform Distortion Criteria

Following figure shows a servovalve and a single ended actuator in "Extent" and "Retract" directions. $\bar{V}$ and $\underline{V}$ are the extent and retract velocities of the actuator piston, respectively; P_S and P_R are the supply and return pressures; $\bar{P}_1$ and $\bar{P}_2$ are the actuator chamber pressures for the extent direction, whereas $\underline{P}_1$ and $\underline{P}_2$ are the chamber pressures for the retract direction; A_1 and A_2 are the tension and compression areas, respectively.

Design criterion for achieving minimum-waveform-distortion for single-ended actuators is to keep the no load pressures, i.e. zero force on the actuator, within the actuator the same for each direction of travel while maintaining the same constant velocity for both the extent and retract directions. This way there will be no pressure discontinuity in the actuator chambers when the actuator piston changes direction of motion.

It is known that for servovalves with matched and symmetric orifices supply pressure can be written in terms of actuator chamber pressures as (Merritt, 1967)

$$P_S = P_1 + P_2 \tag{2.36}$$

In Equation (2.36) it is assumed that the return pressure is zero. We can write the following for the no load ($P_L = 0$) pressure case

$$P_1 \cdot A_1 = P_2 \cdot A_2 \tag{2.37}$$

Notice that P_1 and P_2 are set to be $\bar{P}_1 = \underline{P}_1 = P_1$ and $\bar{P}_2 = \underline{P}_2 = P_2$, and $\bar{V} = \underline{V} = V$ as the “minimum-wave-form-distortion” criteria requires. From (2.36) and (2.37) we can write

$$P_1 = \frac{A_2}{A_1 + A_2} P_S \tag{2.38}$$

$$P_2 = \frac{A_1}{A_1 + A_2} P_S \tag{2.39}$$

By using above constraints $\overline{P}_1 = \underline{P}_1 = P_1$, $\overline{P}_2 = \underline{P}_2 = P_2$ and $\overline{V} = \underline{V} = V$ in parallel with (2.36) and (2.37), we can find the valve port window ratios necessary for achieving minimum waveform distortion for single ended actuators.

Four flows shown in Figure 2.5 can be found using Bernoulli's equation; note that in the following equations P_R is set to zero. For the extent direction, flows are

$$q_1 = A_1 \cdot V = K_v w_1 x_{sv} \sqrt{P_S - P_1} \tag{2.40}$$

$$q_2 = A_2 \cdot V = K_v w_2 x_{sv} \sqrt{P_2} \tag{2.41}$$

and for the retract direction, flows are

$$q_3 = A_1 \cdot V = K_v w_3 x_{sv} \sqrt{P_1} \tag{2.42}$$

$$q_4 = A_2 \cdot V = K_v w_4 x_{sv} \sqrt{P_S - P_2} \tag{2.43}$$

Where w_1, w_2, w_3 and w_4 are valve port window widths, x_{sv} is the servovalve spool displacement, which is taken to be the same for each direction, and K_v is a constant. Notice that the port window width times the servovalve spool displacement gives us the orifice area. From (2.40), (2.41), (2.42) and (2.43) we can write the following

$$K_v w_1 x_{sv} = \frac{A_1 V}{\sqrt{P_S - P_1}} \tag{2.44}$$

$$K_v w_2 x_{sv} = \frac{A_2 V}{\sqrt{P_2}} \tag{2.45}$$

$$K_v w_3 x_{sv} = \frac{A_1 V}{\sqrt{P_1}} \tag{2.46}$$

$$K_v w_4 x_{sv} = \frac{A_2 V}{\sqrt{P_S - P_2}} \tag{2.47}$$

The servovalves provided for LHPOST have rated peak flow value of 2700gpm when there is 1000psi pressure drop across the actuator control ports- 500psi drop on an individual flow path, and the valve port window is fully open. 2700gpm rating is for the actuator compression area to return flow path, which is indicated with the label number three in Figure 2.5. Port number three has the maximum window width of 10in (Gram, Marty from MTS, personal communication). Therefore port window widths for the four flow paths will be normalized with respect to the port window three.

By using (2.36), (2.37) and (2.44), (2.45), (2.46), (2.47) we can find port window ratios required for minimum waveform distortion as follows

$$\frac{w_1}{w_3} = \left(\frac{A_2}{A_1}\right)^{1/2} \quad \frac{w_2}{w_3} = \left(\frac{A_2}{A_1}\right)^{3/2} \quad \frac{w_3}{w_3} = 1 \quad \frac{w_4}{w_3} = \frac{A_2}{A_1} \tag{2.48}$$

Notice that the port windows are a function of actuator areas. For LHPOST, actuator piston area ratio is designed as $A_2 / A_1 = 0.64$; by using it, we can find the numerical values of the ratios given in (2.48)

$$\frac{w_1}{w_3} = 0.8 \quad \frac{w_2}{w_3} = 0.512 \quad \frac{w_3}{w_3} = 1 \quad \frac{w_4}{w_3} = 0.64 \tag{2.49}$$

For a given servovalve spool displacement, with these port window ratios velocity of the actuator piston and the pressure inside the actuator chambers will be the same for each direction, therefore achieving minimum waveform distortion criteria. Figure 2.6 shows the orifice port windows for LHPOST servovalves designed to compensate for unequal area actuators. x_v^{max} is the valve stroke, which is manufactured to be $\pm$ 0.75in.

Now consider the case in which a standard servovalve with same orifice areas is used. We can write the flows for the extent and retract directions respectively as follows,

$$q_1 = A_1\bar{V} = K_v w_{sv} x_{sv}\sqrt{P_S - \bar{P}_1} \tag{2.50}$$

$$q_2 = A_2\bar{V} = K_v w_{sv} x_{sv}\sqrt{\bar{P}_2} \tag{2.51}$$

And

$$q_3 = A_1\underline{V} = K_v w_{sv} x_{sv}\sqrt{\underline{P}_1} \tag{2.52}$$

$$q_4 = A_2\underline{V} = K_v w_{sv} x_{sv}\sqrt{P_S - \underline{P}_2} \tag{2.53}$$

Notice that, one of the requirements, (2.36), for minimum waveform distortion must be relaxed which in turn automatically relaxes the same velocity for each direction requirement. From (2.37) and (2.50), (2.51), (2.52), (2.53) we can find the actuator chamber pressures in *psi* for the extent and retract directions as follows (here the supply pressure is assumed to be 3000psi),

$$\bar{P}_1 = 623 \;\; \bar{P}_2 = 974 \;\; \underline{P}_1 = 1521 \;\; \underline{P}_2 = 2376 \tag{2.54}$$

With these pressure values, one can find that the extent velocity is 25% larger than the retract velocity and also there will be a discontinuity in chamber pressures when ever the actuator piston changes directions.

2.3. Single-ended Actuators

Figure 2.7 shows the flows Q_1 and Q_2 from servovalve going in and out of the actuator chambers and another flow path within the actuator chambers indicated with dotted arrows. Continuity equations can be written for the actuator chambers (i.e., control volumes) 1 and 2 by neglecting the flows within the actuator chambers as follows

$$\begin{aligned} \frac{dM_1}{dt} &= \frac{d\left(\rho \cancel{V_1}\right)}{dt} = \rho \frac{d\cancel{V_1}}{dt} + \cancel{V_1} \frac{d\rho}{dt} \\ \frac{dM_2}{dt} &= \frac{d\left(\rho \cancel{V_2}\right)}{dt} = \rho \frac{d\cancel{V_2}}{dt} + \cancel{V_2} \frac{d\rho}{dt} \end{aligned} \tag{2.55}$$

where M_1 and M_2 are the liquid masses inside the actuator chambers 1 and 2, respectively, and $\cancel{V_1}$ and $\cancel{V_2}$ are the instantaneous actuator chamber volumes 1 and 2, respectively. By using the fact that density of the fluid inside control volumes changes in small amounts as a function of pressure only therefore using just the linear terms of the Taylor's series expansion of $d\rho$ (Merritt, 1967), and assuming that the temperature remains constant inside the chambers, (2.55) can be simplified

$$\begin{aligned} Q_1 &= \frac{d\cancel{V_1}}{dt} + \frac{\cancel{V_1}}{\beta_e} \frac{dP_1}{dt} \\ Q_2 &= \frac{d\cancel{V_2}}{dt} + \frac{\cancel{V_2}}{\beta_e} \frac{dP_2}{dt} \end{aligned} \tag{2.56}$$

where β_e is the effective bulk modulus of fluid within the chambers. By substituting $V_1 = V_{10} + x_p A_1$ and $V_2 = V_{20} - x_p A_2$ for the first terms in (2.56), where x_p is the piston displacement, and V_{10} and V_{20} are the initial chamber volumes when the actuator piston is centered, equations of continuity for actuator chambers 1 and 2 can be obtained

$$\begin{aligned} Q_1 &= A_1 \frac{dx_p}{dt} + \frac{V_1}{\beta_e}\frac{dP_1}{dt} \\ Q_2 &= -A_2 \frac{dx_p}{dt} + \frac{V_2}{\beta_e}\frac{dP_2}{dt} \end{aligned} \tag{2.57}$$

First and second terms in (2.57) are the flows needed to satisfy the continuity equation due to the motion of the piston and due to the compressibility of the fluid inside the chambers. Instantaneous actuator chamber volumes as a function of piston displacement can be written as follows

$$\begin{aligned} V_1(t) &= V_{10}\left(1 + \frac{x_p(t)}{x_p^{max}}\right) \\ V_2(t) &= V_{20}\left(1 - \frac{x_p(t)}{x_p^{max}}\right) \end{aligned} \tag{2.58}$$

where x_p^{max} is the actuator stroke. Substituting (2.58) into (2.57) and after rearranging terms, equations for chamber pressures P_1 and P_2 can be found

$$\begin{aligned} P_1 &= \frac{\beta_e x_p^{max}}{V_{10}} \int \frac{Q_1 - A_1 \dfrac{dx_p}{dt}}{L_p + x_p} dt \\ P_2 &= \frac{\beta_e x_p^{max}}{V_{20}} \int \frac{Q_2 + A_2 \dfrac{dx_p}{dt}}{L_p - x_p} dt \end{aligned} \tag{2.59}$$

where integrals are evaluated over the duration of a time step. Using P_1 and P_2, actuator driving force can be obtained as $F_{act} = A_1 P_1 - A_2 P_2$.

In Figure 2.7, another flow path from the 1st actuator chamber to the 2nd is indicated with the dotted arrows. This flow is called the actuator cross-port leakage. Actuator cross-port leakage flow is proportional to the load pressure, indicated as P_L in the figure, and can be written as $q_l = c_l P_L$. c_l is the leakage coefficient and it accounts for damping within the actuators (Dyke et al., 1995; Conte and Trombetti, 2000; Williams et al., 2001; Zhao et al., 2005). In this paper, damping due to the cross-port leakage and other sources of viscous damping are included within the mechanical subsystem. Mechanical subsystem model will be presented in Chapter 6.

2.4. Accumulator Model

In order to simulate the average supply pressure drop, adiabatic gas law will be applied to two "fictitious" accumulators attached one on each actuator. Adiabatic condition exists when there is no heat gain or loss by the system (e.g., accumulator tank). For this condition to hold, it is assumed that the gas chamber volume is not changing too quickly (i.e. no internal friction or very little exists in the gas), and there is no heat flow through the walls of the tank. Based on these assumptions, adiabatic gas law can be written

$$P_1 V_1^{\gamma} = P_2 V_2^{\gamma} \tag{2.60}$$

where P_1 and P_2 are gas chamber pressures associated with volumes V_1 and V_2, respectively, and γ is the adiabatic exponent. Note that smaller volume is associated with high pressure and larger volume is associated with smaller pressure.

Equation (2.60) can be used to compute hydraulic supply pressure change with flow demand. Flow demand in excess of hydraulic pump flow discharges the accumulators which in turn cause supply pressure to drop. On the other hand, an excess of hydraulic pump flow charges the accumulators, hence causing the supply pressure to rise. Implementation details along with other modeling issues for the accumulator model used in this work are discussed in Chapter 10.

LIST OF FIGURES

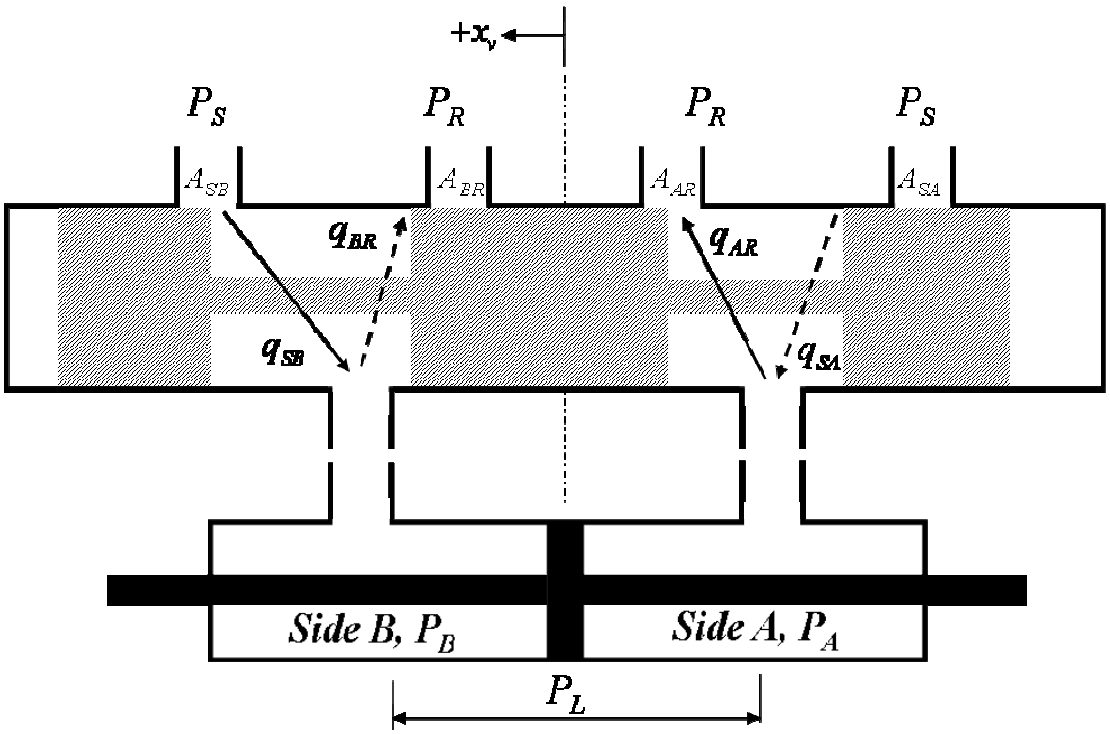

Figure 2.1: Sketch of a three-land four-way servovalve.

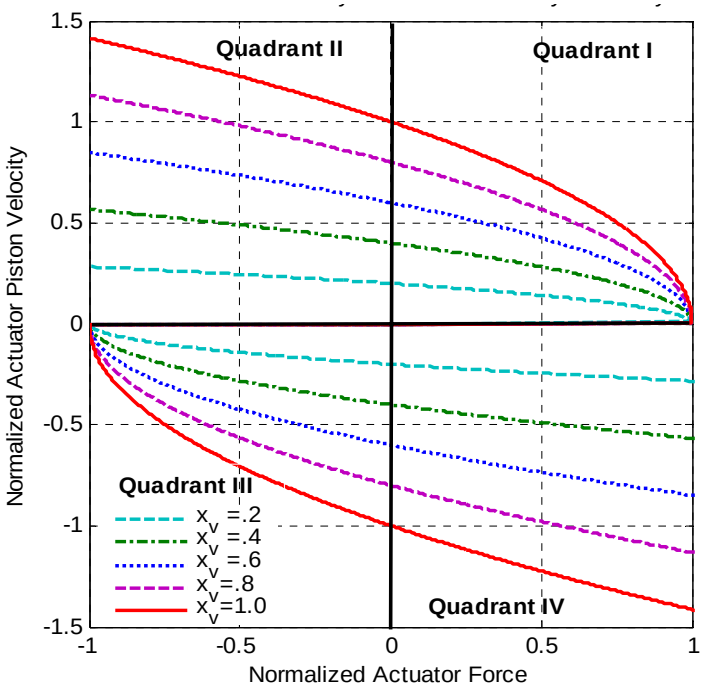

Figure 2.2: Normalized force-velocity curves for a servo-hydraulic system.

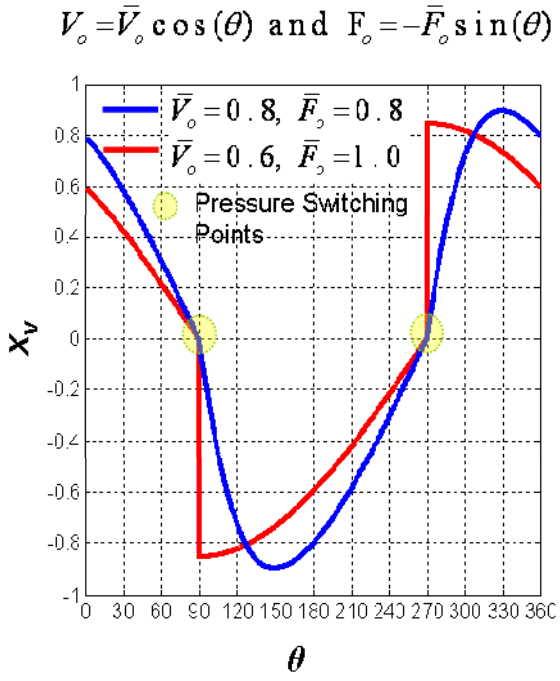

Figure 2.3: Effect of pressure switching on servovalve spool movement.

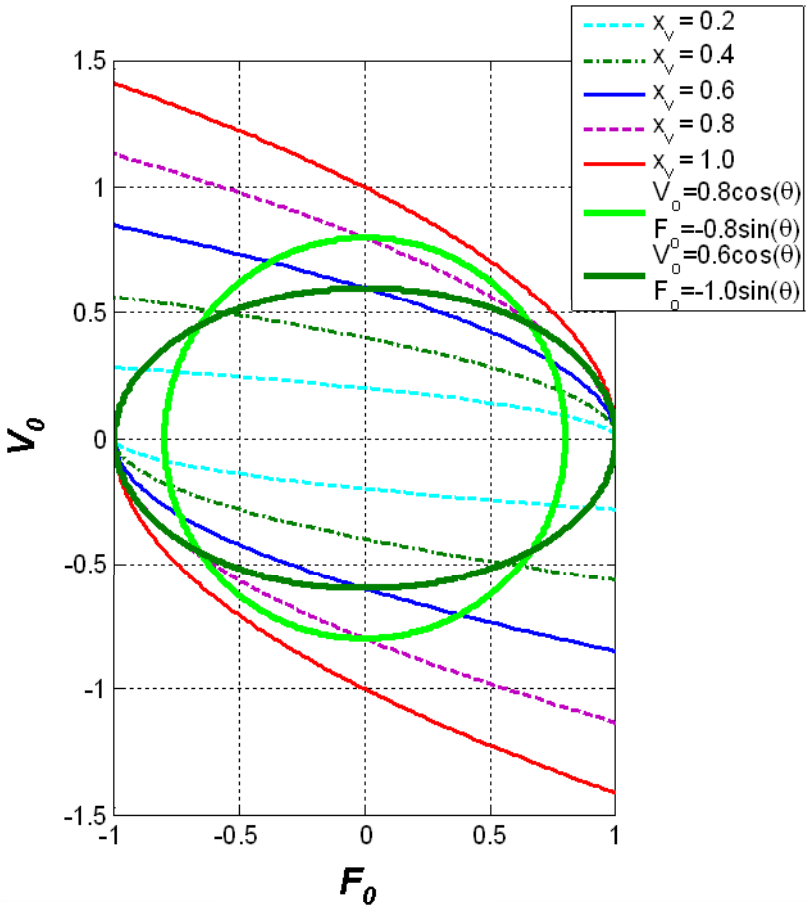

Figure 2.4: Harmonic motions on the phase plot.

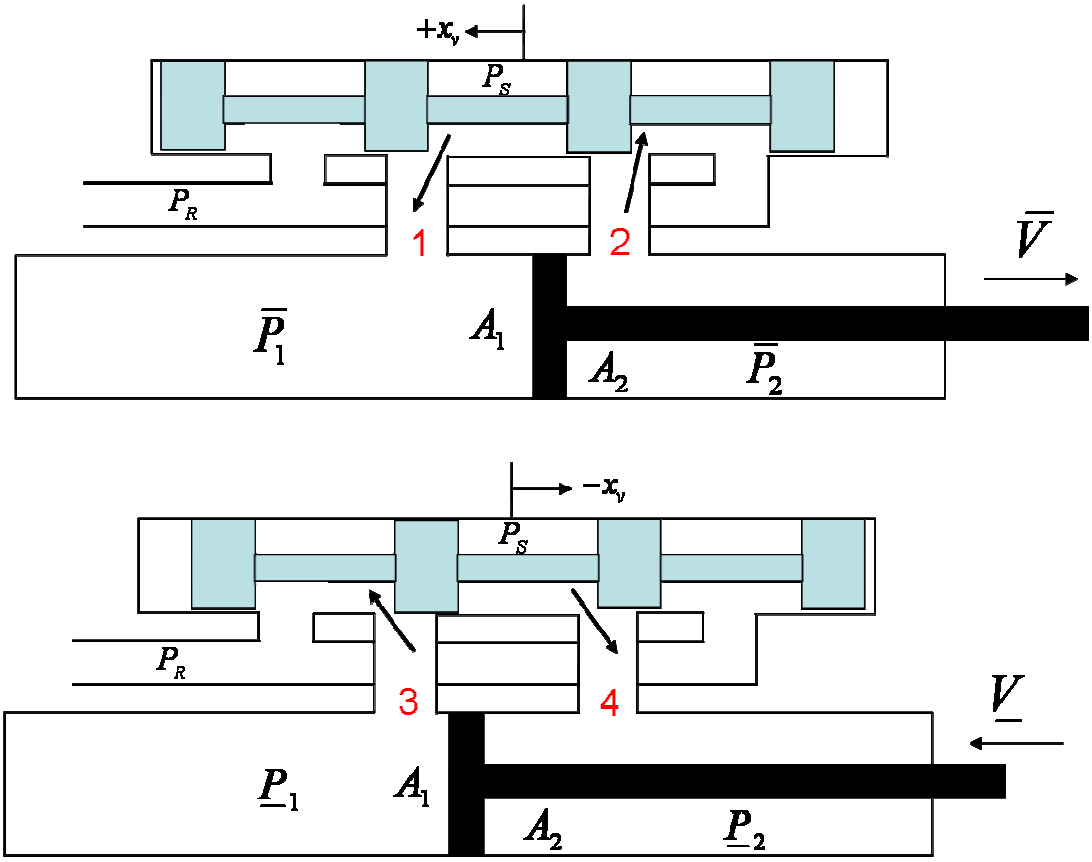

Figure 2.5: 4th stage of the LHPOST servovalve in extent and retract directions and corresponding four flow paths.

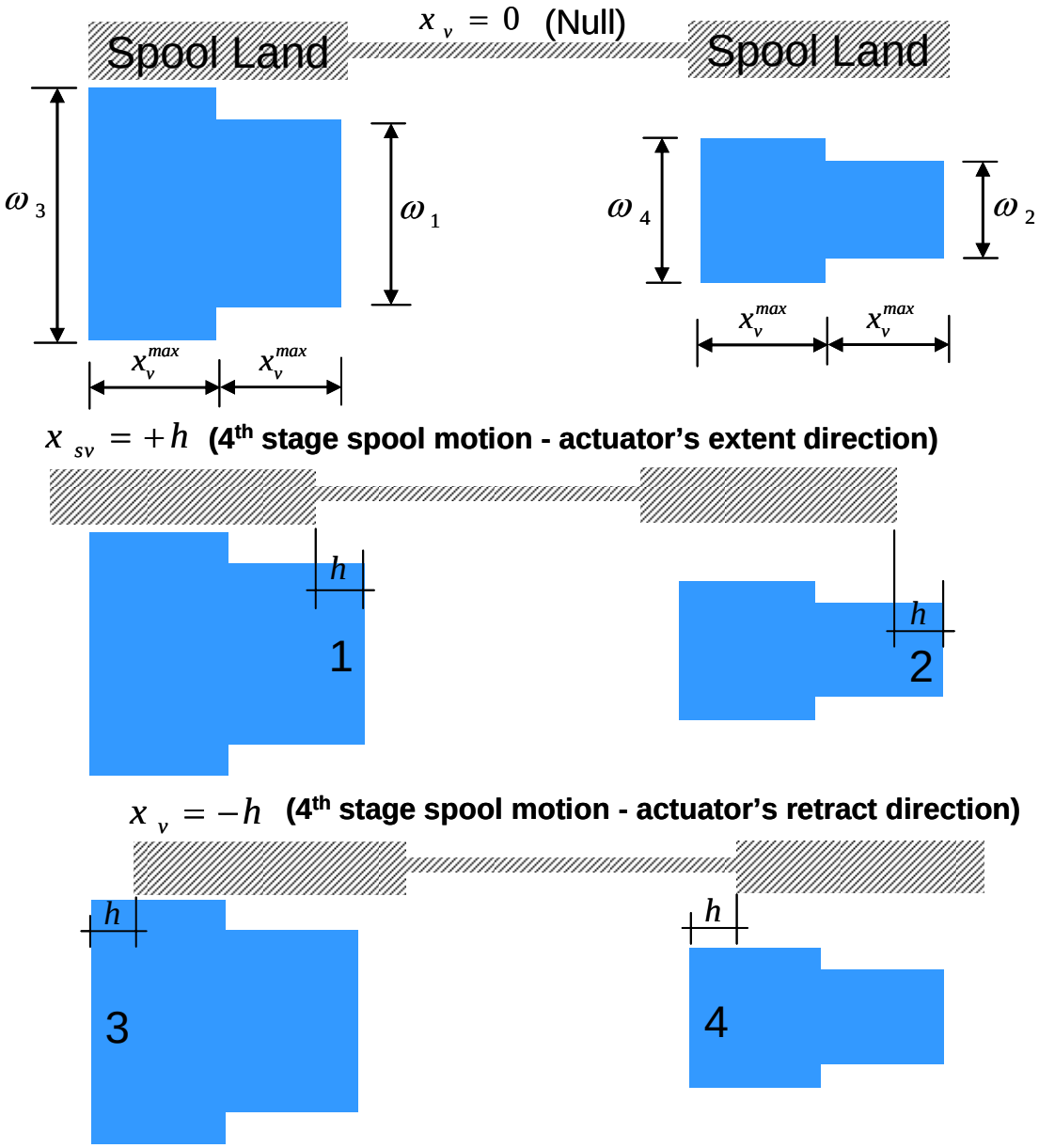

Figure 2.6: Orifice port windows of LHPOST servovalves built for to compensating for unequal piston area actuators.

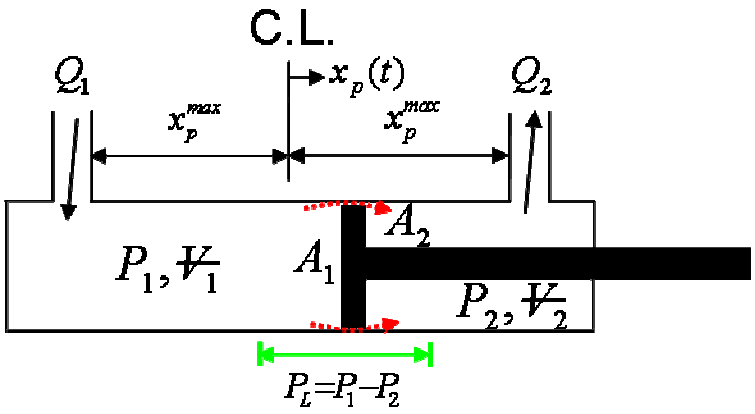

Figure 2.7: Sketch of a snapshot of a single-ended actuator.

REFERENCES

Clark, A.J. (1983). “Sinusoidal and Random Motion Analysis of Mass Loaded Actuators and Valves.” *Proc. National. Conference Fluid Power*, Vol. 37: 168-171.

Conte, J.P., and Trombetti, T.L., Linear Dynamic Modeling of a Uni-axial Servo-Hydraulic Shaking Table System. *Earthquake Engineering and Structural Dynamics*, 29(9), 1375-1404, 2000.

Dyke, S. J., Spencer, B. J., Quast, P., and Sain, M. K. (1995). “Role of control-structure interaction in protective system design.” *J. Eng. Mech., 121(2), 322-338.*

Merritt, H. (1967). *Hydraulic Control Systems*, John Wiley & Sons, New York.

Williams, D. M., Williams, M. S., and Blakeborough, A., Numerical Modeling of a Servohydraulic Testing System for Structures. *Journal of Engineering Mechanics, ASCE*, 127(8), 816-827, 2001.

Zhao, J., Shield, C., French, C., Posbergh, T., Nonlinear System Modeling and Velocity Feedback Compensation for Effective Force Testing. *Journal of Engineering Mechanics*, 131(3), 244-253, 2005.

CHAPTER 3

EXPERIMENTAL CHARACTERIZATION, MODELING AND IDENTIFICATION OF THE NEES-UCSD SHAKE TABLE MECHANICAL SYSTEM

3.1. Introduction

3.1.1. Objectives of the Study

Large servo-hydraulic shaking table systems are essential tools in experimental earthquake engineering. They provide effective ways to subject structural components, substructures, or entire structural systems to dynamic excitations similar to those induced by real earthquakes. In general, components of shake tables can be grouped into three sub-systems: mechanical, hydraulic and electronic. Typically, the steel platen, vertical and lateral bearings, hold-down struts, and actuators are included in the mechanical category; pumps, accumulators, servo-valves, actuators and surge tank are included in the hydraulic category, and finally, controller, signal conditioning units, and feedback sensors are included in the electronic category. A mathematical model of the complete shake table system is required for the planning of future experiments, for the development of safety measures, and for the optimization of the system. The first objective of this study is to develop a simplified analytical model for the mechanical

sub-system of the new NEES-UCSD Large High Performance Outdoor Shaking Table (LHPOST) located at the Englekirk Structural Engineering Center at Camp Elliot Field Station. The second objective is to identify the parameters of the model using the experimental data generated during the extensive shake down tests of the NEES-UCSD LHPOST. The third objective is to validate the model and identified parameters through detailed comparisons of analytical predictions and corresponding experimental data from tests of different types including periodic tests, white noise tests and earthquake simulation tests. Analytical modelling of shake table systems addressing the complex dynamic interaction between the various sub-systems has been and remains the subject of significant research (Hwang et al., 1987; Rinawi et al., 1991; Clark, A., 1992; Conte and Trombetti, 2000; Williams et al., 2001; Shortreed et al., 2001; Crewe and Severn, 2001; Trombetti and Conte, 2002; Twitchell and Symans, 2003; Thoen and Laplace, 2004). A final objective of this paper is to add to this body of knowledge by specific consideration of the large NEES-UCSD LHPOST. It is envisioned that the resulting analytical model of the mechanical sub-system will be used in future studies to comprehensively model the entire shake table system including all sub-systems mentioned above.

3.1.2. Overview of the NEES-UCSD LHPOST

The new NEES-UCSD LHPOST located at a site 15 km away from the main campus of the University of California at San Diego ($32^{\circ}53'37''N$ and$117^{\circ}06'32''W$), is a unique outdoor experimental facility that enables next generation seismic tests to be conducted on very large structural and soil-foundation-structure interaction systems

(Figure 3.1). The LHPOST consists of a moving steel platen (7.6m wide by 12.2m long); a reinforced concrete reaction block; two servo-controlled dynamic actuators with a force capacity in tension/compression of 2.6MN and 4.2MN, respectively; a platen sliding system (6 pressure balanced vertical bearings with a force capacity of 9.4MN each and a stroke of ±0.013m); an overturning moment restraint system (a pre-stressing system consisting of two Nitrogen-filled hold-down struts with a stroke of 2m and a hold-down force capacity of 3.1MN each); a yaw restraint system (two pairs of slaved pressure balanced bearings along the length of the platen); a real-time multi-variable controller, and a hydraulic power supply system. The technical specifications of the LHPOST include a stroke of ±0.75m, a peak horizontal velocity of 1.8m/s, a peak horizontal acceleration of 4.2g for bare table conditions and 1.0g for a rigid payload of 400 tons, a horizontal force capacity of 6.8MN, an overturning moment capacity of 50MN-m, and a vertical payload capacity of 20MN. The frequency bandwidth is 0-20Hz. Other detailed specifications of the NEES-UCSD LHPOST can be found elsewhere (Van Den Einde et al., 2004).

3.1.3. Model Formulation and Identification Approach

The large lateral displacement of the platen of ± 0.75m and the resulting rotation and elongation of the hold-down struts raise the possibility of non-negligible nonlinear terms in the equations of motion of the mechanical system. As a first task, the equations of motion including nonlinear terms are derived using a Lagrangian approach, and the order of magnitude of the nonlinear terms is estimated. On the basis of the known physical properties of the system and of the operational limits of the

shake table, it is shown that the contributions of the nonlinear terms are small and that a simplified model with a mass, horizontal stiffness, and a dissipative mechanism composed of Coulomb friction and viscous resisting forces is sufficient to capture the salient characteristics of the mechanical sub-system of the LHPOST. Even though more complex models are available in the literature for modelling friction and viscous forces (Bondonet and Filiatrault, 1997), classical discontinuous Coulomb friction and viscous damping models are adopted in this initial study.

The characteristics of the mechanical system are obtained by analysis of the hysteresis loops relating the total feedback actuator force with the feedback displacement, velocity and acceleration of the platen recorded during periodic tests. The procedure takes advantage of the periodicity of the table motion to isolate the inertial, elastic and dissipative forces and their respective dependence on acceleration, displacement and velocity. The approach is restricted to periodic tests, but does not assume *a priori* a linear model. Other complementary identification approaches will be presented elsewhere.

3.1.4. Shakedown Test Program

A large shakedown test program was performed on the LHPOST system to verify compliance with the design specifications, and also to identify the fundamental characteristics of the NEES-UCSD shake table. The tests included periodic, earthquake, and white noise tests. Twelve sinusoidal (S) and twelve triangular (T) tests with rounded waveforms were used with amplitude and frequency characteristics spanning the operational frequency range of the system Table 3.1 and 1.2). For the

earthquake tests, full and scaled versions of historical earthquake records with different characteristics were used. Finally, several white noise tests with different root-mean-square accelerations were performed.

The periodic tests were performed with forces of 0, 1042 and 2085 kN in each of the two hold-down struts. These forces correspond to internal pressures in the hold down struts of 0, 6.9 and 13.8 MPa, respectively. These tests were aimed at determining the effective horizontal stiffness associated with the hold-down struts and also to investigate the effect of vertical loads on the dissipative (friction, damping) forces. All other tests were performed with the operational force of 2085 kN (13.8 MPa Nitrogen pressure) in each of the two hold-down struts. All tests were repeated at least two times to check for repeatability.

3.1.5. Sensors and Data Acquisition System.

Data were acquired by the same built-in sensors and data acquisition (DAQ) system used to control the shake table. The DAQ system has low-pass anti-aliasing filtering capabilities and a default sampling rate of 1024Hz. The displacement of the platen relative to the reaction block was measured by two digital displacement transducers (Temposonics® linear transducers) located on the East and West actuators. The platen acceleration response was measured by two Setra®-Model 141A accelerometers with a range of $\pm 8g$ and a flat frequency response from DC to 300Hz. However, the signal conditioners used for the accelerometers included a built-in analog low-pass filter with cut-off frequency set at 100 Hz. Pressure in the actuator chambers were measured by four Precise Sensors®-Model 782 pressure transducers

with a pressure range from 0 to 68.9 MPa and a (sensor/DAQ) resolution of 689.5 Pa. These pressure transducers are located near the end caps of each actuator. Measured pressures are converted to actuator forces by multiplying them by the corresponding actuator piston areas and combining the contributions from both chambers. The pressure recordings were high-pass filtered to remove static pressure components, but were not low-pass filtered. The velocity of the platen is not measured directly but is estimated by use of a crossover filter that combines the differentiated displacement with the integrated acceleration (Thoen, 2004). The MTS 469D Seismic Controller Recorder software was used to record the digitized data. The sampling rate of the recorder was set at 512 Hz during the tests, and the built-in anti-aliasing digital filter was enabled during the tests.

In all the tests performed, two apparent harmonic signals at 10.66 Hz and 246 Hz were observed repeatedly mainly in the total actuator force and, to a lesser degree, on the table acceleration records. The signal at 10.66 Hz corresponds to the oil column frequency of the system (Conte and Trombetti, 2000; Thoen and Laplace, 2004) which is excited when there is a sudden change in the motion of the platen such as a direction reversal. The most likely source of the second harmonic signal at 246 Hz is the resonance between the pilot stage and the third stage of the servo-valves. Due to low-pass filtering of the acceleration records at 100 Hz, this 246 Hz harmonic signal can be observed only slightly in the acceleration records.

3.2. Analytical Model of the Mechanical Sub-System of the Shake Table

3.2.1. Mechanical Components of the Shake Table System

Figure 3.2 shows a three-dimensional rendering of the mechanical components of the LHPOST including the moving steel platen, two servo-controlled dynamic actuators, a platen sliding system composed of six pressure-balanced bearings, a yaw restraint system with two pressure-balanced bearings on each longitudinal side of the platen, and two pre-stressed Nitrogen-filled hold-down struts providing the overturning moment restraint. The forces exerted on the platen by the horizontal actuators are balanced by: (1) the inertia force due the mass of the platen, hold-down struts and moving parts of the actuators; (2) the elastic restoring force due to the Nitrogen pressure inside the hold-down struts that are inclined when extended; (3) the Coulomb type dissipative forces due to (i) sliding of the platen (wear plates) on the vertical and lateral bearings, (ii) rotation of hinges (swivels) at both ends of the hold-down struts, and (iii) sliding of the actuator arm and piston inside each of the two horizontal actuators; and finally (4) the viscous type dissipative forces due to various sources, such as (i) oil film between the wear plates and the vertical and lateral bearings, (ii) air flow in and out of the hold-down struts, and (iii) cross-port leakage in the horizontal actuators, which accounts for the damping within the actuators (Zhao et al., 2005). It is important to note that the sub-system considered here does not include the compressible oil columns in the actuator chambers. The recorded actuator forces obtained from the pressures on both sides of the pistons already incorporate the oil column effect. However, some contamination with the oil column arises because the

pressure transducers are located at the end caps of the actuators and not directly on the pistons.

3.2.2. Conceptual Model and Summary of Equations of Motion

As a first approximation, the platen is treated as a rigid body of mass M_{pl} which undergoes a total translation u_x along the longitudinal x-axis. The six vertical bearings and the four lateral bearings are modeled as dissipative elements including Coulomb friction and viscous damping. The hold-down struts contribute to the inertial, elastic and dissipative forces on the system. The equation of motion for the mechanical sub-system of the NEES-UCSD LHPOST can be written as

$$F_I(t) + F_E(t) + F_D(t) = F_A(t) \tag{3.1}$$

where $F_A(t)$ is the resultant horizontal longitudinal force from both actuators, and F_I, F_E, and F_D are the inertia, elastic, and damping forces, respectively. These forces can be expressed as

$$F_I = M_e \ddot{u}_x + 2\bar{M}'_e \left(\frac{u_x}{h}\right)^2 \ddot{u}_x + 2\bar{M}'_e \left(\frac{\dot{u}_x}{h}\right)^2 u_x \tag{3.2}$$

$$F_E = K_e u_x + K'_e \left(\frac{u_x}{h}\right)^2 u_x \tag{3.3}$$

$$F_D = \left[F_\mu + C_e \left|\dot{u}_x\right|^\alpha + 2c_\beta \left|\frac{u_x}{h}\right|^{1+\beta} \left|\dot{u}_x\right|^\beta + \mu_e^{(iv)} F_{hd} \left(\frac{u_x}{h}\right)^2 \right] sign(\dot{u}_x) \tag{3.4}$$

where the meaning of the various terms is given below.

Effective Masses. The effective mass terms appearing in Equation (3.2) are given approximately by

$$M_e = M_{pl} + 2M_{act} + 2\bar{M}_e, \qquad \bar{M}_e = \frac{1}{3}M_1\left(\frac{l_0}{h}\right)^2 + \frac{1}{3}M_2$$
$$\bar{M}'_e = \frac{1}{2}\left[\frac{5}{3}M_2 - \frac{4}{3}M_1\left(\frac{l_0}{h}\right)^2\right] \tag{3.5}$$

where M_{pl} is the mass of the platen; M_{act} is the mass of the moving parts of a single actuator; M_1 and M_2 are the masses of the piston and cylinder of one hold down strut, respectively; and l_0 and h are the corresponding lengths.

The second term in Equation (3.2) amounts to less than 0.05% of the first term, and can be ignored. The last term in Equation (3.2) corresponds to a force of less than 0.25 kN which is also negligible. Thus only the first term in Equation (3.2) is significant. Finally, the combined effective mass $2\bar{M}_e$ of the hold-down struts is of the order of 3% of the mass M_{pl} of the platen.

Effective Horizontal Stiffness due to Hold-Down Struts. Assuming adiabatic conditions, the effective stiffness terms appearing in Eq. (3.3) can be obtained from

$$K_e = \frac{2p_0A}{h}, \qquad K'_e = \frac{1}{2}\left(\frac{\gamma h}{l_0} - 1\right)K_e \tag{3.6}$$

where p_0 is the initial pressure inside the Nitrogen-filled chamber of a hold-down strut, *A* is the cross-section area of the strut cylinder, h is the (fixed) height from pin-to-pin of the hold-down strut in its initial configuration ($u_x = 0$), l_0 is the initial length of the piston, and γ is the gas constant corresponding to the ratio of the heat capacity at constant pressure to that at constant volume. For the hold-down struts of the UCSD-

NEES Table, $h = 3.3m$, $l_0 = 2.1m$, $\gamma = 1.44$ and $u_x \le 0.75m$. In this case, the ratio $\bar{K}_e' \left(u_x / h\right)^2 \Big/ \bar{K}_e$ amounts to less than 3.3 percent. Therefore, the relative contribution of the nonlinear elastic restoring force term is small and can be neglected in most cases. However, for large displacements ($u_x \approx 0.75$ m), the elastic force associated with the nonlinear term can reach a value of about 30 kN which is comparable to some of the components of the dissipative force.

Effective Lateral Dissipative Forces. Finally, the first term in Equation (3.4) corresponds to the Coulomb frictional force given by

$$F_\mu = \mu_e' F_{hd} + \mu_e'' F_{pl+act} + \mu_e''' F_l, \quad \mu_e' = \mu_e'' + 2\mu_{hg}\kappa\left(\frac{a}{h}\right) \tag{3.7}$$

where $F_{hd} = 2p_0 A$ is the initial vertical force due to pre-charge Nitrogen pressure in the hold-down struts, F_{pl+act} is the combined weight of the platen and part of the actuators supported by the vertical bearings; F_l is the time dependent total normal force on the lateral bearings; μ_e'' and μ_e''' are the Coulomb friction coefficients on the vertical and lateral bearings, respectively; μ_{hg} is the Coulomb friction coefficient in the swivels of the hold-down struts; a is the radius of the hinge and κ is a constant that depends on the distribution of forces on the hinge. The second term in Equation (3.4) represents viscous damping in the actuators in which C_e is an effective viscous damping constant and $0 \le \alpha \le 1$. The third term in Equation (3.4) represents viscous damping in the hold down struts with $0 \le \beta \le 1$. Finally, the last term in Equation

(3.4) is a nonlinear term involving friction on the hinges of the hold down struts. In that term

$$\mu_e^{(iv)} = 2\mu_{hg}\kappa\left(\frac{a}{h}\right)\frac{\gamma}{2}\left(\frac{h}{l_0}\right) \tag{3.8}$$

3.3. Parameter Estimation by Analysis of Hysteresis Loops

In this section, the hysteresis loops relating actuator force to displacement, velocity, or acceleration of the table during periodic triangular or sinusoidal tests will be used to determine the most important characteristics of the shake table mechanical system. The basic conceptual model of the system, inspired in part by Equations (3.1) through (3.4) is expressed by

$$M_e\left(u_x\right)\ddot{u}_x\left(t\right) + F_E\left(u_x\right) + F_D\left(\dot{u}_x\right) = F_A\left(t\right) \tag{3.9}$$

where $u_x\left(t\right)$ is the horizontal longitudinal total displacement of the platen, M_e is the effective mass, and F_E, F_D, and F_A are the total elastic, dissipative, and actuator forces, respectively. It is assumed that $M_e\left(u_x\right)$ is an even function of u_x, and that $F_E\left(u_x\right)$ and $F_D\left(\dot{u}_x\right)$ are odd functions of u_x and $\dot{u}_x$, respectively. The simplified model given by Equation (3.9) excludes dependence of F_E and F_D on the history of u_x and $\dot{u}_x$, and ignores certain possible inertial and dissipative terms that depend on products of u_x and $\dot{u}_x$.

The data from periodic tests used in the parameter identification were low-pass filtered, except where noted, with a cut-off frequency of 4 times the fundamental frequency of the test in an attempt to keep the first few harmonics of the potentially

nonlinear response while filtering out higher frequencies. To ensure that the steady-state response had been reached, the analysis of the response was based on the second to last cycle of each test. Finally, in the case of the triangular tests, only the portions of the time histories over which constant velocities had been reached were used in the identification procedure.

The identification approach used here takes advantage of the periodic nature of $u_x(t)$, $\dot{u}_x(t)$, and $\ddot{u}_x(t)$ during a test cycle $(0<t<T)$. Selecting the cycle of test data so that the displacement $u_x(t)$ is positive over the first half $(0<t<T/2)$ of the cycle; the following time instants t_1, t_2, t_3, and t_4 are considered: $0<t_1<T/4$, $t_2=T/2-t_1$, $t_3=T/2+t_1$, and $t_4=T-t_1$. With this notation, the periodicity leads to

$$\begin{aligned} u_x(t_2)&=u_x(t_1),\ \ \dot{u}_x(t_2)=-\dot{u}_x(t_1),\ \ \ddot{u}_x(t_2)=\ddot{u}_x(t_1)\\ u_x(t_4)&=u_x(t_3),\ \ \dot{u}_x(t_4)=-\dot{u}_x(t_3),\ \ \ddot{u}_x(t_4)=\ddot{u}_x(t_3)\end{aligned} \tag{3.10}$$

and

$$\begin{aligned} u_x(t_4)&=-u_x(t_1),\ \ \dot{u}_x(t_4)=\dot{u}_x(t_1),\ \ \ddot{u}_x(t_4)=-\ddot{u}_x(t_1)\\ u_x(t_3)&=-u_x(t_2),\ \ \dot{u}_x(t_3)=\dot{u}_x(t_2),\ \ \ddot{u}_x(t_3)=-\ddot{u}_x(t_2)\end{aligned} \tag{3.11}$$

Applying Equation (3.9) at times t_1 and t_2, t_3 and t_4, t_1 and t_4, and t_2 and t_3 leads to

$$M_e\left(u_x(t_1)\right)\ddot{u}_x(t_1)+F_E\left(u_x(t_1)\right)=\left[F_A(t_1)+F_A(t_2)\right]/2 \tag{3.12}$$

$$M_e\left(u_x(t_3)\right)\ddot{u}_x(t_3)+F_E\left(u_x(t_3)\right)=\left[F_A(t_3)+F_A(t_4)\right]/2 \tag{3.13}$$

$$F_D\left(\dot{u}_x(t_1)\right)=\left[F_A(t_1)+F_A(t_4)\right]/2 \tag{3.14}$$

$$F_D\left(\dot{u}_x(t_2)\right)=\left[F_A(t_2)+F_A(t_3)\right]/2 \tag{3.15}$$

Equations (3.14) and (3.15) indicate that the dissipative forces can be obtained directly from the data. On the other hand, Equation (3.12) and (3.13) indicate that additional considerations need to be made to separate the inertial and elastic forces.

3.3.1. Estimation of Elastic Forces and Effective Horizontal Stiffness

To separate the elastic forces from the inertial and dissipative forces, use is made of the results of periodic triangular tests in which the horizontal acceleration $\ddot{u}_x$ of the platen is zero for intervals of time. In this case, Equations (3.12) and (3.13) reduce to

$$\begin{aligned} F_E\left(\bar{u}_x(t)\right) &= \frac{1}{2}\left[F_A(t) + F_A(T/2 - t)\right] \\ \bar{u}_x(t) &= \frac{1}{2}\left[u_x(t) + u_x(T/2 - t)\right], \qquad (0 < t < T/4) \end{aligned} \tag{3.16}$$

and

$$\begin{aligned} F_E\left(\bar{u}_x(t)\right) &= \frac{1}{2}\left[F_A(t) + F_A(3T/2 - t)\right] \\ \bar{u}_x(t) &= \frac{1}{2}\left[u_x(t) + u_x(3T/2 - t)\right], \qquad (T/2 < t < 3T/4) \end{aligned} \tag{3.17}$$

which provide estimates of $F_E\left(\bar{u}_x\right)$ for $\bar{u}_x > 0$ and $\bar{u}_x < 0$, respectively.

The basic data for the procedure are illustrated in Figure 3.3 (Left) which shows time histories of the recorded platen displacement, velocity and acceleration, and of the actuator force $F_A(t)$ for one cycle of test $T6$ ($u_{\max} = 62.5$ cm , $\dot{u}_{\max} = 25.0$ cm/s , $T = 10$ s). The plots show the original unfiltered data as well as the filtered data after use of a low-pass filter with a cut-off frequency of 0.4 Hz. The unfiltered actuator force data contain harmonic components at the oil

column frequency of 10.66Hz and at 246 Hz. It is apparent from Figure 3.3 (Left) that over portions of the cycle the displacement varies linearly with time, and that the acceleration is practically zero during these intervals.

The relation between F_E and u_x can be obtained from Equations (3.16) and (3.17) by using the time *t* as an internal variable relating $F\left[u_x(t)\right]$ and $u_x(t)$. As an illustration, the results obtained for test T4 ($u_{\max} = 50$ cm, $\dot{u}_{\max} = 10$ cm/s, $T = 20$ s) for pressures of 0, 6.9 MPa, and 13.8 MPa in the hold-down struts are shown in Figure 3.4. It is apparent from Figure 3.4 that the total elastic restoring force depends linearly on the platen displacement, that the elastic force is essentially zero when the hold-down force is zero, and that the elastic force for a hold-down pressure of 6.9 MPa is half of that for the operational hold-down pressure of 13.8 MPa.

The results in Figure 3.4 as well as similar results for other triangular tests, indicate that the elastic restoring force acting on the platen is essentially provided by the Nitrogen pre-charge pressure in the hold-down struts. The effective horizontal stiffness values obtained from the slopes of the lines in Figure 3.4 correspond to $K_e = 1.27$ MN/m for the operational pressure of 13.8 MPa, and $K_e = 0.65$ MN/m for a pressure of 6.9 MPa. The estimates of the stiffness K_e at the operational pressure (13.8 MPa) obtained from all triangular tests are listed in Table 3.1 decreases slightly for tests involving velocities above 50 cm/s (T9-T11). Since the triangular pulses are severely distorted at high velocities, the average stiffness $K_e = 1.266$ MN/m from tests T1-T8 will be taken as the representative value for the effective stiffness. The

experimentally obtained stiffness $K_e = 1.266\,\mathrm{MN/m}$ agrees almost exactly with the theoretical combined stiffness $K_e = 2Ap_0/h$ of the two hold-down struts which takes the value $K_e = 1.26\,\mathrm{MN/m}$ for $A = 0.15\ \mathrm{m}^2$ (effective cross-section area of Nitrogen chamber in each strut), $p_0 = 13.8\ \mathrm{MPa}$ (internal pressure), and $h = 3.3\ \mathrm{m}$ (length of hold-down struts).

Finally, the theoretical equations of motion presented in Section 2 indicate that the total non-dissipative force for $\ddot{u}_x = 0$ can be expressed by $K_e u_x + K'_e \left(u_x/h\right)^2 u_x + 2\bar{M}'_e \left(\dot{u}_x/h\right)^2 u_x$ where K_e, K'_e, and $\bar{M}'_e$ are given by Equations (3.5) and (3.6). The linear nature of the experimentally determined elastic force F_E confirms that the second (cubic) term is negligible compared with the first term. The last term $2\bar{M}'_e \left(\dot{u}_x/h\right)^2 u_x$ is an inertial term associated with the rotation of the hold-down struts. For triangular tests in which $\dot{u}_x^2$ is constant, this term can be confounded with the first term $K_e u_x$ as both are proportional to u_x. The results in Fig. 4 for tests with different velocities, as well as the vanishing stiffness obtained for zero hold-down pressure confirm that the effect of this inertia term is negligible.

3.3.2. Estimation of Effective Mass

Having established that $F_E\left(u_x\right) = K_e u_x$ where $K_e = 1.266\,\mathrm{MN/m}$ $\left(\text{for } p_0 = 13.8\mathrm{MPa}\right)$, then Equations (3.12) and (3.13) can be used to obtain estimates of the effective mass $M_e\left(u_x\right)$ in the form

$$M_e\left(\bar{u}_x(t)\right)\ddot{\bar{u}}_x(t)=\frac{1}{2}\left[F_A(t)-K_e u_x(t)\right]+\frac{1}{2}\left[F_A(T/2-t)-K_e u_x(T/2-t)\right]$$
$$\ddot{\bar{u}}_x(t)=\frac{1}{2}\left[\ddot{u}_x(t)+\ddot{u}_x(T/2-t)\right],\qquad (0<t<T/4) \tag{3.18}$$

for $\ddot{\bar{u}}_x>0$, and

$$M_e\left(\bar{u}_x(t)\right)\ddot{\bar{u}}(t)=\frac{1}{2}\left[F_A(t)-K_e u_x(t)\right]+\frac{1}{2}\left[F_A(3T/2-t)-K_e u_x(3T/2-t)\right]$$
$$\ddot{\bar{u}}_x(t)=\frac{1}{2}\left[\ddot{\bar{u}}_x(t)+\ddot{\bar{u}}_x(3T/2-t)\right],\qquad (T/2<t<3T/4) \tag{3.19}$$

for $\ddot{\bar{u}}_x<0$.

Since during triangular tests, the acceleration spikes at the time of change in velocity and is nearly zero at any other times, sinusoidal tests are preferred to determine the effective horizontal mass. The typical data including $u_x(t)$, $\dot{u}_x(t)$, $\ddot{u}_x(t)$, and $F_A(t)$ are illustrated in Figure 3.3 (Right) for one cycle of the sinusoidal test S9 $\left(u_{\max}=20\text{ cm},\ \dot{u}_{\max}=75.4\text{ cm/s},\ \ddot{u}_{\max}=0.29g,\ T=1.67\text{s}\right)$ performed under the operational hold-down pressure of 13.8 MPa. The original data and the data after a low-pass filter with cut-off frequency of 2.4 Hz had been applied are superimposed in Figure 3.3 (Right). The unfiltered data includes components at the oil-column frequency of 10.66 Hz which are excited each time the velocity of the table changes sign.

The relation between the inertia force $M_e\left(u_x\right)\ddot{u}_x$ and the acceleration $\ddot{u}_x$ for sine tests S9 $\left(\ddot{u}_{\max}=0.29g\right)$ and S10 $\left(\ddot{u}_{\max}=0.51g\right)$ is shown in Figure 3.5 for the operational hold-down pressure of 13.8 MPa. The results obtained indicate that the inertial force for the sinusoidal tests is essentially a linear function of the acceleration

$\ddot{u}_x$, and consequently, that the effective mass M_e is a constant. The slope of the curves in Figure 3.5 indicate that $M_e = 144$ tons. The results for other sinusoidal tests with peak accelerations in the range between 0.1g and 1.2g are similar as shown in Table 3.2: For tests (S1, S2, S3) involving extremely small accelerations (< 0.2% g), the inertial forces are extremely small and the results obtained are not reliable. For test S12 involving large velocities (180 cm/s) and accelerations (1.6g) the sinusoidal pulses are distorted and the results for M_e are not reliable.

The estimate of the effective horizontal longitudinal mass ($M_e = 144$ tons) can be compared with the mass of the platen estimated from drawings to be about 134.8 tons. Also, data recorded on the six vertical pressure balance bearings when the hold-down struts were not pressurized indicate a total weight of 1.613 MN including the weight of the platen and of the cylinders of the two hold-down struts, and part of the weights of the two actuators. The corresponding total mass is 164.5 tons. The effective lateral mass should be smaller than the total vertical mass obtained from the vertical bearings because only the mass of the pistons of the actuators and a fraction of the mass of the hold-down struts affect the lateral mass. Also, the flexibility of the platen, albeit small, would result in a smaller effective mass.

3.3.3. Estimation of the Effective Total Dissipative Forces

Equations (3.14) and (3.15) are used here to separate the total dissipative forces from the inertial and elastic components of the total actuator force. In particular, the dependence of the total dissipative forces on velocity is given by

$$F_D\left(\dot{\bar{u}}_x(t)\right) = \left[F_A(t) + F_A(T-t)\right]/2$$
$$\dot{\bar{u}}(t) = \left[\dot{u}_x(t) + \dot{u}_x(T-t)\right]/2 \qquad (3.20)$$

with $0 < t < T/4$ for $\dot{u}_x > 0$, and $T/4 < t < T/2$ for $\dot{u}_x < 0$.

The typical data required to apply the proposed identification procedure is illustrated in Figure 3.3 (Center) which includes one cycle of the filtered and unfiltered time history plots of the platen response and the total actuator force obtained during test S4 ($\dot{u}_{\max} = 10\,cm/s$, $T = 2.5\,\text{s}$). The unfiltered time history of the total actuator force shows that the signal is contaminated by high frequency noise and by two harmonic signals at 10.66 Hz and 246 Hz. A close examination of the velocity and the total actuator force time histories reveals that a jump in the total actuator force occurs whenever the platen changes direction of motion (i.e., velocity changes sign). To preserve this jump while removing other spurious signals, a FIR filter of order 512 with a cut-off frequency of 8 Hz was used for all tests. This cut-off frequency is well above the frequencies of the tests, but is below the oil-column frequency. The filtered time history in Figure 3.3 (Center) shows that the jump in the total actuator force is preserved, while the high frequency components of this signal are filtered out.

Figure 3.6 illustrates the relation between the total dissipative force and platen displacement (a, b) as well as the relation between the total dissipative force and platen velocity (c, d) for sinusoidal tests S1 ($\dot{u}_{\max} = 1.0$ cm/s), and S4 ($\dot{u}_{\max} = 10$ cm/s). It is apparent from the results in Figure 3.6 and from additional results for tests S2 ($\dot{u}_{\max} = 1.5$ cm/s), and S3 ($\dot{u}_{\max} = 2.5$ cm/s) that the total dissipative force, after reaching a peak of 35 - 45 kN at very low velocities, decreases slightly to 30-35 kN at

a velocity of 1-2 cm/s, and then increases again to about 40 kN for a velocity of 10 cm/s. The initial drop may be associated with a change of the Coulomb friction coefficient from its static value to its dynamic value. The increment of the total dissipative force at higher velocities probably reflects viscous type dissipative forces which do not appear to increase linearly with velocity. Finally, the slightly different behavior at low velocities for the different tests suggests that the dissipative force is not only a function of the instantaneous velocity, but also of some other characteristics of the time-history of motion.

The variation of the total dissipative force at higher velocities can be studied by considering the total dissipative forces obtained at the maximum achieved platen velocities in each of the sinusoidal and triangular tests performed under 13.8, 6.9 and 0.0 MPa Nitrogen pressures in the hold-down struts. The results shown as individual points in Figure 3.7 indicate that the total dissipative force increases with both hold-down pressure and some fractional power of velocity. After some numerical experimentation, it was decided to consider a model of the type

$$F_D(t) = F_{\mu_e} + C_e \left|\dot{u}_x(t)\right|^{0.5} \tag{3.21}$$

in which F_{μ_e} denotes a Coulomb friction force, while C_e is a fractional-power viscous damping coefficient. When this model was applied to the sinusoidal tests for the nominal hold-down pressure of 13.8 MPa, best-fit values of $F_{\mu_e} = 26.00$ kN and $C_e = 44.58$ kN/(m/sec)$^{1/2}$ were obtained. The parameter C_e was then kept fixed at 44.58 kN/(m/sec)$^{1/2}$ and the best fit values of F_{μ_e} for the six groups of tests shown in

Figure 3.7 were obtained. The resulting values of F_{μ_e} for sinusoidal tests with hold-down pressures of 0.0, 6.9, and 13.8 MPa are 5.63, 15.65 and 26.00 kN, respectively. The corresponding values of F_{μ_e} for the triangular tests are 9.69, 16.75 and 25.74 kN, respectively. Clearly, the parameters obtained for the sinusoidal and triangular tests are in reasonable agreement for hold-down pressures of 6.9 and 13.8 MPa. The comparisons of the model and data shown in Figure 3.7 also show a reasonable agreement for these pressures but not for the case of zero pressure.

3.3.4. Decomposition of the Total Dissipative Force

To study further the nature of the dissipative forces, the average of the values of the terms F_{μ_e} obtained from sinusoidal and triangular tests are plotted in Figure 3.8 versus the total vertical force F_z acting on the vertical bearings for the three different hold-down pressures considered. The average values of F_{μ_e} for hold-down Nitrogen pressures of 0.0, 6.9, and 13.8 MPa are 7.66, 16.20, and 25.87 kN, respectively. The corresponding resultant vertical forces F_z based on pressure readings on the six vertical bearings are 1.613, 3.698, and 5.783 MN, respectively. The results in Figure 3.8 indicate that there is a linear relation between F_{μ_e} and F_z, i.e. $F_{\mu_e} = \mu_e F_z$, implying that the term F_{μ_e} does represent a Coulomb friction force acting on the vertical bearings with a friction coefficient of $\mu_e = 0.44\%$. This result would also suggest that the friction force on the lateral bearings is negligible.

The results shown in Figure 3.7 (a, b) indicate that the dissipative forces obtained during the low velocity tests (S1, S2, S3, T1, T2, T3) are somewhat larger

than those calculated from the model. An enlargement of the low velocity zone shown in Figure 3.7 (c, d) indicates that the small differences between model and data appear to be independent of the hold-down pressure level. As shown in Figure 3.7 (c, d), these differences can be accounted for by the additional term $12.04 \cdot e^{(-78.5|\dot{u}_x|)}$ kN for $\dot{u}_x$ in m/sec. This term could represent a correction to the assumed $|\dot{u}_x|^{0.5}$ velocity dependence for low velocities, or a transition from static to dynamic friction coefficients.

The assumed decomposition of the dissipative force as

$$F_D(t) = \mu_e F_z + C_e |\dot{u}_x|^{0.5} + ae^{(-b|\dot{u}_x|)} \tag{3.22}$$

where $\mu_e = 0.44\%$, $C_e = 44.58$ kN/(m/sec)$^{1/2}$, $a = 12.04$ kN and $b = 78.5$ s/m, is shown in Figure 3.9 (low velocity correction is not shown) for the case of nominal hold-down Nitrogen pressure $(F_z = 5{,}783 \text{ kN})$. In this case, the Coulomb friction force in the vertical bearings amounts to 26.0 kN, while the viscous component adds a dissipative force of 44.6 kN at a velocity of 1.0 m/s. The low-velocity correction term adds a force of 12.0 kN at zero velocity, but this term becomes negligibly small for velocities higher than 3 cm/s.

To verify the quality of the identified model of the dissipative forces, the identified and simulated total dissipative forces vs. table displacement curves for tests S1 and S4 are compared in Figure 3.6 (a, b). Also shown in Figure 3.6 (c, d) are the corresponding identified and simulated total dissipative force versus table velocity

curves. It is apparent that the low-velocity correction term needs to be included for test S1 in which the peak velocity is only 1 cm/s.

A final comparison is presented in Figure 3.10 in which the scatter plot of instantaneous values of $F_D(t)$ versus $\dot{u}_x(t)$ for tests S1 through S11 is shown together with the analytical model given by Equation (3.22). It is apparent from Figure 3.10: that the model fits the general trend of the data, and that the scatter is of the order of ± 20 kN. Clearly, it is difficult to isolate the dissipative forces from the inertial and elastic forces as the amplitudes of these forces are significantly larger. The dissipative forces are typically less than 0.08 MN (Test S10) while the inertial and elastic forces can be as large as 2.3 MN (Test S12) and 0.95 MN (Test T8), respectively.

3.3.5. Hysteresis Loops for Triangular Tests

The previous discussion of the dissipative forces is based mostly on the results obtained during sinusoidal tests which involve platen displacements that do not exceed 20 cm. On the other hand, many of the triangular tests involve platen displacements that exceed 50 cm and velocities exceeding 50 cm/s. Because of the large volumes of oil involved (large swept displacements), these triangular tests are of short duration (3-12 seconds) and include only a few (2-3) cycles. Under these conditions, the hysteresis loops for triangular tests exhibit some features which are not clearly observable in the hysteresis loop for the sinusoidal tests.

Figure 3.11 (a, b) show the hysteresis loops relating the instantaneous reduced force, $F_R(t) = F_A(t) - M_e\ddot{u}_x(t) - K_e u_x(t)$, and the corresponding recorded platen displacement $u_x(t)$ for tests T8, and T10. These tests are characterized by maximum

platen velocities of 50, and 100 cm/s, respectively. The values of K_e listed in Table 3.1 ($K_e = 1.27MN/m$ for T8, and $K_e = 1.25MN/m$ for T10) were used in an attempt to have the reduced force $F_R(t)$ represent the total dissipative force $F_D(t)$ without contamination by the apparent changes of stiffness. A value of $M_e = 144$ tons was used in both cases. Also shown in Figure 3.11 (a, b) are the values of $F_D(t)$ calculated by use of Equation (3.22) for the maximum velocity attained during each test. The results suggest that there is an additional nonlinear component of the dissipative force not included in Equation (3.22), which appears to increase with both instantaneous displacement and velocity. This additional dissipative force reaches a peak of 20-70 kN and appears to be significant only when the platen displacement exceeds 50 cm and the platen velocity exceeds 75 cm/s.

3.4. Model Validation

The parameters of the NEES-UCSD LHPOST model identified in the previous section are based on system response data for periodic sinusoidal and triangular excitations. It is important to verify that the resulting model is also capable of representing the more common shake table tests involving earthquake ground motions and white noise excitations. To verify the accuracy of the model, the total actuator force will be simulated by using

$$F_A(t) = M_e \ddot{u}_x(t) + K_e u_x(t) + \left(C_e \left| \dot{u}_x(t) \right|^{\alpha} + F_{\mu_e} \right) sign(\dot{u}_x(t)) \qquad (3.23)$$

and the results will be compared with the total actuator force recorded during various tests. Note that the simulations are based on the actual recorded displacement, velocity and acceleration.

Comparisons of the recorded and simulated total actuator force time- histories for three different tests are shown in Figure 3.12. The comparisons correspond to triangular test T4 ($u_{\max} = 50$ cm, $\dot{u}_{\max} = 10$ cm/s, $T = 20$ s), to an earthquake simulation test using the Northridge 1994 Cedar Hills Station ground motion with a peak acceleration of 1.81g, and a white noise test with 0.10g root mean square acceleration (WN10%g). In order to see the details of the comparisons, only amplified segments of the time histories are shown. It is apparent from the results in Figure 3.12 and, from the rest of the time histories, that the model given by Equation (3.23), with the model parameters estimated previously, is capable of reproducing the recorded total actuator force for different types of tests.

An alternative type of verification consists of using the model to obtain the motion of the platen by integration of Equation (3.23) using the recorded total actuator force as input. The results of such analysis for sinusoidal test SR9 ($u_{\max} = 0.38$ m, $\dot{u}_{\max} = 1.20$ m/s, $\ddot{u}_{\max} = 0.384g$, $T = 2$ s) are shown in Figure 3.13. The recorded total actuator force was low-pass filtered with cut-off frequency of 0.6 Hz and Equation (3.23) was integrated numerically using the fixed-step Runge-Kutta method. The agreement between the recorded and simulated table velocity and displacement is excellent.

3.5. Conclusions

1. A mathematical model for the mechanical components of the NEES-UCSD LHPOST has been presented. It has been shown that several non-linear terms arising from the significant displacements and rotations of the hold-down struts are small, and that a simplified model including an effective horizontal mass, an effective horizontal stiffness due to the pre-charge pressure in the hold-down struts, and dissipative force terms composed of classical Coulomb friction and viscous damping elements is sufficient to simulate the response of the system.

2. The identification of the parameters of the mechanical sub-system of the NEES-UCSD LHPOST by use of the experimental hysteresis loops leads to the following conclusions:

(i) The experimental results indicate that the elastic restoring force acting on the platen is essentially provided by the pre-charge Nitrogen pressure in the hold-down struts, the elastic force is essentially a linear function of the longitudinal displacement of the platen, and the effective horizontal stiffness corresponds to $K_e = 1.27\,\mathrm{MN/m}$ for the operational pressure of 13.8 MPa.

(ii) The best estimate of the effective horizontal longitudinal mass of the table is $M_e = 144$ tons. This vertical mass includes the mass of the platen and of the cylinders of the two hold-down struts, and part of the mass of the two actuators. The experimental data confirm that non-linear inertial terms are small within the range of table motions considered.

(iii) The analysis appears to show that the total dissipative force can be broken down into three main components: (*i*) Coulomb friction acting on the vertical bearings with a friction coefficient of 0.44%, (*ii*) a viscous force proportional to the square root of the velocity and with a damping constant of $44.6\,\text{kN/(m/sec)}^{0.5}$, and (*iii*) a small force decreasing exponentially with the table velocity given by $12.04 \cdot e^{(-78.5|\dot{u}_x|)}$ kN for velocity in m/s. This last component may reflect a transition from static to dynamic friction and becomes negligibly small once the velocity has exceeded a threshold of say 5 cm/s. Additional dissipative forces, not fully identified, arise for large platen displacements (> 50 cm) and velocities (> 75 cm/s).

3. Although the parameters of the model considered herein have been identified by use of the response during periodic sinusoidal and triangular excitations, it has been shown that the resulting model is also capable of representing the more common shake table tests involving earthquake ground motions and white noise excitations.

Chapter 3 is a reprint of the material accepted for publication in Earthquake Engineering and Structural Dynamics (2008), Ozcelik, O., Luco, J.E., Conte, J.P., Trombetti, T., and Restrepo, J.I. The dissertation author was the first author of this paper.

LIST OF TABLES

Table 3.1: Estimates of the Effective Horizontal Stiffness K_e from Triangular Tests

(13.8 MPa Hold-Down Nitrogen Pressure)

Test	**T1**	**T2**	**T3**	**T5**	**T7**	**T9**	**T4**	**T6**	**T10**	**T12**	**T8**	**T11**
Frequency [Hz]	0.05	0.05	0.05	0.10	0.10	0.40	0.05	0.10	0.40	0.67	0.17	0.50
$u_{\max}$ [cm]	5	7.50	12.50	25	37.50	46.88	50	62.50	62.50	67.50	75	75
$\dot{u}_{\max}$ [cm/s]	1	1.50	2.50	10	25	75	10	25	100	180	50	150
K_e [MN/m]	1.25	1.27	1.27	1.25	1.27	1.25	1.27	1.27	1.25	1.24	1.27	1.25

Table 3.2: Estimates of Effective Horizontal Longitudinal Mass M_e from Sinusoidal Tests (13.8 MPa Hold-Down Nitrogen Pressure)

Test	**S4**	**S6**	**S5**	**S7**	**S9**	**S10**	**S8**	**S11**	**S12**
Frequency [Hz]	0.40	0.40	1.00	0.80	0.60	0.80	1.20	1.20	1.43
$u_{\max}$ [cm]	4	10	4	10	20	20	10	20	20
$\dot{u}_{\max}$ [cm/s]	10.05	25.12	25.12	50.24	75.36	100.48	75.36	150.72	179.61
$\ddot{u}_{\max}$ [g]	0.026	0.064	0.161	0.257	0.29	0.515	0.579	1.158	1.644
M_e [tons]	150	158	144	144	144	144	144	144	120

LIST OF FIGURES

Figure 3.1: NEES-UCSD LHPOST with a full-scale 21m high wind turbine mounted on it.

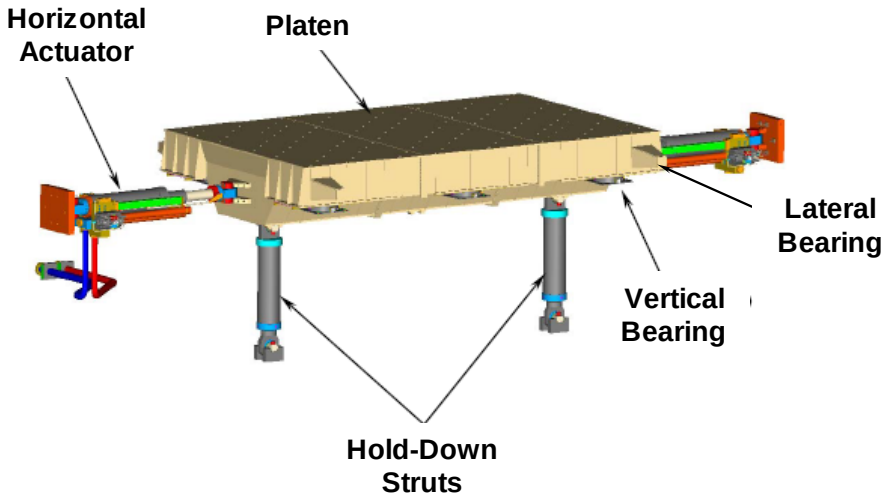

Figure 3.2: Mechanical sub-system of NEES-UCSD LHPOST.

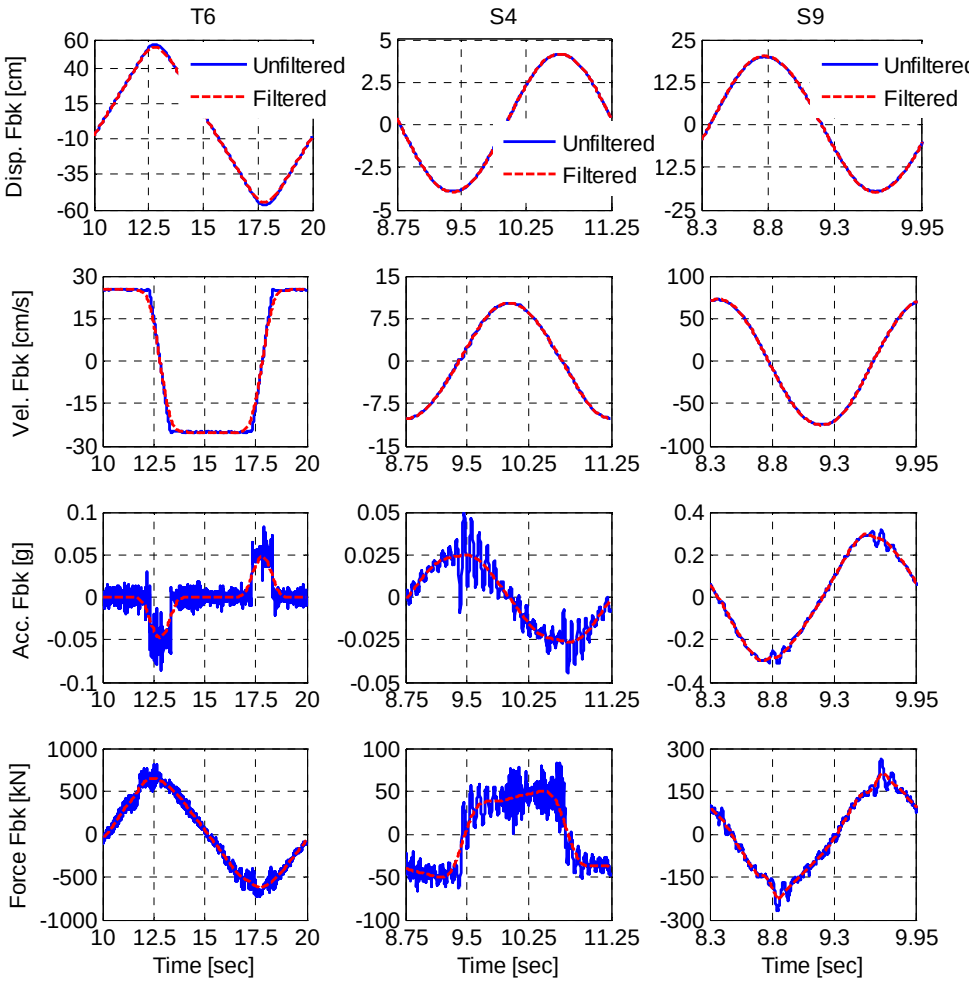

Figure 3.3: Filtered and unfiltered time history plots of tests T6, S4, and S9.

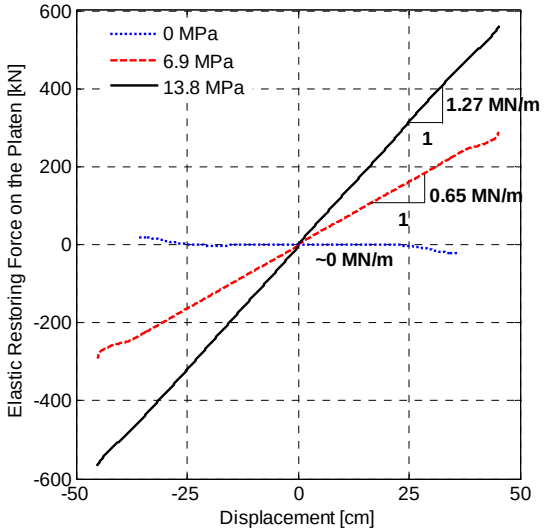

Figure 3.4: Estimates of the horizontal stiffness by hysteresis loop approach from triangular test T4 for 0, 6.9 and 13.8 MPa Nitrogen pressure in the hold-down struts.

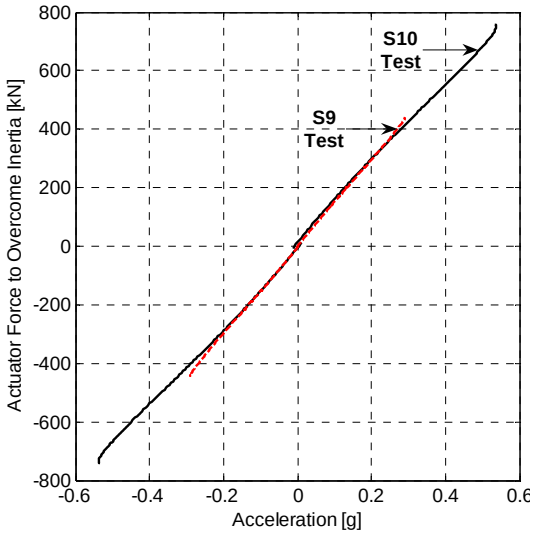

Figure 3.5: Estimates of effective mass obtained by hysteresis loop approach from sinusoidal tests S9 and S10 for 13.8 MPa Nitrogen pressure in the hold-down struts.

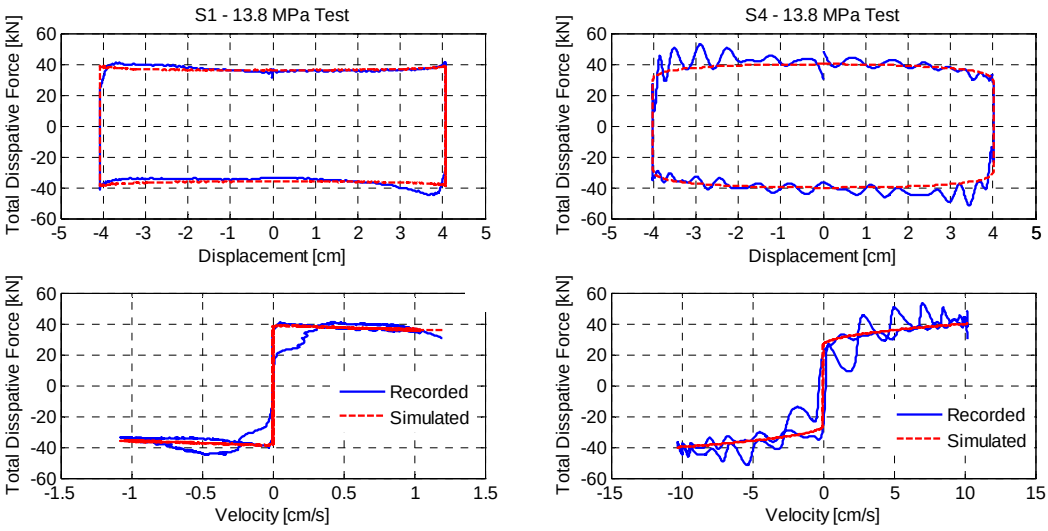

Figure 3.6: Comparison of recorded and simulated total dissipative forces vs. table displacement (a-b) and velocity (c-d) for tests S1 and S4 (13.8 MPa Nitrogen pressure in hold-down struts).

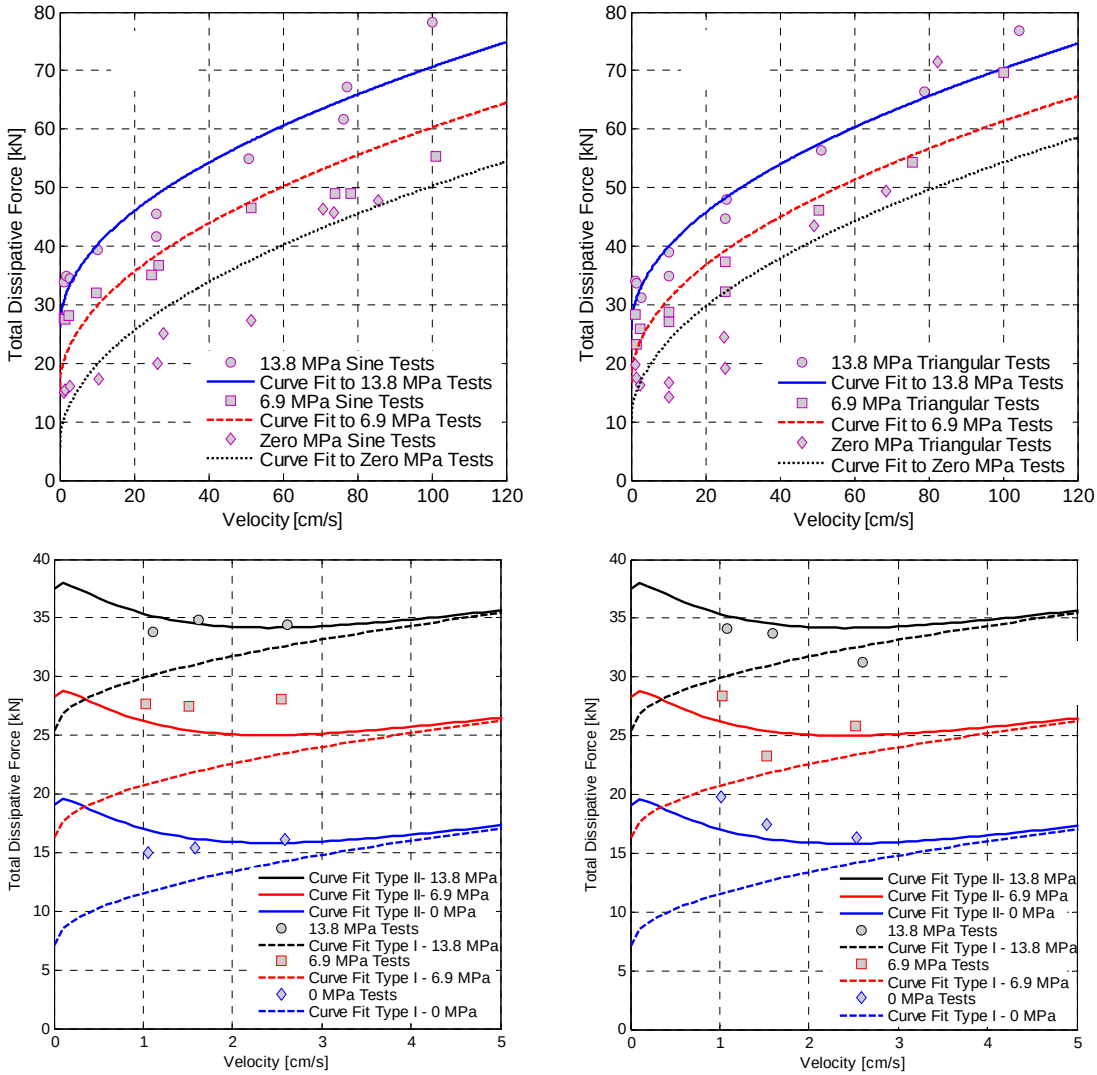

Figure 3.7: Total dissipative forces at maximum obtained velocities during sinusoidal (a), and triangular tests (b) performed under 0.0, 6.9, and 13.8 MPa Nitrogen pressures in the hold-down struts, and total dissipative forces observed during the sinusoidal (c), and triangular (d) low velocity tests. Curves labeled I and II correspond to Eqs. (3.22) and (21), respectively.

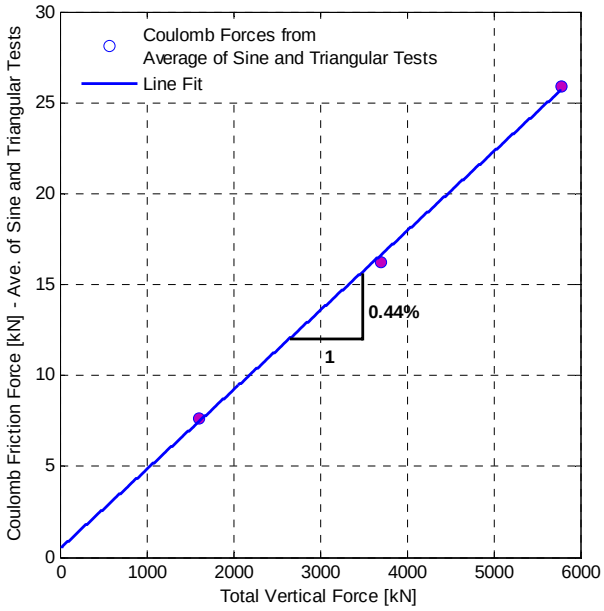

Figure 3.8: Coulomb friction force obtained from average of sinusoidal and triangular test results as a function of total vertical force.

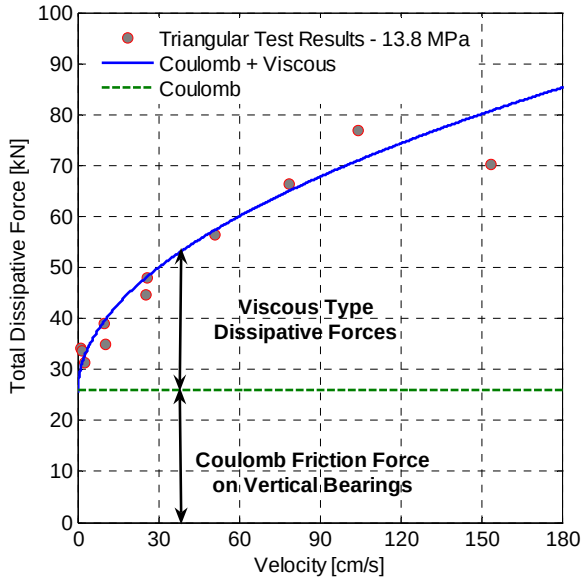

Figure 3.9: Decomposition of the total dissipative force into its major components.

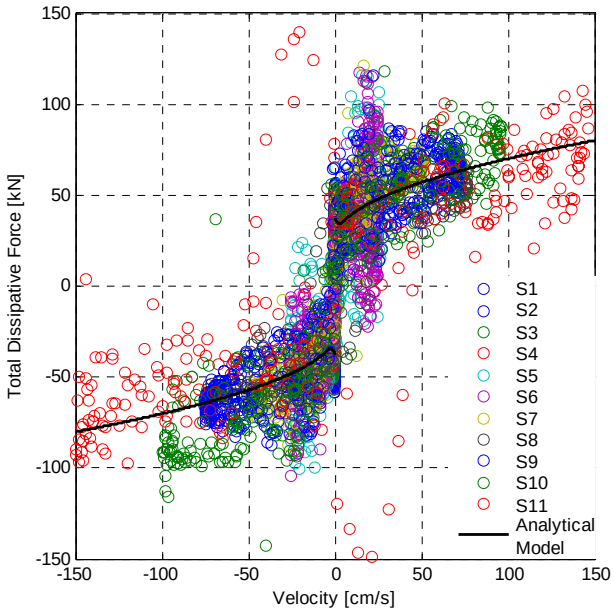

Figure 3.10: Scatter plot of instantaneous dissipative force vs. instantaneous velocity for tests S1 through S11 (13.8 MPa Nitrogen pressure in the hold-down struts). Analytical model is shown as solid line.

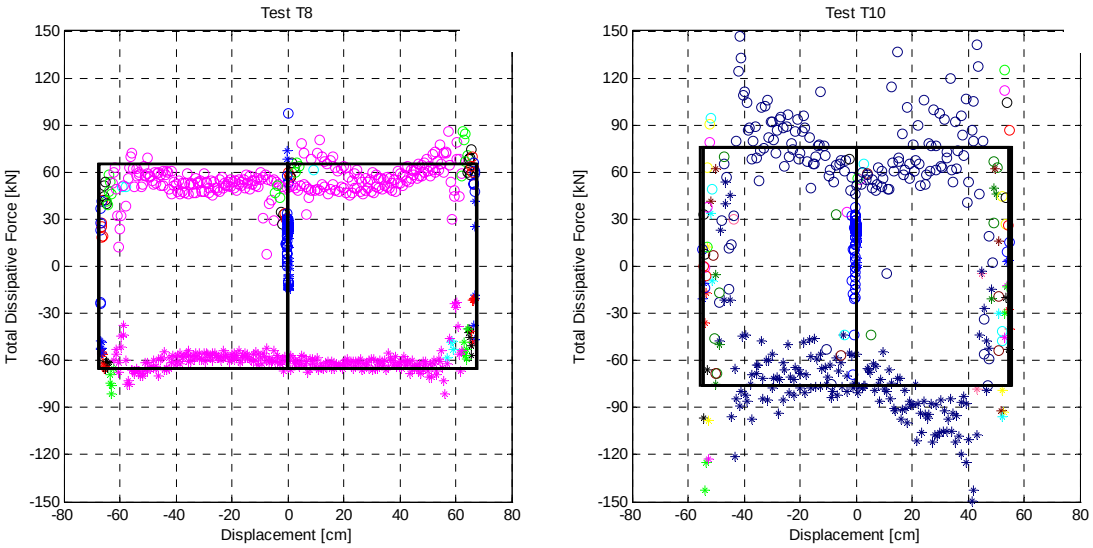

Figure 3.11: Instantaneous total dissipative forces vs. instantaneous platen displacement for Tests T8 (a), and T10 (b) (13.8 MPa Nitrogen pressure in the hold-down struts). Analytical model is shown with solid lines.

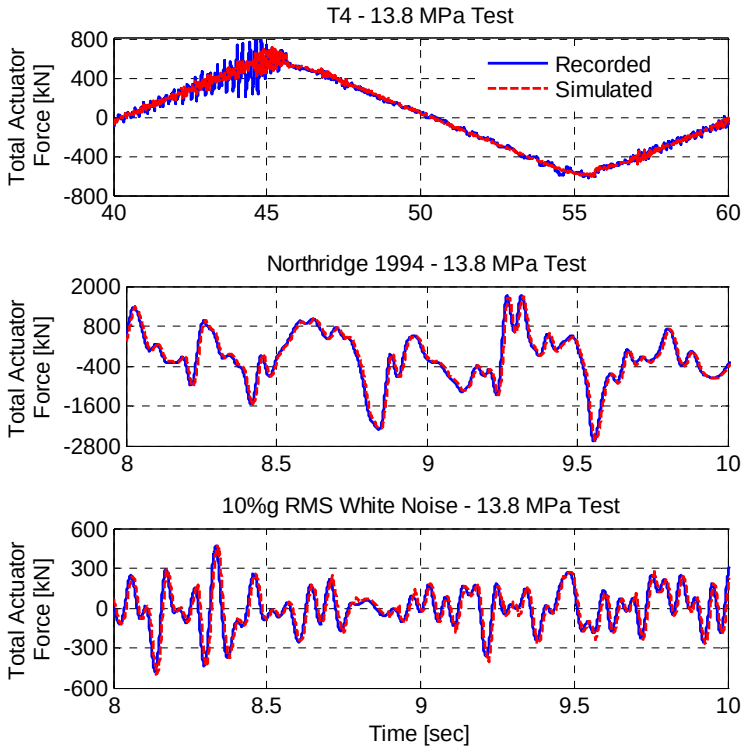

Figure 3.12: Comparisons of recorded and simulated total actuator forces for the following tests: (a) T4, (b) Northridge-1994 earthquake (100%), and (c) WN10%g (13.8 MPa Nitrogen pressure in the hold-down struts).

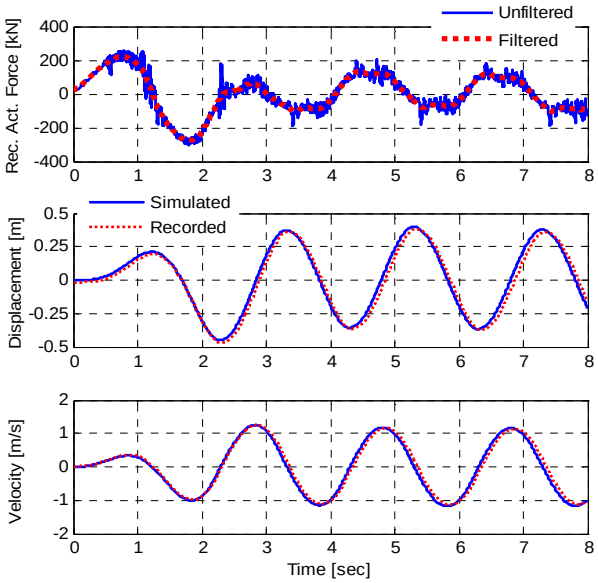

Figure 3.13: Comparison of recorded and simulated table velocity (a) and displacement (b) using as input the recorded total actuator force (c) for test SR9.

REFERENCES

Hwang, J. S., Chang, K. C., and Lee, G. C., The System Characteristics and Performance of a Shaking Table. *NCEER Report No. 87-0004, National Center for Earthquake Engineering Research, State University of New York at Buffalo,* NY, 1987.

Rinawi, A. M., and Clough, R. W., Shaking Table-Structure Interaction. EERC Report No. 91/13, Earthquake Engineering Research Center, University of California at Berkeley, CA, 1991.

Clark, A., Dynamic Characteristics of Large Multiple Degree of Freedom Shaking Tables. *Proc. 10th World Conf. on Earthquake Engineering*, Madrid, Spain, 2823-2828, 1992.

Conte, J.P., and Trombetti, T.L., Linear Dynamic Modeling of a Uni-axial Servo-Hydraulic Shaking Table System. *Earthquake Engineering and Structural Dynamics*, 29(9), 1375-1404, 2000.

Williams, D. M., Williams, M. S., and Blakeborough, A., Numerical Modeling of a Servohydraulic Testing System for Structures. *Journal of Engineering Mechanics, ASCE*, 127(8), 816-827, 2001.

Shortreed, J. S., Seible, F., Filiatrault, A., and Benzoni, G., Characterization and Testing of the Caltrans Seismic Response Modification Device Test System. *Phil. Trans. R. Soc. Lond. A*, 359, 1829-1850, 2001.

Crewe, A. J., Severn, R. T., The European Collaborative Programme on Evaluating the Performance of Shaking Tables. *Phil. Trans. R. Soc. Lond. A*, 359, 1671-1696, 2001.

Trombetti, T.L., and Conte, J.P., Shaking Table Dynamics: Results from a Test Analysis Comparison Study. *Journal of Earthquake Engineering,* 6(4), 513-551, 2002.

Twitchell, B. S., and Symans, M. D., Analytical Modeling, System Identification, and Tracking Performance of Uniaxial Seismic Simulators. *Journal of Engineering Mechanics*, 129(12), 2003.

Thoen, B. K., and Laplace, P. N., Offline Tuning of Shaking Tables. *Proc. 13th World Conf. on Earthquake Engineering*, Vancouver, B.C., Canada, Aug. 1-6, 2004, Paper No. 960.

Van Den Einde, L., Restrepo, J., Conte, J. P., Luco, E., Seible, F., Filiatrault, A., Clark, A., Johnson, A., Gram, M., Kusner, D., and Thoen, B., Development of the George E. Brown Jr. Network for Earthquake Engineering Simulation (NEES) Large High Performance Outdoor Shake Table at the University of California, San Diego. *Proc. of 13-th World Conference on Earthquake Engineering*, Vancouver, BC Canada, August 1-6, 2004, Paper No. 3281.

Website: http://nees.ucsd.edu/

Bondonet, G. and Filiatrault, A., Frictional Response of PTFE Sliding Bearings at High Frequencies. *Journal of Bridge Engineering, ASCE,* 2(4), 139-148, November, 1997.

Thoen, B. K., 469D Seismic Digital Control Software. MTS Corporation, 2004.

Kusner, D. A., Rood, J. D., and Burton, G. W., Signal Reproduction Fidelity of Servohydraulic Testing Equipment. *Proc. 10th World Conference on Earthquake Engineering*, Rotterdam, 2683-2688, 1992.

Zhao, J., Shield, C., French, C., Posbergh, T., Nonlinear System Modeling and Velocity Feedback Compensation for Effective Force Testing. *Journal of Engineering Mechanics*, 131(3), 244-253, 2005.

CHAPTER 4

IDENTIFICATION OF THE MECHANICAL SUBSYSTEM OF THE NEES-UCSD SHAKE TABLE BY A LEAST SQUARES APPROACH

4.1. Introduction

The new UCSD-NEES Large High Performance Outdoor Shaking Table (LHPOST) located at the Englekirk Structural Engineering Center at Camp Elliot Field Station, a site 15 km away from the main UCSD campus, is a unique facility that enables next generation seismic experiments to be conducted on very large structural and soil-foundation-structure-interaction systems. Large tests of a 21 m tall wind turbine, and a tall seven story, reinforced concrete shear wall building model (Figure 4.1) have been conducted on the table. Optimization of the shake table performance during the tests, as well as the optimization of the experiments themselves, including sensor location and safety precautions, requires the use of a detailed and reliable mathematical model of the complete facility. In general, a complete model of a shake table system needs to include the mechanical, hydraulic and electronic sub-systems. Typically, the steel platen, vertical and lateral bearings, hold-down struts, and actuators are included in the mechanical sub-system; pumps, accumulator bank, line accumulators, servo-valves, and surge tank are part of the hydraulic sub-system; and

finally, controller, signal conditioners, sensors and built-in analog filters are included in the electronic sub-system.

In a previous paper (Ozcelik et al., 2008) the authors developed a simplified analytical model for the mechanical sub-system of the UCSD-NEES Shaking Table, identified the parameters of the model using the data collected during the extensive shake down tests of the table, and validated the model by detailed comparisons with experimental data. The model and parameter identification approach used in the previous study was based on analysis of the hysteresis loops relating the feedback total actuator force to the feedback displacement, velocity and acceleration of the platen recorded during periodic tests (both triangular and harmonic). The procedure took advantage of the periodicity of the motion of the table during sinusoidal or triangular tests, to isolate the inertial, elastic and dissipative forces and their respective dependence on acceleration, displacement and velocity. The approach is restricted to periodic tests, but does not assume a priori a linear model. Since the table motion for most future pre-tests will consist of scaled down seismic motions or random white noise acceleration signals, it is necessary to develop and test identification methods that do not depend on the periodicity of the excitation.

The first objective of this study is to test the applicability of a parameter identification approach based on the standard least square method for shake table tests with very different excitations including periodic tests, white noise tests and seismic tests. Of primary interest is the robustness of the parameter estimates across different types of tests. A second objective is to compare the results of the least squares

identification approach with those obtained by consideration of the hysteresis loops for periodic tests. A third objective of the study is to further validate the model and identified parameters by detailed comparisons with experimental data from different types of tests. Finally, the steady-state frequency response of the shake table mechanical sub-system to commanded harmonic displacement of the shake table is examined. This analysis provides an additional verification of the non-linear damping model used in the study and illustrates the response of the table in the vicinity of the characteristic frequency of the mechanical sub-system. It is envisioned that the analytical model of the mechanical sub-system obtained in this and the previous paper (Ozcelik et al., 2007) will be used in future studies to model the entire shake table system including all subsystems mentioned previously.

It is expected that the present study will add to the growing literature on the modelling of shake table systems (Hwang et al. 1987; Rinawi and Clough 1991; Clark 1992; Conte and Trombetti 2000; Williams et al. 2001; Shortreed et al. 2001; Crewe and Severn 2001; Trombetti and Conte 2002; Twitchell and Symans 2003; Thoen and Laplace 2004).

4.1.1. Overview of the UCSD-NEES Shake Table

The Large High Performance Outdoor Shaking Table (LHPOST) consists of a moving steel platen (7.6m wide by 12.2m long); a reinforced concrete reaction block; two servo-controlled dynamic actuators with a force capacity in tension/compression of 2.6MN and 4.2MN, respectively; a platen sliding system (6 pressure balanced vertical bearings with a force capacity of 9.4MN each and a stroke of ±0.013m); an

overturning moment restraint system (a pre-stressing system consisting of two Nitrogen-filled hold-down struts with a stroke of 2m and a hold-down force capacity of 3.1MN each); a yaw restraint system (two pairs of slaved pressure balanced bearings along the length of the platen); a real-time multi-variable controller, and a hydraulic power supply system. The technical specifications of the LHPOST include a stroke of ±0.75m, a peak horizontal velocity of 1.8m/s, a peak horizontal acceleration of 4.2g for bare table conditions and 1.0g for a rigid payload of 3.92 MN, a horizontal force capacity of 6.8MN, an overturning moment capacity of 50MN-m, and a vertical payload capacity of 20MN. The frequency bandwidth is 0-20Hz. Other detailed specifications of the NEES-UCSD LHPOST can be found elsewhere (Van den Einde et al. 2004).

4.1.2. Experimental Data

The experimental data used to model and identify the fundamental characteristics of the UCSD-NEES shake table were recorded during shake-down tests which were performed in the period June-September, 2004 to verify that the performance of the shake table complies with the design specifications.

The tests designed for system characterization and identification purposes include periodic, earthquake, and white noise tests. For the periodic tests, sinusoidal (S) and triangular (T) waveforms were used with amplitude and frequency characteristics carefully selected so as to span the entire operational frequency range of the system. For the earthquake tests, full and scaled versions of historic earthquake records with different characteristics were used. Finally, several white noise tests with

different root mean square table accelerations were performed on the system. All of these tests were incorporated in the identification process to make sure that the identified fundamental characteristics of the system do not change across test types and test characteristics. The details of the tests performed on the system are summarized in Table 4.1 and Table 4.2.

Triangular and sinusoidal tests were performed with zero, 1042.4 kN (6.9 MPa Nitrogen pressure), and 2084.8 kN (13.8 MPa Nitrogen pressure) forces in each of the two hold-down struts in order to determine the effective horizontal stiffness produced by the hold-down struts, and also to investigate the effect of vertical forces on the dissipative (friction, damping) forces. All triangular waves were rounded at their peak displacement values (at the change of velocity) with a phase of duration equal to 1/10 of the wave period and constant acceleration not exceeding 2g's. All earthquake and white noise tests were performed with a force of 2084.8 kN (13.8 MPa Nitrogen pressure) in each of the two hold-down struts. All triangular, sinusoidal, earthquake and white noise tests were conducted several times in order to check for repeatability of the results.

The total actuator force recorded during the last two sine and triangular tests, namely S11, S12, T11 and T12, which had a maximum velocity near the velocity capacity of the table, were distorted to such an extent that they could not be used for the purpose of parameter identification. For this reason, these four tests were not considered in all facets of this study.

4.1.3. Sensors and Data Acquisition System

Data were acquired by the built-in sensors and data acquisition (DAQ) system used for controlling the shaking table. The sampling frequency of the DAQ system is set at the default rate of 1024Hz. This DAQ system also has low-pass anti-aliasing filtering capabilities. The displacement of the platen relative to the reaction block was measured by two digital displacement transducers (Temposonics® linear transducers) located on the East and West actuators. The platen acceleration response was measured by two Setra®-Model 141A accelerometers with a range of ±8g's and a flat frequency response from DC to 300Hz. It should be noted here that the signal conditioners used for the accelerometers include a built-in analog low-pass filter with cut-off frequency set at 100 Hz; implying that acceleration records have frequency content only up to 100 Hz. Pressure in the various actuator chambers were measured by four Precise Sensors®-Model 782 pressure transducers (located in the tension and compression chambers of each actuator) with a pressure range from 0 to 68.9 MPa and a (sensor/DAQ) resolution of 689.5 Pa. These pressure transducers are located near the end caps of each actuator. Measured pressures are converted to actuator forces by multiplying them with the corresponding actuator piston areas and combining the contributions from both chambers. At this point, it is important to mention that pressure recordings were high-pass filtered to remove their static pressure components, but were not low-pass filtered. The velocity of the platen is the only response quantity measured indirectly. To obtain a wideband estimate of velocity, the differentiated displacement sensor signal is combined with the integrated acceleration

sensor signal via a crossover filter. This filter ensures that the velocity estimate of the platen consists primarily of differentiated displacement at low-to-medium frequencies for which the displacement sensor is more accurate, and integrated acceleration at medium-to-high frequencies for which the acceleration sensor is more accurate (Thoen 2004).

The MTS 469D Seismic Controller Recorder software was used to record the digitized data; this software is an integral part of the MTS 469D Digital Controller. The sampling rate of this software can be set at a different rate than the one used by the controller (1024 Hz). The sampling rate of the recorder was set at 512 Hz during the tests. Again, to prevent aliasing, the anti-aliasing digital filter built-in the recorder was enabled during the tests. The sampling rate used on the recorder was sufficiently high for all the tests performed on the system.

To interpret the results presented in the following sections, two important general observations about the recorded data need to be pointed out here. In all the tests performed, two harmonic signals at 10.66 Hz and 246 Hz were observed repeatedly mainly in the total force and table acceleration records. The signal at 10.66 Hz corresponds to the oil column frequency of the system. The effective table mass of the system and the oil column within the actuators give rise to a mass-spring system with a natural frequency referred to as the oil column frequency (Thoen and Laplace 2004; Conte and Trombetti 2000; Kusner et al. 1992). This oil column resonance frequency tends to be excited when there is a sudden change in the motion of the platen such as a direction reversal. The most likely source of the second harmonic

signal at 246 Hz is the resonance between the pilot stage and the third stage of the servo-valves. Due to low-pass filtering of the acceleration records at 100 Hz, this 246 Hz harmonic signal can be observed only slightly in the acceleration records, but it is clearly observed in the actuator force records that are only subjected to high-pass filtering. The discrepancy between the filtering of the actuator force and platen acceleration data does not allow to simulate the high frequency harmonic components of the total actuator force by use of the recorded table motion.

4.2. Model and Parameter Estimation by Least Squares Approach

4.2.1. Conceptual Model

A detailed analysis of the dynamics of the platen and hold-down struts (Ozcelik et al., 2007) indicates that several non-linear terms affecting the inertial and elastic forces are small and can be neglected. Under these conditions, a simplified mathematical model of the shake table system with a relatively small number of unknown parameters can be formulated. This model is represented in Figure 4.2, where $F_{act}(t)$ = the total effective actuator force applied on the pistons of the two horizontal actuators, M_e = effective mass of the platen (including the mass of the moving parts of the horizontal actuators and a portion of the mass of the hold-down struts), K_e = total effective horizontal stiffness provided by the two hold down struts, C_e = effective viscous damping coefficient, and F_{μ_e} = effective Coulomb friction force due to various sources, and $u_x(t)$ = total horizontal displacement of the platen along the longitudinal direction.

According to this simplified model, the equation of motion of the shake table can be written as

$$M_e\ddot{u}_x(t)+K_e u_x(t)+\left(C_e\left|\dot{u}_x(t)\right|^{\alpha}+F_{\mu_e}\right)sign(\dot{u}_x(t))=F_{act}(t) \tag{4.1}$$

where the exponent α is a constant. The model parameters to be identified (M_e, K_e, C_e, F_{μ_e}, α) are all effective in nature, as different sources are lumped into the same type of resisting force (e.g. various physical sources of energy dissipation contribute to the viscous damping coefficient C_e).

4.2.2. Basic Least Squares Formulation

The parameters (M_e, K_e, C_e, F_{μ_e}) of the mathematical model given in (4.1) are identified by use of the linear least squares method for a given value of α. The objective function to be minimized is given by

$$\bar{\in}^2=\frac{\sum_{i=1}^{N}\lambda_i\int_0^{T_i}\left[F_{act}(t)-M_e\ddot{u}_x-K_e u_x-\left(C_e\left|\dot{u}_x\right|^{\alpha}+F_{\mu_e}\right)sign(\dot{u}_x)\right]^2dt}{\sum_{j=1}^{N}\lambda_j\int_0^{T_j}F_{act}^2(t)dt} \tag{4.2}$$

where $\bar{\in}$ = normalized error to be minimized for a given value of α, N = number of tests considered, T_i = duration of the i^{th} test, and λ_i = weight assigned to the i^{th} test. Equation (4.2) can be rewritten in the following alternative form:

$$\bar{\in}^2=1+\mathbf{y}^T\mathbf{a}\mathbf{y}-\mathbf{b}^T\mathbf{y}-\mathbf{y}^T\mathbf{b} \tag{4.3}$$

where $\mathbf{y}$, $\mathbf{a}$, and $\mathbf{b}$ are defined as:

$$\mathbf{y}^T = \left(M_e, \quad K_e, \quad C_e, \quad F_{\mu_e} \right) \tag{4.4}$$

$$\mathbf{a} = \sum_{i=1}^{N} \bar{\lambda}_i \int_0^{T_i} \mathbf{R}\mathbf{R}^T dt \tag{4.5}$$

$$\mathbf{b} = \sum_{i=1}^{N} \bar{\lambda}_i \int_0^{T_i} \mathbf{R} F_{act}(t) dt \tag{4.6}$$

in which

$$\mathbf{R}^T = \left(\ddot{u}_x(t), \quad u_x(t), \quad \left|\dot{u}_x(t)\right|^{\alpha} sign\left(\dot{u}_x(t)\right), \quad sign\left(\dot{u}_x(t)\right) \right) \tag{4.7}$$

The normalized weights $\bar{\lambda}_i$ appearing in Equations (4.5) and (4.6) are defined as

$$\bar{\lambda}_i = \frac{\lambda_i}{\sum_{j=1}^{N} \lambda_j \int_0^{T_j} F_{act}^2(t) dt} \tag{4.8}$$

Vectors $\mathbf{y}$ and $\mathbf{R}$ are referred to as the parameter vector and the measured response vector, respectively. It should be noted that the components of the response vector $\mathbf{R}$ as well as the actuator force $F_{act}(t)$ are known from the recorded test data.

The model parameters $\mathbf{y}_0$ that minimize the error measure $\bar{\in}^2$ satisfy the normality conditions

$$\frac{\partial \bar{\in}^2}{\partial \mathbf{y}} = \mathbf{0} \tag{4.9}$$

which after considerations of (4.3) leads to

$$\mathbf{a}\mathbf{y}_0 = \mathbf{b} \tag{4.10}$$

After finding the optimum parameters, $\mathbf{y}_0$, by solving (4.10), the minimum squared error can be obtained as

$$\bar{\in}_0^2 = 1 - \mathbf{b}^T \mathbf{y}_0 \tag{4.11}$$

Since the tests performed on the system involve widely different amplitudes (Table 4.1 and Table 4.2), it is necessary to consider the use of weighting factors λ_i. For this purpose, we define $\in_i$ as the normalized weighted error in the i^{th} test for the optimum values of the parameters as

$$\in_i = \frac{\int_0^{T_i} \left[F_{act}(t) - M_e \ddot{u}_x - K_e u_x - \left(C_e \left| \dot{u}_x \right|^{\alpha} + F_{\mu_e} \right) \mathrm{sign}(\dot{u}_x) \right] F_{act}(t)\, dt}{\int_0^{T_i} F_{act}^2(t) dt} \tag{4.12}$$

By using (4.12), the minimum squared error $\bar{\in}_0^2$ can be written as

$$\bar{\in}_0^2 = \sum_{i=1}^{N} \left[\bar{\lambda}_i \left\{ \int_0^{T_i} F_{act}^2(t)\, dt \right\} \in_i \right] \tag{4.13}$$

One possible choice for the weights λ_i is given by

$$\lambda_i = 1 \Big/ \int_0^{T_i} F_{act}^2(t) dt \tag{4.14}$$

In this case, the minimum squared error reduces to

$$\bar{\in}_0^2 = \frac{1}{N} \sum_{i=1}^{N} \in_i \tag{4.15}$$

indicating that the choice of λ_i given in (4.14) has the advantage of assigning equal relative importance to all tests, regardless of their force amplitudes.

A second possible choice is to select $\lambda_i = 1 \quad (i = 1, \ldots, N)$. In this case, the minimum squared error takes the form

$$\bar{\in}_0^2 = \sum_{i=1}^{N} \left(\int_0^{T_i} F_{act}^2(t)dt \Big/ \sum_{j=1}^{N} \int_0^{T_j} F_{act}^2(t)dt \right) \in_i \tag{4.16}$$

Indicating that the tests performed at lower force amplitudes are given less relative importance than those performed at larger force amplitudes. Many other choices are possible for λ_i and some are considered in the sequel.

4.2.3. Estimation of Parameter α

The proposed linear least square approach to determine the model parameters (M_e, K_e, C_e, F_{μ_e}) presumes that the parameter α controlling the viscous dissipative force model ($C_e |\dot{x}|^{\alpha}$) is known. In an attempt to determine the optimum value of α, the minimum least square error $\bar{\in}_0$ was computed for a set of values of α in the range from 0.0 to 1.0. In this process, all the triangular tests for a Nitrogen pressure of 13.8 MPa in the hold-down struts were considered with four choices for the weights λ_i, namely $\lambda_i^{(1)} = 1$, $\lambda_i^{(2)} = 1/\int_0^{T_i} (\dot{u}_x)^2 dt$, $\lambda_i^{(3)} = 1/\left[\int_0^{T_i} (\dot{u}_x)^2 dt\right]^{1/2}$ and $\lambda_i^{(4)} = 1/\int_0^{T_i} F_{act}^2(t)dt$, were used.

The results obtained for $\bar{\in}_0$ as a function of α and the types of weights λ_i are presented in Figure 4.3 which shows that $\bar{\in}_0$ is relatively independent of the types of weights λ_i and of the value of parameter α. These results indicate that the overall minimum least square error combining several tests may not be the best criterion to determine the optimum value of the parameter α. Instead, the stability of the parameters C_e and F_{μ_e} identified from individual tests at different amplitudes is used to determine the optimum value of parameter α. Thus, the least square identification procedure was applied separately to the data from each of the sinusoidal tests S1 through S10 of increasing peak velocity for several values of parameter α. The resulting estimates of F_{μ_e} and C_e for α = 1 and α = 1/2 are presented in Figure 4.4. In the case of a linear viscous force model (α =1), the estimate of the Coulomb friction force F_{μ_e} is relatively constant from test to test (Figure 4.4a), but the viscous coefficient C_e decreases with test order and velocity (Figure 4.4c). This result indicates that the dissipative forces during sinusoidal tests cannot be represented by a simple combination of Coulomb friction and linear viscous damping. The results for a nonlinear viscous force (α = 1/2) show a more constant estimate for C_e (Figure 4.4d), but the estimated friction force F_{μ_e} changes somewhat from test to test in this case (Figure 4.4b). Attempts with other values of α do not lead to results significantly more uniform than those obtained for α = 1/2. Thus, the value α = ½ was adopted in this study.

Figure 4.4e and Figure 4.4f show the estimated total dissipative force at the maximum achieved velocity for each test plotted versus the peak velocity. The total dissipative force is calculated as

$$F_d = \left(C_e \left| \dot{u}_x \right|^{\alpha} + F_{\mu_e} \right) sign(\dot{u}_x) \tag{4.17}$$

where F_{μ_e} and C_e are the parameter values estimated by the least squares approach for each particular test. Comparison of the results in Figure 4.4e and Figure 4.4f indicate that two significantly different models ($\alpha = 0.5$ and $\alpha = 1.0$) lead to essentially the same total dissipative force. Thus, it appears that individual test data may not be sufficient to discriminate between the different combinations of α, F_{μ_e} and C_e (i.e., eliminate compensation effects).

4.2.4. Equivalent Linear Viscous Damper

To understand the trade-offs between the Coulomb friction force $F_{\mu_e} \text{sign}\left(\dot{u}_x\right)$ and the viscous damping force $C_e \left| \dot{u}_x \right|^{\alpha} \text{sign}\left(\dot{u}_x\right)$, it is convenient to introduce an equivalent linear viscous damper characterized by the damping coefficient $\tilde{C}_e$. This constant, $\tilde{C}_e$, is defined such that the energy dissipated by the equivalent linear viscous damper over a cycle of periodic response of duration T is equal to that dissipated by the complete model in Eq. (4.17). The resulting expression for $\tilde{C}_e$ is given by

$$\tilde{C}_e = \gamma_1 F_{\mu_e} / v + \gamma_2 C_e / v^{1-\alpha} \tag{4.18}$$

where v denotes the peak velocity, and

$$\gamma_1 = v\int_0^T |\dot{u}_x|\,dt \Big/ \int_0^T \dot{u}_x^2\,dt \tag{4.19}$$

$$\gamma_2 = v^{1-\alpha}\int_0^T |\dot{u}_x|^{1+\alpha}\,dt \Big/ \int_0^T \dot{u}_x^2\,dt \tag{4.20}$$

In the particular case of a periodic triangular test with velocity v and period T, it can be shown that $\gamma_1 = \gamma_2 = 1$ and $\tilde{C}_e = F_{\mu_e}/v + C_e/v^{1-\alpha}$. In the case of a sinusoidal test with velocity $\dot{u}_x(t) = v\sin(2\pi t/T)$ characterized by the peak velocity v and period T, the factors γ_1 and γ_2 become

$$\gamma_1 = \left(\frac{4}{\pi}\right) \tag{4.21}$$

$$\gamma_2 = \frac{2^\alpha}{\pi}\left(\frac{\alpha}{1+\alpha}\right)\frac{\Gamma^2(\alpha/2)}{\Gamma(\alpha)} \tag{4.22}$$

where $\Gamma(\cdot)$ denotes the Gamma function. In particular, for the special case $\alpha = 1/2$, then $\gamma_1 = 1.273$, $\gamma_2 = 1.113$, and $\tilde{C}_e = 1.273F_{\mu_e}/v + 1.113C_e/\sqrt{v}$.

Equation (4.18) indicates that for a given value of the peak velocity v, different combinations of F_{μ_e} and C_e can lead to the same equivalent linear viscous damping coefficient and thus to the same total energy dissipation. Hence, to properly identify the Coulomb and viscous dissipative forces, it is necessary to consider simultaneously several tests with very different velocities. The last term in Eq. (4.18)

and the results in Figure 4.4c for the estimated linear viscous damping coefficient ($\alpha = 1$) suggest that an effective viscous damper with a fractional power law is a more suitable representation of the data.

In what follows, the data from different sets of tests will be pooled together, and the parameter α will be set to 0.5 on the basis of the relative stability of the estimates of F_{μ_e} and C_e obtained from different tests. The resulting estimates of M_e, K_e and of the total dissipative force are relatively independent of the assumed value for the parameter α.

4.3. Parameter Estimation

The parameter identification was conducted separately for nine sets of pooled data. Three of the sets consist of the combination of 10 sinusoidal tests for hold-down pressures of 0, 6.9, and 13.8 MPa, respectively. A second group of three sets involve the combination of 10 triangular tests also for hold-down Nitrogen pressures of 0, 6.9, and 13.8 MPa, respectively. The seventh set corresponds to the three scaled El Centro seismic tests at the operating hold-down Nitrogen pressure of 13.8 MPa. The eighth set consists of data from three white noise tests with rms amplitudes 0.03g, 0.05g, and 0.07g, respectively, conducted at the operating hold-down Nitrogen pressure. Finally, the ninth set is defined by two white noise tests with rms amplitude of 0.10g and 0.13g, respectively, conducted at the operating hold-down Nitrogen pressure.

4.3.1. Effective Mass Estimation

The results of the least squares identification for the effective mass M_e are presented in Table 4.3 for two choices of the weights corresponding to $\lambda_i = \lambda_i^{(1)}$ and $\lambda_i = \lambda_i^{(2)}$. With one exception, the estimated effective masses obtained from different test types, different Nitrogen pressure conditions in the hold-down struts, and different weights are in good agreement. It appears that M_e increases slightly with the nitrogen pressure in the hold-down struts, thus suggesting some correlation with the effective stiffness K_e. The average of the estimates of M_e for the periodic tests at the hold-down Nitrogen operating pressure of 13.8 MPa is 144 tons. The estimate of M_e from the white noise tests at 0.10g and 0.13g rms acceleration is also 144 tons matching the average result for the triangular and sine tests. The average estimates of the effective mass from the white noise tests with smaller amplitudes (0.03-0.05-0.07g rms acceleration) is 143.6 tons, which is also close to the average estimate from the periodic tests. The estimates of M_e from higher frequency earthquake tests are on the average 1.4 percent larger than those obtained from lower frequency triangular and sine tests.

The one deficient estimate of the effective system mass occurs for the sinusoidal tests at zero hold-down Nitrogen pressure and for the weights $\lambda_i = \lambda_i^{(2)}$. The problem is associated with the low amplitudes, velocities, and accelerations achieved during tests S1 through S4. When these four tests are removed from the pool, the estimate of the effective mass increases from 114.1 to 146.9 ton. Also, when all S1

through S10 tests are used but the viscous damping coefficient is constrained (as described later), then the estimate of the effective mass is 146.1 ton.

4.3.2. Effective Horizontal Stiffness Estimation

The results obtained for the effective horizontal stiffness, K_e, are reported in Table 4.4. It should be noted here that, for tests corresponding to zero Nitrogen pressure in the hold-down struts there is no horizontal stiffness acting on the system.

The estimates of the effective stiffness K_e obtained from the periodic tests increase linearly with the Nitrogen pressure in the hold-down struts from an average value of 0.635 MN/m for a pressure of 6.9 MPa to an average value of 1.263 MN/m for a pressure of 13.8 MPa. The triangular tests involve larger forces in the hold-down struts and smaller inertia forces than the sinusoidal tests and appear to yield more stable estimates of K_e.

The average estimate of K_e obtained from the El Centro tests is 1.238 MN/m, which is 2% lower than the corresponding average estimate obtained from the periodic tests. The results in Tables 3 and 4 indicate that for the earthquake tests there is some compensation effects between the estimates of M_e and K_e, with M_e being 1.3% larger and K_e 2% lower than the corresponding estimates from the periodic tests. The average estimate of K_e from the 0.10 and 0.13g RMS acceleration white noise tests is 1.405 MN/m, which is 11.2% larger than the corresponding average estimate from the periodic tests. The estimates of K_e based on the low-amplitude (0.03, 0.05, and 0.07g RMS acceleration) white noise tests are significantly higher than the other estimates

and appear to be in error. The low amplitude white noise tests involve extremely small displacements but significant accelerations. Under these conditions the elastic forces are much smaller than the inertia forces, and the stiffness can not determined accurately.

From the above results, it can be concluded that the effective horizontal stiffness of the system is approximately 1.263 MN/m in the nominal case corresponding to a Nitrogen pressure of 13.8 MPa in the hold-down struts. For a Nitrogen pressure of 6.9 MPa, the effective stiffness is reduced to 0.63 MN/m.

4.3.3. Estimation of Dissipative Force

The estimates of the dissipative force parameters F_{μ_e} and C_e obtained from the nine pooled sets of data for $\alpha = 0.5$ and weighting factors ($\lambda_i = \lambda_i^{(1)}$ and $\lambda_i = \lambda_i^{(2)}$) are reported in Table 5 in the columns labelled “unconstrained”. The results indicate that both F_{μ_e} and C_e increase with the hold-down Nitrogen pressure. The average values of F_{μ_e} over the two weighting factors and the two types of tests (triangular and sinusoidal), are 16.7, 25.9, and 29.5 kN for the three hold-down Nitrogen pressures (0.0, 6.9, and 13.8 MPa). The corresponding average values of C_e are 18.4, 34.5, and 46.0 $kN(s/m)^{0.5}$. Although the unconstrained estimates of F_{μ_e} are fairly stable for a given hold-down Nitrogen pressure, the corresponding unconstrained estimates of C_e vary significantly with weighting factor and test type.

A second set of estimates for F_{μ_e} was obtained by repeating the least-squares based estimation process with C_e constrained to be equal to 46.0 [$\mathrm{kN(s/m)^{0.5}}$]

corresponding to the average estimate of C_e over the sinusoidal and triangular tests for a hold-down nitrogen pressure of 13.8 MPa. The resulting constrained estimates of F_{μ_e} are also given in Table 4.5. The constrained estimates of F_{μ_e} are more stable across test type and weighting factor. The average constrained value of F_{μ_e} over the sinusoidal and triangular tests and the two weighting factors are 8.2, 22.1 and 26.5 kN for the hold-down Nitrogen pressures of 0, 6.9, and 13.8 MPa, respectively. The constrained estimates of the friction force F_{μ_e} from the scaled El Centro tests and from the two sets of white noise tests are 28.3, 26.1, and 24.4 kN, respectively, which are close to the average estimate of 26.5 from the periodic tests. The deviations from the average of the periodic tests are as high as 8%, but these differences amount to less 2.1 kN which is well within the margin of error in estimating the dissipative forces from the measured data.

Both the constrained and unconstrained estimates of F_{μ_e} suggest that the friction forces depend on the hold-down Nitrogen pressure and, consequently, are mostly associated with friction on the vertical bearings of the platen. The unconstrained estimates of the effective viscous damping coefficient C_e also depend on the hold-down Nitrogen pressure suggesting that the dissipative viscous forces are also related to the vertical bearings. The constrained estimate of C_e is selected to be independent of the hold-down Nitrogen pressure and would be consistent with viscous forces in the lateral bearings of the platen and in the actuators instead of the vertical bearings. Both set of estimates of F_{μ_e} and C_e lead to essentially the same total

dissipative forces (within the margin of error) and, consequently, it is not possible to discriminate between these two possibilities. The constrained estimates will be used in the sequel.

The results given in Table 4.7 indicate that the constrained estimate of F_{μ_e} based on the scaled El Centro tests is within 7% of the average value of F_{μ_e} based on sinusoidal and triangular tests. The corresponding difference for white noise tests is less than 8%. Thus, the constrained least squares approach can identify the total friction force from a variety of tests.

4.3.4. Decomposition of the Total Friction Force

The two major sources of Coulomb-type friction in the system are the vertical and lateral bearings. The inferred values for the total friction force F_{μ_e} obtained from tests performed under different hold-down Nitrogen pressures can be used to quantify these two sources of friction. The average of the estimates of F_{μ_e} obtained from sinusoidal and triangular tests for different levels of Nitrogen pressure in the hold-down struts are shown in Figure 4.5 versus the total corresponding vertical force acting on the vertical bearings. The total vertical force was obtained experimentally from readings of the pressures on the vertical bearings for the different hold-down pressures. The forces correspond to 1.613, 3.698, and 5.783 MN for hold-down Nitrogen pressures of 0.0, 6.9 and 13.8 MPa, respectively. A least square fit to the three points thus obtained leads to a line with a slope of 0.39% and an intercept of 4.1 kN. It appears then that the total friction force F_{μ_e} can be expressed as

$F_{\mu_e} = F_{\mu,lat} + \mu_e F_z$, where F_z = total vertical force acting on the vertical bearings, $F_{\mu,lat} = 4.1$ kN = friction force exerted by the lateral bearings, and $\mu_e = 0.39\%$ = Coulomb friction coefficient in the vertical bearings.

A decomposition of the dissipative forces into friction components on the horizontal and vertical bearings, and viscous forces is presented in Figure 4.6 based on tests performed under the nominal hold-down Nitrogen pressure of 13.8 MPa. Similar results were found from triangular tests performed under the same hold-down Nitrogen pressure.

The results in Figure 4.6 indicate that for a table velocity of 75 cm/sec for example, 6% of the total dissipative force is due to Coulomb friction on the lateral bearings, 34% to Coulomb friction on the vertical bearings, and 60% to viscous damping forces.

Figure 4.6 also shows a comparison between the total dissipative force obtained by use of the overall inferred model represented by Eq. (4.1) (curve in Figure 4.6) and the corresponding forces obtained through (constrained) least squares parameter estimation for individual sinusoidal and triangular tests (symbols in Figure 4.6). It is observed that the inferred model slightly underestimates the total dissipative force for sinusoidal tests, but overestimates the total dissipative force for triangular tests.

4.4. Comparison of Parameters Identified by Periodic, White Noise, and Earthquake Simulation Tests

Before comparing the parameter identification results obtained by applying the least squares method to different types of tests including periodic, white noise and earthquake tests, a comparison of the results obtained from two different identification methods based on periodic sinusoidal and triangular test data is presented. The values of the parameters identified in the present paper by the (constrained) least squares approach are compared in Table 6 with those obtained previously (Ozcelik et al., 2007) by analysis of the observed hysteresis loops. The estimates of the effective mass, M_e, and effective stiffness, K_e, obtained using the two identification methods are in excellent agreement. The details of the parameters related to the dissipative forces are slightly different, but the values of the viscous damping coefficient C_e are within 3 %. Also, the total static Coulomb friction forces F_{μ_e} obtained by the two methods differ by 2.7% corresponding to 0.7 KN, which is well below the margin of error. The results obtained by the least squares approach lead to slightly larger dissipative forces (2.8% at a velocity of 1 m/sec), but the difference amounts to about 2.0 KN for a velocity of 1 m/sec.

Next, we examine the stability of the results of parameter identification by the least squares method when applied to different types of tests including periodic, white noise and earthquake tests. A summary of the results obtained is presented in Table 7. Comparison of the results indicates that for the scaled earthquake tests, the estimated mass is slightly larger (1.4%), the estimated stiffness slightly smaller (2.0%), and the

(constrained) friction force slightly larger (6.8%) than for the periodic tests. The estimate of the effective mass based on the white noise tests is accurate but the effective stiffness is overestimated.

Table 4.5 includes two sets of estimates for the viscous damping coefficient, C_e, and the Coulomb friction force. In the first set, the values of C_e were left unconstrained while in the second set, the constants C_e were constrained to $46.0\,\text{kN(s/m)}^{0.5}$. It is apparent that the constrained parameter estimation results for the Coulomb friction are similar across the various types of tests; but the unconstrained estimates of the viscous damping coefficient and Coulomb friction force obtained from the white noise tests are in error.

In conclusion, the least squares approach appears to be equally capable of identifying the key system parameters from scaled earthquake tests and periodic sinusoidal and triangular tests. For white noise tests, the approach leads to the correct effective mass, but the obtained values for the other parameters are questionable.

4.5. Experimental Validation of the Proposed Model of the NEES-UCSD Shake Table Mechanical System

4.5.1. Comparison between Analytical and Experimental Total Actuator Force

The results of the least squares parameter identification obtained here are very similar to those obtained previously by analysis of the observed hysteresis loops. Those results had been validated by detailed comparisons of simulated and recorded actuator forces for test T4, 100% Northridge earthquake simulation test, and a white

noise test with a 10%g root mean square amplitude (Ozcelik et al., 2008). As additional validation, the total actuator force recorded during the 300% El Centro earthquake test will be compared with the simulated actuator force obtained from Eq. (4.1) using the recorded actual table displacement, velocity and acceleration as inputs and $\alpha = 0.5$.

Figure 4.7 shows a 2-seconds segment of the recorded and simulated total actuator force time-histories for the El Centro earthquake record scaled to PGA= 1.11g. It is observed that the analytical prediction based on the estimated model parameters given above is in excellent agreement with the recorded total actuator force. An alternative way of comparing test results with simulations is presented in Figure 4.8 that shows plots of recorded and simulated total actuator forces versus recorded platen velocities for the 300% El Centro earthquake test. For sake of clarity, only one sec segment of the test is shown. Again, the agreement between analytical and experimental results is excellent.

4.5.2. Comparison between Analytical and Experimental Steady-State Frequency Response

The mechanical system described by Eq. (4.1) has an undamped natural frequency given by $\omega_e = \sqrt{K_e / M_e}$ corresponding to a frequency of 0.471 Hz (period of 2.12 sec). One way of testing the energy dissipation model included in Eq. (4.1) is to consider the steady-state response of the system to harmonic excitation with frequencies in the vicinity of the system natural frequency ω_e. In the vicinity of ω_e,

the inertial and elastic forces approximately cancel each other, and the actuator force is approximately equal to the damping force.

With the above objective in mind, the equation of motion of the system, Eq.(4.1), was integrated numerically for a sinusoidal actuator force $F_{act}(t) = F_0 \sin(2\pi f t)$, and the peak amplitude $u_{\max}$ of the steady-state displacement was obtained for different values of the excitation frequency f and the force amplitude F_0. Theoretical dynamic amplification factors $R_d = u_{\max}/(F_0 / K_e)$ for different values of F_0 in the range from 49 to 250 kN were calculated and are shown versus frequency f (in Hz) in Figure 4.9 in the form of several frequency response curves. Also shown in Figure 4.9 are the values of the experimental ratios $u_{\max}/(F_{\max} / K_e)$ obtained for several sinusoidal tests plotted versus the frequency of the test. Since the system is nonlinear, these two ratios are not strictly comparable. In the experimental ratio, $u_{\max}$ is the maximum value of the feedback table displacement (which may not be exactly sinusoidal) for a commanded sinusoidal displacement, and $F_{\max}$ is the peak value of the recorded total actuator force which also may not be exactly sinusoidal. In the theoretical dynamic amplification factor R_d, the actuator force is sinusoidal, but the calculated displacement response is not exactly sinusoidal. In spite of these differences, the theoretical dynamic amplification factors (curves in Figure 4.9) and the experimental ratios (black dots in Figure 4.9) follow the same trends. The experimental ratios for tests S3, SR7 and SE4, all with frequencies below the frequency of the system, fall on the left branches of the dynamic amplification

curves. The measured peak actuator forces during these tests were 83, 262, and 384 kN, respectively, and the corresponding experimental ratios fall close to the dynamic amplification curves shown for 100.8 and 250 kN. The experimental ratios for tests SE5, SR9, S9, S7 and S5, which have peak actuator forces in the range from 133 to 242 KN, fall between the descending branches of the dynamic amplification curves for 100 and 250 kN. The experimental ratio for test S6 which has a peak actuator force of 66.4 kN falls on the dynamic amplification curve for 66.4 kN. Finally, the experimental ratio for test S4 with a peak actuator force of 49 kN falls very close to the amplification curve for 49 kN. The comparisons between analytical and experimental results in Figure 4.9 give further indication that the inferred model of the NEES-UCSD shake table mechanical system is consistent with the data.

A better understanding of the dynamic response of the shake table can be reached by obtaining estimates of the equivalent linear viscous damping ratio ξ_e for different velocities of the table. This equivalent damping ratio can be obtained from

$$\xi_e = \frac{\tilde{C}_e}{2M_e\omega_e} \tag{4.23}$$

where $\tilde{C}_e$ is the equivalent viscous damping coefficient given by Eq. (4.18). Substitution from (4.18) into (4.23) leads to

$$\xi_e = \frac{\gamma_1}{2}\left(\frac{F_{\mu_e}}{K_e}\right)\frac{\omega_e}{v} + \frac{\gamma_2}{2}\left(\frac{C_e\omega_e}{K_e}\right)\frac{1}{v^{1-\alpha}} \tag{4.24}$$

where v denotes the peak table velocity in m/s. After substitution of the inferred values of the model parameters, (4.24) reduces to

$$\xi_e = \left(3.97/\nu + 5.97/\sqrt{\nu}\right)/100 \tag{4.25}$$

Numerical values for the equivalent linear viscous damping ratio ξ_e for different platen velocities are given in Table 4.8.

The approximate equivalent linear viscous damping ratio ξ_e can be used to estimate the frequency f_m at which the amplification ratio reaches its peak value A_m. The standard relations for the equivalent linear system are

$$f_m = f_e\sqrt{1-2\xi_e^2}, \quad A_m = 1/\left(2\xi_e\sqrt{1-\xi_e^2}\right) \tag{4.26}$$

where $f_e = 2\pi/\omega_e$. The amplitudes of the platen displacement and the actuator force at the peak amplification point (f_m, A_m) are given by $u_{\max} = \nu/(2\pi f_m)$, and $F_0 = K_e u_{\max}/A_m$, respectively. The values of $f_m, A_m, u_{\max}$ and F_0 are also given in Table 4.8. The points (f_m, A_m) as a function of $u_{\max}$, ν, or F_0 describe the approximate locus of the peak amplification points in Figure 4.9 and can be used to define future sinusoidal tests of the shake table that would help to further validate the dissipative force model described herein.

4.6. Conclusions

In this paper, the parameters characterizing a mathematical model of the mechanical sub-system of the NEES-UCSD large shake table are estimated from test data by use of a least squares approach. The parameters identified include the effective mass, effective horizontal stiffness induced by the Nitrogen-filled hold-down struts,

the Coulomb friction forces on the vertical and lateral bearings, and the effective viscous damping coefficients.

In the case of periodic sinusoidal and triangular tests, the parameter estimates obtained in the present paper by the least squares approach are in close agreement with those obtained previously (Ozcelik et al., 2008) by analysis of the observed hysteresis loops. The effective mass, M_e, and effective horizontal stiffness, K_e, obtained by two methods are essentially the same. The viscous damping coefficients C_e and total Coulomb friction forces F_{μ_e} obtained by the two methods differ by about 3%. The results obtained by the least squares approach lead to slightly larger dissipative forces (3%) but the differences amounting to about 2 kN for a velocity of 1 m/s are well below the margin of error in estimating the dissipative forces from the measured data.

The main finding of the paper is that the least squares approach appears to be equally capable of identifying the key system parameters from scaled earthquake tests, and periodic sinusoidal and triangular tests. For white noise tests, the least squares approach leads to the correct effective mass, and the correct total friction force if the viscous damping coefficient is constrained, but the values obtained for the effective stiffness are in error. The smaller the amplitude of the white noise tests, the larger the error in the estimate of the effective stiffness. If the viscous damping coefficient is left unconstrained, the identified values for the friction force and viscous damping coefficient from white noise tests are very different from those estimated from periodic and earthquake tests.

The NEES-UCSD shake table mechanical sub-system considered, which does not include the effects of the oil columns in the actuators, has a frequency of 0.47 Hz that is clearly observable in the theoretical and experimental steady-state frequency response curves for the system. This characteristic frequency is of course very different from the oil column frequency, which for the NEES-UCSD shake table system is 10.66 Hz. The theoretical dynamic amplification (or frequency response) curves depend on the amplitude of the actuator force and match closely the experimental results.

As part of the study presented herein, it has also been found that the relationship between the viscous forces and table velocity is not linear but can be represented by a power law; that the friction forces on the vertical bearings can be separated from those on the lateral bearings; and that the dissipative forces typically represent a very small fraction of the total actuator force.

Chapter 4 is a reprint of the material accepted for publication in the Journal of Engineering Mechanics (2008), Ozcelik, O., Luco, J.E., and Conte, J.P. The dissertation author was the first author of this paper.

LIST OF TABLES

Table 4.1: Characteristics of the Triangular and Sinusoidal Tests Performed on the System

Tests	Displacement [cm]	Velocity [cm/s]	Frequency [Hz]	Tests	Displacement [cm]	Velocity [cm/s]	Acceleration [g]	Frequency [Hz]
T1	5.00	1.00	0.05	**S1**	4.00	1.00	0.0003	0.04
T2	7.50	1.50	0.05	**S2**	4.00	1.51	0.0006	0.06
T3	12.50	2.50	0.05	**S3**	4.00	2.51	0.0016	0.10
T4	50.00	10.00	0.05	**S4**	4.00	10.05	0.0257	0.40
T5	25.00	10.00	0.10	**S5**	4.00	25.12	0.1608	1.00
T6	62.50	25.00	0.10	**S6**	10.00	25.12	0.0643	0.40
T7	37.50	25.00	0.167	**S7**	10.00	50.24	0.2573	0.80
T8	75.00	50.00	0.167	**S8**	10.00	75.36	0.5789	1.20
T9	46.88	75.00	0.40	**S9**	20.00	75.36	0.2895	0.60
T10	62.50	100.00	0.40	**S10**	20.00	100.48	0.5146	0.80
T11	75.00	150.00	0.50	**S11**	20.00	150.72	1.1578	1.20
T12	67.50	180.00	0.667	**S12**	20.00	179.61	1.6442	1.43

Table 4.2: Characteristics of Earthquake and White Noise Tests Performed on the System

Tests	PGA [g]	RMS Amplitude [g]	Scaling [%]
El Centro - 1	0.07	*N/A*	20
El Centro - 2	0.37	*N/A*	100
El Centro - 3	1.11	*N/A*	300
Northridge	1.84	*N/A*	100
WN3%g	0.12	0.03	100
WN5%g	0.22	0.05	100
WN7%g	0.32	0.07	100
WN10%g	0.45	0.10	100
WN13%g	0.49	0.13	100

Table 4.3: Estimates of the Effective Mass of the System for Different Test Types and Different Levels of Nitrogen Pressure in the Hold-Down Struts ($\alpha = 0.5$)

Test Type – Nitrogen Pressure	M_e [tons]	
	$\lambda_i = \lambda_i^{(1)},\ i = 1,\ldots,12$	$\lambda_i = \lambda_i^{(2)},\ i = 1,\ldots,12$
Sine – 0.0 MPa	134.7	114.1
Triangular – 0.0 MPa	138.4	139.0
Sine – 6.9 MPa	143.2	143.5
Triangular – 6.9 MPa	144.3	144.4
Sine – 13.8 MPa	143.9	144.5
Triangular – 13.8 MPa	143.9	143.8
El Centro Tests – 13.8 MPa	146.2	145.7
WN (0.03, 0.05, 0.07g RMS) – 13.8 MPa	143.6	143.5
WN (0.10, 0.13g RMS) – 13.8 MPa	144.0	144.0

Table 4.4: Estimates of the Effective Horizontal Stiffness of the Hold-down Struts for Different Test Types and Different Levels of Nitrogen Pressure in the Hold-Down Struts ($\alpha = 0.5$)

Test Type – Nitrogen Pressure	K_e [MN/m]	
	$\lambda_i = \lambda_i^{(1)},\ i = 1,\ldots,12$	$\lambda_i = \lambda_i^{(2)},\ i = 1,\ldots,12$
Sine – 6.9 MPa	0.611	0.640
Triangular – 6.9 MPa	0.644	0.645
Sine – 13.8 MPa	1.246	1.281
Triangular – 13.8 MPa	1.261	1.262
El Centro Tests – 13.8 MPa	1.221	1.255
WN (0.03, 0.05, 0.07g RMS) – 13.8 MPa	1.916	2.132
WN (0.10, 0.13g RMS) – 13.8 MPa	1.392	1.417

Table 4.5: Estimates of Coulomb Friction Force and Viscous Damping Coefficients Obtained by Least Squares Approach with Pooled Datasets ($\alpha = 0.5$)

Tests Types – Nitrogen Pressure	Unconstrained				Constrained			
	F_{μ_e} [KN]		C_e $[kN(s/m)^{1/2}]$		F_{μ_e} [KN]		C_e $[kN(s/m)^{1/2}]$	
	$\lambda^{(1)}$	$\lambda^{(2)}$	$\lambda^{(1)}$	$\lambda^{(2)}$	$\lambda^{(1)}$	$\lambda^{(2)}$	$\lambda^{(1)}$	$\lambda^{(2)}$
Sine – 0.0 MPa	17.4	16.6	21.4	17.6	12.4	5.7	45.9	45.9
Triangular – 0.0 MPa	17.1	15.8	13.1	21.5	8.7	5.9	45.9	45.9
Sine – 6.9 MPa	26.1	26.8	41.1	36.1	23.8	19.8	45.9	45.9
Triangular – 6.9 MPa	24.8	26.0	31.2	29.4	20.7	24.2	45.9	45.9
Sine – 13.8 MPa	30.1	30.6	49.4	48.4	27.5	23.9	45.9	45.9
Triangular – 13.8 MPa	27.9	29.2	42.3	43.8	25.9	28.6	45.9	45.9
El Centro Tests – 13.8 MPa	25.6	28.0	51.3	62.1	26.4	30.2	45.9	45.9
WN (0.03, 0.05, 0.07g RMS) – 13.8 MPa	14.14	14.6	140.03	149.8	25.8	26.3	45.9	45.9
WN (0.10, 0.13g RMS) – 13.8 MPa	9.19	9.4	120.21	123.1	24.3	24.4	45.9	45.9

Table 4.6: Comparison of Model Parameters Estimated from Two Different Methods Based on Data from Periodic Tests (Sinusoidal and Triangular) Performed Under Nominal Hold-Down Nitrogen Pressure of 13.8 MPa

Model Parameters	**Least Squares**	**Hysteresis Loops Approach**
M_e [tons]	144	144
K_e [MN/m]	1.263	1.266
C_e [KN (s/m)^0.5]	46.0	44.6
μ_e [%]	0.39	0.45
$F_{\mu,lat}$ [KN]	4.1	0.0
F_{μ_e} [KN]	26.7	26.0

Table 4.7: Comparison of Model Parameters Identified Based on Periodic, Earthquake, and White Noise Tests (Hold-Down Nitrogen Pressure of 13.8 MPa)

Model Parameters	**Periodic Tests**	**El Centro Tests**	**White Noise Tests** ***(10-13%g RMS)***	**White Noise Tests** ***(3-5-7%g RMS)***
M_e [tons]	144.0	146.0	144.0	143.6
K_e [MN/m]	1.263	1.238	1.405	2.024
C_e [kN(s/m)$^{0.5}$]*	45.9	45.9	45.9	45.9
Coulomb Friction Force [kN]*	26.5	28.3	24.4	26.1
C_e [kN(s/m)$^{0.5}$]**	45.9	57.6	121.7	144.9
Coulomb Friction Force [kN]**	27.7	26.8	9.3	14.4

* C_e ***constrained***

** C_e ***unconstrained***

Table 4.8: Equivalent Linear Viscous Damping Ratio, (4.25), for Different Platen Velocities, and Characteristics of Peak Amplification Points

v	ξ_e	f_m	A_m	$u_{\max}$	F_0
[cm/sec]	[%]	[Hz]	-	[cm]	[kN]
20.00	33.20	0.416	1.60	7.65	60.5
25.12	27.72	0.433	1.88	9.23	62.2
50.24	16.32	0.458	3.11	17.46	71.1
75.36	12.15	0.464	4.15	25.85	78.9
100.5	9.91	0.466	5.07	34.32	85.7
125.00	8.52	0.468	5.89	42.51	91.2
150.72	7.50	0.468	6.69	51.26	97.0
180.00	6.67	0.469	7.52	61.08	102.8

LIST OF FIGURES

Figure 4.1: Seven-story full-scale R/C building slice, 19.2m high.

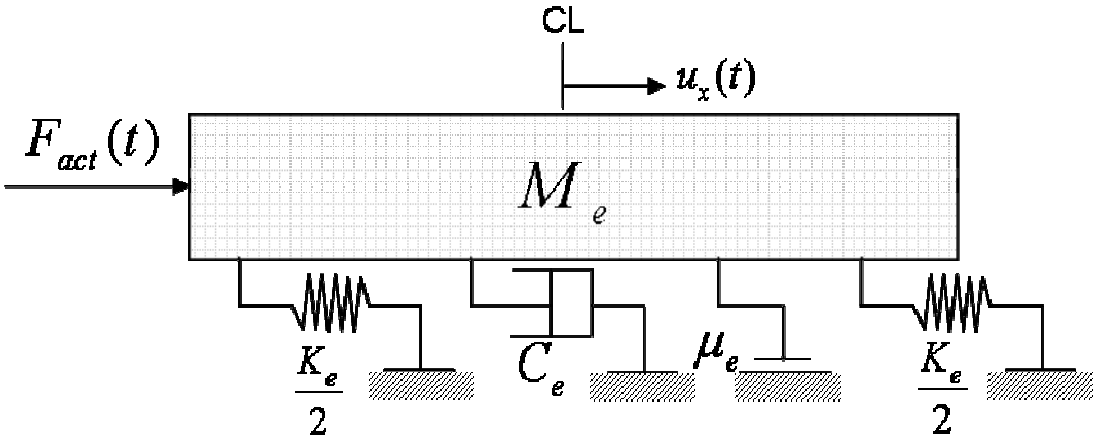

Figure 4.2: Conceptual mechanical model of the table with model parameters M_e, K_e, C_e, and F_{μ_e} to be identified through periodic, earthquake and white noise tests.

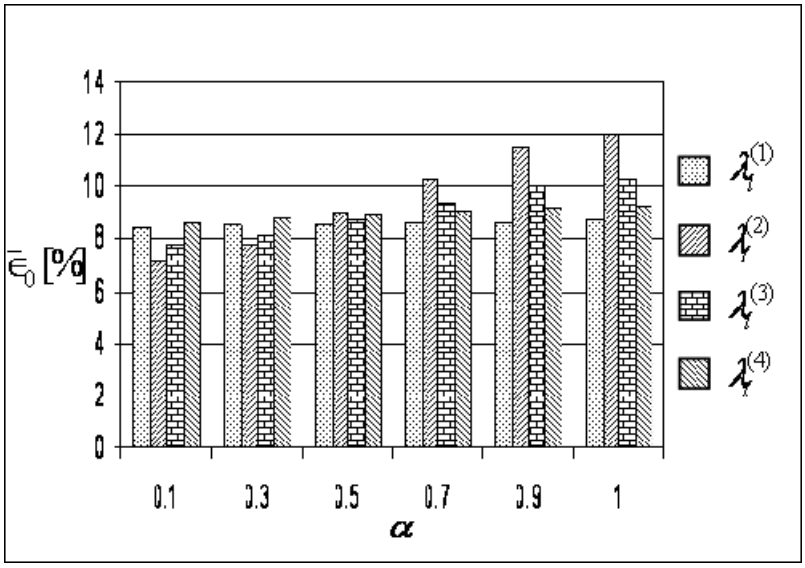

Figure 4.3: Minimum least square error $\bar{\in}_0$ as a function of parameter α and for different types of weights λ_i ($i = 1 \ldots 12$).

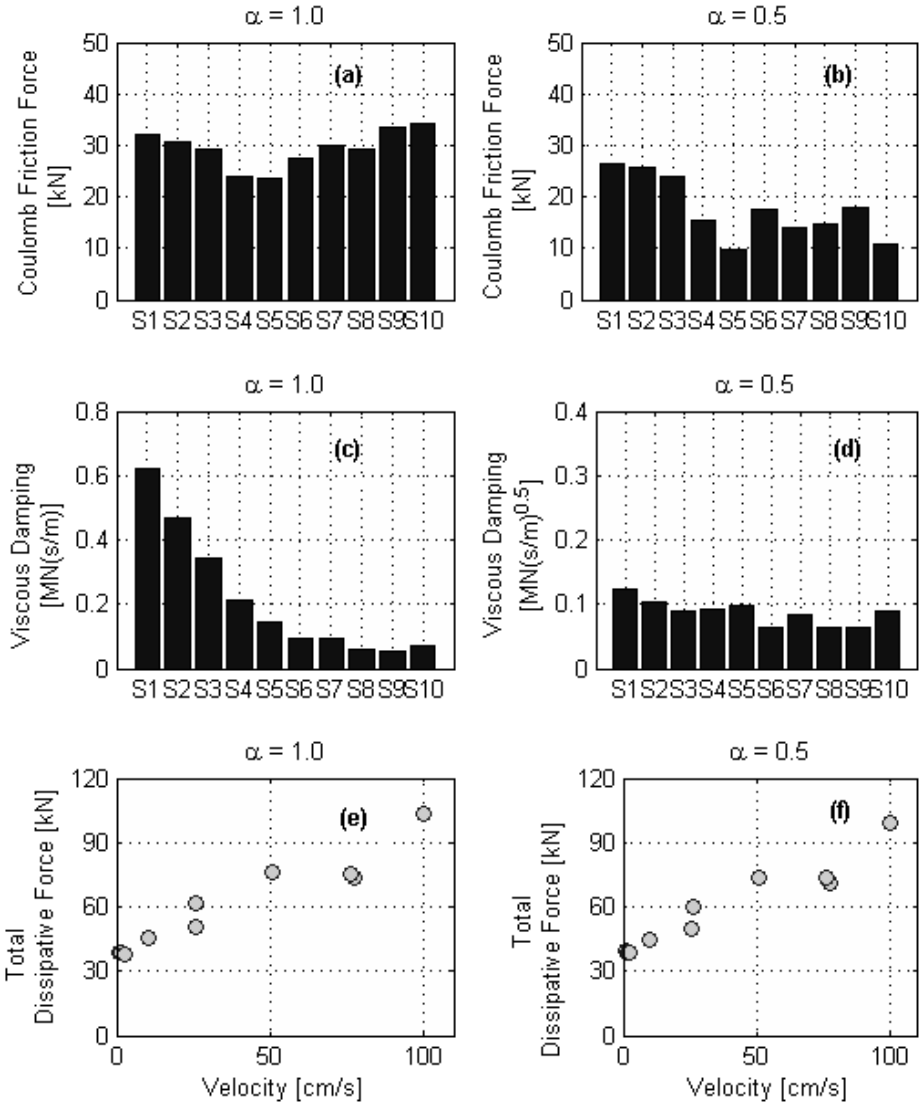

Figure 4.4: (a), (b): Coulomb friction forces; (c), (d): viscous damping coefficient; and (e), (f): total dissipative force estimated from each of 10 different sine tests for $\alpha = 1.0$ and $\alpha = 0.5$.

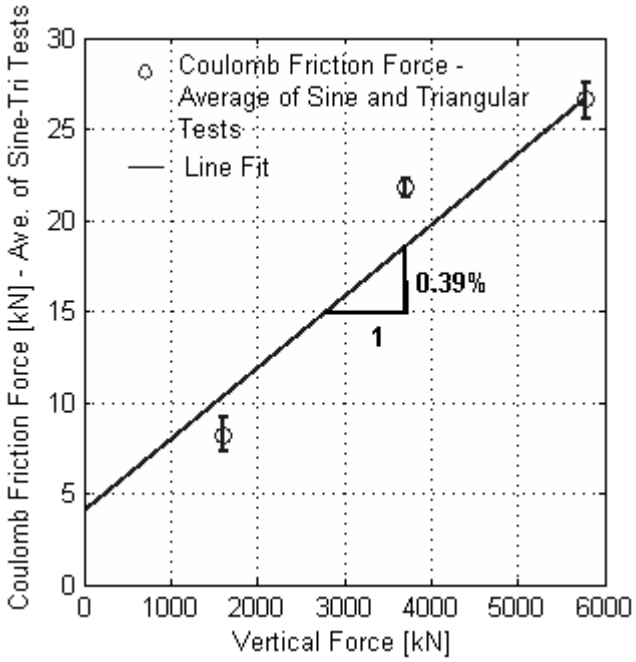

Figure 4.5: Average Coulomb friction forces ($\lambda^{(1)}$ and $\lambda^{(2)}$) as a function of total vertical force on vertical bearings (dispersion bounds for sine and triangular tests).

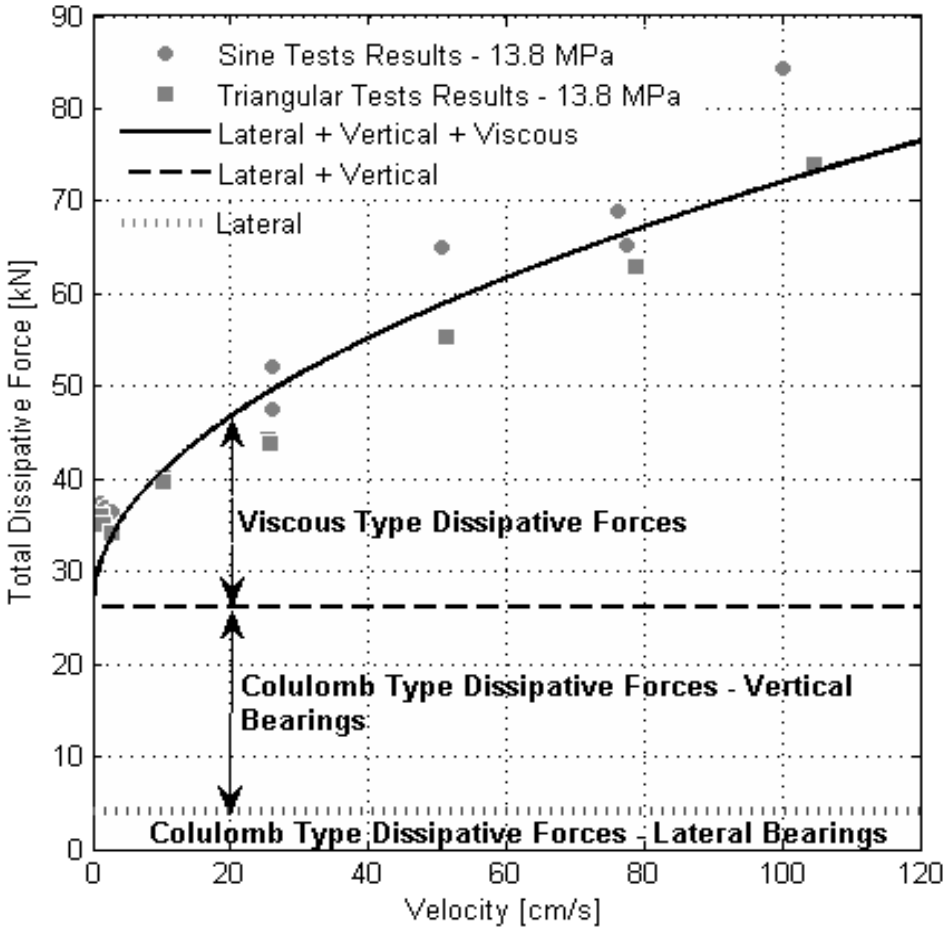

Figure 4.6: Decomposition of the total dissipative force into its three major components.

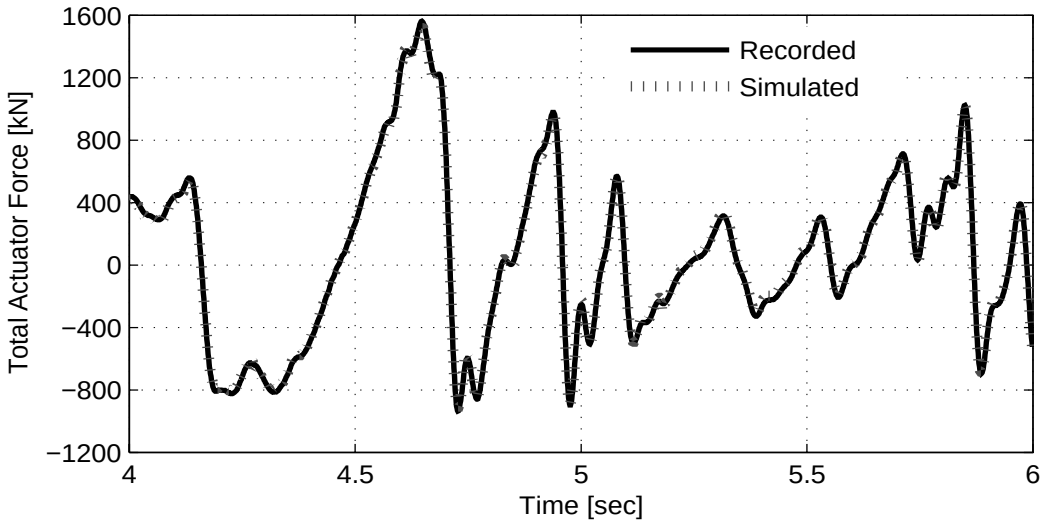

Figure 4.7: Comparison of recorded and simulated total actuator forces for the 300% El Centro earthquake test (13.8 MPa Nitrogen pressure in the hold-down struts).

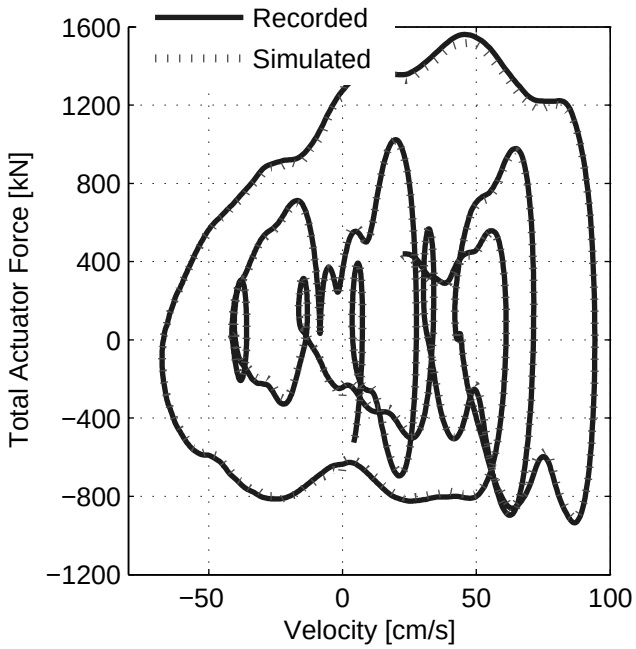

Figure 4.8: Recorded and simulated total actuator force versus recorded table velocity plots for 300% El Centro earthquake test (13.8 MPa pressure in the hold-down struts).

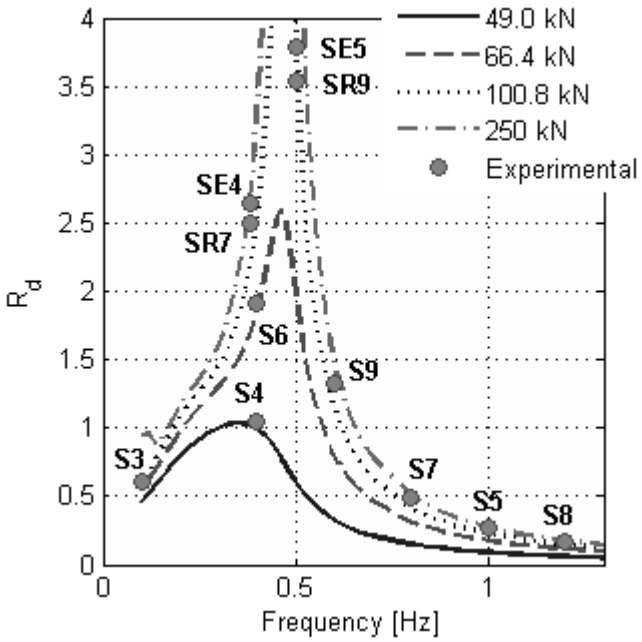

Figure 4.9: Dynamic amplification curves for the nonlinear model in (4.1) of the NEES-UCSD shake table mechanical system.

REFERENCES

Bondonet, G., Filiatrault, A. (1997). “Frictional Response of PTFE Sliding Bearings at High Frequencies.” *Journal of Bridge Engineering, ASCE,* 2(4), 139-148.

Clark, A. (1992). “Dynamic Characteristics of Large Multiple Degrees of Freedom Shaking Tables.” *Proc. 10th World Conf. on Earthquake Engineering*.

Conte, J. P., Trombetti, T. L. (2000). “Linear Dynamic Modeling of a Uni-axial Servo-Hydraulic Shaking Table System.” *Earthquake Engineering and Structural Dynamics*, 29(9), 1375-1404.

Crewe, A. J., Severn R. T. (2001). "The European Collaborative Programme on Evaluating the Performance of Shaking Tables.” *Phil. Trans. R. Soc. Lond. A*, 359, 1671-1696.

Hwang, J. S., Chang, K. C., and Lee, G. C. (1987). “The System Characteristics and Performance of a Shaking Table.” *NCEER Report No. 87-0004,* National Center for Earthquake Engineering Research, State University of New York at Buffalo, NY.

Kusner, D. A., Rood, J. D., and Burton, G. W. (1992). “Signal Reproduction Fidelity of Servohydraulic Testing Equipment.” *Proc. 10th World Conference on Earthquake Engineering*, Rotterdam, 2683-2688.

Ozcelik, O., Luco, E. J., and Conte, J. P., Trombetti, T. L., and Restrepo, J. I. (2007). “Experimental Characterization, Modeling and Identification of the UCSD-NEES Shake Table Mechanical System.” *Earthquake Engineering and Structural Dynamics*, in press.

Rinawi, A. M., Clough, R. W. (1991). “Shaking Table-Structure Interaction.” *EERC Report No. 91/13*, Earthquake Engineering Research Center, University of California at Berkeley, CA.

Shortreed, J. S., Seible, F., Filiatrault, A., and Benzoni, G. (2001). “Characterization and Testing of the Caltrans Seismic Response Modification Device Test System.” *Phil. Trans. R. Soc. Lond. A*, 359, 1829-1850.

Twitchell, B. S., and Symans, M. D. (2003). “Analytical Modeling, System Identification, and Tracking Performance of Uniaxial Seismic Simulators.” *Journal of Engineering Mechanics, ASCE*, 129(12).

Thoen, B. K., and Laplace, P. N. (2004). “Offline Tuning of Shaking Table.” *Proc. 13th World Conf. on Earthquake Engineering*, Vancouver, B.C., Canada, Aug. 1-6, Paper No. 960.

Van Den Einde, L., Restrepo, J., Conte, J. P., Luco, E. J., Seible, F., Filiatrault, A., Clark, A., Johnson, A., Gram, M., Kusner, D., and Thoen, B. (2004). “Development of the George E. Brown Jr. Network for Earthquake Engineering Simulation (NEES) Large High Performance Outdoor Shake Table at the University of California, San Diego.” *Proc. of 13-th World Conference on Earthquake Engineering*, Vancouver, BC Canada, August 1-6, Paper No. 3281.

Williams, D. M., Williams, M. S., and Blakeborough, A. (2001). “Numerical Modeling of a Servohydraulic Testing System for Structures.” *Journal of Engineering Mechanics, ASCE*, 127(8), 816-827.

Thoen, B. K. (2004). *469D Seismic Digital Control Software*, MTS Corporation.

Zhao, J., Shield, C., French, C., and Posbergh, T. (2005). “Nonlinear System Modeling and Velocity Feedback Compensation for Effective Force Testing.” *Journal of Engineering Mechanics*, 131(3), 244-253.

CHAPTER 5

2D MODEL OF THE ASSEMBLY OF THE PLATEN AND A GENERIC SPECIMEN

5.1. Introduction

The simple conceptual mathematical model for the mechanical subsystem of the NEES-UCSD shake table is given below. For the detailed discussion about the one-dimensional model refer to Ozcelik et al., (2008)(1).

$$M_e \ddot{u}_x(t) + K_e u_x(t) + \left(C_e \left| \dot{u}_x(t) \right|^{\alpha} + \mu_e F_v \right) sign(\dot{u}_x(t)) = F_{act}(t) \tag{5.1}$$

where M_e is the effective mass, K_e is the effective stiffness, C_e is the effective viscous damping, μ_e is the effective Coulomb friction coefficients and F_v is the vertical force acting on the vertical bearings. Identified parameters of the model in (5.1) are given in Table 5.1.

The equation of motion given in (5.1) can be extended to incorporate the rigid motion of the platen in three degrees-of-freedom $\begin{bmatrix} u_{0x} & u_{0z} & \theta_{0y} \end{bmatrix}^T$ while preserving the nature of the identified dissipative mechanism (i.e. $\left(C_e \left| \dot{u}_x(t) \right|^{\alpha} + \mu_e F_v \right) sign(\dot{u}_x)$). It

is anticipated that these three degrees of freedom would be enough to simulate the table-specimen dynamic interaction to a sufficient degree.

The reaction block and the surrounding soil are assumed to be rigid and this assumption has been proven to be sufficient by experimental observations (Luco et al., 2008). The platen is also assumed to be rigid. This assumption may not be realistic when the table platen is loaded with heavy specimens (e.g., more than two times the weight of the platen).

The assembly of the rigid platen, a generic specimen and the rigid reaction block is given in Figure 5.1. The mechanical components such as vertical bearings, hold-down struts are represented as linear springs and the identified dissipative mechanism is represented by dashpots and Coulomb friction elements. Spring constants for the vertical bearings were not estimated from experimental data but by considering the physical characteristics of the vertical bearings, i.e. effective bearing area, oil column length, bulk modulus of the oil. The generalized coordinates where the equation of motion has been derived for is indicated as “O” in Figure 5.1.

The main purpose of the derivations given here is to extend the model given in (5.1) to two-dimension so that it incorporates the dynamic effects of rigid body motion of the platen and a generic specimen. In order to be more general in the derivations, eccentricity of e_x is introduced between the center line of the platen, “G”, and the center line of the specimen, “O”, and it is assumed to be negative to the left of point “O”.

The motion of the platen at point “O” is defined as

$$\mathbf{u}_0 = \begin{bmatrix} u_{0x} & u_{0z} & \theta_{0y} \end{bmatrix}^T \tag{5.2}$$

The parameters of the assembly introduced in Figure 5.1 are K_{vb} = stiffness of one of the vertical bearings; K_e = total horizontal stiffness provided by the hold-down struts; C_e and μ_e = effective viscous damping and the Coulomb friction coefficients of the identified dissipative mechanism, respectively; M_e and $I_{\theta y}$ = effective mass and mass moment of inertia about the principal y axis of the platen, respectively; $F_{actW}(t)$ and $F_{actE}(t)$ = scalar actuator forces on the west and the east side of the platen, respectively (these forces are generated by the servo-hydraulic components of the shake table (Chapter 2); and $\overline{u}_i$ = relative floor displacement of the specimen (note that any specimen model can be coupled to the mechanical subsystem). Point "G" in Figure 5.1 indicates the center of gravity of the platen, and it is assumed to be positive downward. Numerical values of the parameters of the mechanical subsystem as well the dimensions of the assembly shown in Figure 5.1 are given in Table 5.2 and 7.3.

Equation of motion of the assembly with respect to the generalized coordinates at "O" can be written as follows

$$\mathbf{M}_0 \ddot{\mathbf{u}}_0(t) = \mathbf{F}_{act}(t) - \mathbf{F}_{spr}(t) - \mathbf{F}_{damp}(t) - \mathbf{F}_{coul}(t) - \mathbf{F}_{spe}(t) \tag{5.3}$$

where $\mathbf{M}_0$ = $[3\times3]$ mass tensor of the platen, $\mathbf{F}_{act}(t)$ = $[3\times1]$ actuator force vector, $\mathbf{F}_{spr}(t)$ = $[3\times1]$ spring forces due to the horizontal and vertical springs, $\mathbf{F}_{damp}(t)$ = $[3\times1]$ viscous dissipative forces, $\mathbf{F}_{coul}(t)$ = $[3\times1]$ Coulomb friction forces,

and $\mathbf{F}_{spe}(t) = [3\times1]$ resisting forces due to the specimen mounted on the platen. In the following sections, details derivations for each of these force components will be given.

5.2. Mass Tensor of the Platen

The mass tensor of the platen with respect to the principal axis passing through point "G" can be written in the following form due to the symmetry of the platen geometry

$$\mathbf{M}_O = \begin{bmatrix} m_{eff} & 0 & 0 \\ 0 & m_{eff} & 0 \\ 0 & 0 & I_{\theta y} \end{bmatrix} \tag{5.4}$$

Following relation exists between the coordinates at "G" and the coordinates at "O"

$$\mathbf{u}_G = \mathbf{R}_{G0}\mathbf{u}_0 \tag{5.5}$$

where

$$\mathbf{R}_{G0} = \begin{bmatrix} 1 & 0 & h_G \\ 0 & 1 & -e_x \\ 0 & 0 & 1 \end{bmatrix} \tag{5.6}$$

By using (5.5) and (5.6) the mass matrix with respect to the generalized coordinates at "O" can be found

$$\mathbf{M}_0 = \mathbf{R}_{G0}^T \mathbf{M}_G \mathbf{R}_{G0}$$

$$\mathbf{M}_0 = \begin{bmatrix} m_{eff} & 0 & h_G m_{eff} \\ 0 & m_{eff} & -e_x m_{eff} \\ h_G m_{eff} & -e_x m_{eff} & h_G^2 m_{eff} + e_G^2 m_{eff} + I_{\theta y} \end{bmatrix} \tag{5.7}$$

5.3. Actuator Force

$F_{actW}(t)$ and $F_{actE}(t)$ are the scalar actuator forces generated by the servo-hydraulic component of the shake table system. Here the details of transforming these scalar quantities to generalized coordinates are given.

Motions at points A_1 and A_2, where the actuators are connected to the platen, are assumed to be in the following form

$$\mathbf{u}_i^{(A)} = \begin{pmatrix} u_{ix} \\ u_{iz} \end{pmatrix}^{(A)} \quad i = 1, 2 \tag{5.8}$$

Transformation matrices which transform these motions to generalized coordinates at "O" for the west and the east actuators, indicated as indices 1 and 2 respectively, can be written as

$$\begin{aligned} \mathbf{u}_1^{(A)} &= \mathbf{R}_{10}^{(A)} \mathbf{u}_0 \\ &= \begin{bmatrix} 1 & 0 & c_a \\ 0 & 1 & -(a + e_x) \end{bmatrix} \mathbf{u}_0 \end{aligned} \tag{5.9}$$

and

$$\begin{aligned}\mathbf{u}_2^{(A)} &= \mathbf{R}_{20}^{(A)}\mathbf{u}_0 \\ &= \begin{bmatrix} 1 & 0 & c_a \\ 0 & 1 & (a-e_x) \end{bmatrix}\mathbf{u}_0 \end{aligned} \tag{5.10}$$

Note that the eccentricity e_x is chosen to be positive to the left of the center line of platen. Actuator vectors between the points where the actuators are connected to the reaction block and the points where the actuators are connected to the platen (A_1 and A_2) are given as

$$\begin{aligned}\mathbf{r}_{A1} &= \begin{bmatrix} u_{1x}^{(A)} + l_a & u_{1z}^{(A)} \end{bmatrix}^T \\ \mathbf{r}_{A2} &= \begin{bmatrix} -u_{2x}^{(A)} + l_a & -u_{2z}^{(A)} \end{bmatrix}^T \end{aligned} \tag{5.11}$$

where l_a is the length of each actuator. If we assume that the norm of the vectors given in (5.11) is approximately equal to l_a, then the scalar actuator forces $F_{actW}(t)$ and $F_{actE}(t)$ can be written in vector form as follows

$$\begin{aligned}\mathbf{F}_{actW}^{(1)}(t) &= \frac{F_{actW}(t)}{l_a}\mathbf{r}_{A1} \\ \mathbf{F}_{actE}^{(2)}(t) &= \frac{F_{actE}(t)}{l_a}\mathbf{r}_{A2} \end{aligned} \tag{5.12}$$

Actuator force vectors in (5.12) can be transformed to point “O” by using equations (5.8) through (5.12)

$$\begin{aligned}\mathbf{F}_{act}(t) = F_{actW}(t)\mathbf{R}_{10}^{(A)^T}\begin{bmatrix}1\\0\end{bmatrix} + \frac{F_{actW}(t)}{l_a}\mathbf{R}_{10}^{(A)^T}\mathbf{R}_{10}^{(A)}\mathbf{u}_0 + \\ F_{actE}(t)\mathbf{R}_{20}^{(A)^T}\begin{bmatrix}1\\0\end{bmatrix} - \frac{F_{actE}(t)}{l_a}\mathbf{R}_{20}^{(A)^T}\mathbf{R}_{20}^{(A)}\mathbf{u}_0 \end{aligned} \tag{5.13}$$

If we carry out the multiplications given in (5.13), the following expression can be found,

$$\mathbf{F}_{act}(t) = F_{actW}(t)\begin{bmatrix}1\\0\\c_a\end{bmatrix} + \frac{F_{actW}(t)}{l_a}\begin{bmatrix}1 & 0 & c_a\\ 0 & 1 & -a-e_x\\ c_a & -a-e_x & c_a^2+(a+e_x)^2\end{bmatrix}\mathbf{u}_0 + F_{actE}(t)\begin{bmatrix}1\\0\\c_a\end{bmatrix} - \frac{F_{actE}(t)}{l_a}\begin{bmatrix}1 & 0 & c_a\\ 0 & 1 & a-e_x\\ c_a & a-e_x & c_a^2+(a-e_x)^2\end{bmatrix}\mathbf{u}_0 \tag{5.14}$$

(5.14) shows that forces are acting on the platen not only along the x-direction (main direction where the actuators are exerting forces on the platen) but also along other degrees of freedom.

Note that the equations given here are very general. For example the geometric parameters of actuators do not have to be the same, meaning that the point of action of each actuator, $(-a,-c_a)$ for the west one and $(a,-c_a)$ for the east one, can be set to different values. This way any manufacturing or construction defect can be taken into account in the simulations. This aspect of the simulation framework presented here is applicable to each component of the equation given in (5.3)

5.4. Vertical Spring Forces

Oil-column effects within each vertical bearing are modeled as vertical springs. The oil-column stiffness, i.e. stiffness of a vertical bearing, can be calculated as follows

$$K_{vb} = \frac{\beta A_{vb}}{L_{oil}} \tag{5.15}$$

where β (0.82 GPa) is the bulk modulus of the oil, A_{vb} (2×0.519 m^2) is the effective area and L_{oil} (0.0127 m) is the oil-column length of a vertical bearing, respectively. The numerical value of K_{vb} is given in Table 5.2.

Motion at each point where the vertical springs are attached to the platen can be transformed to the motion at point "O" using the following relation

$$u_{zi}^{(VB)} = \mathbf{R}_{i0}^{(VB)}\mathbf{u}_{0x} \quad i=1,2,3 \tag{5.16}$$

where

$$\begin{aligned}\mathbf{R}_{10}^{(VB)} &= \begin{bmatrix}0 & 1 & -(a_v+e_x)\end{bmatrix}\\ \mathbf{R}_{20}^{(VB)} &= \begin{bmatrix}0 & 1 & -e_x\end{bmatrix}\\ \mathbf{R}_{30}^{(VB)} &= \begin{bmatrix}0 & 1 & (a_v-e_x)\end{bmatrix}\end{aligned} \tag{5.17}$$

Vertical force on each vertical bearing can be written as

$$F_{zi}^{(VB)} = K_{vb}u_{zi}^{(VB)}(t) \quad i=1,2,3 \tag{5.18}$$

Using equations (5.16) through (5.18), forces at point "O" due to the vertical springs can be found as

$$\mathbf{F}_{spr}^{(VB)} = K_{vb}\left(\mathbf{R}_{10}^{(VB)^T}\mathbf{R}_{10}^{(VB)} + \mathbf{R}_{20}^{(VB)^T}\mathbf{R}_{20}^{(VB)} + \mathbf{R}_{30}^{(VB)^T}\mathbf{R}_{30}^{(VB)}\right)\mathbf{u}_0 \tag{5.19}$$

If we carry out the multiplications in (5.19) the following equation can be found

$$\mathbf{F}_{spr}^{(VB)}(t) = K_{vb}\left(\begin{bmatrix} 0 & 0 & 0 \\ 0 & 1 & -a_v - e_x \\ 0 & -a_v - e_x & (-a_v - e_x)^2 \end{bmatrix} + \begin{bmatrix} 0 & 0 & 0 \\ 0 & 1 & -e_x \\ 0 & -e_x & e_x^2 \end{bmatrix} + \begin{bmatrix} 0 & 0 & 0 \\ 0 & 1 & a_v - e_x \\ 0 & a_v - e_{xv} & (a_v - e_x)^2 \end{bmatrix}\right)\mathbf{u}_0 \tag{5.20}$$

5.5. Horizontal Spring Forces

Horizontal springs, K_e, shown in Figure 5.1 represent the effect of nitrogen filled hold-down struts. Its identified value is given in Table 5.2.

The motion at points where the hold-down struts are attached to the platen can be transformed to the motion at point "O" using the following relation

$$u_{xi}^{(HD)} = \mathbf{R}_{i0}^{(HD)}\mathbf{u}_{0x} \quad i = 1, 2 \tag{5.21}$$

where

$$\begin{aligned} \mathbf{R}_{10}^{(HD)} &= \begin{pmatrix} 1 & 0 & c_h \end{pmatrix} \\ \mathbf{R}_{20}^{(HD)} &= \begin{pmatrix} 1 & 0 & c_h \end{pmatrix} \end{aligned} \tag{5.22}$$

Horizontal force at each spring can be written as

$$F_{xi}^{(HD)} = \frac{K_e}{2} u_{xi}^{(HD)}(t) \quad i = 1, 2 \tag{5.23}$$

By using the relations given in (5.21), through (5.23) the forces at point "O" due to the horizontal springs can be found as

$$\mathbf{F}_{spr}^{(HD)}(t) = \frac{K_e}{2}\left(\mathbf{R}_{10}^{(HD)^T}\mathbf{R}_{10}^{(HD)} + \mathbf{R}_{20}^{(HD)^T}\mathbf{R}_{20}^{(HD)}\right)\mathbf{u}_0 \tag{5.24}$$

If we carry out the multiplications given in (5.24), $\mathbf{F}_{spr}^{(HD)}(t)$ can be written as follows

$$\mathbf{F}_{spr}^{(HD)} = \frac{K_e}{2}\left(\begin{bmatrix} 1 & 0 & c_h \\ 0 & 0 & 0 \\ c_h & 0 & c_h^2 \end{bmatrix} + \begin{bmatrix} 1 & 0 & c_h \\ 0 & 0 & 0 \\ c_h & 0 & c_h^2 \end{bmatrix}\right)\mathbf{u}_0 \tag{5.25}$$

Equation (5.25) models the portion of the hold-down forces acting on the platen which are functions of the platen displacements. Hold-down struts also exert constant vertical forces on the platen in order to increase the overturning moment capacity of the table. Effects of the vertical forces will be included in the simulation model by transforming the point of action of these forces to point "O" using the following transformation matrices

$$\begin{aligned} \mathbf{R}_{10z}^{(HD)} &= \begin{bmatrix} 0 & 1 & -\left(a_H + e_x\right) \end{bmatrix}^T \\ \mathbf{R}_{20z}^{(HD)} &= \begin{bmatrix} 0 & 1 & \left(a_H - e_x\right) \end{bmatrix}^T \end{aligned} \tag{5.26}$$

where a_H is the horizontal distance between the midpoint of the platen to the points where hold-down struts are attached, and e_x is the eccentricity between center of gravity of the platen and the center line of the specimen (i.e., specimen offset). Using (5.26), hold-down forces at point "O" can be found as follows

$$\mathbf{F}_{const}^{(HD)} = \begin{bmatrix} 0 \\ 1 \\ -\left(a_H + e_x\right) \end{bmatrix} F_z^{(HD)} + \begin{bmatrix} 0 \\ 1 \\ \left(a_H - e_x\right) \end{bmatrix} F_z^{(HD)} \tag{5.27}$$

where $F_z^{(HD)}$ is the constant vertical hold-down force from one hold-down strut which is equal to 2.085×10^6 N. Notice that the hold-down struts are in tension.

Using (5.20), (5.25), and (5.27) total force acting on the platen due vertical, horizontal springs as well as constant vertical hold-down forces at the generalized coordinates “O” can be found

$$\mathbf{F}_{spr}(t) = \mathbf{F}_{spr}^{(VB)}(t) + \mathbf{F}_{spr}^{(HD)}(t) + \mathbf{F}_{const}^{(HD)} \tag{5.28}$$

5.6. Viscous Damping Forces

Dissipative force mechanism identified for the mechanical subsystem for the shake table includes Coulomb friction, and nonlinear viscous damping components. For convenience, the identified viscous dissipative model of the mechanical sub-system is repeated below

$$F_{damp}(t) = \frac{C_e}{2}\left|\dot{u}_{xi}^{(DP)}\right|^{\alpha} sign(\dot{u}_{x0}) \quad i = 1,2 \tag{5.29}$$

where, $\dot{u}_{xi}^{(DP)}(t)\ i = 1,2$ is the horizontal motion of the points where fictitious viscous dampers are attached to the platen, Figure 5.1, and $\dot{u}_{x0}(t)$ is the horizontal motion of the platen (recall that the platen is assumed to be rigid). The points where these viscous dampers are attached (A_1 and A_2) to the platen were decided based on the fact that the most of the viscous damping comes from the cross-port leakage within the actuators (Zhao, 2005). As detailed in Ozcelik et al. (2008)(1), the viscous coefficient C_e identified for the mechanical subsystem is an effective value representing the various viscous damping sources within the system; but the most important of these sources identified to be the cross-port leakage.

Likewise before, the motion at the points where the viscous dashpots are attached can be transformed to the motion at point “O” by the following equation

$$\dot{u}_{xi}^{(DP)} = \mathbf{R}_{i0}^{(DP)} \dot{\mathbf{u}}_{0x} \quad i = 1,2 \tag{5.30}$$

where

$$\begin{aligned} \mathbf{R}_{10}^{(DP)} &= \begin{pmatrix} 1 & 0 & c_a \end{pmatrix} \\ \mathbf{R}_{20}^{(DP)} &= \begin{pmatrix} 1 & 0 & c_a \end{pmatrix} \end{aligned} \tag{5.31}$$

By using (5.29), (5.30), and (5.31) the viscous damping forces acting at these points can be transformed to the generalized coordinates at “O”

$$\mathbf{F}_{damp}(t) = \frac{C_e}{2} \left(\mathbf{R}_{10}^{(DP)^T} \left| \mathbf{R}_{10}^{(DP)} \dot{\mathbf{u}}_0 \right|^{\alpha} + \mathbf{R}_{20}^{(DP)^T} \left| \mathbf{R}_{20}^{(DP)} \dot{\mathbf{u}}_0 \right|^{\alpha} \right) sign(\dot{u}_{ox}) \tag{5.32}$$

5.7. Coulomb Friction Forces

Dissipative forces identified for the mechanical subsystem includes also a Coulomb friction component as mentioned earlier. For convenience, the identified Coulomb friction force model is repeated below

$$F_{coul}(t) = \mu_e \left| F_{zi}(t) \right| sign(\dot{u}_{x0}) \quad i = 1,2,3 \tag{5.33}$$

where, $F_{zi}(t)$ is the vertical force acting on each vertical bearing, and $\dot{u}_{x0}(t)$ is the horizontal motion of the platen at “O”, and μ_e is the identified effective Coulomb friction coefficient representing the various Coulomb friction sources within the mechanical subsystem (Ozcelik et al., 2008(1)). The force $F_{zi}(t)$ can be written as a function of vertical motion at each vertical bearing as follows

$$F_{zi}(t) = K_{vb} u_{zi}^{(VB)}(t) \quad i = 1,2,3 \tag{5.34}$$

The vertical motions at these points can be transformed to the motion at point "O" by the following relation

$$u_{zi}^{(VB)} = \mathbf{R}_{i0}^{(VB)} \dot{\mathbf{u}}_{0x} \; i = 1,2,3 \tag{5.35}$$

where

$$\begin{aligned} \mathbf{R}_{10}^{(VB)} &= \begin{bmatrix} 0 & 1 & -(a_v + e_x) \end{bmatrix} \\ \mathbf{R}_{20}^{(VB)} &= \begin{bmatrix} 0 & 1 & -e_x \end{bmatrix} \\ \mathbf{R}_{30}^{(VB)} &= \begin{bmatrix} 0 & 1 & (a_v - e_x) \end{bmatrix} \end{aligned} \tag{5.36}$$

Effective Coulomb fiction force identified in (5.33) is acting along the longitudinal direction, x, therefore Coulomb forces acting on the horizontal plane at the interface between the vertical bearings and wear plates (Figure 5.1) must be transformed to point "O" with transformation vectors different than the ones given in (5.36), these vectors are given as follows, and they are indicated with subscript "x" to distinguish them from (5.36)

$$\begin{aligned} \mathbf{R}_{10x}^{(VB)} &= \begin{bmatrix} 1 & 0 & c_v \end{bmatrix} \\ \mathbf{R}_{20x}^{(VB)} &= \begin{bmatrix} 1 & 0 & c_v \end{bmatrix} \\ \mathbf{R}_{30x}^{(VB)} &= \begin{bmatrix} 1 & 0 & c_v \end{bmatrix} \end{aligned} \tag{5.37}$$

By using equations (5.34) through (5.37), the Coulomb friction forces acting at these points can be transformed to the generalized coordinates at "O" as

$$\mathbf{F}_{coul,dyn}(t) = \mu_e K_{vb} \begin{pmatrix} \mathbf{R}_{10x}^{(VB)^T} \left| \mathbf{R}_{10z}^{(VB)} \mathbf{u}_0 \right| + \mathbf{R}_{20x}^{(VB)^T} \left| \mathbf{R}_{20z}^{(VB)} \mathbf{u}_0 \right| + \\ \mathbf{R}_{30x}^{(VB)^T} \left| \mathbf{R}_{30z}^{(VB)} \mathbf{u}_0 \right| \end{pmatrix} sign(\dot{u}_{0x}) \tag{5.38}$$

Above equations formulate the vertical displacement dependent part of the Coulomb friction forces on the vertical bearings. Due to the weight of the platen and the vertical hold-down forces, constant Coulomb friction forces exist in the system. This constant friction force $F_{\mu e}$ has been estimated in Ozcelik et al. (2008)(1) to be 26.70×10^{3} N. Since only three bearings were modeled in the 2D model of the platen-specimen assembly, constant Coulomb force on each vertical bearing is $F_{\mu e1}=F_{\mu e2}=F_{\mu e3}=0.89\times10^{3}$ N (Figure 5.1). These forces can be transformed to point "O" using the following expression

$$\mathbf{F}_{coul,const}=\left\{\begin{bmatrix}1\\0\\c_v\end{bmatrix}F_{\mu e1}+\begin{bmatrix}1\\0\\c_v\end{bmatrix}F_{\mu e2}+\begin{bmatrix}1\\0\\c_v\end{bmatrix}F_{\mu e3}\right\}sign\left(\dot{u}_{0x}\right) \tag{5.39}$$

Using (5.38) and (5.39), the total Coulomb force acting on the platen at point "O" can be found as follows

$$\mathbf{F}_{coul}(t)=\mathbf{F}_{coul,dyn}(t)+\mathbf{F}_{coul,const} \tag{5.40}$$

5.8. Resisting Forces due to Specimen

The total floor displacement $\mathbf{u}_t$ of a generic specimen is given below

$$\mathbf{u}_t=\bar{\mathbf{u}}+\boldsymbol{\alpha}\mathbf{u}_0 \tag{5.41}$$

where $\boldsymbol{\alpha}$ is the $[3N\times3]$ matrix of totally geometric quantities, i.e. influence vector, which transforms the input motion $\mathbf{u}_0$ to story motions (story degrees of freedom), N is the number of nodes. In other words, $\boldsymbol{\alpha}\mathbf{u}_0$ is the rigid body motion of the specimen

due to the input motion at point "O". As an example, $\mathbf{u}_t$ for a two story shear-frame is given below where in this case $\boldsymbol{\alpha}$ would be a $[2\times 3]$ matrix

$$\mathbf{u}_t = \begin{pmatrix} \bar{u}_1 \\ \bar{u}_2 \end{pmatrix} + \begin{bmatrix} 1 & 0 & -h_{spe} \\ 1 & 0 & -2h_{spe} \end{bmatrix} \begin{pmatrix} u_{0x} \\ u_{0z} \\ \theta_{0y} \end{pmatrix} \tag{5.42}$$

The equation of motion for the specimen excited by effective forces given in (5.41) can be written as follows

$$\mathbf{M}_{spe}\ddot{\bar{\mathbf{u}}} + \mathbf{C}_{spe}\dot{\bar{\mathbf{u}}} + \mathbf{K}_{spe}\bar{\mathbf{u}} = -\mathbf{M}_{spe}\boldsymbol{\alpha}\ddot{\mathbf{u}}_0 \tag{5.43}$$

where $\mathbf{M}_e$ is the mass, $\mathbf{C}_{spe}$ is the damping and $\mathbf{K}_{spe}$ is the stiffness matrices of the specimen. Damping in the specimen is modeled as Rayleigh damping

$$\mathbf{C}_{spe} = a_0\mathbf{M}_{spe} + a_1\mathbf{K}_{spe} \tag{5.44}$$

a_0 and a_1 are the Rayleigh damping coefficients which can be obtained by setting damping ratios of any two modes to a specified damping ratio (Chopra, 2007).

From the relative floor responses (i.e., $\bar{\mathbf{u}}$) total resisting forces at point "O" can be calculated from the absolute floor accelerations

$$\mathbf{F}_{spe}(t) = \boldsymbol{\alpha}^T\mathbf{M}_{spe}\boldsymbol{\alpha}\ddot{\mathbf{u}}_0 + \boldsymbol{\alpha}^T\mathbf{M}_{spe}\ddot{\bar{\mathbf{u}}} \tag{5.45}$$

Force terms given in (5.45) are due to rigid body motion, and flexibility of the specimen. Notice that $\mathbf{F}_{spe}(t)$ is calculated from the absolute floor accelerations, therefore it includes also the damping forces.

5.9. Implementation Details of Equation of Motion

Equation of motion given in (5.3) can be written in the following alternative form in order to implement in Simulink

$$\ddot{\mathbf{u}}_0(t) = \mathbf{M}_0^{-1}\left\{\mathbf{F}_{act}(t) - \mathbf{F}_{spr}(t) - \mathbf{F}_{damp}(t) - \mathbf{F}_{coul}(t) - \mathbf{F}_{spe}(t)\right\} \tag{5.46}$$

For linear specimen models with not many degrees of freedom, the specimen can be modeled within Simulink. For such cases the implementation of (5.2) in block diagram format is given in Figure 5.2.

For cases in which specimen can not be modeled linearly with few degrees of freedom, a general finite element program will be necessary to model it. Figure 5.3 shows the implementation of (5.46) again with one difference: instead of modeling the specimen within Simulink, in this case specimen is modeled within OpenSees by the custom block developed to integrate OpenSees and Simulink called OpenSimConn.dll (Chapter 9).

Simulink implementation of the mechanical subsystem shown in Figure 5.3 can easily be integrated with the rest of the shake table model which includes the controller and the servo-hydraulic components of the shake table system.

5.10. Linearized Equation of Motion of the Platen with Linear Two-Story Shear Frame

In this section, the linearized model of the platen in 2D will be given. This linearized model will be used later on in the study to test the implementation details of some of the components of the shake table model due to its simplicity. The linearized

model presented here will have the platen, actuator, vertical, and horizontal springs components same as the nonlinear model presented above. Only difference between the linear and nonlinear models will arise due to dissipative force mechanisms assigned to them. In the nonlinear case, the identified nonlinear dissipative force mechanisms is used (Eq.(5.1)) whereas for the linear model, the nonlinear mechanism is linearized using an equivalent linear viscous dashpot. The details of this linearization are given in Chapter 5, and the result is repeated below for convenience

$$c_{eq} = 1.273 F_{\mu_e} / v + 1.113 C_e / \sqrt{v} \tag{5.47}$$

where F_{μ_e} is the effective Coulomb friction force, C_e is the effective viscous damping constant, and v is the velocity of the platen. Numerical values for these parameters are given in Table 5.4. Note that the equivalent linear viscous damping coefficient is velocity dependent (Ozcelik et al., 2008(2)). At 100 cm/s platen velocity, equivalent viscous damping is equal to 84.82×10^3 Ns/m.

The platen and the reaction block are assumed to be rigid. The assembly of the platen with a two-story shear-frame along with the other linearized mechanical components are shown in Figure 5.4. Note that the mechanical components are discretized with linear springs and dashpots. Equation of motion of this assembly with respect to point "O" can be written as follows

$$\mathbf{M}_O \ddot{\mathbf{u}}_O = \mathbf{F}_{act} - \mathbf{F}_{spr} - \mathbf{F}_{diss} - \mathbf{F}_{spe} \tag{5.48}$$

where $\mathbf{M}_o$ is the $[3\times3]$ mass matrix of the platen, $\mathbf{F}_{act}(t)$ is the $[3\times1]$ actuator force vector, $\mathbf{F}_{spr}(t)$ is the $[3\times1]$ spring forces due to both the horizontal and vertical

springs, $\mathbf{F}_{diss}(t)$ is the $[3\times1]$ dissipative forces due to horizontal equivalent viscous dashpots, and $\mathbf{F}_{spe}(t)$ is the $[3\times1]$ resisting force vector acting on the platen due to the specimen mounted on the platen. Notice the similarities between (5.48) and (5.3). Since the details regarding $\mathbf{M}_o$, $\mathbf{F}_{act}(t)$, and $\mathbf{F}_{spr}(t)$ are the same as in the previous discussion, in the following sections only the details regarding $\mathbf{F}_{diss}(t)$ and $\mathbf{F}_{spe}(t)$ will be given.

Viscous Damping Forces. Dissipative forces identified for the mechanical subsystem of the plant includes Coulomb friction type nonlinearity, and also a nonlinear viscous damping force component (refer to the Earthquake Engineering and Structural Dynamics paper for details). Here in this study, an equivalent linear viscous damping coefficient is used to model the dissipative forces in the plant. For this purpose two linear dashpots are used for representing viscous type dissipative forces, and they are assumed to be attached at the two points where the actuators are attached; but note that these simplifications are not necessary for the framework presented here; fully nonlinear dissipative force model can be used with the same framework.

Likewise before, the motion at the points where the linear viscous dashpots are attached can be transformed to the motion at point "O" by the following relations

$$u_{xi}^{(DP)} = \mathbf{R}_{iO}^{(DP)}\mathbf{u}_{Ox} \quad i=1,2 \tag{5.49}$$

where

$$\begin{aligned}\mathbf{R}_{10}^{(DP)} &= \begin{pmatrix}1 & 0 & c_a\end{pmatrix}\\ \mathbf{R}_{20}^{(DP)} &= \begin{pmatrix}1 & 0 & c_a\end{pmatrix}\end{aligned} \tag{5.50}$$

By using the relations given in (5.50), the viscous damping forces acting at these points can be transformed to the point "O"

$$\mathbf{F}_{diss}^{(HD)} = c_{eq}\left(\mathbf{R}_{10}^{(DP)^T}\mathbf{R}_{10}^{(DP)} + \mathbf{R}_{20}^{(DP)^T}\mathbf{R}_{20}^{(DP)}\right)\dot{\mathbf{u}}_O \tag{5.51}$$

(5.51) can be written in more detailed format

$$\mathbf{F}_{diss} = c_{eq}\left(\begin{pmatrix} 1 & 0 & -c_a \\ 0 & 0 & 0 \\ -c_a & 0 & c_a^2 \end{pmatrix} + \begin{pmatrix} 1 & 0 & -c_a \\ 0 & 0 & 0 \\ -c_a & 0 & c_a^2 \end{pmatrix}\right)\mathbf{u}_O \tag{5.52}$$

Resisting Forces due to Shear Specimen. The total floor displacement $\mathbf{u}_t$ is given below

$$\mathbf{u}_t = \bar{\mathbf{u}} + \boldsymbol{\alpha}\mathbf{u}_O \tag{5.53}$$

where $\boldsymbol{\alpha}$ is a purely geometric matrix with size $[2\times 3]$. (5.53) can be written in a detailed way as follows

$$\mathbf{u}_t = \begin{pmatrix} \bar{u}_1 \\ \bar{u}_2 \end{pmatrix} + \begin{bmatrix} 1 & 0 & h_s \\ 1 & 0 & 2h_s \end{bmatrix}\begin{pmatrix} u_{Ox} \\ u_{Oz} \\ \theta_{Oy} \end{pmatrix} \tag{5.54}$$

Equation of motion for the specimen can be written as follows

$$\mathbf{M}_{spe}\ddot{\bar{\mathbf{u}}} + \mathbf{C}_{spe}\dot{\bar{\mathbf{u}}} + \mathbf{K}_{spe}\bar{\mathbf{u}} = -\mathbf{M}_{spe}\boldsymbol{\alpha}\ddot{\mathbf{u}}_O \tag{5.55}$$

The matrices describing the equation of motion of the specimen are given below

$$\begin{aligned} \mathbf{M}_{spe} &= \begin{bmatrix} m_{spe} & 0 \\ 0 & m_{spe} \end{bmatrix} \\ \mathbf{K}_{spe} &= \begin{bmatrix} 2k_{spe} & -k_{spe} \\ -k_{spe} & k_{spe} \end{bmatrix} \\ \mathbf{C}_{spe} &= a_0\mathbf{M}_{spe} + a_1\mathbf{K}_{spe} \end{aligned} \tag{5.56}$$

Damping in the specimen is modeled using Rayleigh damping, note this damping is inherent to only specimen, and a_0 and a_1 are the Rayleigh damping coefficients which can be obtained by setting damping ratios of first two modes to be any damping ratio; but here it is set to 3%.

From relative floor displacements resisting forces at point "O" can be calculated as follows

$$\mathbf{F}_{spe}(t) = \boldsymbol{\alpha}^T \mathbf{M}_{spe} \boldsymbol{\alpha} \ddot{\mathbf{u}}_O + \boldsymbol{\alpha}^T \mathbf{M}_{spe} \ddot{\bar{\mathbf{u}}} \tag{5.57}$$

First term in (5.57) is the force due to the rigid motion of the specimen, and the second term is due to the flexibility of the specimen. Notice that $\mathbf{F}_{spe}(t)$ is calculated from the absolute floor accelerations, and therefore it includes also the damping forces.

The linear 2D mechanical subsystem presented here will be used later on in the study to check implementation issues.

LIST OF TABLES

Table 5.1: Identified model parameters for the mechanical subsystem.

M_e [tons]	K_e [MN/m]	C_e [KN (s/m)^0.5]	μ_e [%]	α
144	1.263	44.6	0.39	0.5

Table 5.2: Numerical values of the mechanical subsystem parameters.

F_z [N]	$I_{\theta y}$ [kg m^2]	K_{vb} [N/m]	$F_{\mu e1,2,3}$ [N]
2.085×10^6	1.843×10^6	$67,020\times10^6$	0.89×10^3

Table 5.3: Dimensions of the mechanical subsystem.

a [m]	e_x [m]	h_G [m]	l_a [m]	a_v [m]	a_h [m]	c_a [m]	c_v [m]	c_h [m]
6.13	0.0	0.87	6.15	4.88	4.92	1.27	1.21	2.21

Table 5.4: Numerical values for the parameters of the linear platen-specimen model.

h_{spe} [m]	c_{eq} [Ns/m]	$F_{\mu e}^{(*)}$ [N]	m_{spe} [kg]	k_{spe} [N/m]
3.50	84.82×10^{3}	26.70×10^{3}	45×10^{3}	1800×10^{3}

(*) $F_{\mu e}$ corresponds to the Coulomb force in which the vertical forces acting on the bearings due to the platen weight and the hold-down struts with pre-charged pressure of 13.8MPa are 5.78 MN.

LIST OF FIGURES

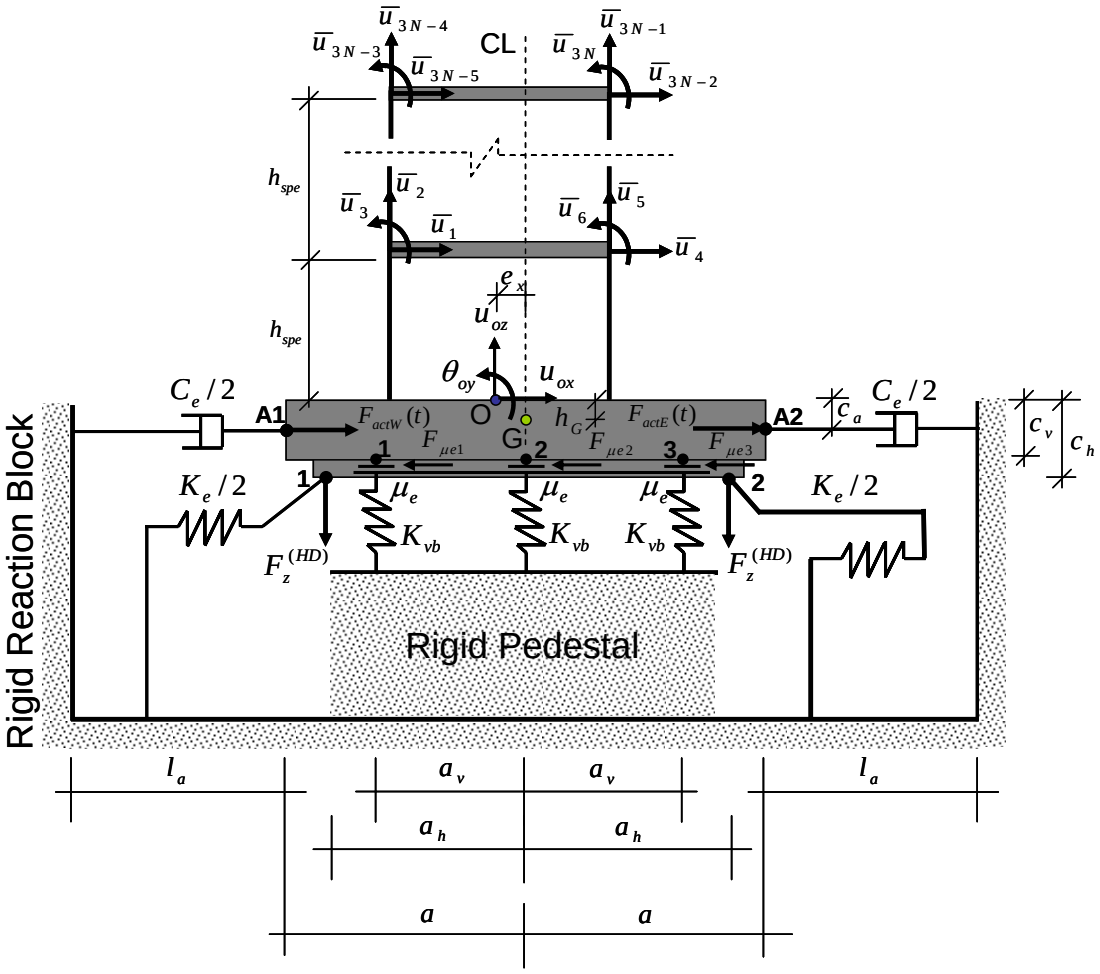

Figure 5.1: Rigid platen, rigid reaction block, rigid soil, and a generic specimen assembly along with springs, dashpots, and Coulomb friction elements to model mechanical subsystem.

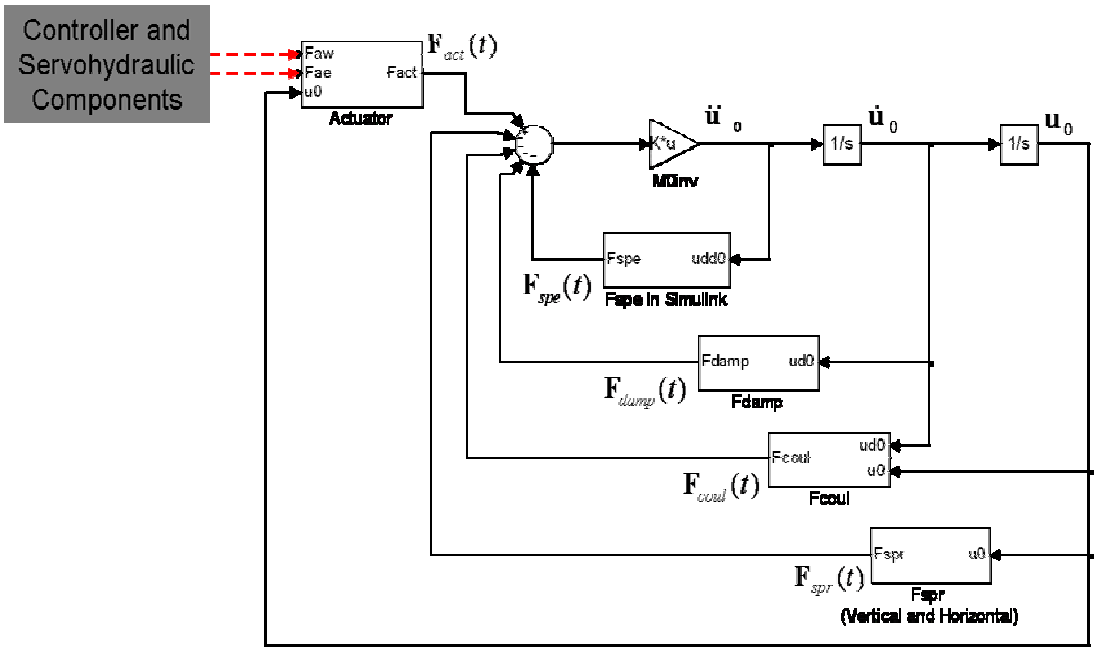

Figure 5.2: Simulink implementation of equation of motion of the mechanical sub-system ("All Simulink Model", i.e. specimen is also modeled in Simulink).

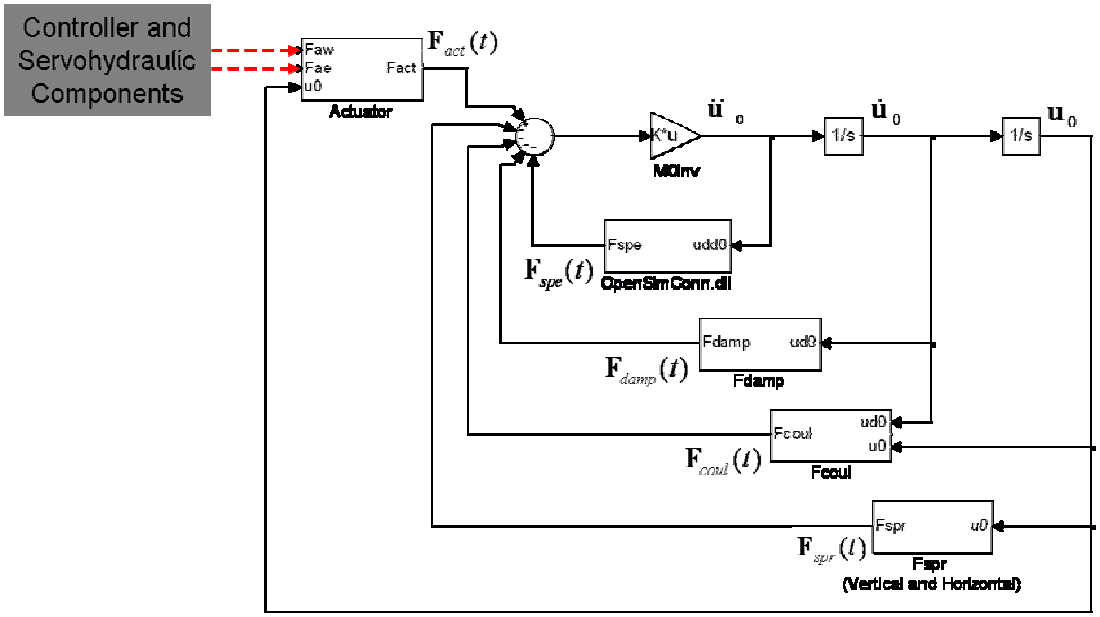

Figure 5.3: Simulink implementation of equation of motion of the mechanical sub-system with OpenSimConn.dll custom block.

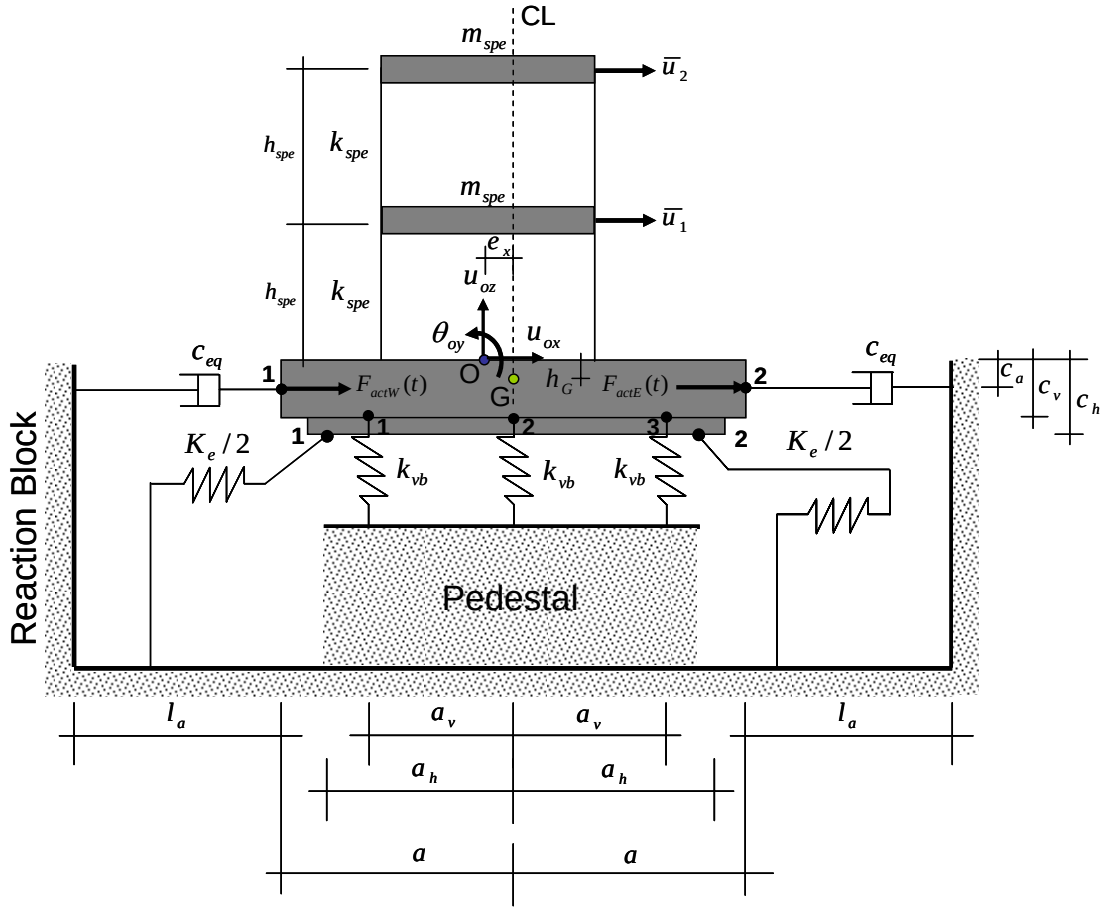

Figure 5.4: Rigid platen and two story shear specimen assembly with linearized dissipative force mechanism.

REFERENCES

Chopra, A.K. (2007). *Dynamics of Structures*, Pearson Prentice Hall, Upper Saddle River, NJ.

Luco, J.E., Conte, J.P., Ozcelik, O. (2008). "Experimental study of the dynamic interaction between the foundation of the NEES-UCSD shake table and surrounding soil." *Under preparation for submission to Soil Dynamics and Earthquake Engineering*.

Ozcelik, O., Luco, E.J., Conte, J.P., Trombetti, T.L., and Restrepo, J.I. (2008)(1). "Experimental characterization, modeling and identification of the UCSD-NEES shake table mechanical system." *Earthquake Engineering and Structural Dynamics*, Volume 37(2), pp. 243-264, doi: 10.1002/eqe.754.

Ozcelik, O., Luco, E.J., Conte, J.P. (2008)(2). "Identification of the Mechanical Subsystem of the NEES-UCSD Shake Table by a Least-Square Approach." *ASCE Journal of Engineering Mechanics*, Volume 134(1), pp. 23-34, doi: 10.1061/(ASCE)0733-9399(2008)134:1(23).

Zhao, J., Shield, C., French, C., Posbergh, T., Nonlinear System Modeling and Velocity Feedback Compensation for Effective Force Testing. *Journal of Engineering Mechanics*, 131(3), 244-253, 2005.

CHAPTER 6

CONTROL-TABLE-STRUCTURE INTERACTION

6.1. Linearized Open and Closed-Loop Table Transfer Functions

6.1.1. Open-Loop Table Transfer Functions

In this section of the study, formulations for open-loop model of a linear servovalve-actuator with rigid platen and a single degree of freedom specimen will be given.

Linearized flow about the origin from a servovalve can be written as

$$q = k_q c - k_c \frac{f}{A} \tag{6.1}$$

where k_q = linearized flow gain, c = valve command, f = force generated by the actuator, k_c = leakage constant, and A = effective actuator piston area. Flow q from the servovalve into actuator chambers can be expressed using the flow continuity equation as follows

$$q = A\dot{x} + \frac{V}{2\beta A}\dot{f} \tag{6.2}$$

where $\dot{x}$ is the velocity of the actuator piston, V is the hydraulic fluid volume for the actuator, and β is the bulk modulus of hydraulic fluid. From (6.1) and (6.2) open-loop actuator dynamics can be obtained

$$\dot{f} = \frac{2\beta A}{V}\left(k_q c - \frac{k_c}{A} f - A\dot{x} \right) \tag{6.3}$$

For the sake of simplicity the platen is assumed to be rigid with an effective mass of m_{pl}. Block diagram representation of (6.3) with a rigid platen is given in Figure 6.1. The open-loop transfer function from c (valve command) to f (actuator force) can be written as follows

$$G_{fc}(s) = \frac{f(s)}{c(s)} = \frac{s\dfrac{2k_q\beta A}{V}}{s^2 + \dfrac{2\beta k_c}{V}s + \dfrac{2\beta A^2}{Vm_{pl}}} \tag{6.4}$$

Equation (6.4) has a very similar form as a linear single degree of freedom (SDOF) system with mass, dashpot, and spring excited by an external force. From (6.4), it can be said that an actuator attached to a mass behaves like a mass-damper-spring system with a single resonant frequency given as

$$\omega_{oil} = \sqrt{\frac{2\beta A^2}{Vm_{pl}}} \tag{6.5}$$

This resonant frequency is called the oil-column frequency. From (6.5), the following can also be defined

$$\frac{2\beta k_c}{V} = 2\xi_{oil}\omega_{oil} \tag{6.6}$$

Notice that the actuator damping is related to leakage constant k_c. Numerical values given in Table 6.1 for model in (6.4) will be used in order to investigate the magnitude response of the open-loop transfer function.

Figure 6.2 shows the magnitude response of the open-loop model in given in (6.4). Figure 6.2 clearly shows the oil column frequency at 11.3 Hz. Notice that the transfer function from the valve command to platen acceleration can be readily obtained by dividing $G_{fc}(s)$ by the platen mass, m_{pl} (i.e. $G_{\ddot{x}c}(s) = \frac{1}{m_{pl}} G_{fc}(s)$).

The model shown in Figure 6.1 can be modified to incorporate the effect of an single-degree-of-freedom specimen. Figure 6.3 shows the modified version of Figure 6.1 when a specimen is mounted on the platen. The transfer function $G_h(s)$ is given as follows

$$G_h(s) = \frac{A}{\frac{V}{2\beta}s + k_c} \tag{6.7}$$

The total resisting force acting on the platen due to a linear SDOF specimen is f_S (i.e. $f_s(s) = m_S(x + x_S)s^2$). The transfer function $G_S(s)$ from the platen acceleration $\ddot{x}$, to the total resisting force f_S, can be written as follows

$$G_S(s) = \frac{f_S(s)}{s^2 x} = m_S\left(1 - \frac{s^2 m_S}{s^2 m_S + s c_S + k_S}\right) \tag{6.8}$$

where m_S is the mass, c_S is the viscous damping constant, and k_S is the stiffness coefficient of the specimen. The block-diagram within the dotted box in Figure 6.3 is denoted as $G_{xf}(s)$. It is the transfer function from the actuator force to the displacement of the platen (or actuator piston displacement, since the platen is assumed to be rigid)

$$G_{xf}(s) = \frac{1}{s^2\left[m_{pl} + G_S(s)\right]} \tag{6.9}$$

By substituting (6.8) into (6.9), the following expression can be found for $G_{xf}(s)$

$$G_{xf}(s) = \frac{x(s)}{f(s)} = \frac{1}{s^2 m_{pl}} \cdot \frac{s^2 + s2\xi_S\omega_S + \omega_S^2}{s^2 + s2(1+\frac{m_S}{m_{pl}})\xi_S\omega_S + (1+\frac{m_S}{m_{pl}})\omega_S^2} \tag{6.10}$$

where ξ_s is the damping ratio, and ω_s is the natural undamped frequency of the specimen. The denominator of (6.10) can be written in a simpler way by defining two new parameters

$$\begin{aligned} \xi_T &= \xi_S\sqrt{1+\frac{m_S}{m_{pl}}} \\ \omega_T &= \omega_S\sqrt{1+\frac{m_S}{m_{pl}}} \end{aligned} \tag{6.11}$$

therefore (6.10) takes the following form

$$G_{xf}(s) = \frac{x(s)}{f(s)} = \frac{1}{s^2 m_{pl}} \cdot \frac{s^2 + s2\xi_S\omega_S + \omega_S^2}{s^2 + s2\xi_T\omega_T + \omega_T^2} \tag{6.12}$$

By using $G_{xf}(s)$, Figure 6.3 can be redrawn in a simpler way as shown in Figure 6.4

By block diagram algebra, the transfer function $G_{fc}^{spe}(s)$ from the valve command c to the actuator force f can be found

$$G_{fc}^{spe}(s) = \frac{k_q G_h(s)}{1 + sAG_{xf}(s)G_h(s)} \tag{6.13}$$

In order to investigate the magnitude and phase response of the open-loop transfer function in (6.13), in addition to the parameters given in Table 6.1 numerical values for the specimen parameters have to be defined (Table 6.2). Figure 6.5 shows the magnitude and phase plots of (6.13).

The open-loop transfer function of the model given in (6.13) can be written in numerical form as follows

$$G_{fc}^{spe}(s) = \frac{s\left(1.31\times10^{8}s^{2} + 1.434\times10^{8}s + 3.003\times10^{10}\right)}{s^{4} + 1.094s^{3} + 5270s^{2} + 3801s + 7.96\times10^{5}} \tag{6.14}$$

Zeros and poles of (6.14) will be helpful for understanding the physical origins of the peaks and valleys seen in the magnitude response plot of (6.14). Zeros of (6.14) are given as follows

$$\begin{aligned} z_1 &= 0 \\ z_2 &= -0.5473 + 15.1307i \\ z_2 &= -0.5473 - 15.1307i \end{aligned} \tag{6.15}$$

One natural frequency can be extracted from the complex-conjugate zero pair given in (6.15) as $\omega_{1z} = 15.1$ rad/s (2.42 Hz). This value corresponds to the natural frequency ω_T, which is defined in (6.11). Therefore it can be said that at this particular

frequency, the open-loop model given (6.13) has limited ability to apply forces (the valley seen in Figure 6.5). The poles of (6.14) are given as follows

$$\begin{aligned} p_1 &= -0.181 + 71.5i \\ p_2 &= -0.181 - 71.5i \\ p_3 &= -0.366 + 12.5i \\ p_4 &= -0.366 - 12.5i \end{aligned} \tag{6.16}$$

Two distinct natural frequencies can be extracted from the two complex-conjugate poles given in (6.16) as $\omega_{1p} = 12.5$ rad/s (1.98 Hz) and $\omega_{2p} = 71.5$ rad/s (11.38 Hz). These frequencies are very close to the natural vibration frequency of the specimen (2.0 Hz), and the oil column frequency (11.3 Hz). Therefore, it can be said that the model given in (6.13) has two resonant frequencies: one corresponds to the specimen natural frequency and the other to the oil column frequency (two peaks seen in Figure 6.5).

6.1.2. Closed-Loop Table Transfer Function

The open-loop model of the servovalve-actuator-rigid platen-specimen model (6.13) is expanded by keeping the model parameters as variables as follows

$$G_{fc}^{spe}(s) = \frac{k_q\left(s^3 + 2\xi_T\omega_T s^2 + \omega_T^2 s\right)}{\left[\begin{array}{l} s^4 + \left(2\xi_T\omega_T + 2\xi_{oil}\omega_{oil}\right)s^3 + \left(\omega_T^2 + 4\xi_{oil}\omega_{oil}\xi_T\omega_T + \omega_{oil}^2\right)s^2 \\ + \left(2\xi_{oil}\omega_{oil}\omega_T^2 + 2\xi_S\omega_S\omega_{oil}^2\right)s + \omega_{oil}^2\omega_S^2 \end{array}\right]} \tag{6.17}$$

Equation (6.17) shows that the numerator contains the valve flow gain, damping and natural vibration frequency of the combined mechanical system of rigid platen and a SDOF specimen, and the 1st, 2nd and the 3rd derivative of the valve

command signal. This last observation is valuable in the sense that in order for actuator to move the table at higher frequency range, any feedforward control signal added onto the valve command signal c shown in Figure 6.4 must be proportional with the velocity, acceleration, and the jerk (3rd derivative) of the command signal in a displacement control strategy. Figure 6.6 shows the block diagram of displacement control strategy with force feedback and feedforward terms applied on the velocity, acceleration, and jerk command signals.

In Figure 6.6 u is the command displacement, k_P is the proportional gain, k_{VF}, k_{AF}, and k_{JF} are the velocity, acceleration and jerk lead gains, respectively, and k_{DP} is the force feedback gain. The closed-loop transfer function from the command displacement u to the actuator force f can be found using the block diagram algebra as follows

$$\bar{G}_{fu}(s) = \frac{k_q G_h(s)\left(k_p + sk_{VF} + s^2 k_{AF} + s^3 k_{JF}\right)}{\left[1 + G_h(s)k_q\left(k_p G_{xf}(s) - k_{DP}\right)\right] + sG_h(s)G_{xf}(s)A} \tag{6.18}$$

Equation (6.18) shows the effective topology of the controller of NEES-UCSD shake table with proportional and force feedback loops, and feedforward terms of velocity, acceleration, and jerk signals.

6.2. Control-Table-Structure Interaction

The roots of the numerator of (6.12) are related to the dynamics of the specimen (i.e. damping, and natural frequency), and the roots of its denominator are related to the dynamics of the combined mechanical system (i.e. rigid platen and

SDOF specimen), which are in turn also closely related to the characteristics of the specimen.

The block diagram given in Figure 6.6 shows that the dynamics of the structure (embedded in $G_{xf}(s)$) directly affect the dynamics of the actuator through a feedback path called the natural velocity feedback (Dyke et al., 1995). This interaction can be seen clearly in the closed-loop transfer function from the command input u to the actuator force f, which is given in (6.18). By representing this transfer function in terms of its respective numerators and denominators, the following equation can be written

$$G_{fu}(s) = \frac{n_{fu}}{d_{fu}} = \frac{\frac{n_h}{d_h} k_q \left(k_p + s k_{VF} + s^2 k_{AF} + s^3 k_{JF} \right)}{\left[1 + \frac{n_h}{d_h} k_q \left(k_p \frac{n_{xf}}{d_{xf}} - k_{DP} \right) \right] + s \frac{n_h}{d_h} \frac{n_{xf}}{d_{xf}} A} \tag{6.19}$$

where n and d stand for numerator and denominator, respectively. Equation (6.19) can be reorganized to obtain the following equation

$$G_{fu}(s) = \frac{n_{fu}}{d_{fu}} = \frac{n_h k_q \left(k_p + s k_{VF} + s^2 k_{AF} + s^3 k_{JF} \right) d_{xf}}{d_h d_{xf} + n_h k_q k_p n_{xf} - k_{DP} d_{xf} + s n_h n_{xf} A} \tag{6.20}$$

From (6.20) it is observed that the poles of the transfer function $G_{xf}(s)$, which are closely related to the specimen, become the zeros of the transfer function $G_{fu}(s)$. Since the poles of the combined mechanical system (i.e. d_{xf}) are the zeros of $G_{fu}(s)$, shake tables exciting a lightly damped structure have a limited ability to apply forces at the natural frequencies of the combined mechanical system. Similar observations have

been done by various researchers for actuators which are directly attached to the specimens (Dyke et al., 1995; Dimig et al., 1999; Zhao et al., 2005).

6.2.1. Three-Variable-Controller (TVC)

In this section, open-loop transfer function given in (6.13) will be integrated with the controller of UCSD-NEES shake table, namely Three-Variable-Controller (TVC). TVC is a displacement controller with a force feedback loop for force stabilization and with feedforward (i.e. lead) terms of velocity, acceleration, and jerk to enhance the table control at higher operating frequencies. Feedforward states in TVC are generated by the Reference Generator. The Reference Generator takes the reference signal, which represents desired displacement, velocity, or acceleration depending on control mode, and creates the reference states u_{xref} , $\dot{u}_{xref}$, $\ddot{u}_{xref}$, and $\dddot{u}_{xref}$. In TVC there are five notch filters to compensate for the resonances and anti-resonances. Measured force feedback is high-pass filtered by TVC before being added to the valve command signal to damp-out oil column resonance.

More details regarding the constitutive parts of TVC and the feedback generator, which is assumed to be the part of the plant (i.e. not a part of TVC), can be found in Thoen (2004) and Chapter 1. The block diagram of TVC is given in Figure 6.7 u_{fbk} , $\dot{u}_{fbk}$, $\ddot{u}_{fbk}$ are the displacement, velocity, and acceleration feedback states which are generated by the feedback generator, and the f_{fbk} is the force feedback filtered by a low-pass filter. It should be noted here that the Feedback Generator and the low-pass force filter are included in the plant, not in TVC, and hence not shown in Figure 6.7.

The transfer function $G_R(s)$ is given as follows

$$G_R(s) = G_{COM}(s)\cdot[(k_{PF}+k_P)G_{RD}(s)\cdot\frac{10}{D_{\max}} + k_{VF}G_{RV}(s)\cdot\frac{10}{V_{\max}} + \\ + k_{AF}G_{RA}(s)\cdot\frac{10}{A_{\max}} + k_{JF}G_{RJ}(s)\cdot\frac{10}{A_{\max}}] \tag{6.21}$$

where

$$G_{COM}(s) = k_M G_{INT}(s)\prod_{i=1}^{5} G_{NOTCH}^{i}(s) \tag{6.22}$$

k_{PF} is the displacement feedforward gain (this gain is rarely, if ever used), k_M is the master gain (always set to unity) and $D_{\max}$, $V_{\max}$, and $A_{\max}$ are the normalization constants corresponding to the maximum displacement, velocity and acceleration that the shake table can reach, respectively. In majority of the shake table tests, the signal desired to be reproduced on the table is an acceleration record (i.e. reference signal is acceleration); therefore TVC is set to run under acceleration control mode. Since this is the case, the transfer functions $G_{RD}(s)$, $G_{RV}(s)$, $G_{RA}(s)$, and $G_{RJ}(s)$ given below are specialized to the acceleration control mode of TVC .Transfer functions corresponding to the other control modes of TVC are given in Chapter 1.

$$G_{RA}(s) = \frac{\ddot{u}_{xref}}{R} = \frac{s^3}{s^3 + (2\zeta+1)\omega_{HP}s^2 + (2\zeta+1)\omega_{HP}^2 s + \omega_{HP}^3} \tag{6.23}$$

$$G_{RD}(s) = \frac{u_{ref}}{R} = \frac{1}{s^2}\frac{\ddot{u}_{ref}}{R}(s) \tag{6.24}$$

$$G_{RV}(s) = \frac{\dot{u}_{ref}}{R} = \frac{1}{s}\frac{\ddot{u}_{ref}}{R}(s) \tag{6.25}$$

$$G_{RJ}(s) = \frac{\dddot{u}_{ref}}{R} = s\frac{\ddot{u}_{ref}}{R} \tag{6.26}$$

where ω_{HP} is the cut-in frequency and ξ is the damping ratio, which always set to 0.707, of the high-pass filter given in (6.23).

The discrete time transfer functions of the notch filters on TVC are given as follows

$$G^i_{NOTCH}(z) = \frac{(w^i_0 + w^i_1 a^i_2) + (w^i_0 + w^i_1)a^i_1 z^{-1} + (w^i_1 + w^i_0 a^i_2)z^{-2}}{1 + a^i_1 z^{-1} + a^i_2 z^{-2}} \quad i = 1\ldots5 \tag{6.27}$$

where

$$\begin{aligned} k^i_1 &= -\cos(2\pi f_{0i} T) \\ k^i_2 &= \frac{1-\tan(\pi bw_i T)}{1+\tan(\pi bw_i T)} \\ a^i_1 &= k^i_1(1+k^i_2) \\ a^i_2 &= k^i_2 \\ w^i_0 &= 1 + depth_i/2 \\ w^i_1 &= -depth_i/2 \end{aligned} \tag{6.28}$$

where T is the sampling time, f_{0i} is the center frequency, bw_i is the width, and $depth_i$ is the depth of the i[th] notch filter. Discrete transfer functions given in (6.27) are transformed into continuous time by Tustin's method (also known as bilinear transformation) using the following mapping between z-domain to s-domain

$$s = \frac{2}{T}\frac{z-1}{z+1} \tag{6.29}$$

The transfer function of the reset integrator $G_{INT}(s)$ is given as follows

$$G_{INT}(s) = 1 + \frac{k_I}{s} \tag{6.30}$$

where k_I is the reset integrator gain. The rest of the transfer functions of TVC are given below

$$G_D(s) = -k_P G_{COM}(s) \cdot \frac{10}{D_{\max}} \tag{6.31}$$

$$G_V(s) = -k_V G_{COM}(s) \cdot \frac{10}{V_{\max}} \tag{6.32}$$

$$G_A(s) = -k_A G_{COM}(s) \cdot \frac{10}{A_{\max}} \tag{6.33}$$

$$G_F(s) = k_{DP} G_{COM}(s) G_{DP}(s) \cdot \frac{10}{F_{\max}} \tag{6.34}$$

$F_{\max}$ is the force normalization constant, and $G_{DP}(s)$ is a second order high-pass Butterworth filter with 3dB cutoff frequency at ω_{DP}

$$G_{DP}(s) = \frac{s^2}{s^2 + \sqrt{2}\omega_{DP} s + \omega_{DP}^2} \tag{6.35}$$

The command to the servovalve c shown in Figure 6.7 can be written as follows

$$c(s) = G_R(s) r(s) + G_D(s) u_{fbk}(s) + G_V(s) \dot{u}_{fbk}(s) + G_A(s) \ddot{u}_{fbk}(s) + G_F(s) f_{fbk}(s) \tag{6.36}$$

where $r(s)$ is the reference signal (in this case it is acceleration).

TVC is implemented in Matlab-Simulink using the above given transfer functions. In order to check the implementation of TVC, Simulink model of TVC is excited by an impulse acceleration (i.e. reference signal is an impulse), and the TVC output (i.e. command to the servovalve(s)) is recorded, then the transfer function between these two signals are estimated. The same impulse acceleration is inputted to the real-time control software 469D and the transfer function between the same input and output is estimated. Then the resulting transfer functions are compared. Table 6.3 and 6.4 gives the numerical values of the TVC parameters used for this comparison.

The feedback gains k_V and k_A (i.e. velocity and acceleration, respectively) are set to zero which is the case for servo-hydraulic control systems (Thoen 2004). Only one notch filter is used, and the numerical values of its parameters are given in Table 6.4.

The comparison of transfer function estimations is shown in Figure 6.8. Agreement between the two transfer functions is excellent. Discrepancies seen in Figure 6.8, mainly in the high frequency range, are due to implementing the continuous time version of TVC in Simulink and in reality discrete time nature of the 469D real-time software.

Closed-loop block diagram of the linear servovalve-actuator-rigid platen-specimen model and TVC as the controller is given in Figure 6.9. The plot also shows the low-pass filter and the Feedback Generator that exist in the real shake table (i.e. real plant). In the real plant, these two components are required due to practical

necessities. Feedback Generator is needed because feedback measurements of displacements and accelerations are done by LVDTs and accelerometers, respectively, and these two types of sensors perform better in different regions of the frequency spectrum (Stoten, 2001). Therefore, it is possible to make better measurements of feedback states and obtain better estimate of unmeasured feedback state (i.e. velocity) by blending displacement and acceleration readings through composite filters. On the other hand low-pass filter is necessary for eliminating the possible control problems due to spurious pressure spikes in pressure transducer measurements. More information about these two components can be found in Chapter 1. There is no need for such components for the linear simulation model presented here, since feedback measurements are done directly (i.e. not through sensors). Therefore low-pass filter and the Feedback Generator are omitted for the rest of the study (i.e. $f = f_{fbk}$, $x = u_{fbk}$, $\dot{x} = \dot{u}_{fbk}$, and $\ddot{x} = \ddot{u}_{fbk}$). The closed loop transfer function from the reference signal to the actuator force is given below

$$H(s) = \frac{k_q G_R(s) G_H(s)}{1 + k_q G_H(s)\left(G_D(s) G_{xf}(s) - G_F(s)\right) + G_H(s) G_{xf}(s)\left[sA + k_q\left(sG_V(s) + s^2 G_A(s)\right)\right]} \tag{6.37}$$

6.3. Effect of TVC Control Gains on the Closed-Loop Transfer Function

In this section, two parametric studies will be presented. The first one is to investigate the effect of feedback and feedforward control gains, and the second one is for to investigate the effect of notch filter parameters on the magnitude-phase response

of the closed-loop transfer function given in (6.37). Input as the reference signal and output as the actuator force is chosen for the parametric study, since the controller-specimen interaction as well as the oil-column resonant peak is more visible in the transfer function between these two signals.

Table 6.5 shows the details of the first parametric study; notch filter parameters and all the other unmentioned TVC gains are set to zero. In order to see the effect of individual TVC gains on the closed system transfer function, gains are changed one at a time while the others are kept zero; except the proportional gain k_P. Results of the first parametric study are given in Figure 6.10 through 7.13. The reference TVC gain setting is assumed to be the case (a2), therefore all the other cases are compared with respect to this one. Equation (6.18) will be used just for the interpretations of some of the results, since it shows clearly the effective topology of the controller TVC.

Figure 6.10, it can be seen that as the value of k_P increases, the magnitude of the system transfer function (i.e. system gain) at low frequency range increases as well, the oil column resonant peak is slightly lowered. The system gain remains unaffected at high frequency range due to changes in k_P. Therefore it can be said the system response can be effectively changed at low-frequency range by the proportional gain k_P.

Figure 6.10 also shows the effect of force feedback gain k_{DP} (i.e. (b1) and (b2)). As the value of k_{DP} increases, the system gain at the vicinity of oil-column frequency (11.3 Hz) decreases. Increase in k_{DP} basically moves the poles

corresponding to the oil-column frequency of the closed-loop system transfer function further toward the left-half of s-plane, therefore the damping of the closed-loop system increases.

Figure 6.11 shows the effect of k_{VF} on the system transfer function. As it can be seen from the figure, as k_{VF} increases the system gain from the natural frequency of the combined mechanical system up to oil-column frequency increases as well. This is due to the fact that the gain k_{VF} is proportional to the derivative of the command signal (i.e. $su(s)$ given in (6.18)). Therefore, if the system gain needs to be adjusted at this frequency range, the velocity feedforward gain should be the main gain candidate to achieve this task.

Figure 6.12 shows the effect of k_{AF} on the system transfer function. Again magnitude response plot shows that this particular gain increases the system gain at high frequency range (i.e. the oil-column frequency and onward). This is due to the fact that the gain k_{AF} is proportional to the second derivative of the command signal (i.e. $s^2u(s)$). Also notice that the k_{AF} exuberates the effect of control-specimen interaction at the combined natural frequency of the specimen and the platen.

Figure 6.13 shows the effect of k_{JF} on the system transfer function. As it is clearly seen from the figure, k_{JF} does not change the system gain at lower frequency range. On the other hand, system gains are highly sensitive to this feedforward gain at medium to high frequency range. Notice that the system gains are particularly

sensitive to this gain at the high-end of the spectrum, since k_{JF} is proportional to the third derivative of the command signal (i.e. $s^3u(s)$).

Table 1.6 shows the details of the second parametric study for to investigate the effect of notch filter parameters on the magnitude and phase response of the system transfer function given in (6.37). All the other gains are set to zero, except the displacement feedback gain k_P, which is set to 1.5. As in the previous parametric study, the effects of notch filter parameters are compared with respect to the reference case (a2).

Figure 6.14 shows the effect of center frequency parameter f_0 on the system transfer function. As it is expected, the notch filter decreases the system gain at the vicinity of the center frequency f_0. The curve labeled as (f1) in Figure 6.14 corresponds to the case where the center frequency of the notch filter is set to 5.0 Hz, therefore the system transfer function shows a sudden magnitude drop at this frequency with respect to the reference case labeled as (a2), whereas the curve labeled as (f2) shows a sudden drop at 11.0 Hz.

Figure 6.15 shows the effect of the notch filter parameter *bw* on the system transfer function. As the width parameter increases (from (g1):2 Hz to (g2): 20 Hz) the system gains drop down over the entire frequency range as well as at the vicinity of the center frequency f_0.

Figure 6.16 shows the effect of notch filter parameter *depth* on the system transfer function. As it is expected, as the *depth* parameter increases (from (f1): -0.2

V/V to (f2): -0.90 V/V), the system gain drops at the vicinity of the center frequency f_0, which is set to 11.0 Hz. Therefore this parameter is particularly useful to filter out fixed (fixed to a particular frequency) mechanical resonances that might exist within the shake system.

LIST OF TABLES

Table 6.1: Numerical values of the parameters used for the open-loop servovalve-actuator-rigid platen model.

A [m^2]	β [MPa]	k_q [m^3/sec/Volts]	V [m^3]	k_c [m^3/MPa]	m_{pl} [kg]
0.3324	819	0.06	0.2493	0.0	144,000

Table 6.2: Numerical values of the parameters of the single degree of freedom specimen model.

m_S [kg]	ξ_S [%]	ω_S [rad/s]
65,000	3%	12.5664

Table 6.3: Numerical values of TVC gains.

k_{PF} [V/V]	k_{VF} [V/V]	k_{AF} [V/V]	k_{JF} [V/V]	k_{P} [V/V]	k_{DP} [V/V]	ω_{DP} [V/V]	k_{M} [V/V]	k_{I} [V/V]
0.00	0.35	0.45	0.0004	1.50	-0.15	0.50	1.00	0.00

Table 6.4: Numerical values of TVC's notch filter.

f_0 [Hz]	*bw* [Hz]	*depth* [V/V]
10.00	5.00	-0.80

Table 6.5: Evolution of the TVC gains for the parametric study.

TVC Gains	**(a1)**	**(a2)**	**(b1)**	**(b2)**	**(c1)**	**(c2)**	**(d1)**	**(d2)**	**(e1)**	**(e2)**
k_P	0.5	1.5	1.5	1.5	1.5	1.5	1.5	1.5	1.5	1.5
k_{DP}	0	0	-0.2	-0.4	0	0	0	0	0	0
k_{VF}	0	0	0	0	0.2	0.6	0	0	0	0
k_{AF}	0	0	0	0	0	0	0.2	0.6	0	0
k_{JF}	0	0	0	0	0	0	0	0	0.02	0.06

Table 6.6: Evolution of the notch filter parameters for the parametric study.

Notch Filter Parameters	**(f1)**	**(f2)**	**(g1)**	**(g2)**	**(h1)**	**(h2)**
f_0	5.0	11.0	11.0	11.0	11.0	11.0
bw	5.0	5.0	2.0	20	5.0	5.0
depth	-0.6	-0.6	-0.6	-0.6	-0.2	-0.9

LIST OF FIGURES

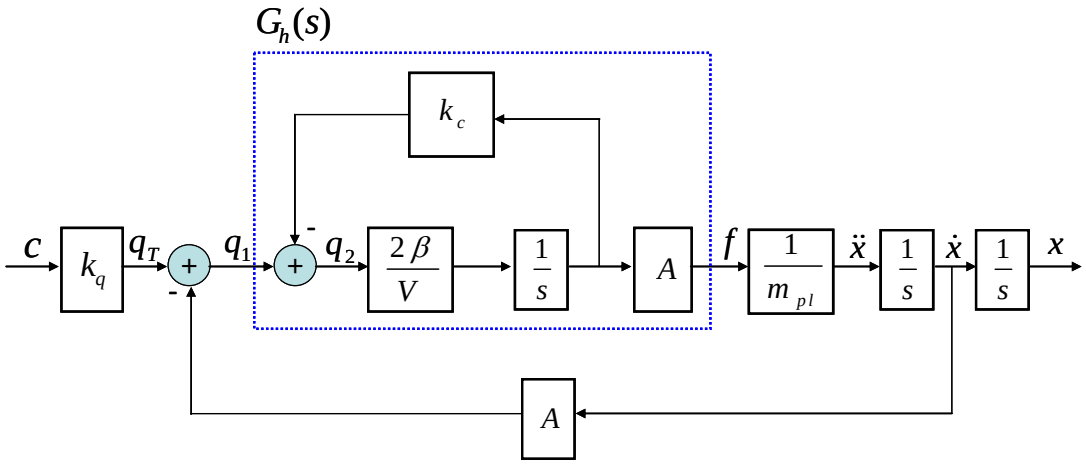

Figure 6.1: Open–Loop servovalve-actuator-rigid platen model.

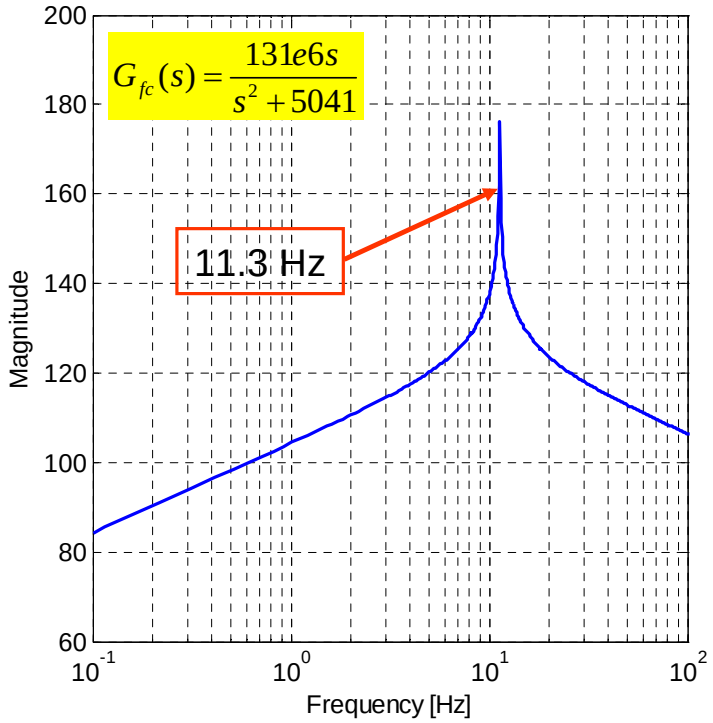

Figure 6.2: Magnitude plot of the open-loop servovalve-actuator-rigid platen model with no servovalve or cross-port actuator leakage.

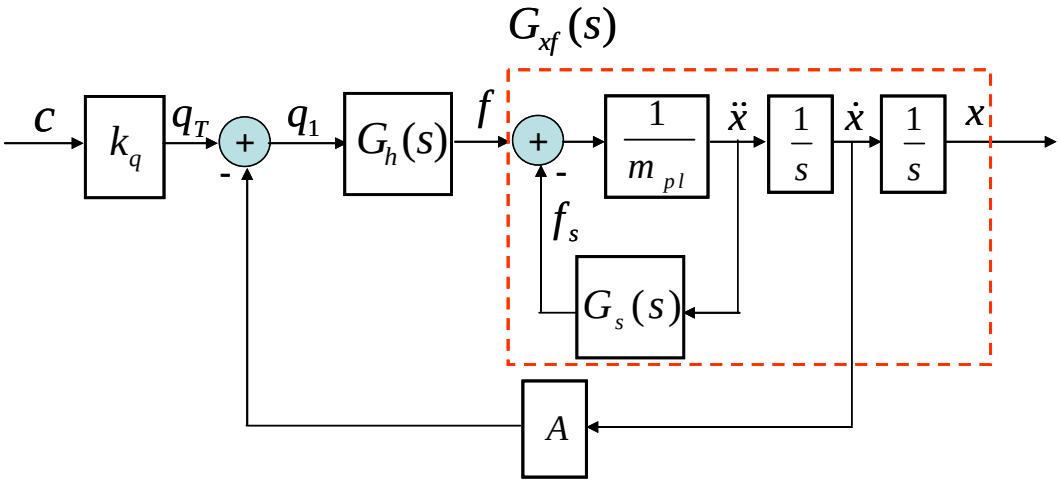

Figure 6.3: Open–Loop servovalve-actuator-rigid platen-specimen model.

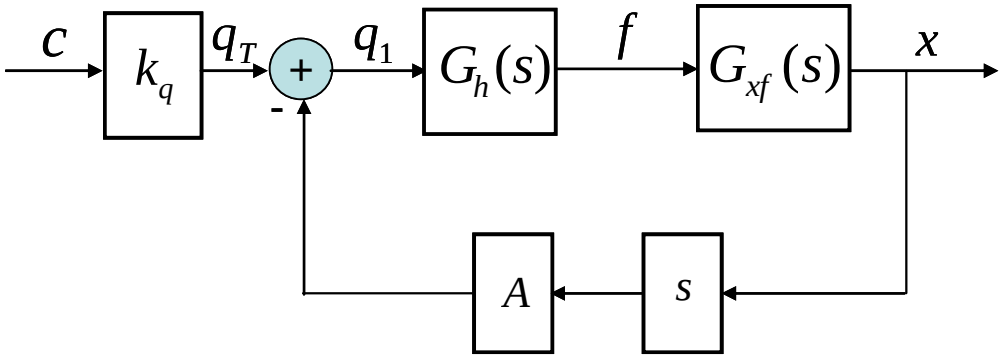

Figure 6.4: Simplified open-loop block diagram of servovalve-actuator-rigid platen-specimen model.

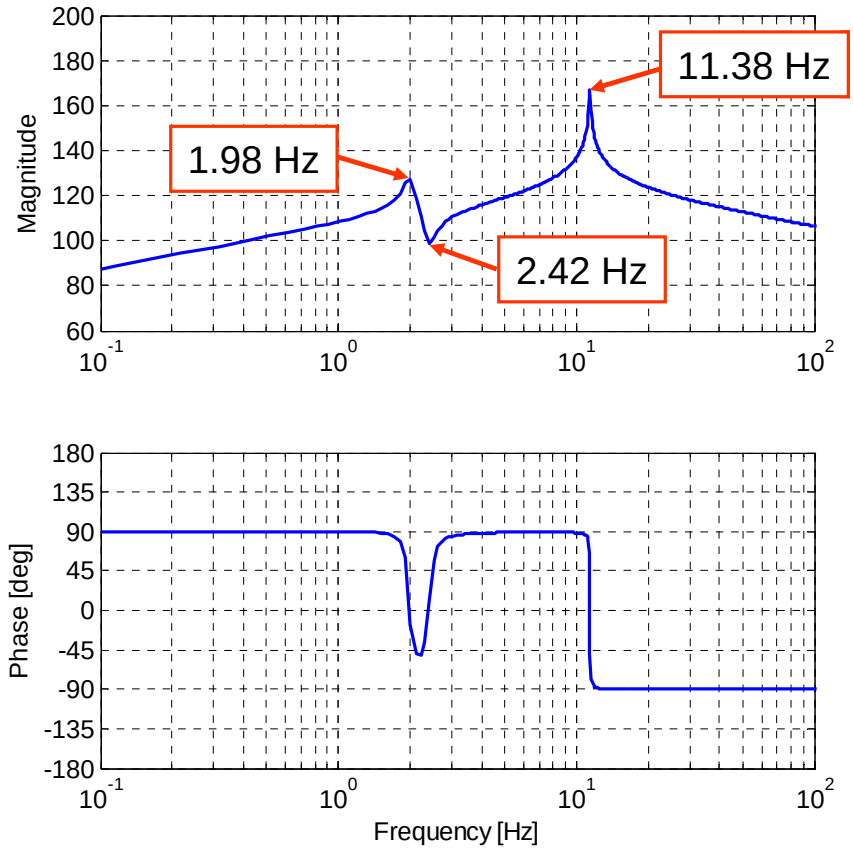

Figure 6.5: Magnitude and phase plot of servovalve-actuator-rigid platen-specimen model.

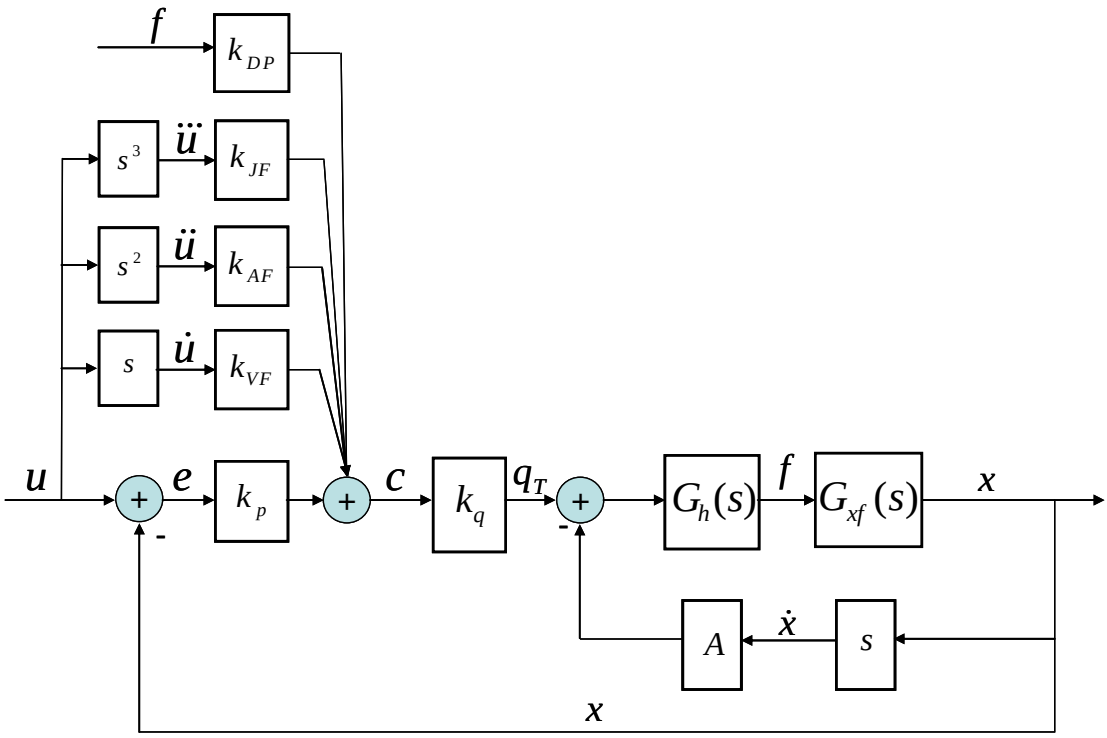

Figure 6.6: Displacement control strategy for servovalve-actuator-rigid platen-specimen model with force feedback, and velocity, acceleration, jerk feedforward gains.

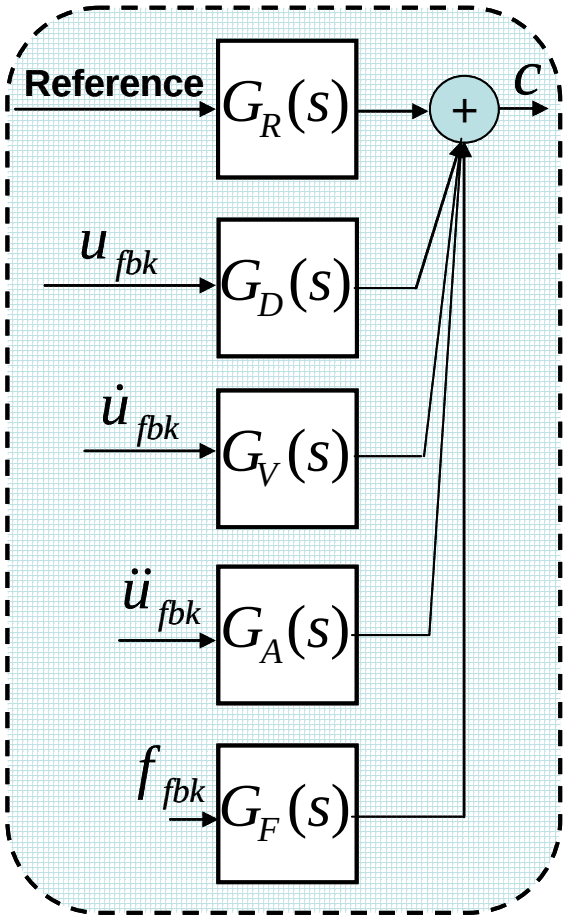

Figure 6.7: Block-diagram of the Three-Variable-Controller.

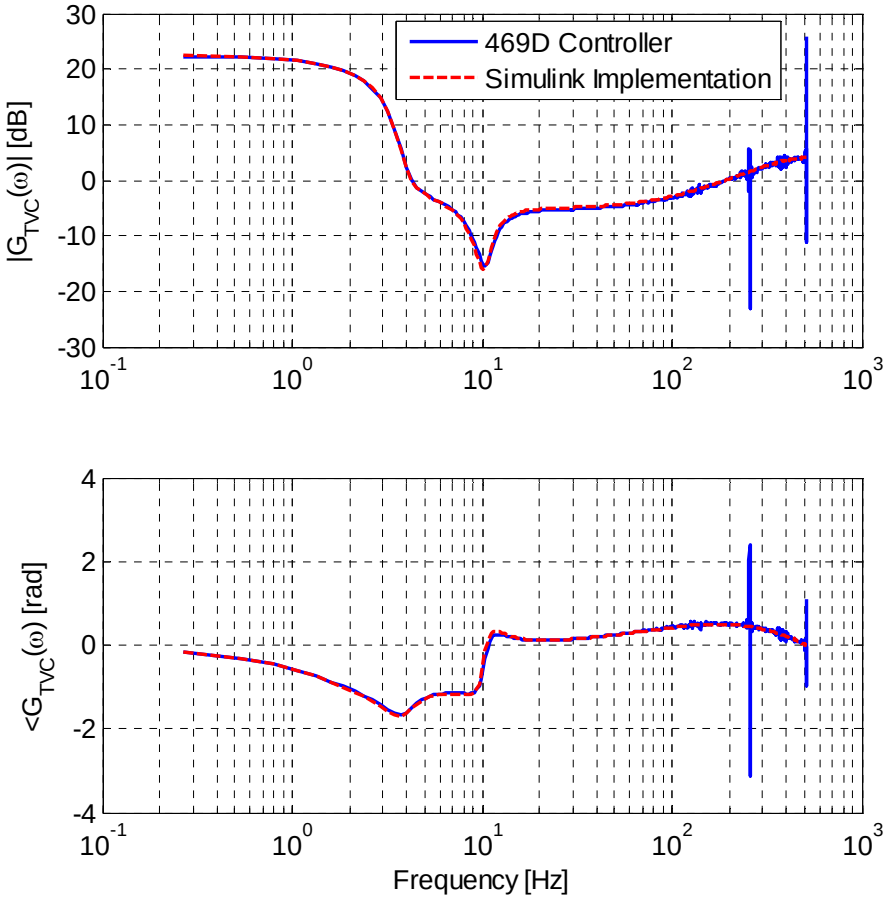

Figure 6.8: Comparison of open-loop transfer function of TVC as implemented in Matlab-Simulink and as obtained from the real-time control software 469D.

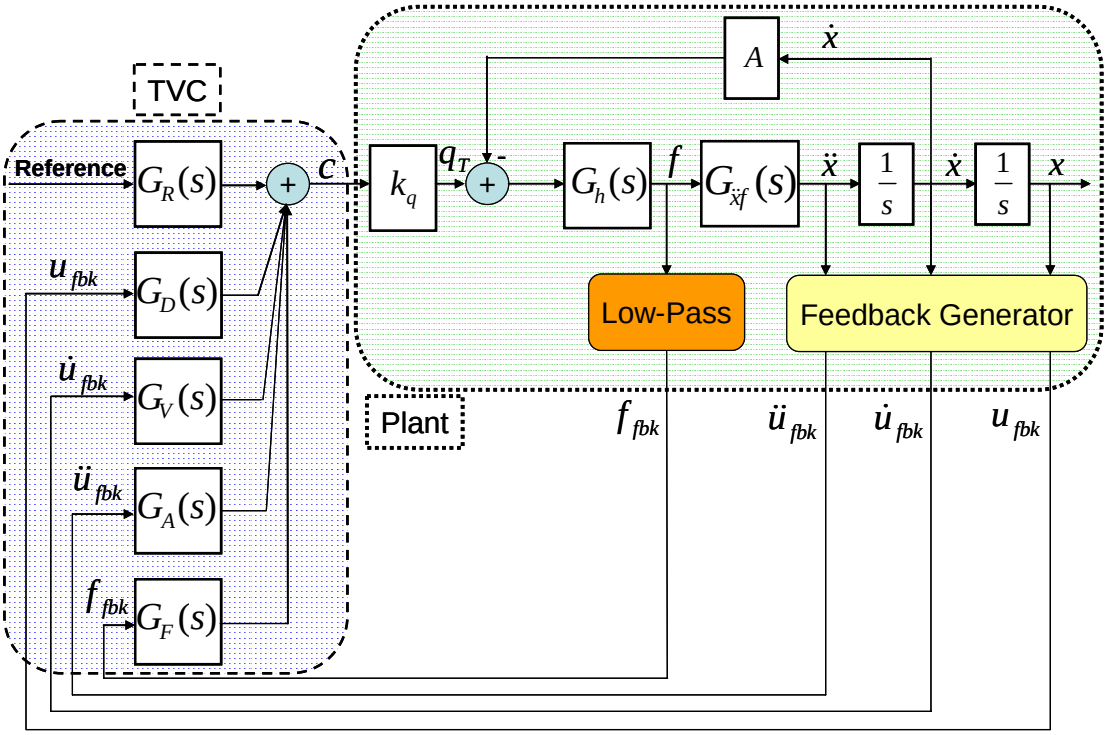

Figure 6.9: Closed-loop block diagram of the linear servovalve-actuator-rigid platen-specimen (i.e. plant) with Three-Variable Controller (TVC).

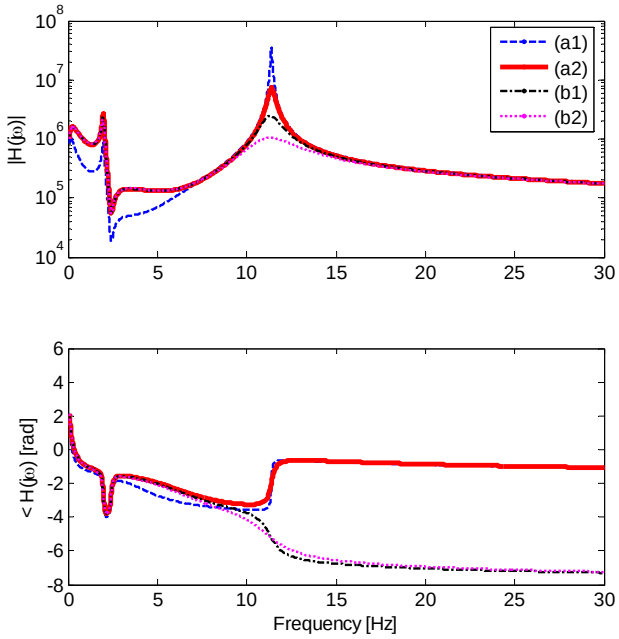

Figure 6.10: (a1), (a2): effect of k_P, and (b1), (b2): effect of k_{DP}.

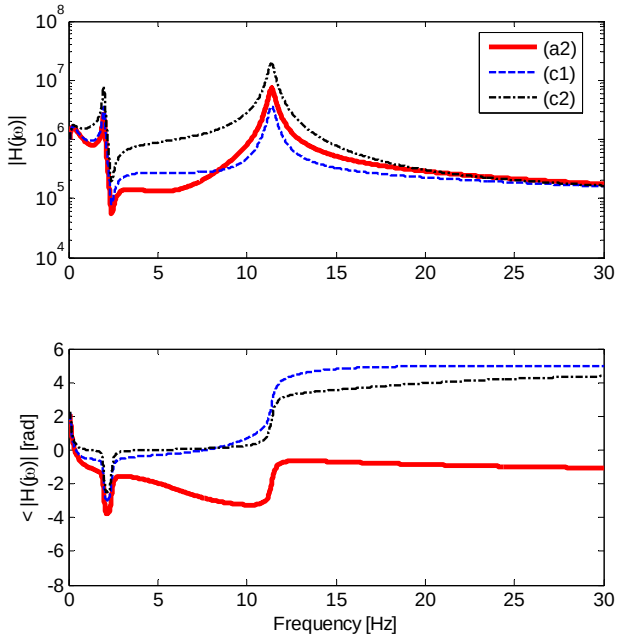

Figure 6.11: (c1), (c2): effect of k_{VF} on the closed-loop transfer function.

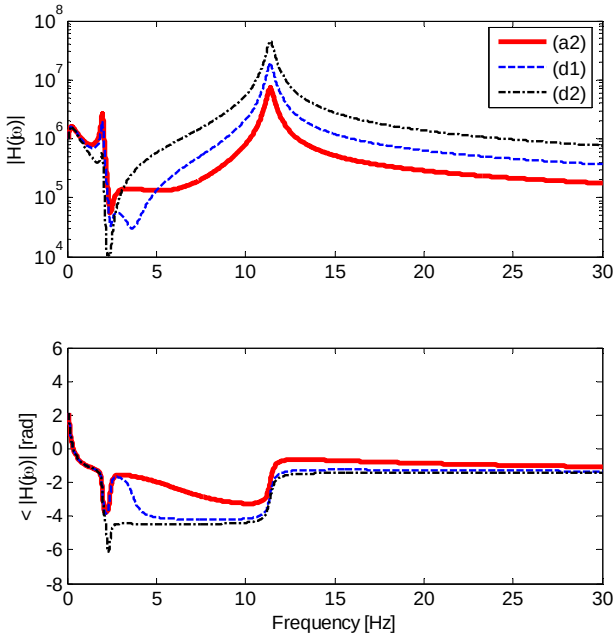

Figure 6.12: (d1), (d2): effect of k_{AF} on the closed-loop transfer function.

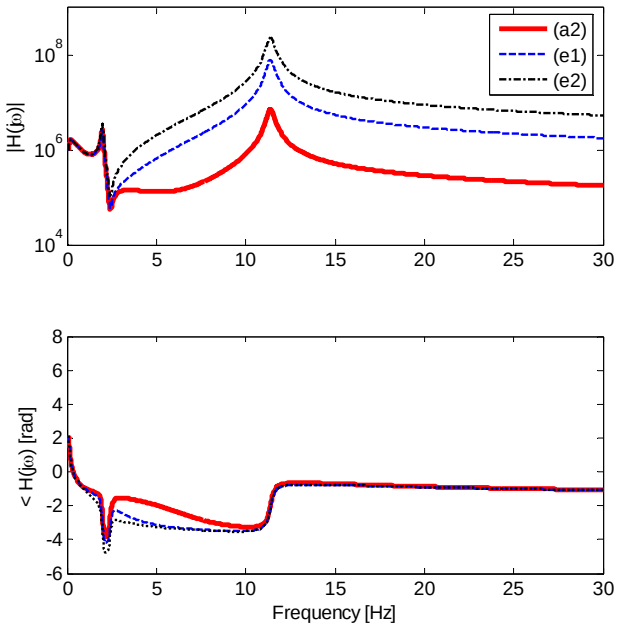

Figure 6.13: (e1), (e2): effect of k_{JF} on the closed-loop transfer function.

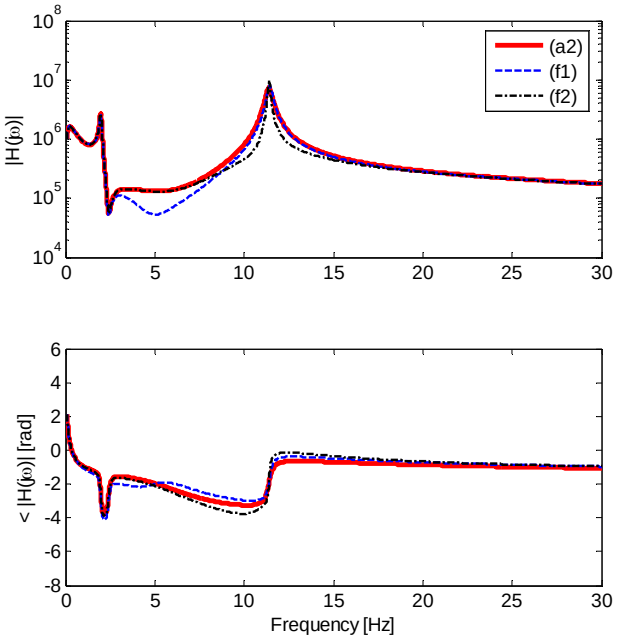

Figure 6.14: (f1), (f2): effect of f_0 on the closed-loop transfer function.

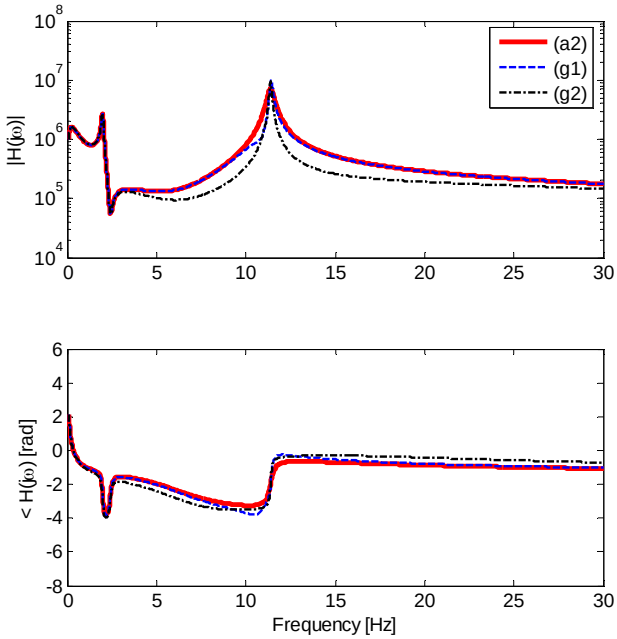

Figure 6.15: (g1), (g2): effect of *bw* on the closed-loop transfer function.

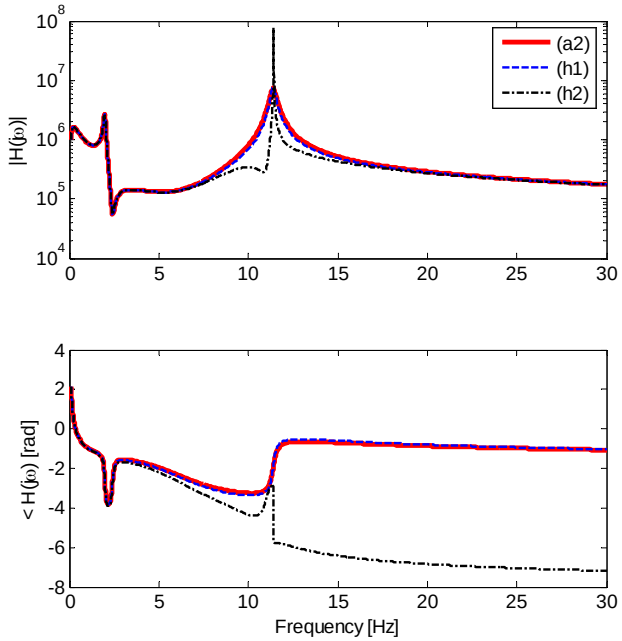

Figure 6.16: (h1), (h2): effect of *depth* on the closed-loop transfer function.

REFERENCES

Dyke, S. J., Spencer, B. J., Quast, P., and Sain, M. K. (1995). "Role of control-structure interaction in protective system design." *J. Eng. Mech., 121(2), 322-338.*

Dimig, J., Shield, C., French, C., Bailey, F., and Clark, A. (1999). "Effective force testing: a method of seismic simulation for structural testing." *J. Struct. Eng.*, 125(9), 1028-1037.

Thoen, B. K., 469D Seismic Digital Control Software. MTS Corporation, 2004.

Stoten, D.P., Gomez, E. (2001). "Adaptive control of shaking tables using minimal control synthesis algorithm." *Phil. Trans. R. Soc. Lond. A*, 359, 1697-1723.

Zhao, J., Shield, C., French, C., Posbergh, T., Nonlinear System Modeling and Velocity Feedback Compensation for Effective Force Testing. *Journal of Engineering Mechanics*, 131(3), 244-253, 2005.

CHAPTER 7

ACCELERATION TRACKING PERFORMANCE OF THE NEES-UCSD SHAKE TABLE

7.1. Introduction

Large servo-hydraulic shake tables such as the NEES-UCSD large high performance outdoor shake table (LHPOST) at the University of California, San Diego, are complex systems designed to subject large structural or geotechnical specimens to extreme seismic environments such as those found in the near source region of major earthquakes. These facilities are used to investigate aspects of structural and geotechnical seismic behavior that cannot be readily extrapolated from testing at smaller scales, or under quasi-static or pseudo-dynamic conditions. The severe environment in which these shake table systems must operate is illustrated by the technical specifications of the LHPOST which include a stroke of ±0.75m, a peak horizontal velocity of 1.8m/s, a peak horizontal acceleration of 4.2g (design value) for bare table conditions and 1.0g (design value) for a rigid payload of 3.92 MN, a horizontal force capacity of 6.8MN, an overturning moment capacity of 50MN-m, a vertical payload capacity of 20MN, a platen area of 7.6mx12.2m, and a platen

effective mass of 144 tons. The frequency bandwidth is 0-25Hz (Ozcelik et al. 2008, Van Den Einde et al. 2004).

The typical shake table system includes a variety of mechanical (platen, yaw/pitch/roll restraining systems, vertical and lateral bearings, reaction block, foundation, and linear/nonlinear specimen), hydraulic (pumps, hydraulic lines, accumulator bank, inline and close-coupled accumulators, servovalves, and actuators), and electronic (controller, various types of transducers, signal conditioning units, data acquisition system) components. The complexity of the system arises from the many linear and nonlinear interactions among various components (Ozcelik et al., 2008; Zhao et al., 2005; Thoen and Laplace, 2004; Williams et al., 2001; Conte and Trombetti, 2000; Kusner et al., 1992; Dyke et al., 1995; Clark, 1983).

The severity of the simulated ground motions, the size of the specimens, and the complexity of the system requires the use of a robust controller to force the table platform to follow (track) a prescribed (command/target) motion. Most existing shake table systems operate in displacement control mode in which a displacement feedback loop is used to control the motion of the table. In this case, the control signal is the weighted error between the table command and feedback (i.e. achieved) displacements. In servo-hydraulic control systems, force stabilization is provided by an additional actuator force feedback loop which helps to damp out the oil column resonance (Conte and Trombetti, 2000; Thoen and Laplace, 2004). Since seismic inertia forces are related to acceleration, the key element in shake table tests is the capability of the system to accurately reproduce prescribed acceleration records which

are usually broad-band signals. For this reason the displacement control strategy is usually augmented with additional feedforward control signals in order to increase the fidelity in acceleration reproduction. Feedforward gains usually act on the velocity and/or acceleration command signals (Crewe, 1998; Thoen, 2004). The controller of the LHPOST falls in the category of displacement control with additional feedforward terms (e.g. velocity, acceleration, and jerk: third derivative of displacement). It also has extra features such as notch filters, adaptive and iterative control techniques to improve the system performance and to compensate for linear and/or nonlinear sources of signal distortion (Thoen, 2004).

The process of "tuning" the shake table to optimize signal reproduction (i.e., maximize fidelity in reproducing the target platen motion) requires adjusting a number of control parameters (e.g., feedback and feedforward gains) and some preconditioning of the command motion. Since there may be a significant interaction between the specimen and the table, the tuning process must be conducted with the specimen mounted on the table. The need to prevent premature damage to the specimen requires that the shake table tuning process be conducted with scaled-down inputs with amplitudes much lower than those of the final or actual test. Even when this precaution is followed, the specimen is subjected to many cycles of motion in the course of tuning, and low-level fatigue damage can result (Thoen and Laplace, 2004). A major concern with tuning at low amplitude is that the fidelity achieved at low amplitudes may not hold for the actual larger amplitude tests. It should be noted that high fidelity is not required in all tests. In many cases, comparisons between the

obtained and calculated structural response can be done a posteriori using the obtained platen motion as input for the calculations of the response. In other cases, such as those involving hybrid testing or geographically distributed testing, accurate tracking is paramount.

The first objective of this Chapter is to investigate the tracking (signal reproduction) capability of the NEES-UCSD shake table system by a series of broad-band and harmonic experiments with different tuning and test amplitudes. A second objective is to obtain quantitative relations between different measures of the signal reproduction error and the amplitude of the excitation used to tune the table. These relations can be used as guidelines for future seismic tests to be performed on the LHPOST, or on shake tables with similar controllers. The third objective is to consider the effectiveness of the existing iterative distortion compensation techniques and their applications. The final objective is to propose some improvements to the current shake table tuning practice.

7.2. 469D Control Software and Tuning of Shake Tables

The Three Variable Controller (TVC) of the LHPOST is an integral part of the MTS control software 469D (Thoen, 2004). TVC can be set to run under displacement, velocity, and acceleration modes. In acceleration and velocity modes (velocity mode is rarely, if ever, used for shake table tests), the controller is still in displacement control, but the control signal to the servovalves is a blend of weighted displacement error and feedforward terms including weighted velocity, acceleration, and jerk command signals.

The process of adjusting multiple control parameters (e.g., feedback and feedforward gains) and of preconditioning the input motion to optimize the response of the shake table system is called “tuning”. Ideally, a tuned shake table system would have a transfer function between the command and feedback signals (total table transfer function) characterized by unit gain and zero phase shift across the entire operating frequency range under loaded (i.e., with a specimen) table conditions. Current shake table tuning practice involves a three step process. The first step involves an iterative process in which the control parameters of the TVC are adjusted iteratively in small increments while the loaded table is in motion. Typically, this step is performed under a band-limited (e.g. 0.25 – 25 Hz) white noise (WN) input acceleration with an RMS amplitude sufficiently high to obtain a good signal to noise ratio in the feedback acceleration and a reliable total transfer function estimation between command and feedback accelerations, but low enough to avoid damage of the specimen. The parameter adjustment process continues until the total table transfer function (estimated recursively) is deemed satisfactory. As an example, Figure 7.1 shows the amplitude of the resulting total table transfer function after TVC tuning of the LHPOST with a white noise acceleration input with 7%g RMS amplitude (~0.25g PGA).

Many shake table tests, but not all, require high fidelity in signal reproduction. In these cases, the tuning process requires two additional steps. The second step corresponds to obtaining an estimate of the inverse model of the plant. This model is provided by the Adaptive Inverse Controller (AIC) program (Thoen 2004) in which

the parameters of the inverse controller are estimated by an adaptive inverse modeling process also known as adaptive controller “training” (Widrow and Stearns 1985). The quality of the estimated inverse model depends on noise level, input amplitude level, and nonlinearities in the system. Inverse model estimation with AIC is also done under white noise acceleration with RMS amplitude matching to that used in the first step to “fine tune” the TVC parameters. An example of the estimated inverse model of the LHPOST plant at the end of AIC training is shown in Figure 7.1.

The third step in the tuning process involves the use of an iterative signal matching technique. The iterative time history matching technique employed in 469D is called Online Iteration. OLI is a control technique that repeatedly modifies the command input to the shake table (e.g. an earthquake acceleration record) until the shake table response gets as close as possible to the desired (e.g. target) motion (Thoen 2004). This online technique generates the next command to the table (e.g. next drive file) by running the table in real-time with the current drive file as the command to the table, calculating the error between the desired and feedback (i.e. achieved), and updating the current drive file by adding a fraction (i.e. determined by the iteration gain) of the response error filtered through the inverse plant model on the current drive. The generation of new drive files are continued until satisfactory match is achieved between the desired and feedback signals. The general trend of response RMS error vs. iteration number during an OLI process is shown in Figure 7.2. Response RMS error is defined as the root mean square of the error between desired and feedback (i.e. achieved) accelerations. Figure 7.2 shows that the response RMS

error initially decreases with iteration number but after a certain iteration is reached the response RMS error starts increasing. The drive file achieving the minimum response RMS error is considered to be the "converged drive file". Theoretically, OLI can correct for any remaining deficiencies in the tuning of TVC, and moreover can compensate for existing linear/nonlinear sources of signal distortions within the system (e.g. friction, servovalves, table/specimen interactions etc). The application of OLI process requires a prior estimate of the inverse plant model provided by the Adaptive Inverse Controller (AIC) program which is wired into the OLI program to serve this purpose (Thoen 2004). The OLI is performed with a scaled-down version of the intended target ground motion to avoid damage of the specimen. After a satisfactory tuning is achieved the converged file is scaled up to the amplitude of the intended ground motion, and the actual tests are performed on the table. The current tuning process is labor intensive and the results are highly dependent on the expertise level of the operator.

7.3. Shake Table Seismic Performance Test Program

An extensive set of 74 shake table tests were performed in December 2007 and January 2008 to assess the fidelity of LHPOST in reproducing a prescribed platen motion. The tests were designed to quantify the effect that the tuning amplitude has on the level of signal fidelity. For this purpose, four different acceleration records corresponding to the 360 degree component of the 1994 Northridge earthquake record at Sylmar station, the north-south component of 1940 Imperial Valley earthquake record at El Centro station, and two harmonic acceleration records with frequencies of

1.0 Hz and 4.1 Hz, were selected. It should be noted that 4.1 Hz corresponds to the corner frequency where the maximum velocity and maximum acceleration that the table can reach intersect. For each of these acceleration records, the table was tuned at scaled down or scaled up versions of the record on the basis of several "Calibration PGA" amplitudes and the corresponding OLI converged files were obtained. Each converged drive file was then scaled up or down according to several "Test PGA" amplitudes and the resulting motions were reproduced on the table. The table fidelity was assessed by comparison of the original acceleration time-history scaled by the Test PGA with the obtained acceleration for a given Calibration PGA. The test matrices for each of the selected acceleration records are listed in Table 7.1. The tests were performed without a specimen on the table and thus represent bare table conditions.

The tuning of the table in preparation for the tests followed the standard three-step procedure. The first two steps are common for all of the tests whereas the third step differs for each acceleration record and Calibration PGA. The first two steps including TVC parameter adjustment and AIC inverse model identification were performed under a band-limited (0.25 – 25 Hz) white noise acceleration input with 7%g RMS amplitude (~0.25g PGA). During the third step of the tuning process corresponding to the OLI preconditioning of the input motion, the tuning results obtained from the previous two steps were kept fixed.

7.4. Test Results

A number of comparisons and measures are used to evaluate the signal reproduction capability of the NEES-UCSD shake table. These include direct comparisons of the acceleration time histories, peak accelerations, and constant ductility response spectra for the achieved and intended platen accelerations. Also to offer a cumulative measure of the error in signal reproduction, the relative root mean square (RMS) error measure defined by

$$\varepsilon_{rel} = \frac{\sqrt{\frac{1}{N}\sum_{n=1}^{N}\left(\ddot{x}_{fbk}[n] - \ddot{x}_{des}[n]\right)^2}}{\sqrt{\frac{1}{N}\sum_{n=1}^{N}\left(\ddot{x}_{des}[n]\right)^2}} \times 100 \qquad (7.1)$$

is used. In Equation (7.1), $\ddot{x}_{des}$ is the desired (command) acceleration, $\ddot{x}_{fbk}$ is the achieved (i.e. feedback) acceleration, and N is the number of data point within the time window chosen to calculate the error. For earthquake records this time window was chosen to be the time interval between the 5% and 95% contribution of the command acceleration to the Arias intensity ($\int \ddot{x}_{des}^2 dt$). The resulting time windows for the Sylmar and El Centro records were found to be between 11.46 to 16.80 seconds and 12.25 to 36.81 seconds, respectively. The achieved acceleration was shifted in time to correct for any delay introduced by the plant. The appropriate shift was found by minimizing the relative RMS error. In the case of harmonic excitation, the time windows for error calculations were chosen so that the maximum amplitude levels for

that particular test was reached which occurs after two cycles of ramping up. The windows covered at least for two cycles.

7.4.1. Comparison of Acceleration Time Histories

To gain an overall view of the signal fidelity performance of the LHPOST, it is convenient to compare the achieved and intended acceleration time-histories. Figure 7.3 shows two time-history reproduction results for the Sylmar record. The top plot corresponds to the case in which the OLI tuning was performed at 0.170g Calibration PGA amplitude while the test was performed at 0.852g Test PGA amplitude by scaling up the converged drive file by the scale factor 0.852/ 0.170. The lower plot shows the case in which both OLI and the test were performed at the same PGA amplitude (i.e. Calibration PGA = Test PGA = 0.852g). In other words, the converged drive file obtained at 0.852g Calibration PGA was reproduced directly on the table without any additional scaling. The time history plots shown in Figure 7.3 indicate that good signal reproduction fidelity (relative RMS error of 10.9%) is obtained when both the OLI tuning and the test are performed at the same high PGA amplitude levels (0.852g in this case). On the other hand, the use of a more realistic lower calibration PGA (0.170g) amplitude and a test with higher test PGA amplitude (0.852g) results in significantly lower fidelity (relative RMS error of 33.3%).

Similar results are shown in Figure 7.3 for the El Centro excitation. The top plot in Figure 7.4 shows the case where OLI was performed at 0.146g Calibration PGA amplitude while the test was performed at 1.098g Test PGA amplitude by scaling up the converged drive file with the scale factor 1.098/ 0.146. The lower plot

in Figure 7.4 shows the case in which both OLI and the test were performed at the same PGA amplitude (i.e. Calibration PGA = Test PGA = 1.098g). Again, the signal reproduction is better (relative RMS error of 16.2% vs. 35.5%) when the tuning is done at the same amplitude as the test.

Figure 7.5 shows the time history plots for a set of tests with intended harmonic accelerations with a frequency of 4.1 Hz and various amplitudes. The results in Figure 7.5(a), 5(b), 5(c) and 5(d), correspond to cases in which the converged OLI drive file was obtained for 0.591g Calibration PGA and then test results at Test PGAs of 0.591, 1.182, 2.364, and 3.547g were obtained by running the appropriately scaled OLI file on the table. It is clear from the plots that although a near perfect replica of the desired signal was achievable in case (a), scaling of the converged drive file to higher test amplitudes resulted in decreasing signal fidelity (i.e. increasing waveform distortion as the scale factor increases). The relative RMS errors for cases (a) through (d) corresponded to 7.9%, 17.0%, 22.8%, and 22.8%, respectively. Fourier amplitude spectra of the achieved signals (i.e. feedback) show that odd harmonics of the test frequency are the predominant causes of this distortion indicating a significant nonlinear system response. Such nonlinear distortions at a specific amplitude can be compensated by OLI, but the converged drive file cannot compensate distortions at a higher amplitude level. Figure 7.5(e) corresponding to the case in which the calibration and test were conducted at the same high amplitude of 2.364g shows that OLI is effective at high amplitudes and to obtain good waveform reproduction, the tuning and the test must be conducted at similar amplitudes.

In the case of harmonic excitation, the MTS 469D control software offers the option of using an Amplitude Harmonic Cancellation (AHC) control method instead of OLI to compensate for nonlinear plant distortions. AHC measures the harmonic distortions for a harmonic input with a specific frequency and amplitude, then in real-time determines and adapts a distortion canceling signal, and applies this additional signal onto the plant input (Thoen, 2004). AHC requires that a forward plant model be estimated. An example of the application of the AHC method instead of OLI is presented in Figure 7.6which shows results obtained from an earlier (2005) set of harmonic tests with a frequency of 3 Hz. For the tests shown in Figure 7.6 the AHC was performed at 0.433g amplitude and the tests were run at 0.433, 0.865, 1.730, 2.595 and 3.464g with properly scaled input files. The time history reproduction results in Figure 7.6 are very similar to the ones obtained from the recent tests with OLI (Figure 7.5) indicating that OLI is not significantly better than AHC compensation. The relative RMS errors for the five cases shown in Figure 7.6 corresponded to 17.5%, 24.7%, 32.6%, 35.0%, and 34.7%, respectively. The forward plant model for the earlier tests was estimated by running WN acceleration with 10%g RMS amplitude on the table.

7.4.2. Error in Peak Accelerations

For tests involving stiff and brittle specimens the reproduction of the peak acceleration is important. The results shown in Figure 7.3 through Figure 7.6 indicate that the obtained peak accelerations can be significantly higher than the intended values. The errors of the achieved peak acceleration with respect to the intended peak

acceleration are shown in Figure 7.7(a) and Figure 7.7(b) for the Sylmar and El Centro excitations, respectively. The errors are shown versus Target PGA for different Calibration PGA. The error can be as large as 30% for high amplitude tests with calibration amplitudes of less than 10%g. Increasing the calibration amplitudes tends to reduce the error in peak accelerations. The results obtained for harmonic excitation shown in Figure 7.8(a) and Figure 7.8(b) exhibit similar trends as those for seismic excitation except that the errors in the harmonic case tend to be larger and, particularly so for the case of 1Hz excitation. Also, the shake table overshoots the target peak accelerations for both harmonic tests.

7.4.3. Reproduction of Response Spectra

The capability of the shake table to reproduce the response spectrum of the prescribed acceleration time-history is another measure of the performance of the table. To investigate the effect of the tuning process on the response spectrum reproduction capability of the table, linear and nonlinear acceleration response spectra from reproduced acceleration time-histories were calculated and compared with the response spectra of the desired acceleration record. For this purpose three different acceleration time-histories have been considered: (i) the original Sylmar acceleration time- history with 0.852g PGA amplitude; (ii) the feedback acceleration time-history of the table when the command input to the table was a modified version of the original Sylmar record which was obtained by OLI at 0.170g Calibration PGA level and scaled up to 0.852g Test PGA level; and (iii) the feedback acceleration time-history of the table when the command to the table was again obtained by OLI but

this time the Calibration PGA level of 0.852g PGA was the same as the Test PGA level.

Linear ($\mu = 1$), and constant ductility (for $\mu = 2$, $\mu = 4$, and $\mu = 8$) pseudo-acceleration response spectra corresponding to these three acceleration time-histories with 3% damping are presented in Figure 7.9. It is clear from the plots that the linear and nonlinear response spectra of the obtained motion match well with the corresponding desired counterparts when the table is tuned at the same amplitude as in the test (0.852g). On the other hand, major discrepancies between the desired and reproduced response spectra can be observed when the table is tuned at lower amplitudes. The largest errors in response spectrum reproduction are observed in the vicinity of the period T = 0.09 sec which corresponds to the oil column resonance of the system. For periods shorter than 0.2 seconds the errors are positive, while for periods longer than 0.5 seconds, the errors are mostly negative.

In the period range from 0.02 to 0.2 seconds, the maximum errors for ductilities of 1, 2, 4 and 8 correspond to 84.7%, 70.1%, 47.6%, and 21.7%, respectively. Thus for short periods, the error tends to decrease as the ductility increases. In the period range from 0.2 to 0.5 seconds, the corresponding maximum errors are 19.2%, 15.0%, 15.1%, and 48.1%, respectively. Finally, in the period range from 0.5 to 1.5 seconds, the maximum errors for ductilities of 1, 2, 4 and 8 correspond to 14.0%, 43.7%, 16.3%, and 17.8%, respectively.

7.4.4. Relative RMS Error

The relative RMS errors obtained for the Sylmar and El Centro excitations are shown in Figure 7.10 as a function of Target PGA for different values of the Calibration PGA. The following general trends are apparent: (i) the relative RMS error for Calibration PGA lower than 0.17g and high Test GPA can reach values in the range from 35 to 55%, (ii) the relative RMS error can be reduced by increasing the Calibration PGA amplitude, (iii) the smallest relative RMS errors of 10.9% and 16.2% are achieved at Calibration PGA amplitudes of 0.852g and 1.098g for the Sylmar and El Centro excitations, respectively, (iv) poor signal reproduction fidelity is obtained when both the Calibration and Test PGA amplitudes are low, (v) the relative RMS error is relatively independent of Target PGA for Target PGA amplitudes larger than 0.75-0.80g, , and (vi) in the unlikely case of high Calibration PGA and low Test PGA, the system performs very poorly in terms of signal reproduction fidelity. The relative RMS errors obtained in an earlier set of tests (September 2005) are shown in Figure 7.11. The tuning approach followed during the earlier tests was the same as the one followed during the recent tests with the exception that TVC parameter adjustments and AIC training for these tests were performed under 10%g RMS amplitude WN acceleration input (~0.35g PGA) instead of the 7%g RMS amplitude WN acceleration input (~0.25g PGA) used in the recent tests. For OLI, the same 1940 Imperial Valley El Centro record was used. Comparison of the results in Figure 7.10 and Figure 7.11 indicate that although the trends observed for Calibration PGA of 0.073g for the two tests are similar, higher fidelity in signal reproduction (i.e. smaller relative RMS

errors) was achieved in the earlier tests. In addition, the earlier relative RMS error curves (Figure 7.11) reach their minima when the Calibration PGA amplitudes coincide with the Test PGA amplitudes. This is a more intuitive result since the table should perform better at the amplitude level in which OLI has been performed. Two possible reasons can be given to explain the differences observed suggest that the quality of the inverse model estimation increases as the RMS amplitude of the white noise input increases and that the table performance is a function of the experience level of the table operator.

Relative RMS error curves for harmonic tests with frequencies of 1.0 Hz and 4.1 Hz are shown in Figure 7.12. The general trends are: (i) For a calibration PGA of 0.144g, the relative RMS error exceeds 20%, (ii) the relative RMS error decreases as the calibration PGA amplitudes increases, (iii) minimum relative RMS errors of the order of 5-8% can be achieved for Calibration PGA larger than 0.577g when the Test and Calibration amplitudes coincide, and (iv) the relative RMS errors for a given Calibration PGA appear to reach an asymptotic value as the Test PGA increases.

7.5. Table Performance Curves

The relative RMS error data shown in Figure 7.10, Figure 7.11 and Figure 7.12 have been used to construct the table performance curves shown in Figure 7.13, Figure 7.14, and Figure 7.15. These curves relate the Calibration PGA and Test PGA for a desired signal fidelity measured by the relative RMS error. These curves are intended to serve as guidance in the selection of appropriate calibration amplitudes for future tests with pre-selected Test PGA and relative RMS error. The curves quantify the

trade-off between higher signal fidelity (smaller relative RMS error) and probability of premature damage to the specimen by use of larger calibration amplitudes.

Figure 7.13 shows a set of RMS error vs. Calibration PGA curves for harmonic tests with 1.0 and 4.1 Hz frequencies and 0.9g and 1.2g Target amplitudes, respectively, Sylmar test with 1.2g, and El Centro test with 0.7g, 1.1g, and 1.5g Target PGA amplitudes. The relative RMS error trends in Figure 7.13 clearly show that achieving higher levels of signal fidelity requires higher Calibration PGA amplitudes. This observation holds for harmonic as well as earthquake records.

Figure 7.14 shows the table performance curves obtained from the earlier set of tests using the same El Centro record but a somewhat stronger white noise excitation (peak acceleration of 0.35g vs. 0.25g for the more recent tests) during the TVC parameter adjustment and for the adaptive inverse modeling (AIC) phase of the OLI. Figure 7.14 can be used to find the OLI calibration amplitude required for a desired level of signal fidelity. For example, these curves suggest that 0.36g Calibration PGA amplitude is necessary in order to have 30% relative RMS error. Results given in Figure 7.14 show the same trends as seen in Figure 7.13: higher fidelity in signal reproduction requires a higher calibration level which in turn brings the problem of higher risk of premature damage to the specimen during table tuning.

The table performance curves for harmonic excitation with frequencies of 1.0 Hz and 4.1 Hz are shown in Figure 7.15. As an example of the use of these curves, assume that a harmonic record with a frequency of 4.1 Hz and peak amplitude of 3.0g needs to be reproduced on the table. If the users of the shake table decide that a

relative RMS error of 20% is satisfactory for their test, then the data in Figure 7.15(b) indicates that the OLI has to be performed at a Calibration PGA of 0.76g to obtain the required level of signal fidelity.

7.6. Conclusions

The results obtained from broadband and harmonic tests performed on the NEES-UCSD Large High Performance Outdoor Shake Table suggest the following conclusions:

(1) High fidelity in reproduction of the platen acceleration (10-20% relative RMS error) is achievable for both broadband and narrowband excitations only if OLI is performed at sufficiently high Calibration amplitudes. Large relative RMS errors should be expected when the Calibration PGA amplitudes are considerably smaller than the actual Test PGA amplitudes. At reasonable Calibration PGA levels (i.e. amplitudes not posing too much risk to specimen during tuning), the relative RMS error ranges between 30-40% for the Sylmar record, and between 30-60% for the El Centro record.

(2) For Calibration PGA amplitudes of the order of 7-8%g and tests at higher amplitudes the obtained platen peak acceleration can be 30% higher than the intended peak acceleration for seismic excitation and substantially higher for harmonic excitations.

(3) Linear and constant ductility response spectra can be accurately reproduced if the Calibration PGA amplitude is sufficiently high (e.g. calibration at 0.852g PGA). At low Calibration PGA but high Test PGA cases (e.g. calibration at 0.170g PGA and

testing at 0.852g PGA for Sylmar record) the ability of the table to reproduce linear and constant ductility response spectra deteriorates and large errors can be obtained particularly for periods shorter than 0.2 seconds.

(4) While it is possible to obtain an almost a perfect replica of a harmonic waveform for a given Calibration PGA amplitude by using OLI when the converged drive file corresponding to this Calibration PGA amplitude is scaled up to another amplitude level, the signal fidelity deteriorates very quickly and large RMS errors and waveform distortions are obtained. The same observation holds for AHC compensation technique. Shake tables are nonlinear systems and therefore a signal fidelity level achieved for a specific amplitude by a certain tuning cannot be maintained at a different amplitude.

(5) Sets of Table Performance Curves have been obtained. These performance curves give the shake table user a quantitative guide to decide on the level of Calibration PGA amplitude that should be used to obtain a desired level of signal fidelity for a given Test PGA amplitude. The curves help to resolve the crucial problem of balancing the increased risk of premature damage to specimens by increasing the calibration amplitudes with the need for adequate signal fidelity.

(6) The RMS amplitude level of the white noise input used for TVC parameter adjustment is also important for obtaining better signal reproduction performance as revealed by comparisons with the earlier El Centro tests. Minimum RMS amplitudes of 0.07-0.10 g appear to be necessary.

(7) Shake table tuning practice with current state-of-the-art control tools is highly dependent on the skills of the operator.

(8) Finally, the difficulties encountered with tuning at low amplitudes and testing at much higher amplitudes indicate the need for an accurate virtual tuning of the table based on a detailed mathematical model of the complete system and, eventually, for a more advanced controller.

LIST OF TABLES

Table 7.1: Calibration and Target PGA test matrices for Sylmar, El Centro and harmonic records.

Sylmar Record					
Calibration PGA [g]	**Test PGA (or Target PGA) [g]**				
0.085	***0.085***	0.170	0.511	0.852	1.193
0.170	0.085	***0.170***	0.511	0.852	1.193
0.511	0.085	0.170	***0.511***	0.852	1.193
0.852	0.085	0.170	0.511	***0.852***	1.193
El Centro Record					
Calibration PGA [g]	**Test PGA (or Target PGA) [g]**				
0.073	***0.073***	0.146	0.366	0.732	1.098	1.464
0.146	0.073	***0.146***	0.366	0.732	1.098	1.464
0.366	0.073	0.146	***0.366***	0.732	1.098	1.464
0.732	0.073	0.146	0.366	***0.732***	1.098	1.464
1.098	0.073	0.146	0.366	0.732	***1.098***	1.464
4.1 Hz Harmonic Tests					
Calibration PGA [g]	**Test PGA (or Target PGA) [g]**				
0.59	**0.59**	1.18	2.36	3.55	3.81
1.18	N/A	**1.18**	2.36	3.55	3.81
2.36	N/A	N/A	**2.36**	3.55	3.81
1.0 Hz Harmonic Tests					
Calibration PGA [g]	**Test PGA (or Target PGA) [g]**				
0.14	**0.14**	0.29	0.58	0.87	0.93
0.29	N/A	**0.29**	0.58	0.87	0.93
0.58	N/A	N/A	**0.58**	0.87	0.93

LIST OF FIGURES

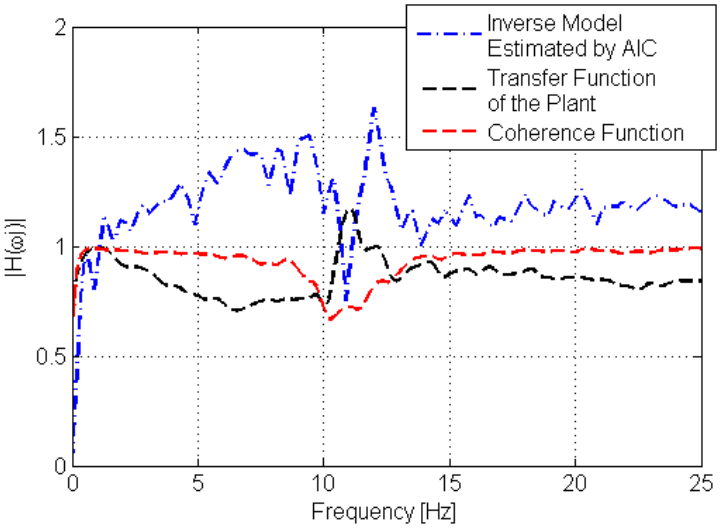

Figure 7.1: Magnitude response plots of the total transfer function of the plant after TVC tuning and the estimated inverse plant model.

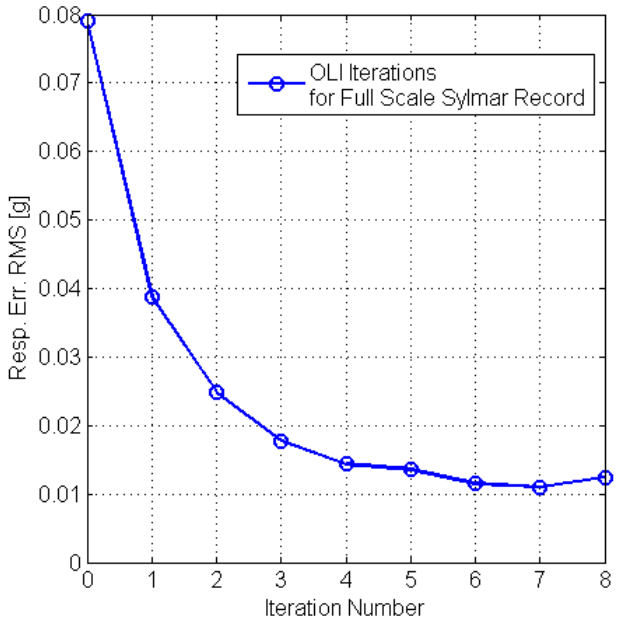

Figure 7.2: Response RMS error vs. OLI iteration number for Sylmar Record at 0.852g Calibration PGA amplitude (for this OLI case the converged drive file is reached at the 7^{th} iteration).

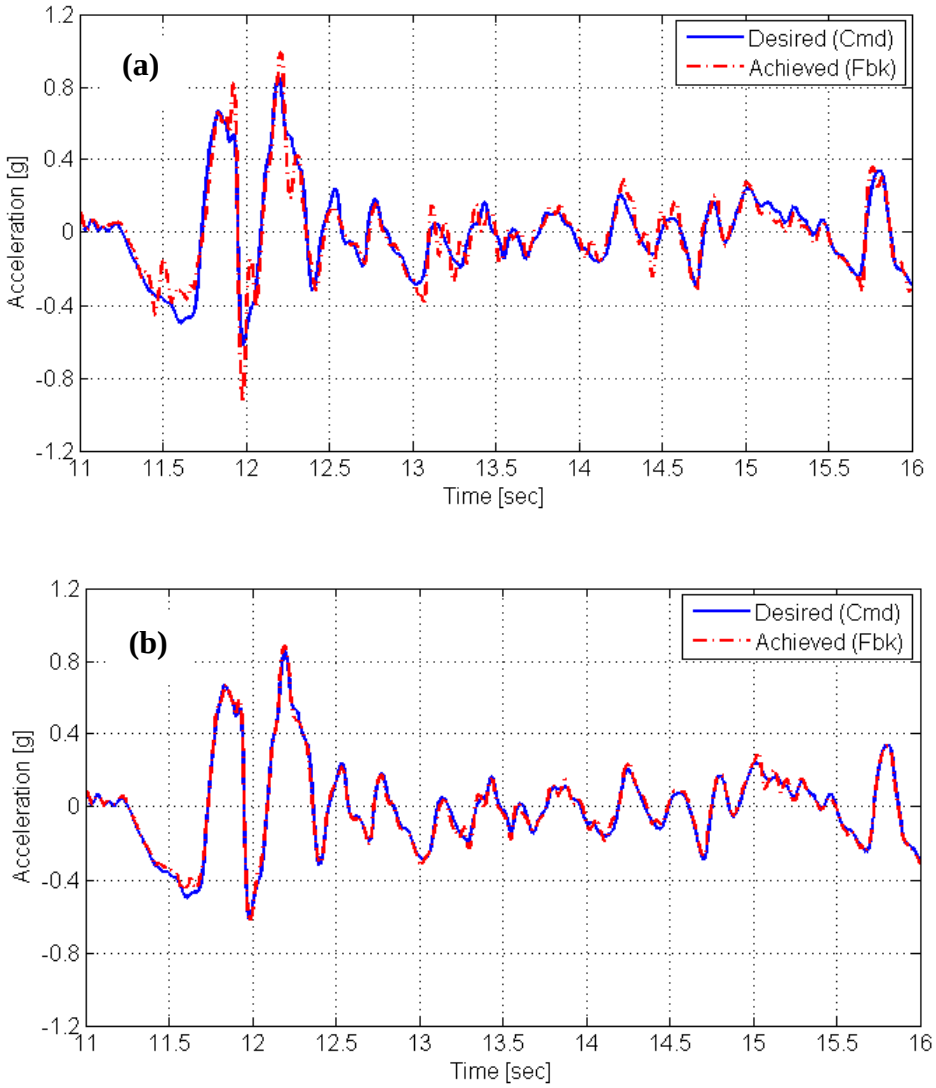

Figure 7.3: Sylmar Tests: (a) OLI performed at 0.170g Calibration PGA amplitude and the test performed at 0.852g Test PGA amplitude (relative RMS Error is 33.3%); (b) OLI performed at 0.852g Calibration PGA amplitude and the test performed at 0.852g Test PGA amplitude (relative RMS Error is 10.9%).

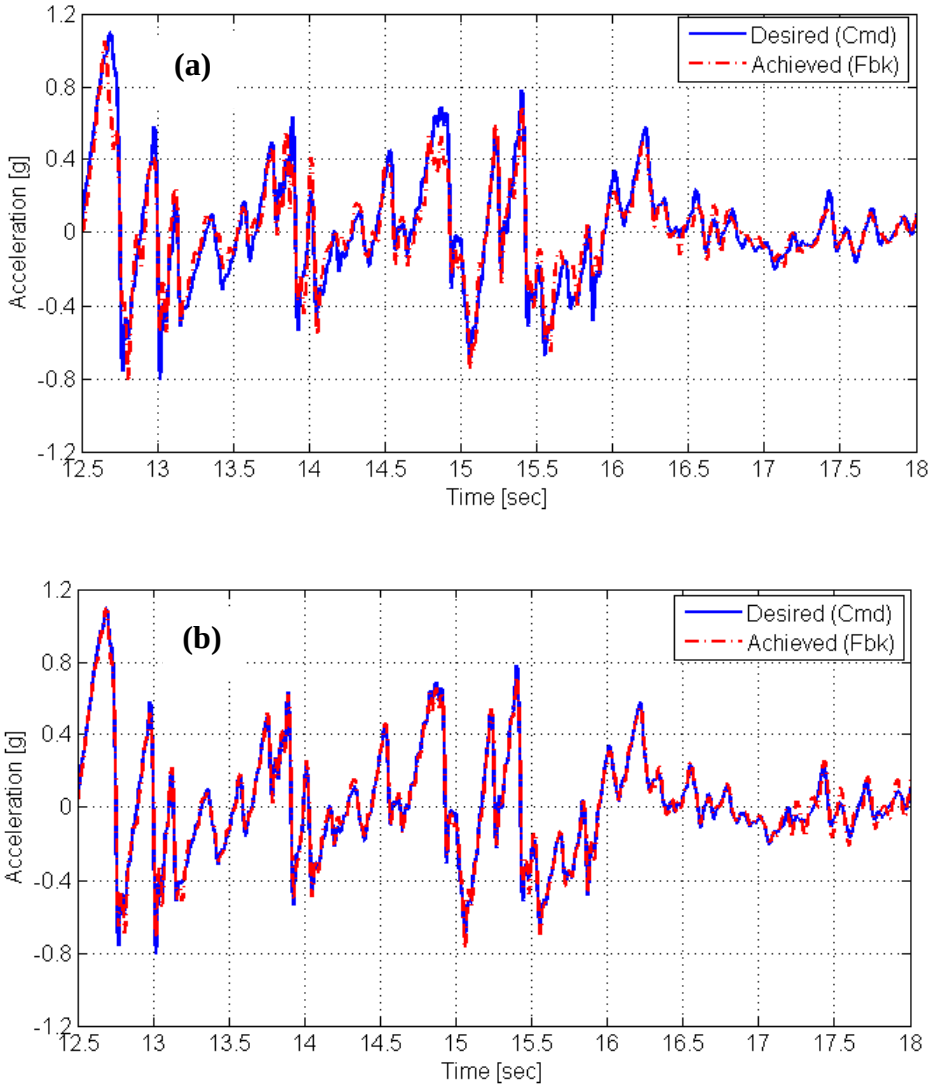

Figure 7.4: El Centro Tests: (a) OLI performed at 0.146g Calibration PGA amplitude and the test performed at 1.098g Test PGA amplitude (relative RMS Error is 35.5%); (b) OLI performed at 1.098g Calibration PGA amplitude and the test performed at 1.098g Test PGA amplitude (relative RMS Error is 16.2%).

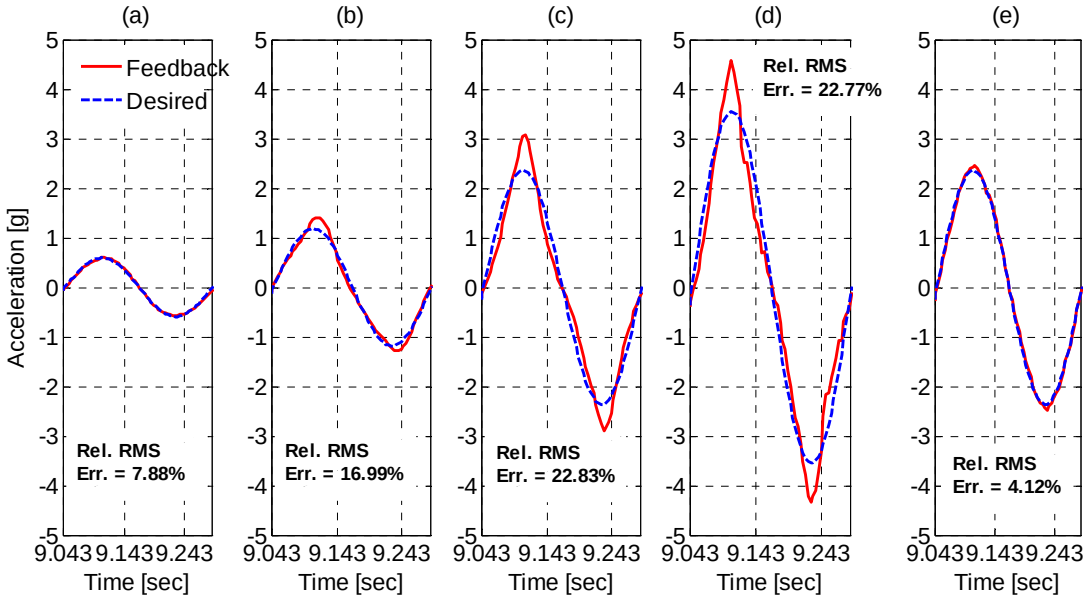

Figure 7.5: 4.1 Hz harmonic tests with corresponding relative RMS errors: (a) OLI and the test are performed at 0.591g PGA amplitude; and OLI is performed at 0.591g Calibration PGA amplitude and the tests are performed at (b) 1.182g, (c) 2.364g, (d) 3.547g Test PGA amplitudes and (e) Calibration PGA is same as Test PGA of 2.364g.

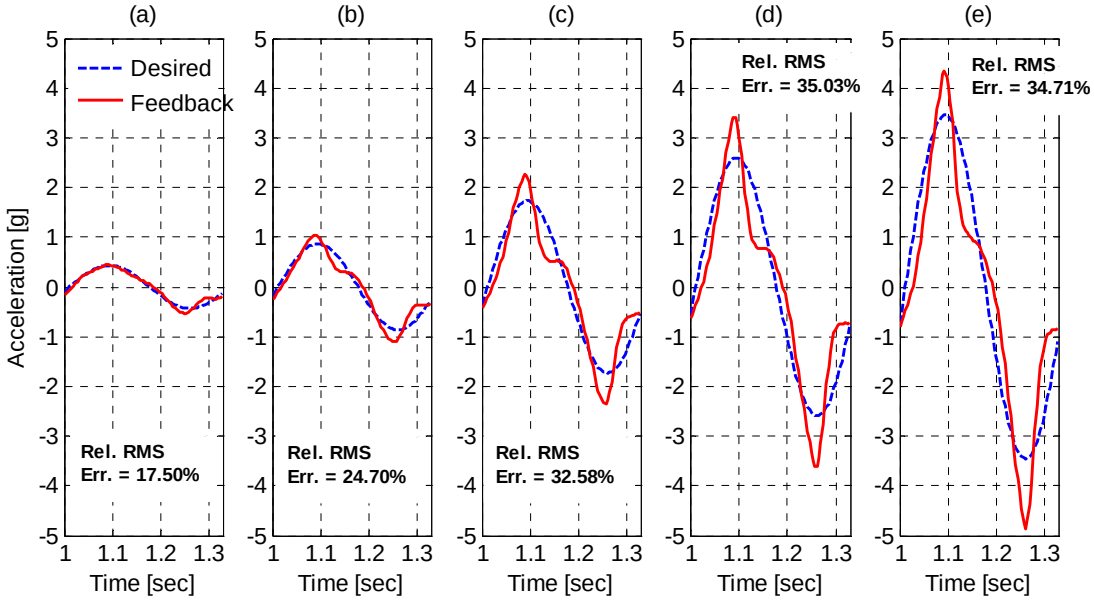

Figure 7.6: 3.0 Hz harmonic tests with corresponding relative RMS errors: (a) AHC and the test are performed at 0.433g PGA amplitude; and AHC is performed at 0.433g Calibration PGA amplitude and the tests are performed at (b) 0.865g, (c) 1.730g, (d) 2.595g, and (e) 3.460g Test PGA amplitudes.

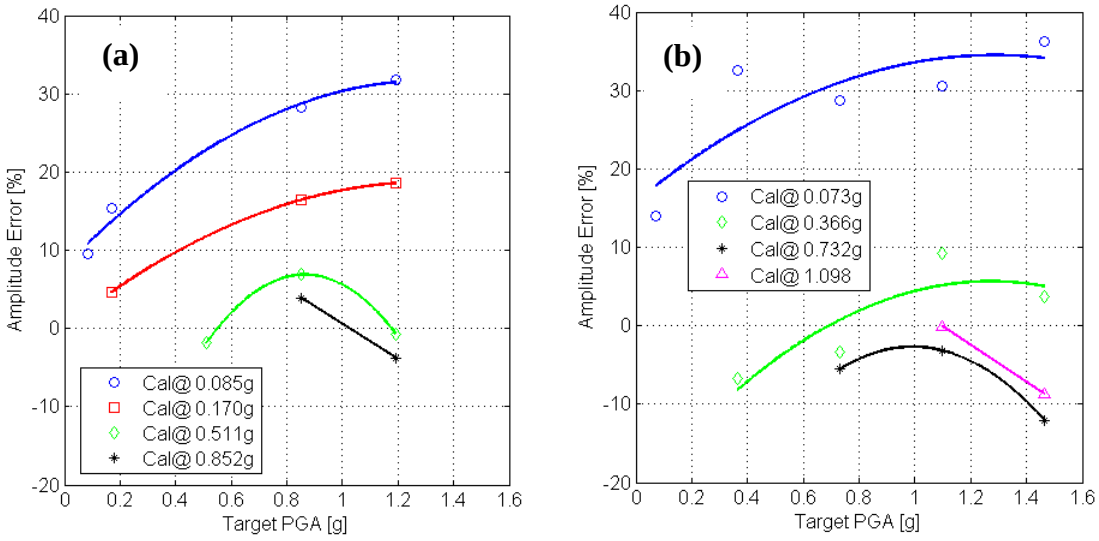

Figure 7.7: Error between the maximum achieved and maximum desired PGA amplitudes, (a) Sylmar and (b) El Centro records.

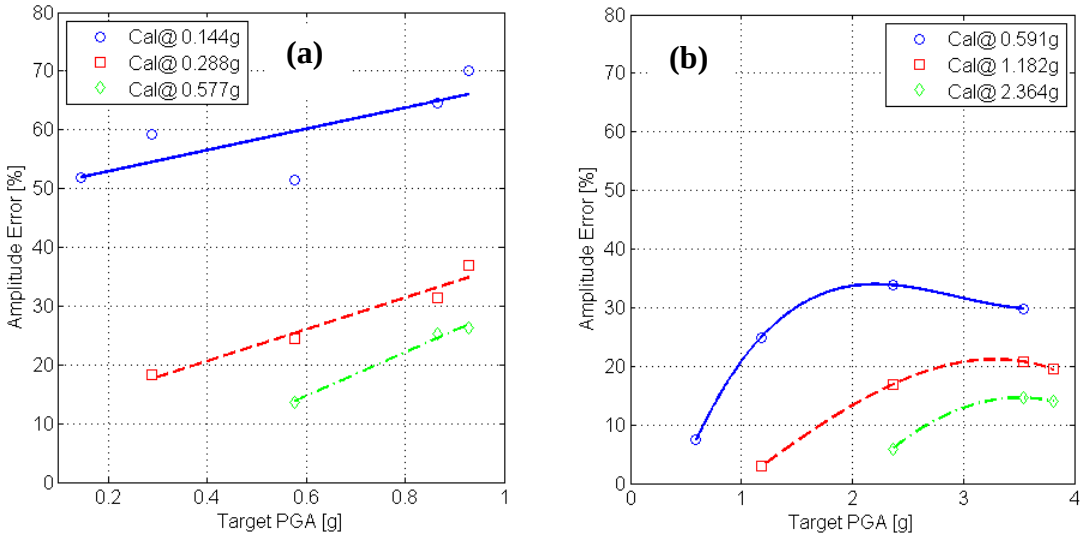

Figure 7.8: Amplitude error vs. Target (or Test) PGA for (a) 1.0 Hz and (b) 4.1 Hz harmonic acceleration records, respectively.

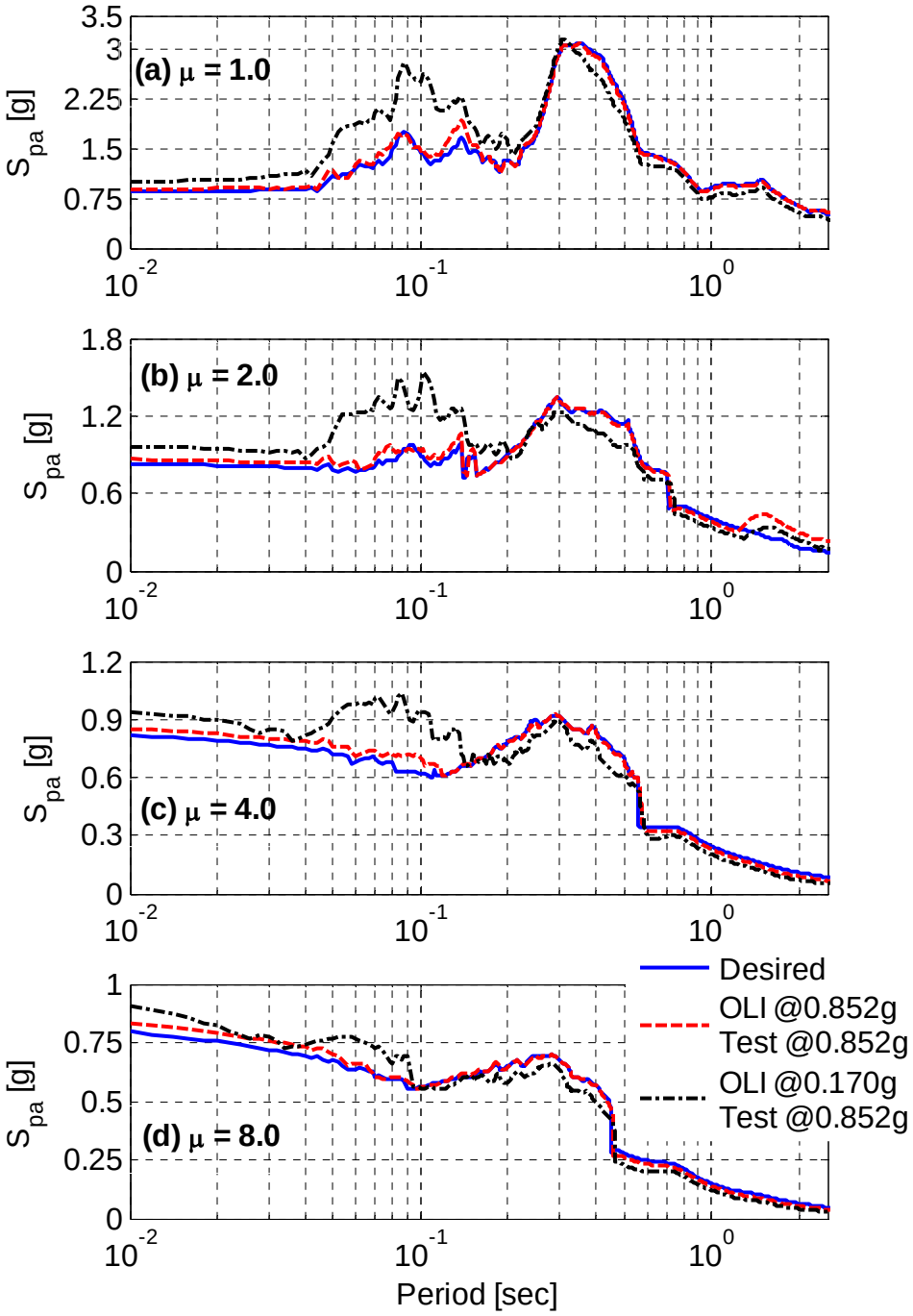

Figure 7.9: Desired and reproduced constant ductility response spectrums for four different ductility levels for Sylmar record.

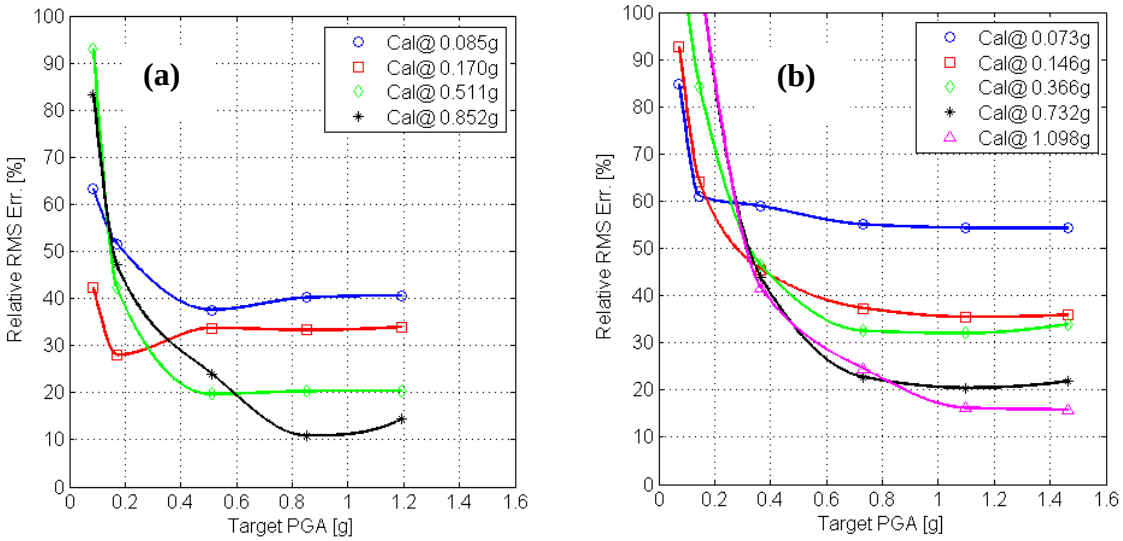

Figure 7.10: Relative RMS error vs. Target (or Test) PGA curves for (a) Sylmar, and (b) El Centro earthquake records. AIC training has been done under 7%g RMS amplitude WN acceleration.

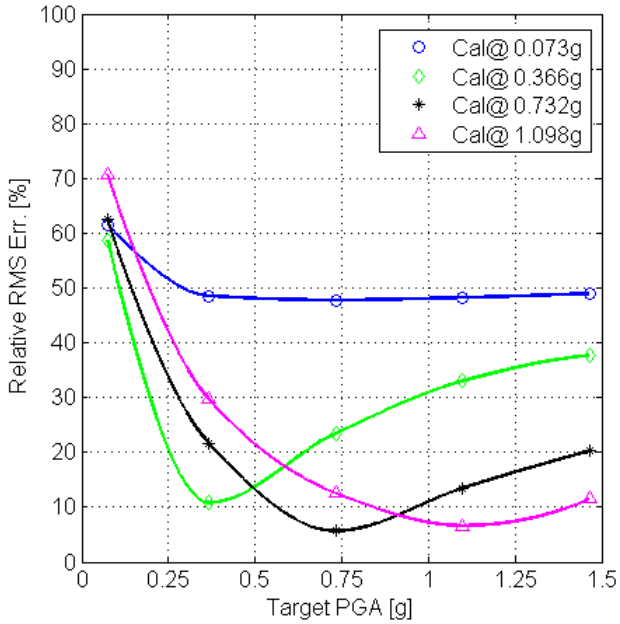

Figure 7.11: Relative RMS error vs. Target (or Test) PGA curves for El Centro record from an earlier set of tests. AIC training has been done under %10g RMS amplitude WN acceleration.

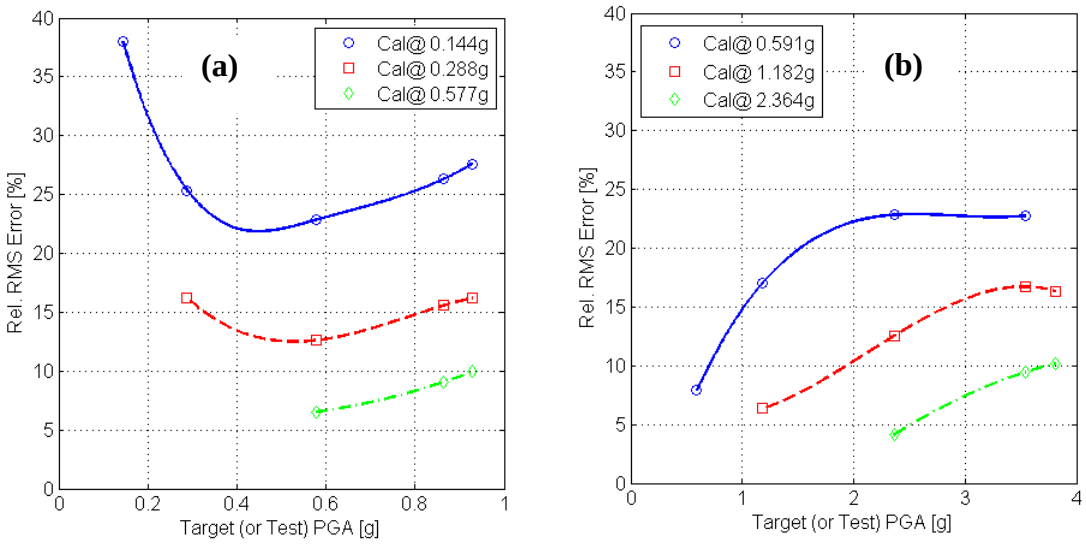

Figure 7.12: Relative RMS error vs. Target (or test) PGA curves for (a) 1.0 Hz, and (b) 4.1 Hz harmonic acceleration tests.

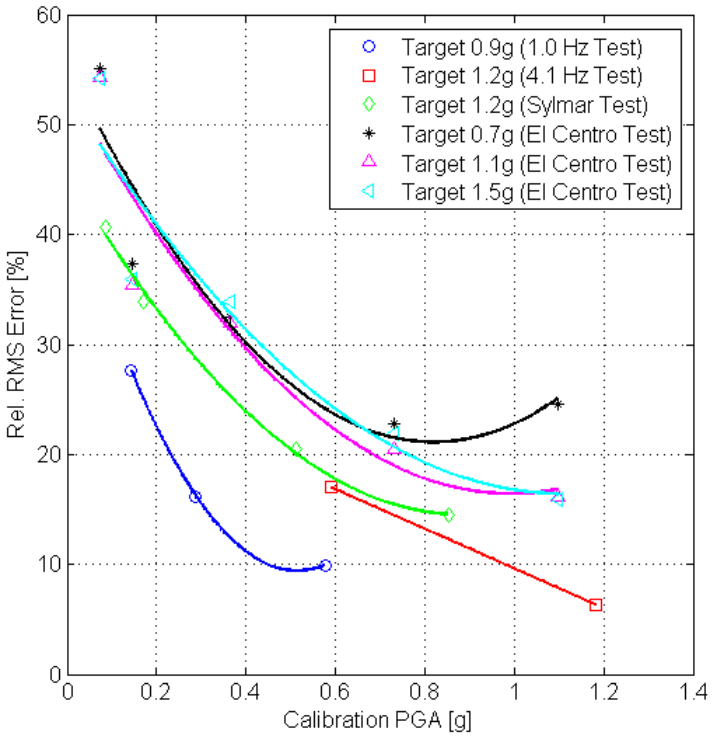

Figure 7.13: RMS Error vs. Calibration PGA curves using harmonic and broadband tests for Target PGA amplitudes between 0.9g and 1.5g.

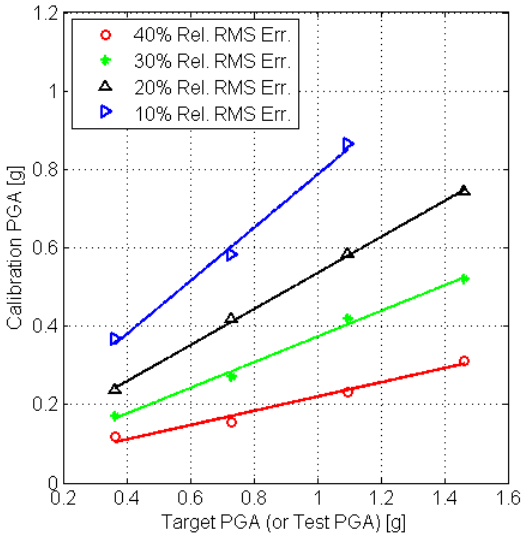

Figure 7.14: Table performance curves obtained from the earlier set of tests for El Centro earthquake record (the inverse plant model is estimated while running 10%g RMS amplitude WN acceleration on the table).

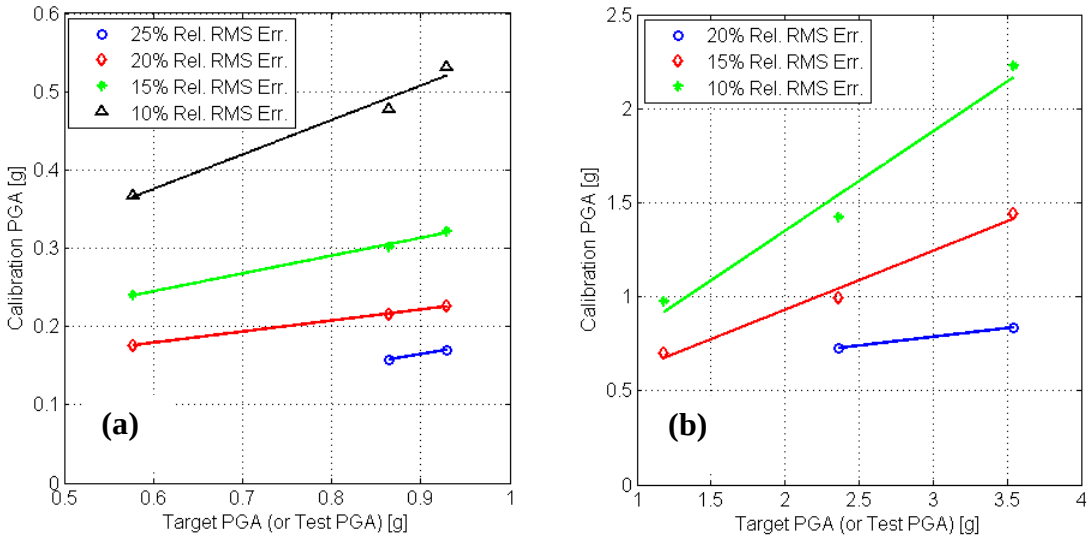

Figure 7.15: Table performance curves for (a) 1.0 Hz and (b) 4.1 Hz harmonic records (the inverse plant model was estimated while running 7%g RMS amplitude WN acceleration on the table)

REFERENCES

Clark, A. (1983). “Sinusoidal and random motion analysis of mass loaded actuators and valves.” *Proc. 39th Annual Meeting On National Conference On Fluid Power*.

Conte, J. P., and Trombetti, T. L. (2000). “ Linear dynamic modeling of a Uniaxial servo-hydraulic shaking table system.” *Earthquake Eng. Struct. Dyn.*, 29(9), 1375-1404.

Crewe, A. J. (1998). “The characterization and optimization of earthquake shaking table performance.” Ph.D. Thesis, University of Bristol.

Dyke, S. J., Spencer, B. J., Quast, P., and Sain, M. K. (1995). “Role of control-structure interaction in protective system design.” *J. Eng. Mech.*, 121(2), 322-338.

Kusner, D. A., Rood, J. D., and Burton, G. W. (1992). “Signal reproduction fidelity of servohydraulic testing equipment.” *Proc. 10th World Conf. On Earthquake Engineering*.

Ozcelik, O., Luco, E. J., Conte, J. P., Trombetti, T. L., and Restrepo, J. I. (2008). “Experimental characterization, modeling and identification of the UCSD-NEES shake table mechanical system.” *Earthquake Eng. Struct. Dyn.*, 37:243-264.

Thoen, B. K. (2004). 469D seismic digital control software, MTS Corporation.

Thoen, B. K., and Laplace, P. N. (2004). “Offline tuning of shaking table.” *Proc. 13th World Conf. On Earthquake Engineering*, Vancouver, B. C., Canada, Aug. 1-6, Paper No. 960.

Van Den Einde, L., et al. (2004). “Development of the George E. Brown Jr. network for earthquake engineering simulation (NEES) large high performance outdoor shake table at the Univ. of California, San Diego.” *Proc. 13th World Conf. On Earthquake Engineering*, Vancouver, B. C., Canada, Aug. 1-6, Paper No. 3,281.

Widrow, B., Stearns, S. D. (1985). Adaptive Signal Processing, Prentice-Hall: New Jersey.

Williams, D. M., Williams, M. S., and Blakeborough, A. (2001). “Numerical modeling of a servohydraulic testing system for structures.” *J. Eng. Mech.*, 127(8), 816-827.

Zhao, J., Shield, C., French, C., and Posbergh, T. (2005). “Nonlinear System Modeling and Velocity Feedback Compensation for Effective Force Testing.” *J. Eng. Mech.*, 131(3), 244-253.

CHAPTER 8

A TOOL DEVELOPED TO INVESTIGATE SHAKE TABLE – SPECIMEN INTERACTION

8.1. Introduction

In this section a simulation tool which would combine simulation capabilities of Matlab-Simulink® and OpenSees (Open System for Earthquake Engineering Simulation) will be developed, tested, and used in order to investigate shake table linear/nonlinear specimen interaction problem. This section will give the details of integrating OpenSees and Simulink.

Simulink provides an excellent platform to model entire shake table systems with linear simple structural systems with few degrees of freedom mounted on the platen. Since shake tables, in general, are used to test specimens going under large inertial forces, tested specimens are almost always forced to go into their nonlinear regimes. Therefore, in order to investigate shake table / nonlinear specimen interaction problem, simulation capabilities of Simulink has to be extended. In this chapter, the details of integrating finite element software OpenSees with Simulink will be given.

OpenSees and Simulink are both large software frameworks. Directly linking and compiling them together would require huge amount of effort if not totally

impossible. One way to achieve this complicated task is to call OpenSees from Simulink at every time step, let OpenSees perform a one-step analysis and send the necessary results back to Simulink, save (e.g., export) the current states of the structural model in a file (e.g., database), turn itself off, and run itself again when Simulink needs it, retrieve the current states from the file (i.e., import the states from the database), and perform the next time step analysis. This importing-exporting process would continue until the end of the entire simulation. As it can be anticipated, "linking" OpenSees and Simulink this way would not be efficient due to the necessity of saving and retrieving the current states of a realistic large structural model at every time step from a file. The efficient communication between OpenSees and Simulink is a crucial problem for the entire simulation tool (i.e., Simulink and OpenSees) to solve large problems.

An efficient but yet still simple way to achieve this integration is to make Simulink the simulation coordinator by enabling it to call the FEA software whenever it is necessary while the FEA software and the structural model are still in the memory, in other words by letting OpenSees to be persistent in the memory so that the communication between Simulink and OpenSees becomes efficient (or easily accessible).

8.2. Integration OpenSees into Matlab-Simulink by Client-Server Technique

In the Client-Server (CS) technique, the finite element analysis (FEA) software OpenSees is set as a server and Simulink as a client. Setting OpenSees as a server enables OpenSees and the structural model to be persistent in the memory, and

therefore the client (Simulink) can connect to the server and request from server to execute OpenSees analysis commands and retrieves the necessary structural responses in order to incorporate their effect into the simulation. Note that the model of the table and the model of the structure mounted on the table are in interaction, in other words their responses affect each other because they are in close loop. The communication between the client and the server is through the standard Internet protocol TCP/IP.

OpenSees is an open source FEA software used for modeling structural systems and simulating their earthquake responses (McKenna et al., 2000). OpenSees' interface is based on a command-driven scripting language Tool Command Language (TCL) which enables OpenSees users to create more-versatile model and input files (Welch, 2000). It is worth to note here that OpenSees does not need to be further programmed to act as the server, it remains intact. Instead a set of TCL functions are used to achieve the communication between the server and the client through a simple TCL network communication channel (or socket) based on TCP network protocol. The client includes few short TCL commands.

The integration using CS technique is schematically described in Figure 8.1. At the server side, OpenSees creates the model and performs gravity load analysis. Then it stops and waits for commands to arrive from the client (Simulink) which will drive further actions. Once OpenSees receives commands and/or inputs (e.g., platen accelerations) for specific action from the client, it performs the requested analysis and sends the required structural responses back to the client. For shake table application, these responses are base shear and overturning moment (e.g., base reaction forces). At

the client side, at every time step an algorithm in Simulink will ask OpenSees to run an analysis with current platen accelerations as inputs. Then it will receive structural responses (e.g., resisting forces) from OpenSees and incorporates these responses to advance the simulation. To perform receiving action from an outside software (in this case OpenSees), a user-defined function within Simulink written in C++ is linked and compiled with a cheap client written also in C++. User-defined functions in Simulink are called the S-functions. The client is a C++ object which persists in the memory therefore holding the connection with the server continuously and handling the communication with it. The framework of server side and client side configurations is given as follows and the details of the whole software are given in the Appendix:

Server Side. In the server side, following TCL scripts are used to create the server

source model.tcl

socket -server accept 7200

vwait forever

where *model.tcl* is the finite element (FE) model of the specimen on the table, the TCL command *source* will run the *model.tcl* to set up the model and to perform analysis under initial loadings (e.g., gravity loads). The second command *socket* creates the server socket with the port number 7200 (it can be any port number) and a callback procedure *accept* to execute commands whenever the client connects to this server socket. The third command *vwait* sets the server to wait for requests from the client. The callback procedure *accept* will accept commands from the client to analyze the

model, get the response from FE analysis, and send necessary responses back to the client through the same socket. Since the model is persistent in the memory, the procedure *accept* can visit any variable in the FE model directly from the memory and can perform certain actions on them and send them back to the client. More information on the TCL commands can be found in the literature (Welch, 2000).

Client Side. The client is a persistent C++ object called *OpenSeesHandler* which is linked to the user-defined S-function *OpenSimConn* in Simulink. To take advantage of the TCL library (e.g., TCP socket), *OpenSimConn* is also linked with this library. In *OpenSeesHandler,* for OpenSees to perform certain actions necessary TCL commands are created and then sent to the server. Detailed discussion about writing C++ S-functions in Simulink can be found in the literature (Dabney and Harman, 2004).

At the very beginning of the entire analysis, *OpenSeesHandler* is created inside the S-function. It will run the following TCL commands in its constructor function in order to set up and hold the connection with the server

set s [socket localhost 7200]

fconfigure $s -buffering none

At every time step Simulink will operate *OpenSeesHandler* client by calling the S-function and will form and run the following commands

puts $s "tryOpenSeesOneStep $currentTime $accel_i"

gets $s

where *puts $s* will pass the command to the server side. "*tryOpenSeesOneStep"* command is a user defined macro written in TCL in the server side to run OpenSees at the time *currentTime* specified or controlled by the client Simulink. Parameters $*accel_i* are the platen accelerations with respect to the generalized coordinate axes defined in Chapter 6. In this version of the software longitudinal, vertical, and rocking accelerations are passed from Simulink to OpenSees. The TCL command "*gets $s"* gets the response from the server and saves them into variable "*s"* which will then be incorporated into simulation by Simulink to advance (continue) the simulation in time.

Advantages of the CS technique in general are as follows: (i) **It is efficient and flexible**. The users are allowed to update the FE model or loading parameters at any time step. The FE model and its state variables in the server side persist in the memory, therefore the server allows all state variables to be visited and updated by the client at any time step. Furthermore with commands like *tryOneStep*, *revertToLastStep*, and *commitOneStep*, FE analysis software is able to work together with implicit (i.e., iterative type) as well as explicit (e.g., Runge-Kutta) solvers developed for solving initial value problems. Data transfer between the client and server can be implemented using TCP/IP or other protocols. The size of the data is usually very small and the speed and quality of this transfer are excellent; (ii) **it is robust**. The connection between the client and server is set up only once at the very beginning of the analysis and will be held at all time. This saves tremendous amount of time (20 times faster than exporting-importing method). Once connection is set up, a reliable communication method between the client and the server is established due

to robustness of the Internet protocol; (iii) **it is easy to program and maintain**. In the client side a cheap component can be easily programmed and integrated into any higher-level software platforms (in this case Simulink). The client C++ object *OpenSeesHandler* is integrated into Simulink with very little programming work; therefore it is easy to change and maintain the integration software.

8.3. 4th Order Runge-Kutta

The shake table simulation model in Simulink is advanced in time suing the 4th order Runge-Kutta (RK) initial value problem solver. Therefore, first a brief description on the 4th order Runge-Kutta will be given and then the details of handling OpenSees for making it compatible with this solver will be presented. For further information on the initial value problem solvers refer to the literature (Bewley, 2008; Lee, 2004).

Consider a vector, first order, possibly nonlinear ordinary differential equation

$$\dot{\mathbf{y}} = \mathbf{f}(t, \mathbf{y}), \quad \mathbf{y}(t_0) = \mathbf{y}_0 \tag{8.1}$$

where $\mathbf{y}(t)$ is the response to be determined for some $t > 0$, $\mathbf{f}(t, \mathbf{y})$ is a function of time t and the solution itself $\mathbf{y}$, and $\mathbf{y}_0$ is the initial conditions. Advancing $\mathbf{y}(t)$ in time can be achieved by evaluating the following integral

$$\mathbf{y}_{n+1} = \mathbf{y}_n + \int_{t_n}^{t_{n+1}} \mathbf{f}(\mathbf{y}, t)dt \tag{8.2}$$

4th order Runge-Kutta method computes (or approximates) the integral given in (8.2) as follows

$$\mathbf{y}_{n+1} = \mathbf{y}_n + \frac{\Delta t}{6}(\mathbf{k}_1 + 2\mathbf{k}_2 + 2\mathbf{k}_3 + \mathbf{k}_4) \tag{8.3}$$

where

$$\begin{aligned} \mathbf{k}_1 &= \mathbf{f}(t_n, \mathbf{y}_n) \\ \mathbf{k}_2 &= \mathbf{f}(t_n + \frac{\Delta t}{2}, \mathbf{y}_n + \frac{\Delta t}{2}\mathbf{k}_1) \\ \mathbf{k}_3 &= \mathbf{f}(t_n + \frac{\Delta t}{2}, \mathbf{y}_n + \frac{\Delta t}{2}\mathbf{k}_2) \\ \mathbf{k}_4 &= \mathbf{f}(t_n + \Delta t, \mathbf{y}_n + \Delta t\mathbf{k}_3) \end{aligned} \tag{8.4}$$

where $\mathbf{k}_1$, $\mathbf{k}_2$, $\mathbf{k}_3$, and $\mathbf{k}_4$ are the slopes at time steps t_n, $t_n + \frac{\Delta t}{2}$, $t_n + \frac{\Delta t}{2}$, and $t_n + \Delta t$, respectively and these time steps are called the minor time steps in Simulink. Notice that $\mathbf{k}_2$, $\mathbf{k}_3$, and $\mathbf{k}_4$ are calculated using the slopes $\mathbf{k}_1$, $\mathbf{k}_2$, and $\mathbf{k}_3$, respectively and in (8.3) the slopes $\mathbf{k}_3$ and $\mathbf{k}_4$ are given more weights for calculating the average slope (second term in (8.3)). Runge-Kutta method is an explicit time marching method meaning that in order to advance the simulation from time n to $n+1$, only $\mathbf{y}_n$ needs to be known. Geometrical interpretation of RK4 method is shown in Figure 8.2.

As mentioned earlier Simulink uses RK4 to simulate the shake table model. OpenSees is integrated into this model using the client-server technique, and therefore must be compatible with the ordinary differential equation solver used in Simulink. OpenSees has to provide the necessary inputs (e.g., reaction forces at the base of the structure) to Simulink during the minor time steps to calculate the average slope and while doing that states of the structural model in OpenSees must not be committed and be committed only at major time steps where the true platen accelerations are

calculated using (8.3). Once the true accelerations are known, Simulink sends OpenSees the true platen accelerations, OpenSees runs the structural model using these accelerations and this time commits the states of the model.

It is clear from the above discussion that Simulink needs to control OpenSees when to commit and when not to commit but just provide the necessary outputs to Simulink in order to be compatible with the RK4 method. To do this, inside Simulink minor and major time steps have to be tracked. This can be done by using Simulink macros *ssIsMinorTimeStep(S)* and *ssIsMajorTimeStep(S)*. Once the simulation time of Simulink is known (i.e., minor and major time steps) OpenSees can be controlled based on this information by using two special commands written and embedded in OpenSees software framework: *tryOneStep* and *commitOneStep*. With *tryOneStep* OpenSees performs intermediate analyses needed for RK4 method (Eq. (8.4)) and returns Simulink the base reaction forces by using the intermediate platen accelerations but does not commit the states of the structural model. With *commitOneStep* OpenSees performs one last analysis using the true platen accelerations and this time commits the states of the structural model. Details of implementing the above outlined procedure are given in Appendix.

8.4. Testing Client-Server Technique using Simple Shake Table Applications

In this section two different approaches will be given for checking Simulink OpenSees integration technique outlined above: (i) by comparing analytically and numerically obtained transfer functions of a simple linear shake table model with a linear SDOF specimen mounted on it; and (ii) by integrating the platen-specimen

assembly excited by “reduced actuator force” using Newmark numerical integration method.

8.4.1. Analytical Vs. Numerical Transfer Function Comparison

Analytical transfer function of the linear shake table with a SDOF specimen controlled by the Three-Variable-Controller has been derived in Chapter 7. For convenience, the closed-loop transfer function of the model shown in Figure 8.3(a) from the reference signal to the actuator force is repeated here

$$H(s)=\frac{k_q G_R(s) G_H(s)}{\left\{\begin{array}{l}1+k_q G_H(s)\left(G_D(s)G_{xf}(s)-G_F(s)\right)+..\\ G_H(s)G_{xf}(s)\left[sA+k_q\left(sG_V(s)+s^2G_A(s)\right)\right]\end{array}\right\}} \tag{8.5}$$

The details and the assumptions made for deriving (8.5) have been given in the related chapter. Bode plot of (8.5) will be compared to the transfer function estimated using the same shake table modeled using Simulink and OpenSees where the link between them is provided by the client-server technique (Figure 8.3(b)).

Table 8.1 and 8.2 show the numerical values of the model parameters used. Control gains used for the simulation are $k_P = 1.50$ V/V , $k_{DP} = -0.15$ V/V , and the rest of the control gains are set to zero (i.e., only nonzero gain is the proportional gain).

The magnitude-phase response plots of the model shown in Figure 8.3(b) was obtained by running the simulation model under a band-limited white noise (WN) input ([0.25 - 20] Hz) with 13%g RMS amplitude. Actuator forces generated by the Simulink-OpenSees model was recorded and a transfer function between the

command input (i.e., command acceleration) and the recorded actuator force has been estimated and it was compared with the analytical transfer function given in (8.5).

Figure 8.4 shows that the analytical and the numerically obtained transfer functions. The match between them is excellent. WN acceleration input was band-limited therefore the system was not excited at very low frequency range (i.e. <0.25 Hz) and therefore discrepancies were observed at very low frequencies. Slight discrepancies may be due to resolution problems in the transfer function estimation procedure (i.e. not due to client-server technique), the peak and notch pair observed around the natural vibration frequency of the SDOF specimen is slightly missed in the numerically obtained transfer function. This estimation was based on the Welch-Bartlett's method which uses input-output data of 120 seconds long white noise excitation with 50% overlapping five Hanning windows, therefore the frequency resolution was 0.042 Hz.

8.4.2. Integration of the Reduced Equation of Motion of the Platen-Specimen Assembly by Newmark Method

In this section, Simulink-OpenSees link will be checked by integrating the equation of motion of the platen-specimen assembly where only the assembly is excited by harmonic reduced actuator force with a certain frequency and amplitude. The reason to use "reduced" actuator force will be clear later. Since the purpose is to check the Simulink and OpenSees link by integrating the same system by another method, only the specimen and platen assembly is considered (i.e., servo-hydraulic model and the controller have taken out of the picture). In order to use Newmark

numerical integration scheme, the nonlinear platen model given in Chapter 6 had to be linearized. Linear version of the platen model is provided also in Chapter 6. Details regarding the derivations of the equation of motion of the platen and with a two story shear-structure (specimen) are given in the related Chapter and repeated below for convenience

$$\mathbf{M}_O\ddot{\mathbf{u}}_O + \mathbf{F}_{spr} + \mathbf{F}_{diss} + \mathbf{F}_{spe} = \mathbf{F}_{act} \tag{8.6}$$

Notice that (8.6) is written for a generalized coordinates at "O" where $\mathbf{M}_O$ is the 3×3 generalized platen mass tensor, $\mathbf{u}_O$ is the 3×1 displacement response of the platen, $\mathbf{F}_{spr}$, $\mathbf{F}_{diss}$, $\mathbf{F}_{spe}$ are the 3×1 elastic spring forces, viscous dissipative forces, and specimen reaction forces acting on the platen, respectively, and $\mathbf{F}_{act}$ is the 3×1 actuator force exciting the assembly. (8.6) can also be written in the following form due to the linear nature of the platen-specimen assembly

$$\mathbf{M}_O\ddot{\mathbf{u}}_O + \mathbf{C}_O\dot{\mathbf{u}}_O + \mathbf{K}_O\mathbf{u}_O + \left(\boldsymbol{\alpha}^T\mathbf{M}_{spe}\boldsymbol{\alpha}\ddot{\mathbf{u}}_O + \boldsymbol{\alpha}^T\mathbf{M}_{spe}\ddot{\bar{\mathbf{u}}}\right) = \mathbf{F}_{act} \tag{8.7}$$

where $\mathbf{C}_O$ and $\mathbf{K}_O$ are the 3×3 viscous damping and stiffness matrices of the platen only, and $\mathbf{M}_{spe}$ is the 2×2 mass matrix of the specimen, $\boldsymbol{\alpha}$ is the 2×3, and $\bar{\mathbf{u}}$ is the 2×1 relative displacement response of the specimen. Notice that the term in the parenthesis is the total force at the base of the specimen and it includes the rigid-body motion of the specimen as well. By rearranging (8.7) the following equation can be found

$$\left(\mathbf{M}_O + \boldsymbol{\alpha}^T\mathbf{M}_{spe}\boldsymbol{\alpha}\right)\ddot{\mathbf{u}}_O + \mathbf{C}_O\dot{\mathbf{u}}_O + \mathbf{K}_O\mathbf{u}_O = \mathbf{F}_{act} - \boldsymbol{\alpha}^T\mathbf{M}_{spe}\ddot{\bar{\mathbf{u}}} = \bar{\mathbf{F}}_{act} \tag{8.8}$$

The right hand side of (8.8) is the modified actuator force that excludes the forces acting on the platen due to the relative motion of the specimen with respect to the platen. This modified actuator force is called the reduced actuator force. Therefore if we know the right hand side of equation (8.8), we can solve for the equation of motion of the platen only by using Newmark-Beta method programmed separately (not using Simulink). Cross-checking will use the results obtained from running the Simulink model of the whole assembly given in Figure 8.5 where the specimen is modeled using OpenSees. In Simulink the solver is set to RK4 which is the default solver for all simulations. Δt is set to 1/1024 seconds (9.765625e-4 sec). Relative displacement of the specimen can be recorded during the simulation. Once the relative displacement of the specimen $\bar{\mathbf{u}}$ are known, modified actuator force $\bar{\mathbf{F}}_{act}$ can be calculated. Using $\bar{\mathbf{F}}_{act}$, equation of motion given in (8.8) can be integrated by Newmark's method. Note that, Newmark's method to solve (8.8) is programmed separately in Matlab. If Simulink implementation of the whole linear platen and specimen assembly is correct then the platen accelerations from both solutions must match.

Figure 8.5 shows the comparison of platen displacements u_{0x} obtained by Simulink and Newmark's method (also, platen accelerations and/or velocities can be compared, they would give the same information). Match between the two solutions is excellent. Therefore it can be concluded that the Simulink implementation of the platen and specimen assembly using OpenSees-Simulink link works correctly.

APPENDIX

TCL Server Source Code

```
# This version is for case of only 3 input accels.
source getTotalResistingForce_currentTime.tcl
proc accept {sock ip port} {
# Configure the socket to be non-blocking.
fconfigure $sock -blocking 1 -buffering none ;#line
# Call the 'respond' proc whenever
# the socket has data for us.
fileevent $sock readable [list respond $sock]
}
proc respond {sock} {
    if {[eof $sock] || [catch {gets $sock data}]} {
            close $sock
            puts "Close $sock" ;# $echo(addr,$sock)"
        } else {
            puts $data
            set command1 [lindex [split $data] 0]
            if {$command1 == "nextRun"} {
            set filename [lindex [split $data] 1]
            wipe
            global fileID
```

```
        if { [catch {eof $fileID}] == 0 } {
                close $fileID
        }
 source model.tcl
 set fileID [open $filename  "w"]
 return
}
elseif {$command1 == "tryOpenSeesOneStep" } {
          eval  $data
          set patternNumber [lindex [split $data] 1];
          global Fx
          global Fz
          global My
          getTotalResistingForce; # into Fx, Fy, Fz, Mx, My, Mz.
          puts $sock  "$patternNumber, $Fx, $Fz, $My"
          flush $sock
         return
        } else {
                eval  $data
                 return
                 }
} }
```

```
source model.tcl

set filename test1

set fileID [open $filename  "w"]

global fileID

global currentTime

global committedTime

set currentTime   0.0

set committedTime   0.0

# Create our server on port 7272

socket -server accept 7272

# Drop Tcl into the event loop

vwait forever
```

The above code uses *GetTotalResistingForce_CurrentTime.tcl* and *model.tcl* files to calculate resisting forces acting on the platen due to the structural model mounted on the platen. The source TCL codes of these procedures are given below.

Source Code of *GetTotalResistingForce_CurrentTime.tcl*

```
proc getTotalResistingForce {} {
 global mass1
 global h
 global Fx
 global Fz
 global My
```

```
 set Fx 0
 set Fz 0
 set My 0
global acc1
global acc2
global acc3
set accel_2_x [nodeAccel 2 1]
set accel_2_x [expr $accel_2_x + $acc1 - $acc3 * $h]
set Fx [expr $mass1*$accel_2_x]
set My [expr -$mass1*$accel_2_x*$h]                    }
proc tryOpenSeesOneStep { numOfTimeStep pCurrentTime currentAcc_1
currentAcc_2 currentAcc_3} {
 global mass1
global h
global acc1
global acc2
global acc3
global committedTime
global currentTime
set currentTime $pCurrentTime
set acc1  $currentAcc_1
set acc2  $currentAcc_2
```

```
set acc3  $currentAcc_3
remove  loadPattern 1
set Hor_Force1 [expr $currentAcc_1 * $mass1- $currentAcc_3 * $h * $mass1]
pattern Plain 1   " Series -time {   $currentTime    } -values {  -1.0 }" {   ;# -1 due to
inertia force
load   2   $Hor_Force1  0  0                    }
set timeStep [expr $currentTime - $committedTime]
tryOneStep  [expr $timeStep]                    }
proc commitOpenSeesOneStep {}  {
# ---- update the history variables --
commitOneStep;
global committedTime
global currentTime
set committedTime $currentTime                }
```

Source Code of *model.tcl*

```
# Linear SDOF Structure
model BasicBuilder -ndm 2 -ndf 3
global mass1
global h
set h 1.0;              # Story Height
set mass1 65.0000e+003;   #
set Area  4.8876e-5;      # 2 Hz
```

```
node  1         0        0       -mass    0.0    0.0     0.0

node  2         $h       0       -mass   $mass1   0.0     0.0

fix  1   1  1 1

fix  2   0  1 1

set E 2.1e11;       # Initial Modulus

uniaxialMaterial Elastic 1 $E

element   truss   1       1      2    $Area    1

 constraints Plain

test NormDispIncr 1.D-12 25  0

algorithm Newton

numberer RCM

system BandGeneral

recorder Node -file Node2L.out -time -node 2 -dof 1 disp

recorder Element -file ele1L.out -time -ele 1 force

set w1 [expr 2.0*3.141593*2.0];

set ksi  0.03

set a0 0.0

set a1 [expr $ksi*2.0/($w1)];

integrator Newmark   0.5     0.25      $a0      0       $a1        0.

analysis Transient
```

Source Code of S-Function OpenSimConn.cpp

```
#include "tcl.h"
```

```
#include "stdlib.h"
#include "stdio.h"
# include "OpenSeesHandler.h"
# include "OpenSeesHandler.cpp"
#define S_FUNCTION_LEVEL 2
#define S_FUNCTION_NAME  OpenSimConn
#include "simstruc.h"
#define  IS_PARAM_DOUBLE(pVal)  (mxIsNumeric(pVal)  &&  !mxIsLogical(pVal)
&&\
!mxIsEmpty(pVal)  &&  !mxIsSparse(pVal)  &&  !mxIsComplex(pVal)  &&
mxIsDouble(pVal))
#define D_macro *mxGetPr(ssGetSFcnParam(S,0))
static void mdlInitializeSizes(SimStruct *S)
{
   // No expected parameters
   ssSetNumSFcnParams(S, 1);
   // Parameter mismatch will be reported by Simulink
   if (ssGetNumSFcnParams(S) != ssGetSFcnParamsCount(S)) {
      return;   }
   // Set the Number of States
   ssSetNumContStates( S, 0);   /* number of continuous states          */
   ssSetNumDiscStates( S, 0);   /* number of discrete states            */
```

```
  // Specify I/O
   if (!ssSetNumInputPorts(S, 1)) return;
   ssSetInputPortWidth(S, 0, 3);
   ssSetInputPortDirectFeedThrough(S, 0, 1);
   ssSetInputPortDirectFeedThrough(S, 1, 1);
   ssSetInputPortDirectFeedThrough(S, 2, 1);
  if (!ssSetNumOutputPorts(S,1)) return;
   ssSetOutputPortWidth(S, 0, 3);
   ssSetNumSampleTimes(S, 1);
   // Reserve place for C++ object
   ssSetNumPWork(S, 1);
   ssSetOptions(S,
              SS_OPTION_WORKS_WITH_CODE_REUSE |
              SS_OPTION_EXCEPTION_FREE_CODE |
              SS_OPTION_USE_TLC_WITH_ACCELERATOR);    }
// Function: mdlInitializeSampleTimes
static void mdlInitializeSampleTimes(SimStruct *S)
{
    ssSetSampleTime(S, 0, INHERITED_SAMPLE_TIME);
   ssSetOffsetTime(S, 0, 0.0);
   ssSetModelReferenceSampleTimeInheritanceRule(S,
DISALLOW_SAMPLE_TIME_INHERITANCE);
```

```
}
// Function: mdlStart
#define MDL_START
static void mdlStart(SimStruct *S)
{
   double dT=D_macro;
   ssGetPWork(S)[0] = (void *) new OpenSeesHandler(7272,3,dT); // store new C++
object in the
        OpenSeesHandler *theHandler = (OpenSeesHandler *) ssGetPWork(S)[0];//
pointers vector
   theHandler->setAccel(0.0,0.0,0.0);
}
// Function: mdlOutputs
static void mdlOutputs(SimStruct *S, int_T tid)
{
   // Get data addresses of I/O
   InputRealPtrsType  u = ssGetInputPortRealSignalPtrs(S,0);
   real_T *y = ssGetOutputPortRealSignal(S,0);
   boolean_T isMajor =  ssIsMajorTimeStep(S);
   boolean_T isMinor =  ssIsMinorTimeStep(S);
   real_T currentTime = ssGetT(S,0);
```

```
  OpenSeesHandler *theHandler = (OpenSeesHandler *) ssGetPWork(S)[0]; // retrieve C++ object from stack
   theHandler->setAccel(*u[0],*u[1],*u[2]);      // prepare accel. data to be sent to opensees
  ofstream * theTemp = new ofstream( "debug.out", ios::app);
   // ====== Mar. 4 2008 ====
   // The sequence is: Major Minor Minor Minor (commit here) Major Minor Minor Minor ...
   //
   if (isMajor){
      *theTemp<<"Major, do commmit. " <<"\n";
      *theTemp<<"current time: " << currentTime <<"\n\n";
      theHandler->commitOpenSeesOneStep();
      theTemp->close();
      return;
   }
   theHandler->setCurrentTime(currentTime);
   theHandler->tryOpenSeesOneStep();                  // run OpenSees once and get response.
   for (int i=0; i<theHandler->getRespSize();i++)
                  y[i] =(theHandler->getResponse())[i];
   if(isMinor){
```

```
        *theTemp<<"Minor, not commit. " <<"\n";
        *theTemp<<"current time: " << currentTime <<"\n";
        *theTemp<<"\n" <<"\n";
    }
    theTemp->close();
}
// Function: mdlTerminate // Abstract:
//   In this function, you should perform any actions that are necessary
//   at the termination of a simulation.  For example, if memory was
//   allocated in mdlStart, this is the place to free it.
static void mdlTerminate(SimStruct *S)
{
    OpenSeesHandler *theHandler = (OpenSeesHandler *) ssGetPWork(S)[0];
    delete theHandler;
}
// Required S-function trailer
#ifdef  MATLAB_MEX_FILE    /* Is this file being compiled as a MEX-file? */
#include "simulink.c"      /* MEX-file interface mechanism */
#else
#include "cg_sfun.h"       /* Code generation registration function */
#endif
```

LIST OF TABLES

Table 8.1: Numerical values of the parameters used for the open-loop servovalve-actuator-rigid platen model.

A [m^2]	β [MPa]	k_q [m^3/s/Volt]	V [m^3]	k_c [m^3/MPa]	m_{pl} [kg]
0.3324	819	0.06	0.2493	0.0	144,000

Table 8.2: Numerical values of the parameters of the single degree of freedom specimen model.

m_S [kg]	ξ_S [%]	ω_S [rad/s]
65,000	3%	12.5664

LIST OF FIGURES

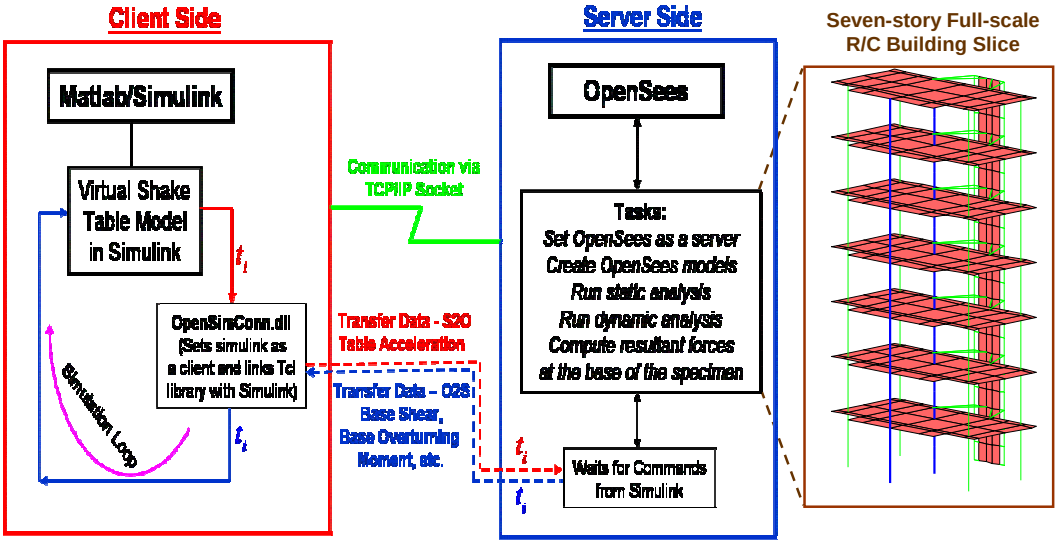

Figure 8.1: Simulink and OpenSees integration via client-server technique using TCP/IP socket.

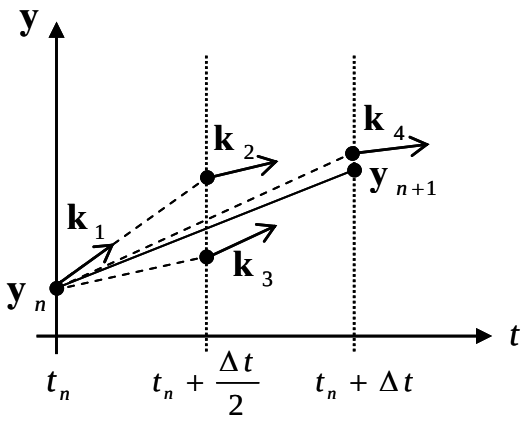

Figure 8.2: Geometric interpretation of 4th order Runge-Kutta method also known as classical Runge-Kutta method. Notice that $\mathbf{k}_1$ is extrapolated from t_n to find $\mathbf{k}_2$, $\mathbf{k}_2$ is extrapolated to from t_n to find $\mathbf{k}_3$, and $\mathbf{k}_3$ is extrapolated to from t_n to find $\mathbf{k}_4$. Average of these four slopes is used to advance (march) $\mathbf{y}_n$ to $\mathbf{y}_{n+1}$.

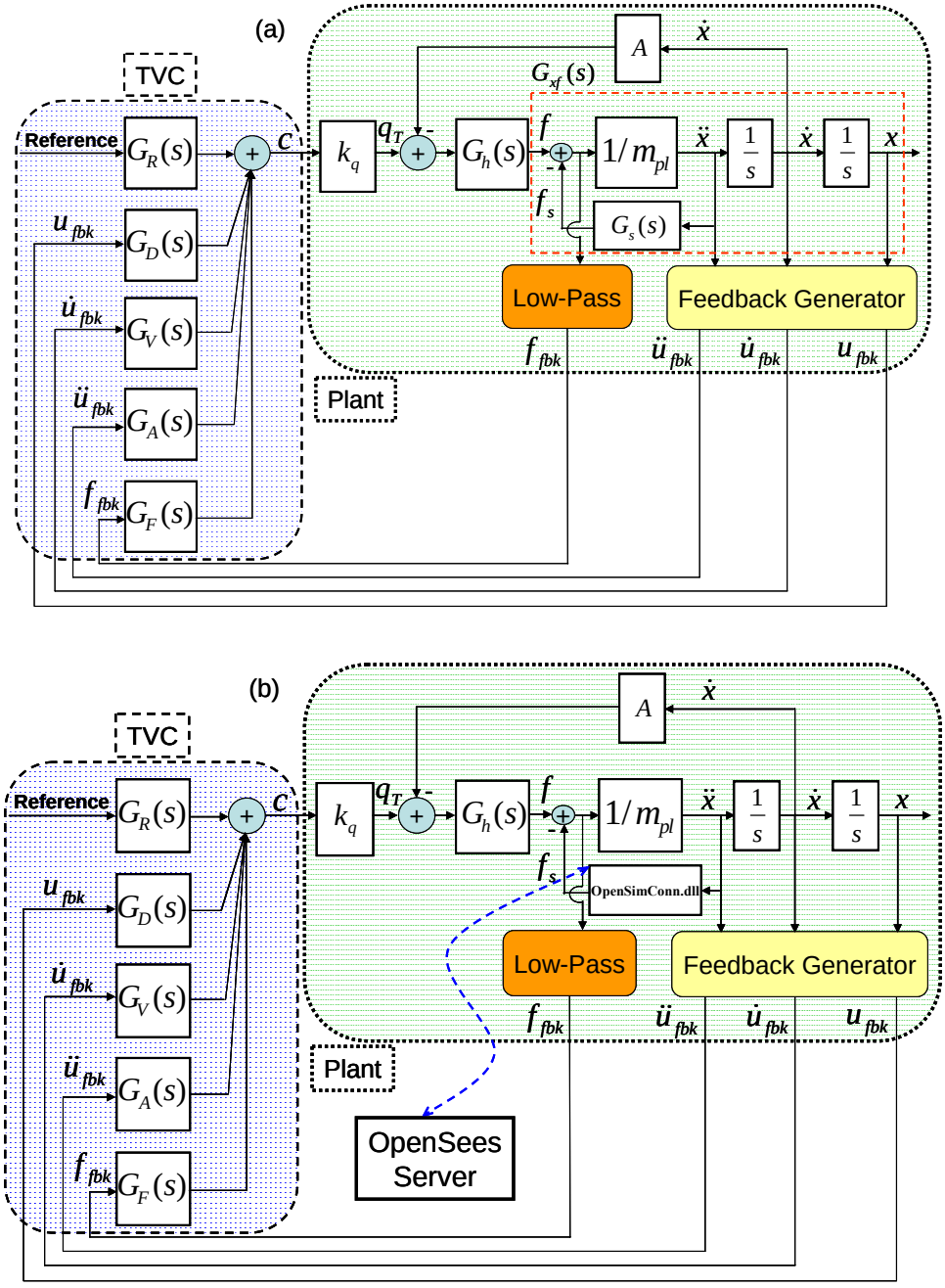

Figure 8.3: Closed-Loop block diagram of the linear servovalve-actuator-rigid platen-specimen with Three-Variable Controller (TVC) with (a) specimen is modeled within Simulink, and (b) specimen is modeled within OpenSees.

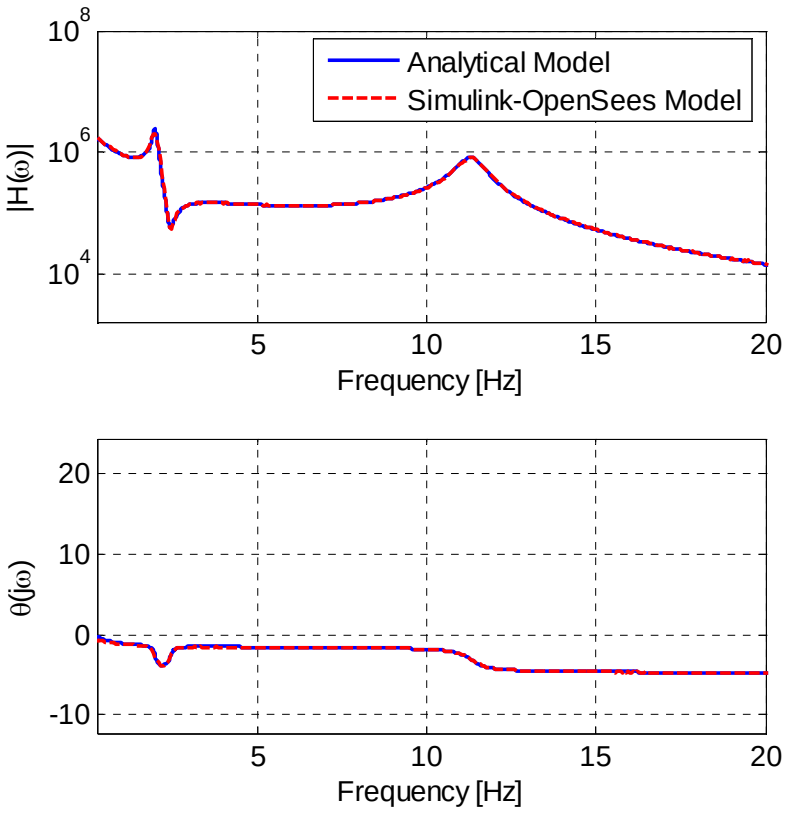

Figure 8.4: Bode plot of the analytical model of the linear table with a SDOF specimen and TVC and force feedback control algorithm with its numerical counterpart using Simulink and OpenSees linked by the client-server technique.

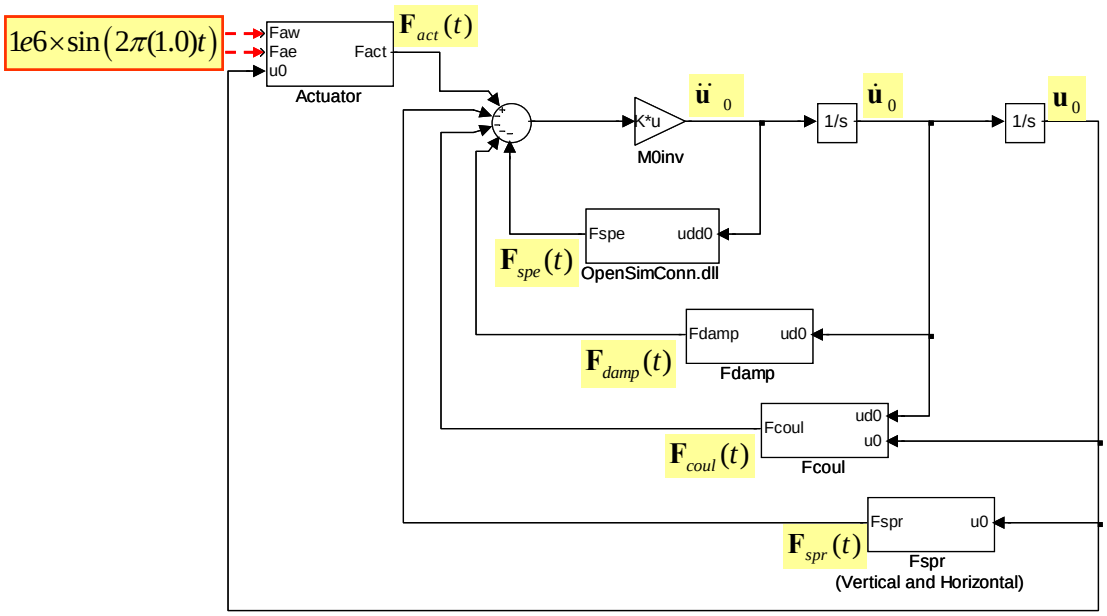

Figure 8.5: Simulink implementation of equation of motion of the linear platen-SDOF specimen assembly where the specimen is model with OpenSees using the custom block OpenSimConn.dll.

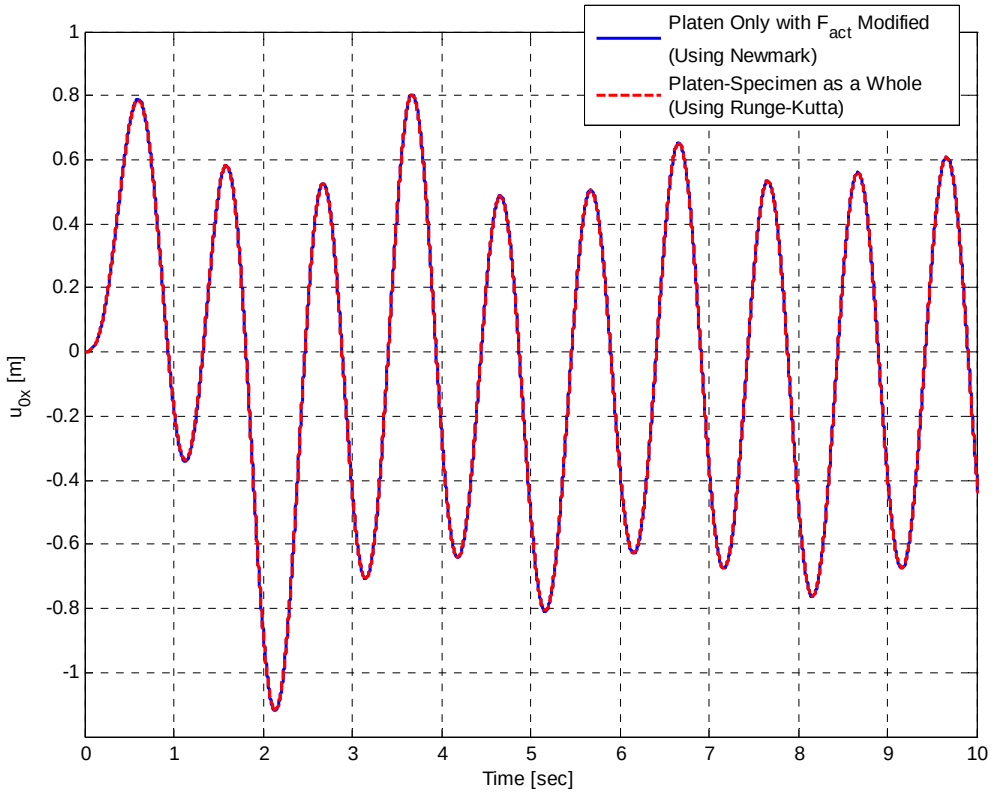

Figure 8.6: Comparison of platen displacements u_{0x} found by using Simulink and Newmark's method.

REFERENCES

Bewley, T. (2008). *Numerical Renaissance,* Renaissance Press, San Diego.

Dabney, J., Harman, T. L. (2004). *Mastering Simulink*, Pearson/Prentice Hall, Upper Saddle River, New Jersey.

Dyke, S. J., Spencer, B. J., Quast, P., and Sain, M. K. (1995). "Role of control-structure interaction in protective system design." *J. Eng. Mech.*, 121(2), 322-338.

Lee, S. (2004). Ordinary and Partial Differential Equation Routines in C, C++, Fortran, Java, Maple, and Matlab, Chapman and Hall/CRC, New York.

McKenna, F., Fenves, G. L., and Scott, M. H. (2000). "Open system for earthquake engineering simulation", http://opensees.berkeley.edu.

Welch, B.B. (2000). *Practical Programming in Tcl and Tk*, 3rd Edition, Prentice-Hall, Inc., Upper Saddle River, New Jersey.

CHAPTER 9

COMPREHENSIVE MECHANICS-BASED VIRTUAL MODEL OF THE NEES-UCSD SHAKE TABLE (BARE TABLE CONDITION)

9.1. Introduction

Large servo-hydraulic shaking table systems are essential tools in experimental earthquake engineering. They provide effective ways to subject structural components, substructures, or entire structural systems to dynamic excitations similar to those induced by real earthquakes. The typical shake table system includes a variety of mechanical (platen, yaw/pitch/roll restraining systems, vertical and lateral bearings, reaction block, foundation, and linear/nonlinear specimen), hydraulic (pumps, hydraulic lines, accumulator bank, distributed accumulators along hydraulic line, servovalves, and actuators), and electronic (controller, various types of transducers, signal conditioning units, data acquisition system) components.

The main objective of a shaking table system is to reproduce prescribed acceleration time history records within a reasonable accuracy thus subjecting structural systems to real time input excitations retaining realistic inertial and damping effects. Currently, the reproduction of a prescribed acceleration time history record

(e.g., earthquake accelerations) with such systems remains imperfect goal (Rinawi and Clough, 1991; Kusner et al., 1992; Clark 1992; Crewe, 1998; Conte and Trombetti, 2000; Crewe and Sewern, 2001; Trombetti and Conte, 2002). Within the Network for Earthquake Engineering and Simulation (NEES) several major shake table facilities have been added to the shake table inventory of the Unites States (e.g., NEES at Buffalo, NEES at Reno, and NEES at San Diego). These large facilities are currently used to investigate aspects of structural and geotechnical seismic behavior that cannot be readily extrapolated from testing at smaller scales, or under quasi-static or pseudo-dynamic conditions. With the recent advancements of experimental test methods, numerical simulation tools, and high-speed communication networks researchers are able to conduct also geographically distributed tests using these state-of-the-art testing facilities. Geographically distributed testing combines the capabilities of two or more sites to conduct tests on structural systems that could not be performed at one site due to limited site capacity (Takahashi and Fenves, 2005). New testing facilities and their innovative use bring new challenges to the field of shake table testing. One of these challenges is in high-fidelity control of shake table systems.

Dynamic tests with shake tables require the table platform to follow a reference signal (e.g., displacement or acceleration). Controller is the electronic device (analog or digital) that supplies the appropriate command to the servovalve(s) in order to drive the table along the correct trajectory (i.e., path). Shake table control systems are usually based on linear control algorithms in which it is assumed that the plant can be modeled as a set of linear differential equations and the dynamic parameters of the

plant are known and fixed during the experiments (Stoten and Gomez, 2001). Linear controllers can be tuned with high degree of precision when the plant has known parameters and behaves linearly. On the other hand, linear controllers are not well suited for non-linear regimes and do not respond as expected if the plant parameters change or have been wrongly estimated (Gomez, 1999). Earlier works on the performance characterization of shake tables reveal that shake tables are highly nonlinear device in which the table response is a function of the input amplitude level at which it operates (Clark, 1983; Kusner et al., 1992; Clark, 1992; Zhao et al., 2005). Some of the major sources of nonlinearities in shake table systems are servovalve(s), nonlinear viscous and friction dissipative sources, total system leakage including servovalve(s) and actuator(s), changes in volumes of actuator chambers, and system pressure fluctuations.

As large shake table facilities become available (e.g., NEES-UCSD shake table in U.S.A and NIED E-Defense table in Japan etc.), testing full scale specimens on shake tables is now more and more frequent. In large scale shake table tests, often the specimen is more massive than the table and can exhibit nonlinear behavior under the reproduced table motion. Also characteristics of the specimen can change suddenly especially if a collapse situation occurs. For such test conditions, one of the most significant problems arises from the fact that the dynamics of the specimen is as relevant to the dynamic model of the overall system as the table itself (Clark, 1984; Crewe, 1998; Gomez 1999; Stoten and Gomez, 2001). Nonlinear table/specimen

interaction as well as other sources of nonlinearities further complicates the accurate control of shake tables with linear controllers.

Adjusting control parameters to optimize the response of the shake table system is called tuning. Ideally, a tuned shake table system would have a transfer function between the reference and achieved signals (total table transfer function) characterized by unit gain and zero phase shift across the entire operating frequency range under loaded (i.e., with a specimen) table conditions. With linear controllers, due to the reasons explained above, it is not possible to achieve such total transfer functions. To remedy the inaccuracies of typical linear controllers a tuning process is employed. The process conducted prior to the actual test usually involves an offline or an online (iterative) time history matching technique. A simple offline approach for compensating the controller deficiencies is to apply a pre-filter (e.g., inverse total table transfer function estimated prior to the test) once to the reference signal which results in a modified reference signal (i.e., drive signal) accounting for the dynamics of the system (Hwang et al., 1987; Twitchell and Symans, 2003). Inverse transfer function is estimated using white noise while the specimen is mounted on the table to take into account the table/specimen interaction. One very important drawback in offline approach is that when the transfer function is estimated, if the amplitude of white noise is too high the specimen on the table may be damaged; on the other hand if the amplitude of white noise is too low then nonlinearities in amplitude scaling of the drive signal may mean that the transfer function estimated from low level amplitude white noise is not representative of the actual system performance with large

amplitude earthquake signals. In online (iterative) time history matching technique, command signal is repeatedly modified by addition of a fraction of the pre-filtered error between the actual and desired table motion. The error is pre-filtered by the inverse of the total table transfer function which can be the initial estimation or an updated one from the last iteration (Crewe, 1998). The iteration process is repeated until the errors fall within a desired level. Online time history matching techniques can deal with repeatable nonlinearities such as servovalve nonlinearities. Both in offline and online techniques, extreme care has to be given to the specimen to avoid premature damage.

A recent test study done by Luco et al. (2008) on the NEES-UCSD shake table investigates the effect of amplitude scaling in tuning of shake tables under bare table conditions. The tests were designed to quantify the effect that the tuning amplitude has on the level of signal fidelity. For these tests, first the table response was optimized, as much as possible, by adjusting the gains of the linear controller. This step was followed by an online time history matching technique applied to a scaled down or scaled up versions of the intended acceleration motions. Drive inputs obtained at the end of the iteration process were scaled up or down according to several test amplitudes and the resulting motions were reproduced on the table. A number of comparisons and measures were used to evaluate the signal reproduction capability of the shake table which included direct comparisons of the acceleration time histories, peak accelerations, constant ductility response spectra for the achieved and intended platen accelerations, and relative root mean square error value to offer a cumulative

measure in signal reproduction. Based on these different comparisons, it was concluded with that the signal fidelity level achieved for a specific amplitude by a certain tuning cannot be maintained at a different amplitude. The difficulties encountered with the typical case of tuning at low amplitudes and testing at much higher amplitudes indicate the need for an accurate virtual tuning of the table based on a detailed mechanics-based model of the complete system and, also, for a more advanced controller. It should be noted here that for a loaded table conditions, tuning at low amplitudes and testing at higher amplitudes is the only option since the specimen can not be sacrificed during table tuning. Offline and/or online time history matching techniques are not the solution to achieve high fidelity in signal reproduction for loaded table conditions.

The complex dynamics of large shaking table systems emanate from multiple dynamic interactions and nonlinearities among various system components (Dyke et al., 1995; Conte and Trombetti, 2000; Trombetti and Conte, 2002; Ozcelik et al., 2008(1); Ozcelik et al., 2008(2)). In the literature, we find a limited number of studies focusing on modeling and simulation of complete servo-hydraulic testing systems (Hwang et al., 1987; Rinawi and Clough, 1991; Clark, 1992; Dyke et al., 1995; Dimig et al., 1999; Conte and Trombetti, 2000; Williams et al., 2001; Twitchell and Symans, 2003; Thoen and Laplace, 2004; Zhao et al., 2005; Zhao et al., 2006). Dyke et al. (1995) developed a linear model for a servovalve/actuator system attached to a linear shear type structure for investigating the role of control-structure interaction; the analytical model also includes a displacement controller and force feedback loop.

Conte and Trombetti (2000) developed a linear analytical model of a small-to-medium size shake table system accounting for servovalve time delay, actuator dynamics, oil leakage through the actuator seals, foundation flexibility, and linear elastic multi-degree-of-freedom (MDOF) specimen dynamics. Williams et al. (2001) have developed a realistic numerical model of a dynamic structural testing system, which includes a nonlinear model of the servovalve actuator system, servovalve leakage, controller, and the specimen modeled as a linear elastic single-degree-of-freedom (SDOF) system. Thoen and Laplace (2004) presented a comprehensive numerical model of a medium size shake table for off-line tuning purposes; their model includes the real-time controller software, servovalve spool dynamics, a nonlinear servovalve-actuator model, an accumulator model, a linear payload model, a nonlinear friction model, and foundation dynamics. Recently, Zhao et al. (2005) presented a numerical model for an effective force testing system in which a detailed nonlinear servovalve model is used where two independent sources of servovalve flow nonlinearities were taken into account. In this work, leakage within the servovalve and inside the actuator chambers is modeled as an effective total system leakage and is found to be equivalent to damping of actuator dynamics.

9.1.1. Overview of the NEES-UCSD LHPOST

The NEES-UCSD Large Performance Outdoor Shake Table (LHPOST) located at a site 15 km away from the main campus of the University of California at San Diego ($32^{\circ}53'37''N$ and$117^{\circ}06'32''W$), is a unique outdoor experimental facility that enables next generation seismic tests to be conducted on very large structural and

soil-foundation-structure interaction systems. A three-dimensional rendering of the overall shake table system is shown in Figure 9.1(a). The LHPOST consists of a moving steel platen (7.6m wide by 12.2m long); a reinforced concrete reaction block; two servo-controlled dynamic actuators with a force capacity in tension/compression of 2.6MN and 4.2MN, respectively; a platen sliding system (6 pressure balanced vertical bearings with a force capacity of 9.4MN each and a stroke of ±0.013m); an overturning moment restraint system (a pre-stressing system consisting of two Nitrogen-filled hold-down struts with a hold-down force capacity of 3.1MN each); a yaw restraint system (two pairs of slaved pressure balanced bearings along the length of the platen); a real-time multi-variable controller, and a hydraulic power supply system. The technical specifications of the LHPOST include a stroke of ±0.75m, a peak horizontal velocity of 1.8m/s, a peak horizontal acceleration of 4.2g for bare table conditions and 1.28g for a rigid payload of 400tons, a horizontal force capacity of 6.8MN, an overturning moment capacity of 50MN-m, and a vertical payload capacity of 2000tons for which the peak platen acceleration reduces to 0.3g. The frequency bandwidth is 0-20Hz. Other detailed specifications of the NEES-UCSD LHPOST can be found elsewhere (Conte et al., 2004; Van Den Einde et al., 2004).

Figure 9.1(b) shows a detailed schematic representation of the major components of LHPOST and the way they interact with each other. There are two pumps in the system providing hydraulic power to various parts of the table. Pump 1 supplies hydraulic power to the servovalves, vertical and yaw bearings (not shown in schematics) by providing 720lit/min flow at 21.0MPa (190gpm at 3000psi) pressure.

Hydraulic line carrying the flow from Pump 1 is indicated as PP which stands for pilot pressure. Pump 2 charges the accumulator bank; flow provided by this pump is 416lit/min at 21.0MPa (114gpm at 5000psi) pressure. A 9500 liter capacity accumulator bank pressured up to 35.0MPa provides the high flow needed to simulate transient earthquake signals. Blow-down valve converts the high pressure oil from the accumulator bank to a system pressure of 21.0MPa for controlling the actuators. Hydraulic supply line carrying the regulated oil is indicated as P which stands for main pressure. Also shown Figure 9.1(b) are the small in-line accumulators each with capacity of 95 liters and charged up to 13.8MPa (2000psi) pressure. There are two actuators on the West and East sides of the table platen. Each actuator has two high performance servovalves attached on them (therefore there are total of four servovalves on the system). Close-coupled (C.C.) accumulators are attached to the actuators and they are 57 liters each and are also charged up to 13.8MPa (2000psi) pressure. Low-pressure return flow is collected in the surge tank. Actuators drive the table platen which slides on low-friction vertical bearings, pre-charged hold-down struts hold the platen down with constant vertical forces in order to restrain the pitch motion of the platen. Forces generated by the system are reacted by the foundation block and surrounding soil. The controller on the system sends control signal computed using the reference and feedback signals to the servovalves in order to move the platen along a desired path.

The reaction block and the surrounding soil are shown in Figure 9.1(b) as parts of the shake table system. Large forces that the actuators of LHPOST exert on the

reaction block and surrounding soil suggests the need to determine the induced ground motion in the vicinity of the table in order to evaluate the effects that any motion of the block itself would have on the control of the shake table. In order to study dynamic soil-foundation interaction effects, an extensive forced vibration test study using eccentric mass shakers has been carried out on the foundation block of LHPOST prior to the construction of the shake table. Forces exerted by the shakers are normalized to the maximum force (6.8MN) that actuators can exert on the foundation. Results of this study reveal that the foundation block essentially translates as a rigid body along East-West (EW) direction with slight out-of-plane deformation of the East and West end walls; the block also bends in addition to rocking about the North-South (NS) axis. The frequency response of the EW motion peaks at 10 Hz with amplification factor of 1.3; vertical frequency response indicates that the amplitudes of the vertical displacements increase with horizontal distance to the NS axis of rotation at least for frequencies below 15 Hz. Experimentally obtained frequency response curves indicate that the maximum scaled horizontal and vertical displacements for the maximum theoretical harmonic actuator force of 6.8MN amplitude at 10 Hz frequency would be 0.26mm and 0.17mm, respectively. These displacements are sufficiently small to have no effect on the control of the shake table which relies on the assumption that the relative displacement of the platen with respect to the reaction block represents the absolute displacement of the platen (Luco et al., 2008).

The main objective of this section is to develop a comprehensive mechanics-based model of the large NEES-UCSD shake table for bare table conditions. The

model includes the virtual replica of the controller, four servovalve models including servovalve spool dynamics and two independent servovalve flow nonlinearities, two single-ended actuators with variable internal volumes, two accumulators modelling the average supply pressure drop, and a two-dimensional mechanical subsystem model generalized from the previously identified one-dimensional mechanical subsystem model which includes the effects of effective mass of the platen, nitrogen-filled hold-down struts, and various viscous and Coulomb dissipative mechanisms. Based on the forced vibration test results of the foundation block, the soil-foundation compliance effects will be ignored in the virtual model. This mechanics-based virtual model will be extremely useful for understanding the underlying coupled nonlinear dynamics of a large shake table system therefore providing insight into the sources of various signal distortions, for off-line tuning of the actual table, and for future advanced control algorithm developments. This model will be used in Chapter 11 to investigate the shake table – nonlinear specimen interaction problem.

9.2. MTS Three-Variable Controller

The control software used in LHPOST is called 469D. The three-Variable-Controller (TVC) is an integral part of the software 469D (Thoen, 2004). TVC can be a classified as a displacement controller with additional feedforward control terms. It is a displacement control since the control signal is the weighted-error between the command and feedback (i.e. achieved) displacement signals. Since seismic inertia forces are related to acceleration, the key element in shake table tests is the capability of the system to accurately reproduce prescribed acceleration records. For this reason,

the displacement control strategy is usually augmented with additional feedforward control signals in order to increase the fidelity in acceleration reproduction. Feedforward terms on TVC are velocity, acceleration, and the jerk (i.e., third derivative of displacement) which are computed from the reference signal. The reference signal (i.e., command signal) can be displacement, velocity, or acceleration depending on the control mode. TVC can be set to run under all these control modes. In acceleration and velocity modes (velocity mode is rarely, if ever, used for shake table tests), the controller is still in displacement control but the control signal to the servovalves is a blend of feedback and reference velocity, acceleration, and jerk feedforward control signals. In displacement control mode, the only control signal is the weighted error between the reference and feedback displacement signals (i.e., no feedforward term is used).

In TVC, force stabilization is provided by an additional actuator force feedback loop which helps to dam out the oil column resonance (Conte and Trombetti, 2000; Dyke et al., 1995). The force measurement is filtered by a high-pass filter before being used as a control signal. Cut-in frequency of the high-pass filter is set by the filter parameter ω_{DP}.

In addition to the above features, TVC also has five notch filters to be used in order to compensate for mechanical resonances and anti-resonances. Notch filters in TVC are implemented in such a way that independent (i.e., orthogonal) tuning of the notch filter parameters center frequency f_0, 3dB bandwidth b_w, and depth *depth* can be possible (Regalia et al., 1988). Orthogonal tuning allows users to independently

tune (i.e., adjust) one notch filter parameter without changing a specified tuning on the remaining ones; but since the phase response of the notch filter changes with changes in notch filter parameters, effects of the fixed parameters on the table response will be altered even though its value remains fixed.

Figure 9.2 shows the block diagram of TVC along with the Reference and Feedback Generators, where k_{PF}, k_{VF}, k_{AF}, k_{JF} are the displacement, velocity, acceleration, and jerk feedforward gains, respectively; k_P, k_V, k_A, k_{DP} are the displacement, velocity, acceleration, and force feedback gains, respectively; and k_M is the master gain which is always set to unity.

Seismic data is usually recorded by accelerometers therefore only acceleration records (i.e., acceleration reference) are readily available before a seismic test. Depending on the control mode, TVC requires other reference states (i.e., velocity, acceleration, and jerk) to be known beforehand for control purposes. Reference Generator in TVC computes these reference states by using the reference signal which represents desired displacement, velocity, or acceleration depending on the control mode, and creating the reference states u_{ref}, $\dot{u}_{ref}$, $\ddot{u}_{ref}$, and $\dddot{u}_{ref}$ using a state variable filter (Thoen, 2004).

Table displacement and acceleration responses are measured using linear-variable-displacement-transformers (LVDTs) and accelerometers, respectively. Often LVDT data is valid over the low-to-medium frequency range (typically 0-15 Hz), but above this range the data is unusable due to the combined effects of mechanism backlash and the problem of resolving small amplitude signals with finite accuracy

analogue-to-digital conversion. On the other hand, accelerometer signals are accurate in the medium-to-high frequency range (typically up to ~50 Hz) (Stoten et al., 2001). Therefore the problem is to determine a suitable combination of displacement and accelerometer signals to cover the entire frequency range of operation. The technique used to do this in MTS 469D control software is composite filtering. The Feedback Generator in 469D combines displacement and acceleration sensors, each with their respective bandwidth limitations, to create wideband estimates of the feedback states u_{fbk}, $\dot{u}_{fbk}$, and $\ddot{u}_{fbk}$. These improvements are intended to provide estimates of unmeasured data (e.g. velocity) and to obtain more consistent estimates of measured data over a wider frequency range (Thoen, 2004).

The TVC block diagram shows that signals with different units are blended together. Blending of different unit signals to obtain a hybrid command signal to the servovalves is possible through normalization of the various signals to their respective maximum values (e.g., D_{max}, V_{max}, A_{max}, and F_{max}) and conversion to Volt units (i.e., respective maximums correspond to 10 Volts).

TVC is implemented in Matlab-Simulink® using the transfer functions describing TVC and Feedback Generator. These transfer functions were provided by MTS Systems Corporation and they can not be given explicitly here due to proprietary reasons. In order to check the Simulink implementation of TVC, Simulink model of TVC is excited by a unit impulse acceleration (i.e. reference signal is an impulse), and the TVC output (i.e., command to the servovalve(s)) is recorded. Then a transfer function between these two signals is estimated. The same unit impulse acceleration is

inputted to the real-time control software 469D and the TVC output is recorded, then a transfer function between these two signals is estimated. Numerical values used for TVC parameters for both the Simulink model and the real-time software are $k_{PF} = 0.0\,\text{V/V},\ \ k_{VF} = 0.35\,\text{V/V},\ \ k_{AF} = 0.45\,\text{V/V},\ \ k_{JF} = 0.0004\,\text{V/V},\ \ \ k_P = 1.50\,\text{V/V},$ $k_{DP} = -0.15\,\text{V/V},\ \omega_{DP} = 0.50\,\text{V/V},\ k_M = 1.0\,\text{V/V}$. These numerical values are typical of those used on the real system. The feedback gains k_V and k_A are set to zero which is the case for servo-hydraulic control systems (Thoen, 2004). Only one notch filter is used, and the numerical values of its parameters are $f_0 = 10.0\,\text{Hz},\ bw = 5.0\,\text{Hz},$ and $depth = -0.80\,\text{V/V}$. It should be mentioned here that $depth < 0$ corresponds a trough and $depth > 0$ corresponds to a peak in the magnitude response of the notch filer. Value of $depth$ must be confined between -1.0 and 1.0. The comparison of transfer function estimations is shown in Figure 9.3. Agreement between the two transfer functions is excellent, therefore it can be said that the Simulink model of TVC can be substituted in place of the real-time TVC in the Simulink model of the entire plant.

9.3. Servovalve Model

9.3.1. LHPOST High Performance Servovalves

There are four four-stage servovalves on LHPOST, two on each actuator. The four stage servovalves on LHPOST consist of an MTS Series 256 three stage servovalve and an additional fourth stage (MTS Systems Corporation, USA). Figure 9.4 shows the picture of an MTS four stage servovalve similar to the ones used on LHPOST. LHPOST servovalves are specially manufactured to achieve the high

performance requirements of the system. MTS Series 256 servovalve is an electro-hydraulic three stage servovalve consisting of a high-flow, four-way (i.e., four flow paths exist) spool valve and a smaller two stage valve (pilot valve). First stage of the pilot valve is the torque motor stage. This stage consists of coils, an upper and lower pole piece, an armature and two magnets. Its purpose is to convert electrical input signal (servovalve control signal) into physical movement of the armature. The second stage of the pilot valve consists of a spool valve which controls hydraulic fluid flow to the third stage and a feedback spring which provides mechanical linkage between the armature/flapper and the spool. Servovalves are driven by the input current sent by the controller. This causes rotation of the electromagnetic flapper assembly (i.e., pilot stage) which in turn causes displacement of the second stage spool. The third stage is similar to the 2^{nd} stage of the pilot valve except that it has a larger spool and its position is monitored by an LVDT. Third stage flow goes into the fourth stage to move the spool at this stage by causing pressure difference between the two ends of the spool. Fourth stage (main stage) of the servovalve has a larger spool than the third stage and its movement is also monitored by an LVDT. LVDTs on the 3^{rd} and the 4^{th} stage spools provide output signals to the valve inner controllers which are proportional to the spool positions. These measured displacement signals are compared to the desired position in the valve inner controller. Any difference between the desired position and the LVDT signal causes the valve controller to alter the servovalve control signal. Figure 9.5 shows the inner as well as outer (i.e., TVC) control loops on LHPOST along with dither and feedback conditioner adjustments.

Inner control loop on the third stage is a proportional-derivative (PD) controller, and the one on the fourth stage is proportional-integral-derivative (PID) controller.

The servovalve model presented in this work does not take into account the dynamics of inner controller loops, conditioner filters, dither, and the dynamics of pilot stage servovalve. These simplifications have been made due to the complexity of the entire shake table system (i.e., the plant) and the need to capture the salient dynamic characteristics of the whole plant with a reasonable complexity. Since the spool movements determine the amount of flow going into the actuators which in turn determines the amount of generated actuator force that moves the platen, most of the servovalve modeling efforts has been focused on the identification of the third and fourth stage spool dynamics. This has been proved to be a reasonable modeling assumption based on the experimental observations.

9.3.2. Servovalve Spool Dynamics

For most physical systems, servovalve spool dynamics is not the primary dynamic element, so it is only necessary to represent the valve spool dynamics throughout a relatively low frequency spectrum. For example if a servovalve-actuator is coupled to a load which exhibits a 50 Hz resonant frequency, it is meaningful only to represent valve dynamic response up 50 Hz (Thayer, 1965). LHPOST's frequency bandwidth is between 0-25 Hz, therefore it is sufficient to model the 3rd and 4th stage spool dynamics with reasonable accuracy up to 25 Hz. Servovalve spool displacement within servovalve exhibit second order dynamics (Thayer, 1965; Thoen and Laplace, 2004; Zhao et al., 2005). On LHPOST these dynamics were measured by exciting the

table with white noise (WN) input and recording the valve driver commands (i.e., c_{3rd} and c_{4th}) and valve spool displacements (i.e., f_{3rd} and f_{4th}) while the main hydraulics was turned off (i.e., actuators are taken off the loop). Eight parametric black-box ARMAX models of type given in (9.1) are fitted to the input-output pairs of the third and fourth stages of four servovalves (WA and WB on the West actuator, and EA and EB on the East actuator)

$$A_i(q)\, f_i(t) = B_i(q)c_i(t-nk) + C_i(q)e_i(t) \;\; i = 1,2,3,4 \tag{9.1}$$

where A_i, B_i, and C_i are model parameters to be estimated with orders 2, 2, and 2, and nk is the delay term between the driver command and feedback spool displacement which is of order 1. Estimation data is a 240 seconds long WN acceleration input band limited between 0.25-40 Hz with 10%g RMS amplitude. Figure 9.6 shows the Bode plots of the estimated parametric models for the 4th stages of the WA and EA servovalves and the non-parametric transfer function estimations using Welch-Bartlett method. Transfer function estimations for the 3rd stage spool dynamics of WA, WB, EA, and EB valves as well for the 4th stage dynamics of WB and EB valves are not shown due to space limitations but have similar qualities as the ones shown. Figure 9.7 shows the comparison of simulation results using the estimated parametric models of WA and EA servovalves and the recorded spool displacements from a WN test. The test was 3%g RMS amplitude WN acceleration band-limited between 0.25-40 Hz commanded to the servovalves. The excellent match between the simulated and the actual displacement responses shows that the estimated

parametric models can be used in the simulation model to capture the 3rd and 4th stage spool dynamics of the actual servovalves. Notice that eight independent spool dynamics are modeled in the virtual model.

9.3.3. Servovalves' Port Orifice Widths

The sctuators on LHPOST are single-ended actuators. Single-ended actuators have unequal piston areas on both sides of the piston. Figure 9.8 shows the assembly of the West single-ended actuator with the 4th stages of WA and WB servovalves. Sketch of the East single-ended actuator and the EA and EB 4th stage spool assembly would look exactly the same except that the East actuator would be the mirror image of the West one. Figure 9.8(a) shows the actuator piston movement along the extent direction (positive direction of the actuator motion) with extent velocity $\overline{V}$ and associated 4th stage spool movement and actuator chamber pressures $\overline{P}_1$ and $\overline{P}_2$; Figure 9.8(b) shows the actuator movement along the retract direction (negative direction of the actuator motion) with retract velocity $\underline{V}$ and associated 4th stage spool movement and actuator chamber pressures $\underline{P}_1$ and $\underline{P}_2$; A_1 and A_2 are the actuator piston areas; P_S and P_R are the supply and return pressures, respectively.

The 4th stage spool position determines the sizes of the orifices which allow flow into and out of actuator control ports WC1 and WC2. When the actuator piston moves along the extent direction, load flow orifices 1 and 2 are open and 3 and 4 are closed and when the piston moves along the retract direction, load flow orifices 3 and 4 are open and 1 and 2 are closed. The same control signal is sent to both servovalves on the West actuator therefore servovalves' load flow orifices open the same amount

with slight differences due to different spool dynamics associated with them. To the servovalves on the East actuator, the same control signal as the one on the West servovalves is sent but with opposite polarity (i.e., the same amplitude but opposite sign). As an example, let's assume that the West actuator piston is moving along the extent direction, so the East actuator piston must move along the retract direction. Hence on the West servovalves load orifices 1 and 2 would be directing flow in and out of the actuator chambers, whereas on the East servovalves load orifices 3 and 4 would be. Something missing, in other words, at each instant of time four load flow orifices are directing flows to two actuators.

Servo-hydraulic actuators which need to perform with high fidelity in signal reproduction are normally made using actuators with equal piston areas (i.e., double-ended). Actuator average internal pressure is $1/2 \times P_S$ in double-ended actuators controlled by servovalves with matched and symmetric orifices regardless of actuator's direction of motion (Merritt, 1967). In single-ended actuators the internal pressure depends on the direction of actuator motion therefore causing pressure discontinuity within the actuator each time the actuator changes direction of motion, which results in waveform distortion (Gram, M., personal communication, MTS System Corp.). On LHPOST, single-ended actuators had to be used in order to reduce the length of the actuator piston and to reduce the excavation cost for the foundation. Therefore, LHPOST servovalves are built in order to compensate for the unconventional nature of the LHPOST actuators. Sleeves of the servovalves on LHPOST (shown in Figure 9.4) are cut with load flow port window widths designed

for the piston area ratio of $\frac{A_2}{A_1} = 0.64$. By imposing $\bar{V} = \underline{V}$ for a given 4th stage servovalve spool displacement x_{sv}, $\bar{P}_1 = \underline{P}_1$, and $\bar{P}_2 = \underline{P}_2$ while no load is attached to the actuators, and using Bernoulli's flow equation for four orifices as shown in Figure 9.8, the following relationships for the port widths as a function of piston area ratio can be found

$$\frac{w_1}{w_3} = \left(\frac{A_2}{A_1}\right)^{1/2} = 0.8, \quad \frac{w_2}{w_3} = \left(\frac{A_2}{A_1}\right)^{3/2} = 0.512$$
$$\frac{w_3}{w_3} = 1, \qquad \frac{w_4}{w_3} = \frac{A_2}{A_1} = 0.6 \tag{9.2}$$

Return pressure P_R is assumed to be zero in the derivation of (9.2). With these orifice port widths, the actuator internal pressures are the same for motions in both the extent and retract directions; this minimizes waveform distortion in single-ended actuators. Also, for a given x_{sv}, velocity is the same for each direction. Notice that port widths in (9.2) are normalized with respect to the port width 3 (i.e., w_3). Figure 9.9 shows the schematics of the load flow ports of one of the servovalves on LHPOST. Notice that there are eight servovalves on LHPOST and each has port windows as shown in Figure 9.9 where x_{sv}^{max} is the stroke of the 4th stage spool.

Figure 9.10 shows the displacement and velocity responses of the table and 4th stage spool displacement of the WA servovalve from a harmonic test with 4.1 Hz excitation frequency and 2.364g amplitude. Amplitudes of the recordings are all normalized with respect to the table velocity so that maxima, minima, and zero

crossings of the responses can easily be compared and be mapped to the flow paths' opening-closing sequences. Four different servovalve-orifice-port states can be identified from Figure 9.10: (i) from "O1" to "a", flow paths 3 and 4 are totally close and flow paths 1 and 2 are closing therefore velocity decreases along extent direction, this is referred to as closing sequence of 1 and 2; (ii) from "a" to "O2", flow paths 1 and 2 are totally close and 3 and 4 are opening therefore velocity is increasing towards retract direction, this is referred to as opening sequence of 3 and 4; (iii) from "O2" to "b", flow paths 1 and 2 are totally close and 3 and 4 are closing therefore velocity is decreasing along retract direction, this is referred to as closing sequence of 3 and 4; (iv) from "b" to "O2", flow paths 3 and 4 are totally close and flow paths 1 and 2 are opening therefore velocity increases towards extent direction, this is referred to as opening sequence of 1 and 2. Notice that the spool displacement follows the velocity response of the table although slightly ahead of the piston velocity, this is due to response delay of the table. All of the servovalve port orifices are closed at points "a" and "b", therefore the table velocity is zero at these points. At zero velocity points (i.e., zero velocity crossings or table motion reversal points), supply pressure to the 4^{th} stage switches from flow path 1 to flow path 4 (i.e., port 1 to 4) or vice versa. This switching has certain implications in table response which will be pointed out later.

9.3.4. Servovalve Nonlinearities

Bernoulli's flow equation which is applicable for steady, inviscid (i.e., nonviscous), turbulent flow can be used to determine flow from an orifice

$$q_1 = \bar{K}_v w_1 x_{sv} \sqrt{P_S - P_1}$$
$$q_2 = \bar{K}_v w_2 x_{sv} \sqrt{P_2 - P_R} \tag{9.3}$$

$$q_3 = \bar{K}_v w_3 x_{sv} \sqrt{P_1 - P_R}$$
$$q_4 = \bar{K}_v w_4 x_{sv} \sqrt{P_S - P_2} \tag{9.4}$$

where $\bar{K}_v$ is flow coefficient of the servovalve that depends on the orifice geometry and the fluid density and it has a unit of $m^2/\left(\sqrt{N}\cdot\sec\right)$, (9.3) is valid for $x_{sv} > 0$ or for extent direction, and (9.4) is valid for $x_{sv} < 0$ or for retract direction. Notice that $w_i x_{sv}$ corresponds to the open area of load flow ports where $i = 1,2,3,4$. Since there are four servovalves on LHPOST, equations (9.3) and (9.4) are implemented four times in the virtual model. Servovalve flows contain two major types of nonlinearity: (i) Pressure drop – flow nonlinearity which is explicitly represented by the square root term; and (ii) nonlinear flow gain or nonlinear flow vs. spool displacement nonlinearity which is related to the term $\bar{K}_v$.

9.3.4.1.Pressure Drop – Flow Nonlinearity

Pressure drop – flow nonlinearity (or square root nonlinearity) reflects the nonlinear relation between the flow through the servovalve orifices (ports) and the pressure drop across the orifice (Zhao et al. 2005). This nonlinearity increases with increasing actuator force demand, and it is also a function of servovalve spool opening. Square-root nonlinearity shows itself in overall spool motion as skewed and anti-symmetric distortion (Clark 1983) and manifests itself clearly in periodic actuator motion as distortions due to the odd harmonics of the test frequency. Another source

of signal distortion is due to the pressure-switching phenomenon which occurs when the actuator force approaches a maximum value (i.e., at zero velocity). This phenomenon is independent from the square-root nonlinearity and it is inherent to the way servovalves work since supply pressure has to switch from one flow path to another in order for the actuator to change direction of motion (Figure 9.10). Pressure switching shows itself in servovalve spool motion as a sudden jump from zero opening to a certain finite value and its pronounced mostly during high force tests compared with the maximum force capacity of the actuator.

9.3.4.2. Flow Gain Nonlinearity

Flow gain K_v is given below

$$K_v = \left(C_d\sqrt{2/\rho}\right) w\sqrt{P_S} = \bar{K}_v w\sqrt{P_S} \tag{9.5}$$

where C_d is the discharge coefficient, ρ is the density of the fluid, and w is the width of the orifice (Meritt, 1967). Notice that K_v has the unit of flow per unit spool opening hence is called the flow gain or no load flow gain. K_v is a nonlinear function due to nonlinearity in flow discharge coefficient C_d. Flow discharge rate decreases as the spool opening increases or in other words as the orifice area $w \times x_{sv}$ increases (Zhao et al. 2005). Also notice that K_v is also a function of P_S, therefore it is affected by supply pressure fluctuations. Generally in a shake table system, supply pressure is regulated by accumulators therefore fluctuations are not that extreme. Especially during shake table tests with light specimens (i.e., specimen masses comparable to the

platen mass) or bare table conditions. In this paper, the change in supply pressure will be taken into account by modeling fictitious accumulators coupled closely to the actuators. Assumptions and details regarding the accumulator model will be presented later in the paper. Nonlinear behavior of flow gain K_v is complicated and experimental identification is usually necessary (Zhao et al. 2005). Zhao et al. (2005) devised a method to identify servovalve flow as a function of spool displacement: Periodic signal with gradually increasing amplitude are commanded to the servovalves while the actuator is detached from specimen (i.e., no load); then by measuring the corresponding actuator piston velocity and calculating the flow controlled by servovalves by multiplying piston velocity and actuator piston area, nonlinear flow vs. spool displacement curves are obtained. Note that the slope of this curve would be the no-load flow gain of the servovalve's ports. This method of identifying flow vs. spool displacement curve is deemed impractical for LHPOST due to actuators being attached to the platen permanently (actuators are not free of load) and also due to multiple servovalves and more complicated nature of servovalves' flow ports. Therefore, in this paper, a more pragmatic approach is taken to assign nonlinear flow curves to the servovalves' ports. It should be noted here that nonlinear flow gain becomes important during high velocity tests compared to the maximum actuator piston velocity.

A nonlinear curve of the type given below is used to construct the backbone of flow vs. spool displacement curves for the four ports of each servovalve

$$Q_i = \beta_i \left(1 - e^{-\alpha_i x_{sv}}\right),\ i = 1, 2, 3, 4 \tag{9.6}$$

where Q_i is the flow from the i^{th} port of one of the servovalves, β_i and α_i are the estimated flow model parameters for the i^{th} port, and x_{sv} is the 4th stage spool displacement. Flow model parameters are estimated minimizing the sum of squares of errors between the exponential function given in (9.6) and the prototype input-output data pair given below

$$\begin{aligned} input &= \begin{pmatrix} 0 & x_{sv}^{trial} & x_{sv}^{max} \end{pmatrix} \\ output_i &= \begin{pmatrix} 0 & \dfrac{Q_{max,i}}{2} & Q_{max,i} \end{pmatrix}, \; i = 1,2,3,4 \end{aligned} \tag{9.7}$$

where x_{sv}^{max} is the stroke of the 4th stage spool, $Q_{max,i}$ is the associated maximum flow from the i^{th} port of one of the servovalves (i.e., at maximum spool opening at system pressure), x_{sv}^{trial} is the spool opening where half of the maximum flow (i.e., $\frac{Q_{max,i}}{2}$) from the i^{th} port occurs. x_{sv}^{trial} is used to calibrate the flow curves based on the observed table responses obtained from the high velocity tests. $Q_{max,i}$ value can be obtained from the rated servovalve flow value which is provided by the manufacturer. Rated flow is the flow in which there is ~3.5 MPa (500 psi) pressure drop on an individual flow path or ~7.0 MPa (1000 psi) pressure drop across the actuator pressure chambers when the servovalve port is fully open. Rated flow value for Q_{rated}^{w3} is provided by the manufacturer for the port number 3 shown in Figure 9.8 (when the 3rd flow path is fully open). Rated flows for the ports 1, 2, and 4 are found using the ratios given in (9.2) and then the rated flows for four ports are extrapolated to the 10.5 MPa

(1500 psi) by multiplying the rated flows by $\sqrt{3}$. 10.5 MPa correspond to the pressure drop on an individual flow path and it is equivalent to 21.0 MPa pressure drop across the actuator pressure chambers. These extrapolated values will be used for $Q_{max,i}$ in order to find the necessary nonlinear flow curves. Figure 9.11 shows the nonlinear flow vs. spool opening curves obtained for one of the servovalves using $x_{sv}^{trial} = \frac{x_{sv}^{max}}{3.5}$ (i.e., $\frac{Q_{max,i}}{2}$ occurs at 29% of spool opening) which gives the best correlation with the test results and this will be shown later in the work. The same nonlinear flow curves shown in Figure 9.11 are assigned to all four servovalves.

9.3.5. Simulink Implementation of Servovalve Model

Figure 9.12(a) shows the Simulink implementation of the WA servovalve model which includes the 3rd and 4th stage spool dynamics, flow vs. spool displacement nonlinearity and pressure drop – flow nonlinearity for each one of four orifices. The gain $x_{sv}^{max}/10$ is used to convert volts to 4th stage spool displacements. Nonlinear flow vs. spool displacement curves are implemented using "Look-Up Table" block in Simulink which finds the flow of each orifice using as input the 4th stage spool displacements. Notice that depending on the direction of the 4th stage spool motion only two of the four servovalve ports are active. Blocks confined with the dotted box are added to the servovalve model since the flow gains have to be adjusted based on the supply pressure fluctuations which is simulated by the accumulator model. Figure 9.12(b) shows the details of the "Pressure Drop – Flow Nonlinearity

Orifice 1" block; other orifices have similar details. There are four servovalves therefore four Simulink models similar to the one shown in Figure 9.12(a) are implemented. Recall that the servovalves on the East actuator are commanded by the same control signal as on the West ones except with opposite polarity. Supply pressure to the 4th stage comes from the accumulator model and return pressure is set to a fixed value. Flows Q_{W1} and Q_{W2} are the flows going in/out actuator chambers depending on the direction of the servovalve motion. These flows will be used as inputs in the actuator model to determine the actuator driving force.

9.4. Actuator Model

Controller and servovalve models developed thus far determine the oil flow into the chambers of the actuators. Differential force (or load pressure) that drives the mass attached to the piston can be derived using equations of continuity (Williams et al, 2001). Figure 9.13 shows the flows Q_1 and Q_2 from servovalve going in and out of the actuator chambers and another flow path within the actuator chambers indicated with dotted arrows. Continuity equations can be written for the actuator chambers (i.e., control volumes) 1 and 2 by neglecting the flows within the actuator chambers as follows

$$\begin{aligned} \frac{dM_1}{dt} &= \frac{d\left(\rho V_1\right)}{dt} = \rho \frac{dV_1}{dt} + V_1 \frac{d\rho}{dt} \\ \frac{dM_2}{dt} &= \frac{d\left(\rho V_2\right)}{dt} = \rho \frac{dV_2}{dt} + V_2 \frac{d\rho}{dt} \end{aligned} \tag{9.8}$$

where M_1 and M_2 are the liquid masses inside the actuator chambers 1 and 2, respectively, and $\forall_1$ and $\forall_2$ are the instantaneous actuator chamber volumes 1 and 2, respectively. By using the fact that density of the fluid inside control volumes changes in a small amount as a function of pressure therefore using just the linear terms of the Taylor's series expansion of $d\rho$ (Merritt, 1967), and assuming that the temperature remains constant inside the chambers, ends to the simplification of (9.8) can further be simplified

$$\begin{aligned} Q_1 &= \frac{d\forall_1}{dt} + \frac{\forall_1}{\beta_e}\frac{dP_1}{dt} \\ Q_2 &= \frac{d\forall_2}{dt} + \frac{\forall_2}{\beta_e}\frac{dP_2}{dt} \end{aligned} \tag{9.9}$$

where β_e is the effective bulk modulus of fluid within the chambers. By substituting $\forall_1 = \forall_{10} + x_p A_1$ and $\forall_2 = \forall_{20} - x_p A_2$ for the first terms in (9.9), where x_p is the piston displacement, and $\forall_{10}$ and $\forall_{20}$ are the initial chamber volumes when the actuator piston is centered, the following equations of continuity for actuator chambers 1 and 2 can be obtained

$$\begin{aligned} Q_1 &= A_1\frac{dx_p}{dt} + \frac{\forall_1}{\beta_e}\frac{dP_1}{dt} \\ Q_2 &= -A_2\frac{dx_p}{dt} + \frac{\forall_2}{\beta_e}\frac{dP_2}{dt} \end{aligned} \tag{9.10}$$

The first and second terms in (9.10) are, respectively, the flows needed to satisfy the continuity equation due to the motion of the piston and due to the compressibility of

the fluid inside the chambers. Instantaneous actuator chamber volumes as a function of piston displacement can be written as follows

$$\begin{aligned} V_1(t) &= V_{10}\left(1+\frac{x_p(t)}{x_p^{max}}\right) \\ V_2(t) &= V_{20}\left(1-\frac{x_p(t)}{x_p^{max}}\right) \end{aligned} \tag{9.11}$$

where x_p^{max} is the actuator stroke. Substituting (9.11) into (9.10) and after rearranging terms, equations for chamber pressures P_1 and P_2 can be found

$$\begin{aligned} P_1 &= \frac{\beta_e x_p^{max}}{V_{10}} \int \frac{\left(Q_1 - A_1 \frac{dx_p}{dt}\right)}{L_p + x_p} dt \\ P_2 &= \frac{\beta_e x_p^{max}}{V_{20}} \int \frac{\left(Q_2 + A_2 \frac{dx_p}{dt}\right)}{L_p - x_p} dt \end{aligned} \tag{9.12}$$

where the integrals are evaluated over the duration of a time step and L_p is the stroke of actuator. Using P_1 and P_2, actuator driving force can be obtained as $F_{act} = A_1 P_1 - A_2 P_2$. Recall that LHPOST has two mirror-imaging single-ended actuators therefore (9.12) has to be implemented twice in order to find the total actuator force exerted on the platen. Once the West and East actuators' chamber pressures are known, total actuator force driving the platen can be found

$$F_{act} = P_{W1}A_1 + P_{E2}A_2 - \left(P_{W2}A_2 + P_{E1}A_1\right) \tag{9.13}$$

where P_{W1}, P_{E1}, and P_{W2}, P_{E2} are the pressures of chambers 1 and 2 of the West and East actuators, respectively. Simulink implementation of (9.12) for the West actuator is given in Figure 9.14. The implementation of the East actuator is the same as for the West actuator.

Interaction of the spring effect of fluid and the mass of mechanical parts results in a resonance in shake table systems. In most cases, this resonance is the main limitation to the dynamic performance (Merritt, 1967). The fluid spring is characterized by the value for the bulk modulus. The modulus of a fluid can be substantially lowered by entrapped air, mechanical compliance, and operating temperature. Typical value for the bulk modulus of petroleum-based fluids without entrapped air is around 1.5 GPa, but 1% entrapped air can reduce this value to as low as 0.36 GPa (Merritt, 1967). Therefore an effective bulk modulus of the oil in the system must be estimated. Oil column resonance of LHPOST is estimated by running the table with low level random excitation and measuring the 4th stage spool feedback displacement as input and actuator force as output and fitting a transfer function between them. The resonance peak seen in the transfer function would be the oil column resonance and the corresponding frequency is the oil column frequency f_{oil}. The effective bulk modulus of the system can now be estimated using f_{oil}

$$\beta_e = \left(2\pi f_{oil}\right)^2 \frac{M_e L_p}{2A_{eq}} \tag{9.14}$$

where M_e is the effective mass of the table platen, and $A_{eq} = A_1 + A_2$ is the piston area of a double-ended actuator equivalent to the two single-ended actuators. The effective

bulk modulus β_e computed by (9.14) represents not only the stiffness of the oil with entrapped air, but also the stiffness of the actuator swivels and additional oil volume inside the servovalves' manifolds (Thoen and Laplace, 2004).

In Figure 9.14, another flow path from the 1st actuator chamber to the 2nd is indicated with the dotted arrows. This flow is called the actuator cross-port leakage. Actuator cross-port leakage flow is proportional to the load pressure, indicated as P_L in the figure, and can be written as $q_l = c_l P_L$, where c_l is the leakage coefficient which it accounts for damping within the actuators (Dyke et al., 1995; Conte and Trombetti, 2000; Williams et al., 2001; Zhao et al., 2005). In this paper, damping due to the cross-port leakage and other sources of viscous damping are included within the mechanical subsystem. The mechanical subsystem model used in this work will be presented later.

9.5. Hydraulic System of LHPOST

In LHPOST hydraulic power is supplied to the actuators by a main accumulator bank. It is charged by a pump with 416 lit/min flow capacity at 35.0 MPa pressure, therefore the accumulator bank can be pressurized up to 35.0 MPa. High-pressure oil in the bank is regulated down to the system pressure of 21.0 MPa before it is sent to the actuators; pressure regulation is achieved by the blow-down control. The blow-down valve at the exit of the accumulator bank regulates the output pressure of the bank using a control algorithm which combines the error signal between the pressure set-point of 21.0 MPa and the pressure readings (i.e., feedback) at a point on

the hydraulic line close to the actuators with the feedforward control signal proportional to the reference velocity. Pressure-regulated oil leaves the blow-down valve, travels along the hydraulic line, and gets passively regulated at several points by in-line accumulators pre-charged to 13.8 MPa pressure. The purpose of these small in-line accumulators is to regulate small pressure drops in the line as well as to filter the possible pressure pulsations (Merritt, 1967).

The pipe carrying the regulated pressurized oil at system pressure is connected to the main pressure entrance of the servovalves which is located at the 4^{th} stage (Figure 9.4). From the 4^{th} stage, pressurized oil is directed to the actuator chambers through the 4^{th} stage flow ports. There is one main pressure entrance at each actuator. On LHPOST, in addition to the accumulator bank and the in-line accumulators, there are two accumulators closely coupled to each actuator pre-charged to 13.8 MPa pressure. Close-coupled accumulators are attached to the same entrance where the main pressure line is attached to the servovalves, therefore regulating the instantaneous pressure drops and filtering the pressure pulsations at the main pressure entrance. The working principle of accumulators can be stated as follows: flow demand in excess of available flow discharges the accumulator which in turn causes the accumulator pressure to drop, whereas flow demand less than the available flow charges the accumulator causing the accumulator pressure to rise.

Platen acceleration and the pressure in the West close-coupled accumulator recorded during two different tests are shown in Figure 9.15. Figure 9.15(a) shows the acceleration and pressure recordings obtained while reproducing 1994 Northridge

earthquake acceleration record at Sylmar station and Figure 9.15(b) shows the acceleration and pressure recordings during a harmonic acceleration test with a frequency of 1.0 Hz and 0.577g amplitude. In both tests, pressure inside the accumulator drops steadily below the nominal system pressure of ~21.0 MPa as the table reproduces the commanded motion. This drop in the system pressure is accompanied by high frequency pressure oscillations around steadily decreasing system pressure. Once the table comes to a rest, high frequency pressure oscillations stop and pressure inside the accumulator starts increasing to the nominal system pressure. These pressure oscillations are due to pressure switching phenomenon occurring every time actuator changes direction and they amount about 8-10% pressure variations from the average supply pressure level.

A complete mechanics-based model of the hydraulic system of LHPOST has to include mathematical models of the pumps, accumulator bank, blow-down valves and their controllers, in-line and close-coupled accumulators, as well as transient flow conditions that might exist within the hydraulic line. The most general transient flow condition within a pipe emerges when both the fluid inertia effects and the elastic effects of fluid and pipe have to be retained in order to obtain an accurate characterization of the flow (Streeter and Wylie, 1975; Larock et al., 2000). Furthermore flow regime (i.e., laminar, transitional turbulence, or turbulent regimes) in the hydraulic line has to be taken into account when formulating the transient flow conditions. In this first mechanics-based modeling effort, only a model for the hydraulic system simulating the steady drop observed at the closed-coupled

accumulators will be given. In this way, the average supply pressure drop at the 4th stages of the West and the East servovalves will be captured to a sufficient degree.

9.5.1. Modeling Average Supply Pressure Drop

In order to simulate the average supply pressure drop at the 4th stage level, adiabatic gas law will be applied to two fictitious effective accumulators attached one on each actuator. Adiabatic condition exists when there is no heat gain or loss by the system (e.g., accumulator tank). For this condition to hold, it is assumed that the gas chamber volume is not changing too quickly (i.e. no internal friction or very little exists in the gas), and there is no heat flow through the walls of the tank. Based on these assumptions, adiabatic gas law can be written

$$P_1 V_1^{\gamma} = P_2 V_2^{\gamma} \tag{9.15}$$

where P_1 and P_2 are gas chamber pressures associated with volumes V_1 and V_2, respectively, and γ is the adiabatic exponent. Note that smaller volume is associated with high pressure and larger volume is associated with smaller pressure. Figure 9.16 shows the sketch of one of the fictitious accumulators at two limit states and the supply line at the 4th stage. These states are: (i) oil within the accumulator tank reaches its maximum level, V_{max}^{oil}; and (ii) gas within the accumulator tank reaches its maximum level, $V_{max}^{gas} = V_{bottle}$, or $V_{min}^{oil} = 0.0$. In Figure 9.16, V_{bottle} is the total volume of the accumulator tank, P_s is the nominal supply pressure in the hydraulic line and P_{pre} is the pre-charged pressure of the accumulator's gas chamber. Accumulators are pre-charged up to a certain pressure with gas (e.g., nitrogen) when there is no or little

supply pressure in the hydraulic line. Therefore when supply pressure reaches to its maximum level, oil volume within the accumulator can only reach $V_{max}^{oil} = V_{bottle}\left(1-\left(\frac{P_{pre}}{P_S}\right)^{1/\gamma}\right)$ (i.e., V_{max}^{oil} is less than V_{bottle} due to the pre-charged gas).

Figure 9.17 shows the Simulink implementation of the fictitious accumulator on the West actuator. Block diagram confined with the dotted box shows the implementation of (9.15) and Q_{pump} is the constant pump flow to the West accumulator at nominal supply pressure. Notice that absolute value of the instantaneous "west actuator flow" is subtracted from the pump flow to find the flow which will either charge or discharge the accumulators. This flow is called the net flow. Net flow can be positive or negative depending on the pump capacity. By integrating the net flow, instantaneous oil volume can be found. This oil volume is set to be bounded between $V_{min}^{oil} = 0.0$ and V_{max}^{oil}. When instantaneous oil volume reaches to its minimum value, supply pressure will be equal to the pre-charge pressure P_{pre}, whereas when it reaches to its maximum value, supply pressure will be equal to the nominal system pressure P_S. At instantaneous oil volumes between these two bounds supply pressure will fluctuate between P_{pre} and P_S.

9.6. Mechanical Subsystem Model

9.6.1. Identified Mechanical Subsystem

A mathematical model for the mechanical components of LHPOST has been proposed, and its model parameters have been identified and validated using an

extensive set of experimental data in a previous work (Ozcelik et al., 2008). In Ozcelik et al. (2008), it has been shown that several non-linear terms arising from the significant displacements and rotations of the hold-down struts are small, and that a simplified model including an effective horizontal mass, an effective horizontal stiffness due to pre-charge pressure in the hold-down struts, and dissipative force terms composed of classical Coulomb friction and viscous damping elements are sufficient to simulate the response of the mechanical subsystem. This model is represented in Figure 9.18(a), where $F_{act}(t)$ = the total effective actuator force applied on the pistons of the two horizontal actuators, M_e = effective mass of the platen (including the mass of the moving parts of the horizontal actuators and a portion of the mass of the hold-down struts), K_e = total effective horizontal stiffness provided by the two hold down struts, C_e = effective viscous damping coefficient, and F_{μ_e} = effective Coulomb friction force due to various sources, and $u_x(t)$ = total horizontal displacement of the platen along the longitudinal direction ($u_x(t) = x_p(t)$ since the platen is assumed to be rigid). The equation of motion of the conceptual mechanical subsystem of LHPOST can be written as follows

$$M_e\ddot{u}_x(t) + K_e u_x(t) + \left(C_e\left|\dot{u}_x(t)\right|^{\alpha} + F_{\mu_e}\right) sign(\dot{u}_x(t)) = F_{act}(t) \tag{9.16}$$

where the exponent α is a constant. Identified model parameters (i.e., M_e, K_e, C_e, F_{μ_e}, α) are all effective in nature, as different sources are lumped into the same type of resisting force (e.g. various physical sources of viscous energy dissipation including

viscous damping due to cross-port actuator leakage contribute to the coefficient C_e of the viscous damping force model). In the next section, the mathematical model given in (9.16) will be extended to 2D in order to take into account the rigid body motion of the platen.

9.6.2. Two-dimensional Mechanical Subsystem

Figure 9.18(b) shows the 2D model of the mechanical subsystem in which the reaction block and the surrounding soil are assumed to be rigid. The mechanical components such as vertical bearings, hold-down struts are represented as linear springs and the identified dissipative mechanism is represented by dashpots and Coulomb friction elements.

Three vertical bearings are attached at points indicated as *V1*, *V2*, and *V3* are represented as springs with constants K_{vb}. Constant friction force $F_{\mu e}$ is evenly distributed to three points *V1*, *V2*, and *V3* on the platen and are represented with constant friction forces $F_{\mu e1}$, $F_{\mu e2}$, and $F_{\mu e3}$. Vertical motion of the platen generates vertical spring forces which in turn generates additional Coulomb forces on the platen. These extra friction forces will be computed using the effective Coulomb friction coefficient μ_e which is estimated in the previous work (Ozcelik et al., 2008). Viscous dissipative forces are modeled with two dashpots each with viscous damping coefficient of $C_e/2$. These dashpots are attached to the points indicated as *W* and *E*. Two vertical hold-down struts are attached to the points on the platen indicated as *H1* and *H2*. Hold-down struts exert horizontal as well as constant vertical forces on these

two points. Horizontal forces due to hold-down struts are represented by two horizontal springs each having spring coefficient $K_e/2$. Constant vertical forces are represented with $F_z^{(HD1)}$ and $F_z^{(HD2)}$. $F_{actW}(t)$ and $F_{actE}(t)$ are scalar time dependent actuator forces generated by the West and East actuators, respectively. Actuator forces are acting to the points on the platen indicated as *W* and *E*.

Dimensions of the platen as well as the locations of points of action of the actuators and the other forces described above are shown in Figure 9.18(b). Point *G* indicates the center of gravity of the equivalent prismatic platen. The equivalent prismatic platen has the same weight and width as the original platen but have different heights. Difference between the center of gravity of the original platen and the equivalent prismatic platen is about 1.0 cm. The terms e_x and h_G represent the horizontal and vertical distances between points *G* and *O*, respectively. The equation of motion of the 2D mechanical subsystem (derived with respect to the generalized coordinates at point *O*) is given by

$$\mathbf{M}_O\ddot{\mathbf{u}}_O(t) = \mathbf{F}_{act}(t) - \mathbf{F}_{spr}(t) - \mathbf{F}_{damp}(t) - \mathbf{F}_{coul}(t) \tag{9.17}$$

where $\mathbf{u}_O = \begin{bmatrix} u_{Ox} & u_{Oz} & \theta_{Oy} \end{bmatrix}^T$, $\mathbf{M}_0$ is the (3×3) mass tensor, $\mathbf{F}_{act}(t)$ is the (3×1) actuator force vector, $\mathbf{F}_{spr}(t)$ is the (3×1) force vector representing the horizontal and vertical spring forces as well as the constant hold-down forces, $\mathbf{F}_{damp}(t)$ is the (3×1) viscous dissipative force vector, and $\mathbf{F}_{coul}(t)$ is the (3×1) Coulomb friction force vector. In the following sections, details of each term in (9.17) will be given.

9.6.2.1. Mass Tensor $\mathbf{M}_O$

The mass tensor of the platen with respect to the principal axis passing through point *G* can be written as follows

$$\mathbf{M}_G = \begin{bmatrix} M_e & 0 & 0 \\ 0 & M_e & 0 \\ 0 & 0 & I_{\theta y} \end{bmatrix} \tag{9.18}$$

where $I_{\theta y}$ is the mass moment of inertia of the prismatic platen. Using the kinematic relationship between points *G* and *O*, the following relation can be written

$$\mathbf{u}_G = \mathbf{R}_{GO}\mathbf{u}_O \tag{9.19}$$

where

$$\mathbf{R}_{G0} = \begin{bmatrix} 1 & 0 & h_G \\ 0 & 1 & -e_x \\ 0 & 0 & 1 \end{bmatrix} \tag{9.20}$$

where h_G and e_x are assumed to be positive downwards and to the right of the center line of platen, respectively. The generalized mass tensor at *O* is then given by

$$\mathbf{M}_O = \mathbf{R}_{GO}^T \mathbf{M}_G \mathbf{R}_{GO} \tag{9.21}$$

9.6.2.2. Actuator Force Vector $\mathbf{F}_{act}$

The scalar actuator forces generated by the West and East actuators are represented by $F_{actW}(t)$ and $F_{actE}(t)$, respectively. The displacement vectors at points *W* and *E* in which the actuators are attached to the platen are given by

$$\mathbf{u}_i^{(A)} = \begin{pmatrix} u_{ix} \\ u_{iz} \end{pmatrix}^{(A)} \quad i = W, E \tag{9.22}$$

The vectors in (9.22) can be related to the motion at point *O* as follows

$$\begin{aligned} \mathbf{u}_W^{(A)} &= \mathbf{R}_{WO}^{(A)} \mathbf{u}_O \\ &= \begin{bmatrix} 1 & 0 & c_a \\ 0 & 1 & -(a + e_x) \end{bmatrix} \mathbf{u}_O \end{aligned} \tag{9.23}$$

and

$$\begin{aligned} \mathbf{u}_E^{(A)} &= \mathbf{R}_{EO}^{(A)} \mathbf{u}_O \\ &= \begin{bmatrix} 1 & 0 & c_a \\ 0 & 1 & (a - e_x) \end{bmatrix} \mathbf{u}_O \end{aligned} \tag{9.24}$$

The displacement vectors between the points where the actuators are attached to the rigid reaction block (i.e., RW and RE) and the points *W* and *E* on the platen can be written as follows

$$\begin{aligned} \mathbf{r}_{WA} &= \begin{bmatrix} u_{Wx}^{(A)} + l_a & u_{Wz}^{(A)} \end{bmatrix}^T \\ \mathbf{r}_{EA} &= \begin{bmatrix} -u_{Ex}^{(A)} + l_a & -u_{Ez}^{(A)} \end{bmatrix}^T \end{aligned} \tag{9.25}$$

where l_a is the length of each actuator. If we assume that the norm of the vectors in (9.25) is approximately equal to l_a, the vector actuator thus can be written in the form

$$\begin{aligned} \mathbf{F}_{actW}(t) &= \frac{F_{actW}(t)}{l_a} \mathbf{r}_{WA} \\ \mathbf{F}_{actE}(t) &= \frac{F_{actE}(t)}{l_a} \mathbf{r}_{EA} \end{aligned} \tag{9.26}$$

where $F_{actW}(t)$ and $F_{actE}(t)$ are the scalar actuator forces. Equation (9.26) can be transformed to point *O* using equations (9.23) through (9.25) as follows

$$\mathbf{F}_{act}(t) = F_{actW}(t)\mathbf{R}_{1O}^{(A)^T}\begin{bmatrix}1\\0\end{bmatrix} + \frac{F_{actW}(t)}{l_a}\mathbf{R}_{1O}^{(A)^T}\mathbf{R}_{1O}^{(A)}\mathbf{u}_O + F_{actE}(t)\mathbf{R}_{2O}^{(A)^T}\begin{bmatrix}1\\0\end{bmatrix} - \frac{F_{actE}(t)}{l_a}\mathbf{R}_{2O}^{(A)^T}\mathbf{R}_{2O}^{(A)}\mathbf{u}_O \tag{9.27}$$

Notice that the actuator force vector given in (9.27) will exert forces on the platen not only along *x* direction but also in the *z* direction. A moment along the *y* axis is also excited.

9.6.2.3. Vertical Spring Force Vector $\mathbf{F}_{spr}^{(VB)}$

The oil column within each vertical bearing acts like a spring. The oil column stiffness of a vertical bearing can be calculated as follows

$$K_{vb} = \frac{\beta_e A_{vb}}{L_{oil}} \tag{9.28}$$

where β_e is the effective bulk modulus of the oil, A_{vb} is the effective bearing area, and L_{oil} is the oil column length.

The vertical force at each vertical spring can be written as

$$F_{zi}^{(VB)} = K_{vb}u_{zi}^{(VB)}(t) \quad i = V1,\ V2,\ V3 \tag{9.29}$$

where $u_{zi}^{(VB)}(t)$ is the vertical motion of the platen at points *V1*, *V2*, and *V3* (notice that these points are fixed to the springs not to the platen). Vertical motions at these points can be related to the motion at point *O* as follows

$$u_{zi}^{(VB)} = \mathbf{R}_{iO}^{(VB)} \mathbf{u}_{Ox} \quad i = V1,\ V2,\ V3 \tag{9.30}$$

where

$$\begin{aligned} \mathbf{R}_{V1O}^{(VB)} &= \begin{bmatrix} 0 & 1 & -(a_v + e_x) - u_{Ox}(t) \end{bmatrix} \\ \mathbf{R}_{V2O}^{(VB)} &= \begin{bmatrix} 0 & 1 & -e_x + u_{Ox}(t) \end{bmatrix} \\ \mathbf{R}_{V3O}^{(VB)} &= \begin{bmatrix} 0 & 1 & (a_v - e_x) - u_{Ox}(t) \end{bmatrix} \end{aligned} \tag{9.31}$$

Using equations (9.29) and(9.30), the generalized spring force vector at *O* due to the vertical spring forces can be written as

$$\mathbf{F}_{spr}^{(VB)} = K_{vb} \left(\mathbf{R}_{V1O}^{(VB)^T} \mathbf{R}_{V1O}^{(VB)} + \mathbf{R}_{V2O}^{(VB)^T} \mathbf{R}_{V2O}^{(VB)} + \mathbf{R}_{V3O}^{(VB)^T} \mathbf{R}_{V3O}^{(VB)} \right) \mathbf{u}_O \tag{9.32}$$

9.6.2.4. Horizontal Spring Force Vector $\mathbf{F}_{spr}^{(HD)}$

The horizontal force at each horizontal spring can be written as

$$F_{xi}^{(HD)} = \frac{K_e}{2} u_{xi}^{(HD)}(t) \quad i = H1,\ \mathrm{H2} \tag{9.33}$$

where $u_{xi}^{(HD)}$ is the horizontal motion at points *H1* and *H2* where the hold-down struts are attached to the platen.

The horizontal motion at points H1 and H2 where the horizontal springs are attached to the platen can be related to the motion at point *O* as follows

$$u_{xi}^{(HD)}(t) = \mathbf{R}_{iO}^{(HD)} \mathbf{u}_{Ox} \quad i = H1,\ H2 \tag{9.34}$$

where

$$\begin{aligned} \mathbf{R}_{H1O}^{(HD)} &= \begin{pmatrix} 1 & 0 & c_h \end{pmatrix} \\ \mathbf{R}_{H2O}^{(HD)} &= \begin{pmatrix} 1 & 0 & c_h \end{pmatrix} \end{aligned} \tag{9.35}$$

Using equations (9.33) and (9.34), the generalized spring force vector at *O* due to the horizontal springs is given by

$$\mathbf{F}_{spr}^{(HD)}(t) = \frac{K_e}{2}\left(\mathbf{R}_{1O}^{(HD)^T}\mathbf{R}_{1O}^{(HD)} + \mathbf{R}_{2O}^{(HD)^T}\mathbf{R}_{2O}^{(HD)}\right)\mathbf{u}_O \tag{9.36}$$

Equation (9.36) models the portion of the hold-down force which is a function of the horizontal platen displacement. Constant vertical forces $F_z^{(HD1)}$ and $F_z^{(HD2)}$ exerted on the platen by the pre-charged hold-down struts can be transformed to point *O* as follows

$$\mathbf{F}_{const}^{(HD)} = \begin{bmatrix} 0 \\ 1 \\ -\left(a_H + e_x\right) \end{bmatrix} F_z^{(HD1)} + \begin{bmatrix} 0 \\ 1 \\ \left(a_H - e_x\right) \end{bmatrix} F_z^{(HD2)} \tag{9.37}$$

Notice that the hold-down struts are in tension.

Using equations (9.32), (9.36), and (9.37), the total force acting on the platen at point O due to vertical and horizontal springs, and the constant hold-drown vertical forces can be written as

$$\mathbf{F}_{spr}(t) = \mathbf{F}_{spr}^{(VB)}(t) + \mathbf{F}_{spr}^{(HD)}(t) + \mathbf{F}_{const}^{(HD)} \tag{9.38}$$

9.6.2.5. Viscous Damping Force $\mathbf{F}_{damp}$

The previously identified viscous dissipative force model is given by

$$F_{damp}(t) = C_e \left|\dot{u}_{xi}^{(DP)}\right|^{\alpha} sign(\dot{u}_{xO}) \quad i = W, E \tag{9.39}$$

where $\dot{u}_{xi}^{(DP)}$ is the horizontal motion at points *W* and *E* where the viscous dampers are attached on the platen. Although the identified viscous damping coefficient C_e is an effective value representing all the viscous damping sources within the system (Ozcelik et al., 2008(1), Ozcelik et al., 2008(2)), it is assumed that the main source of viscous dissipative forces is the cross-port leakage within the actuators, therefore dashpot elements are attached to the same points on the platen where the West and East actuators are attached.

Horizontal motion at points *W* and *E* can be transformed to point O as follows

$$\dot{u}_{xi}^{(DP)} = \mathbf{R}_{iO}^{(DP)} \dot{\mathbf{u}}_{Ox} \quad i = W,\ E \tag{9.40}$$

where

$$\begin{aligned} \mathbf{R}_{WO}^{(DP)} &= \begin{pmatrix} 1 & 0 & c_a \end{pmatrix} \\ \mathbf{R}_{EO}^{(DP)} &= \begin{pmatrix} 1 & 0 & c_a \end{pmatrix} \end{aligned} \tag{9.41}$$

Using equations (9.39) and (9.40), the viscous damping forces can be transformed to point O by

$$\mathbf{F}_{damp}(t) = \frac{C_e}{2}\left(\mathbf{R}_{WO}^{(DP)^T} \left| \mathbf{R}_{WO}^{(DP)} \dot{\mathbf{u}}_O \right|^{\alpha} + \mathbf{R}_{EO}^{(DP)^T} \left| \mathbf{R}_{EO}^{(DP)} \dot{\mathbf{u}}_O \right|^{\alpha} \right) sign(\dot{u}_{Ox}) \tag{9.42}$$

9.6.2.6. Coulomb Friction Force $\mathbf{F}_{coul}$

The vertical motion of the platen will generate vertical spring forces on the bearings which in turn will generate Coulomb friction forces. These forces for each bearing can be written as

$$F_{coul}(t) = \mu_e \left| F_{zi}(t) \right| sign(\dot{u}_{xO}) \quad i = V1,\ V2,\ V3 \tag{9.43}$$

where $F_{zi}(t)$ are the vertical spring forces acting on the platen at points *V1*, *V2*, and *V3* due to vertical motion of the platen. Thus forces are given in (9.29). The coefficient μ_e is the identified effective Coulomb friction coefficient (Ozcelik et al., 2008). Vertical motions at points *V1*, *V2*, and *V3* can be transformed to point *O* using (9.30) and(9.31). Coulomb fiction forces given in (9.43) are acting along x direction and can be transformed to point *O* using the following transformation vectors

$$\begin{aligned} \mathbf{R}_{V1Ox}^{(VB)} &= \begin{bmatrix} 1 & 0 & c_v \end{bmatrix} \\ \mathbf{R}_{V2Ox}^{(VB)} &= \begin{bmatrix} 1 & 0 & c_v \end{bmatrix} \\ \mathbf{R}_{V3Ox}^{(VB)} &= \begin{bmatrix} 1 & 0 & c_v \end{bmatrix} \end{aligned} \tag{9.44}$$

Using equations(9.29), (9.30), (9.31), and (9.43), the Coulomb friction forces due to the vertical motions at *V1*, *V2*, and *V3* can be transformed to point *O* as follows

$$\mathbf{F}_{coul,dyn}(t) = \mu_e K_{vb} \begin{pmatrix} \mathbf{R}_{V1Ox}^{(VB)^T} \left| \mathbf{R}_{V1O}^{(VB)} \mathbf{u}_O \right| + \mathbf{R}_{V2Ox}^{(VB)^T} \left| \mathbf{R}_{V2O}^{(VB)} \mathbf{u}_O \right| + \\ \mathbf{R}_{V3Ox}^{(VB)^T} \left| \mathbf{R}_{V3O}^{(VB)} \mathbf{u}_O \right| \end{pmatrix} sign(\dot{u}_{Ox}) \tag{9.45}$$

Equation (9.45) gives the part of the Coulomb friction forces related to vertical motion. Due to the weight of the platen and the vertical hold-down forces, a constant Coulomb friction force identified as $F_{\mu e}$ also has to be taken into account. Since only three bearings are modeled in the 2D model of the mechanical subsystem, constant Coulomb force on each vertical bearing is set to $F_{\mu e1} = F_{\mu e2} = F_{\mu e3} = F_{\mu e} / 3$. These forces can be transformed to point *O* using the following expression

$$\mathbf{F}_{coul,const} = \left\{ \begin{bmatrix} 1 \\ 0 \\ c_v \end{bmatrix} F_{\mu e1} + \begin{bmatrix} 1 \\ 0 \\ c_v \end{bmatrix} F_{\mu e2} + \begin{bmatrix} 1 \\ 0 \\ c_v \end{bmatrix} F_{\mu e3} \right\} sign\left(\dot{u}_{0x}\right) \tag{9.46}$$

Using (9.45) and(9.46), the total Coulomb forces acting on the platen at point *O* can be found

$$\mathbf{F}_{coul}(t) = \mathbf{F}_{coul,dyn}(t) + \mathbf{F}_{coul,const} \tag{9.47}$$

Figure 9.19 shows the Simulink implementation of the 2D mechanical subsystem given in(9.17). The terms $F_{actW}(t)$ and $F_{actE}(t)$ are the scalar actuator forces generated by the West and East actuators, respectively. Platen acceleration vector $\ddot{\mathbf{u}}_O$ is integrated once to obtain platen velocity vector $\dot{\mathbf{u}}_O$, the platen velocity vector is integrated one more time to obtain platen displacement vector $\mathbf{u}_O$. Platen responses along x direction are sent back to TVC to control the motion of the table.

9.7. Simulink Implementation of the Complete Shake Table

In order to perform the simulation, it is necessary to assign numerical values to the numerous model parameters introduced in the previous sections. The values used for the simulation work are given in Table 9.1. The majority of these are specific to the equipment used and were taken from the manufacturer's technical specifications. Mechanical subsystem parameters and effective bulk modulus are estimated by previous experimental work. Values assigned for the hydraulic system parameters Q_{pump}, V_{bottle}, and P_{pre} are not taken from product specifications but are chosen so that the average simulated supply pressure drop at the 4th stage of

servovalves can capture the average supply pressure drop during actual tests. Control parameters are taken directly from actual TVC settings which are used for set of bare table tests.

Figure 9.20 shows the Simulink implementation of the complete virtual model of LHPOST under bare table conditions. The virtual model of LHPOST is implemented in a modular fashion such that different versions of a table component can easily be replaced without changing the whole wiring of the virtual model. For instance, a new controller can easily be added to the model to assess the performance of the new controller without changing anything else in the model. Similarly, an improved version of the existing servovalve model can replace the current version without changing the model for the actuators.

9.7.1. Bare Table Experiments

The quality of simulations using the mechanics-based virtual model is evaluated by comparing the simulation results to those of experiments performed on the actual table. Results from four bare table tests will be used for comparison purposes: (i) harmonic input with 4.1 Hz frequency and 0.591g amplitude (Input H1); (ii) harmonic input with 4.1 Hz frequency and 3.547g amplitude (Input H2); (iii) 360 degree component of the 1994 Northridge earthquake record at Sylmar station (Input Q1); and (iv) the north-south component of 1940 Imperial Valley earthquake record at El Centro station scaled up to 300% (Input Q2). Inputs H1, Q1, and Q2 are the modified versions of the original signals by using an iterative time history matching technique called the Online Iteration in order to increase the fidelity in reproducing

these signals on the table. Input H2 is the scaled up version of the modified input H1 by a factor of six. Inputs commanded to the actual table are commanded to the simulation model of the table. More on the Online Iteration technique for input modifications can be found in Chapter 8.

The motivation of using modified inputs is that these inputs are compensated for the deficiencies of the TVC tuning and for the nonlinearities of the real system; therefore if the simulation model has the same underlying dynamics and nonlinearities as the real table, modified inputs should compensate the same deficiencies and nonlinearities of the simulation model. Comparisons of platen acceleration, velocity, displacement, actuator driving force, closed coupled accumulator pressures, and 4^{th} stage spool displacements obtained using the simulation model with those recorded during the experiments are presented in the following section. It should be noted here that TVC control gains on the virtual model are the same as those used on the real system (Table 9.1).

9.7.2. Test-Simulation Correlations

9.7.2.1. Harmonic Tests

Figure 9.21(a) shows a comparison of the simulated platen acceleration, velocity, and displacements with the corresponding experimental quantities when the command is Input H1. Actual platen responses match very well with the simulation results. The top figure in Figure 9.21(a) also shows the desired acceleration signal. The delay between the desired and the actual feedback is captured by the simulation model. Figure 9.21(b) shows the recorded and simulated 4^{th} stage spool displacements

of four servovalves. Simulation and the actual recorded spool displacements match very well. Figure 9.22(a) shows the comparison of recorded and simulated actuator driving forces. The match between these quantities is also excellent. Figure 9.22(b) shows the comparisons of the recorded pressure in the West and East close-coupled accumulators and the simulated supply pressures at the 4^{th} stages of the West and East servovalves. It is clear that the simulation model captures the average of the pressure fluctuations in the real system with in a reasonable degree. Note that the high frequency oscillations seen in the real pressure recordings do not have any effect on the platen responses.

Figure 9.23 and Figure 9.24 show the comparison of recorded and simulated table responses when the command to the actual table and the simulation model is Input H2. All the recorded and simulated responses match very well except for the pressures at the 4^{th} stages of the servovalves. Note that the high pressure oscillations and overshooting of the nominal system pressure (~21.0 MPa) have no effect on the platen responses. The key finding is that the distortions seen in the actual platen acceleration response are captured by the simulation model indicating that the virtual model is capable of simulating the existing nonlinearities in the actual table.

9.7.2.2. Earthquake Tests

Figure 9.25(a) shows the comparison of the simulated platen acceleration, velocity, and displacement with those experimentally recorded when the command to the virtual model and the actual table is Input Q1. Actual platen acceleration, velocity, and displacement responses are captured very well by the simulation model. Figure

9.25(b) shows the recorded and simulated 4th stage spool displacements of the four servovalves. The simulation and actual recorded spool displacements match perfectly. Figure 9.26(a) shows the comparison of recorded and simulated actuator driving forces. The match between the two signals is very good. Figure 9.26(b) shows the comparisons of the recorded pressures in the West and East close-coupled accumulators and the simulated pressures at the 4th stages of the West and East servovalves. The simulation model is able to capture the average pressure drop observed during the test. Notice that the amplitude of pressure oscillations increase at instants where high flow is required to reproduce high amplitude motions.

Figure 9.27 shows the power spectrum estimations of the actual feedback (i.e., recorded feedback) and the simulated feedback accelerations. Comparison of the power spectra of the feedback signals show that the frequency content of the actual and simulated feedback acceleration signals match well. Discrepancies are observed mainly at frequencies higher than ~3.0 Hz, and mainly around the oil-column frequency of the system at ~11.0 Hz. In general, the simulation model overshoots slightly the frequencies above 3.0 Hz.

Figure 9.28 and Figure 9.29 show the comparison of recorded and simulated table responses when the command is Input Q2. All the recorded and simulated responses match very well including the average pressure drops at the 4th stages of the servovalves (except the high pressure oscillations which seem to have no effect on the platen responses).

9.7.2.3. Simulations with Linear Vs. Nonlinear Servovalve Models

Based on the test-simulation correlation study presented above, it can be said that the current simulation model is able to capture the main dynamics and nonlinearities of the actual table under harmonic and earthquake inputs. Harmonic inputs are especially useful in pointing out some of the sources of signal distortions observed in the system. Since they contain only one frequency, any multiple of the fundamental frequency observed in the reproduced signal will be due to a source of nonlinearity. For instance, distortions in the acceleration feedback shown in Figure 9.23(a) are due to the odd harmonics of the fundamental frequency.

Since the virtual model is mechanics-based, it is possible to determine the mechanical sources of signal distortions. One such simulation result is presented in Figure 9.30 where two harmonic inputs with the same frequency (4.1 Hz) but two different amplitudes (0.591g and 3.547g) are commanded to the virtual model of the table. Figure 9.30(a) and Figure 9.30(b) show the cases where the amplitudes of the harmonics are 0.591g and 3.547g, respectively. Two different simulations are performed: (i) table with linear servovalve model; and (ii) table with nonlinear servovalve model. In the linear servovalve model, flow into the actuator chambers is computed by multiplying the 4^{th} stage spool displacements by the flow-gain constant. The models for the other parts of the shake table are kept exactly the same.

In the simulations with linear servovalves, distortions seen in the harmonic signal reproduction disappears, whereas the distortions are clearly visible in the simulation results with nonlinear servovalves. Therefore, it can be said that the

mechanical source of this distortion is the nonlinearities in the servovalve model (i.e., the pressure drop-flow and the flow gain nonlinearities). It was found that the odd harmonics of the fundamental frequency cause this distortion in the feedback signal.

Figure 9.31(a) and (b) show the comparison of experimental results from a harmonic test with 1.0 Hz frequency and 0.769g amplitude (unmodified) with those obtained using the virtual model with two different servovalve models: (i) linear servovalve; and (ii) nonlinear servovalve models. Figure 9.31(a) shows the simulation results obtained using the linear servovalve model. It is clear that with linear servovalves, the simulation model is not able to capture the distortions seen in the actual acceleration and velocity feedback signals whereas the simulation model with nonlinear servovalves captures the distortions seen in the actual feedback signals with a reasonable accuracy as shown in Figure 9.31(b).

9.8. Conclusions

A mechanics-based virtual model for the NEES-UCSD shake table has been presented. The virtual model includes: (i) a virtual replica of the controller; (ii) four servovalve models including servovalve spool dynamics and two independent servovalve flow nonlinearities; (iii) two single-ended actuators with variable internal volumes; (iv) two accumulators modelling the average supply pressure drop at the 4^{th} stages of the servovalves; and (v) two-dimensional mechanical subsystem model based on a previously identified one-dimensional mechanical subsystem model. Based on the results of extensive forced vibration test of the foundation block, the soil-foundation compliance effects are not included in the virtual model.

The virtual shake table model is able to replicate the actual platen responses under narrow and broadband inputs with the same TVC gain settings as those on the actual system. Moreover, 4^{th} stage spool displacements and actuator driving force from the actual tests are reproduced accurately with the simulation model. Pressure drops and oscillations observed during the actual tests at the 4^{th} stages of the servovalves are captured well in the average sense with the fictitious accumulator model. It is observed that the nonlinearities in servovalves are the main source of signal distortion in servo-hydraulic shake table systems. The virtual shake table model with a linear servovalve is not capable of capturing the distortions seen in the actual feedback signals. Both the pressure drop - flow nonlinearity (square-root nonlinearity) and the flow gain nonlinearity need to be incorporated in the servovalve model in order to match the actual responses of the table with the simulated ones. The virtual model developed in this study can be used for offline tuning purposes. Based on the test-simulation correlation studies, it is observed that the simulation results are sensitive to flow gain nonlinearity therefore experimental determination of these curves for each orifice on four servovalves are deemed necessary for using the simulation model developed here safely for offline tuning purposes.

LIST OF TABLES

Table 9.1: Parameter values used for the virtual model.

Parameter	Value
Controller	
Displacement feedforward gain k_{PF}	0.0 V/V
Velocity feedforward gain k_{VF}	0.382 V/V
Acceleration feedforward gain k_{AF}	0.45 V/V
Jerk feedforward gain k_{JF}	0.00469 V/V
Proportional gain k_P	1.50 V/V
Velocity feedback gain k_V	0.0 V/V
Acceleration feedback gain k_A	0.0 V/V
Dynamic force gain k_{DP}	-0.145 V/V
Dynamic force frequency ω_{DP}	0.50 V/V
Master gain k_M	1.0 V/V
Notch center frequency f_0	11.3 Hz
Notch bandwidth bw	15.0 Hz
Notch depth $depth$	-0.90 V/V
Servovalves	
Port width 1 w_1	203.2 mm
Port width 2 w_2	130.05 mm
Port width 3 w_3	254.0 mm
Port width 4 w_4	152.4 mm
4th stage maximum spool displacement x_{sv}^{max}	19.05 mm
Rated flow port 1 Q_{rated}^{w1}	8176 lt/min
Rated flow port 2 Q_{rated}^{w2}	5233 lt/min
Rated flow port 1 Q_{rated}^{w3}	10220 lt/min
Rated flow port 1 Q_{rated}^{w4}	6540 lt/min
Maximum drive voltage V_{max}	10 Volts
Actuators	
Maximum piston displacement x_p^{max}	0.75 m
Internal volume of chamber 1 V_{10}	0.152 m^3
Internal volume of chamber 2 V_{20}	0.097 m^3
Piston cross-sectional area A_1	0.2027 m^2
Piston cross-sectional area A_2	0.1297 m^2

Table 9.1 (Contd.): Parameter values used for the virtual model.

Parameter	Value
Hydraulic Supply System	
Nominal supply pressure P_S	21.0 MPa
Return pressure P_R	0.35 MPa
Effective pump flow to each actuators Q_{pump}	2274 lt/min
West and East fictitious accumulator bottle volume V_{bottle}	$0.7571 m^3$
Accumulators' pre-charge pressure P_{pre}	19.8 MPa
Adiabatic gas constant γ	1.8
Effective bulk modulus β_e	0.82 Gpa
Mechanical Subsystem	
Effective platen mass M_e	144,000 kg
Effective horizontal stiffness K_e	1.266 MN/m
Effective viscous damping C_e	$44.6 kN(s/m)^{0.5}$
Effective Coulomb friction coefficient μ_e	0.39%
Dissipative force constant α	0.5
Effective Coulomb friction forces on each bearing $F_{\mu ei}$	8.9 kN
Constant vertical hold-down force $F_z^{(HD1)}$, $F_z^{(HD2)}$	2085 kN
Vertical bearings' oil column length L_{vb}	12.7 mm
Vertical bearings' effective bearing areas $2 \times A_{vb}$	$2 \times 0.519 m^2$
Vertical bearings' spring constant K_{vb}	67.02 GPa
Platen Dimensions	
h_G	0.87 m
e_x	0.0 m
a	6.13 m
a_v	4.88 m
a_h	4.92 m
c_a	1.27 m
c_v	1.21 m
c_h	2.21 m
l_a	6.15 m

LIST OF FIGURES

(a)

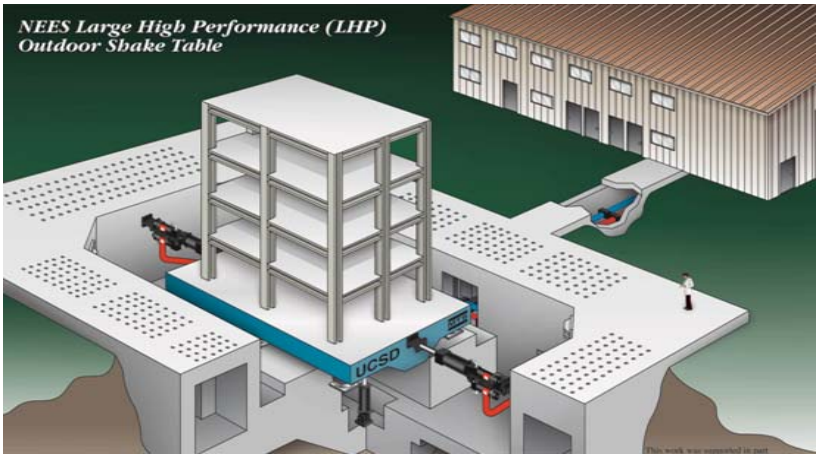

(b)

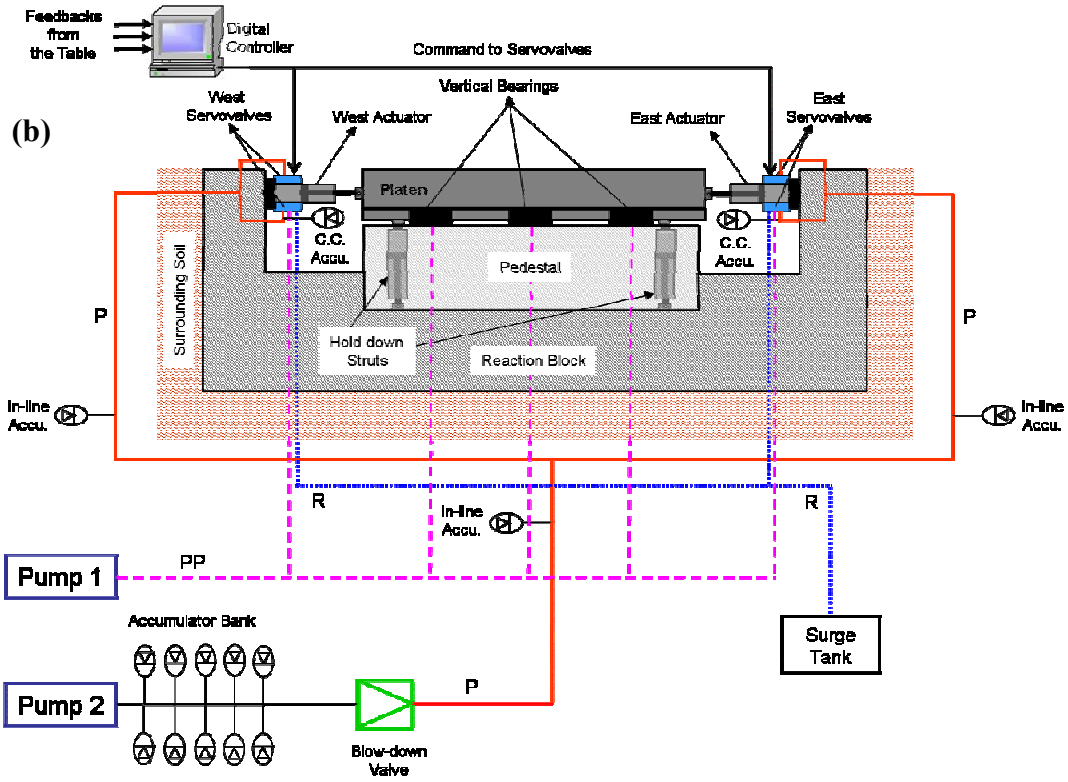

Figure 9.1: (a) 3D rendering of the NEES-UCSD shake table; (b) schematics of the overall hydraulic, mechanical, and electronic components.

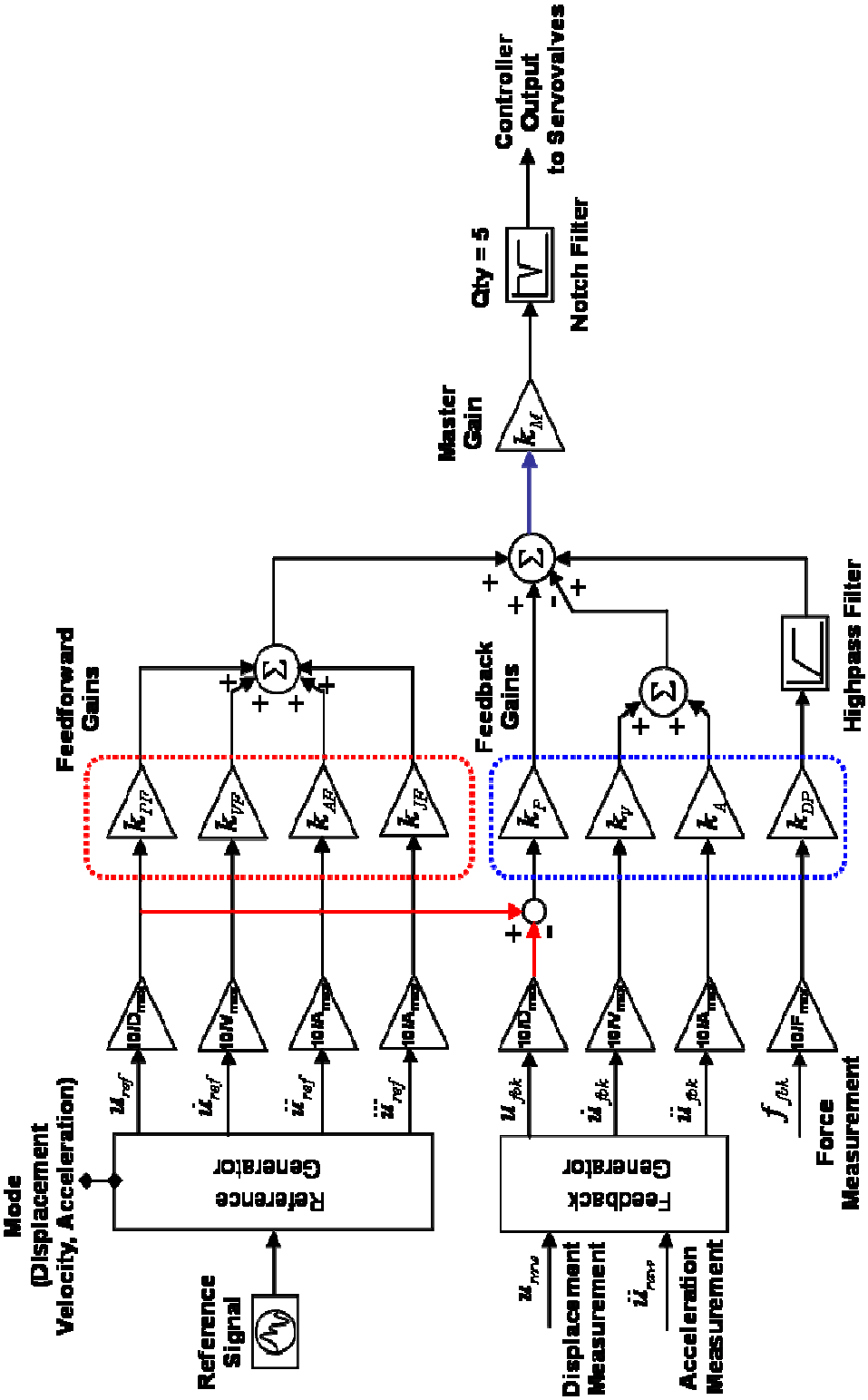

Figure 9.2: Block diagram representation of Three-Variable-Controller with

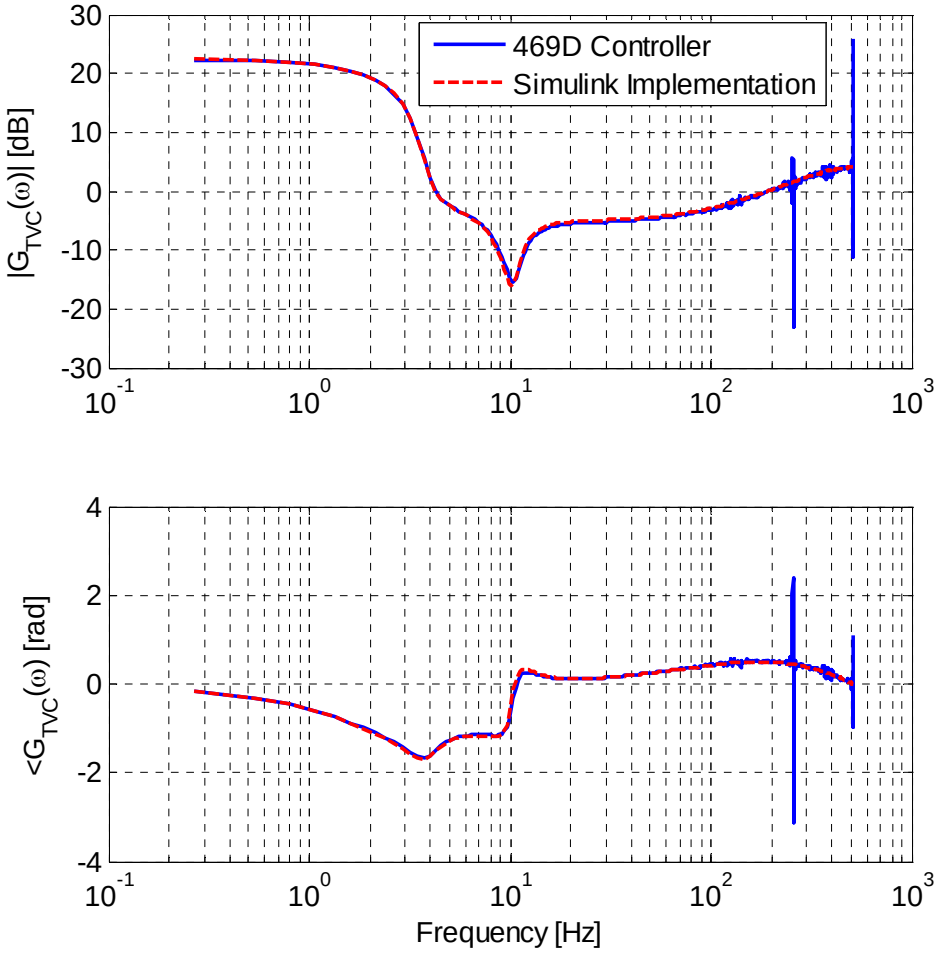

Figure 9.3: Bode plot comparison of the transfer functions of the real-time TVC and its Simulink implementation.

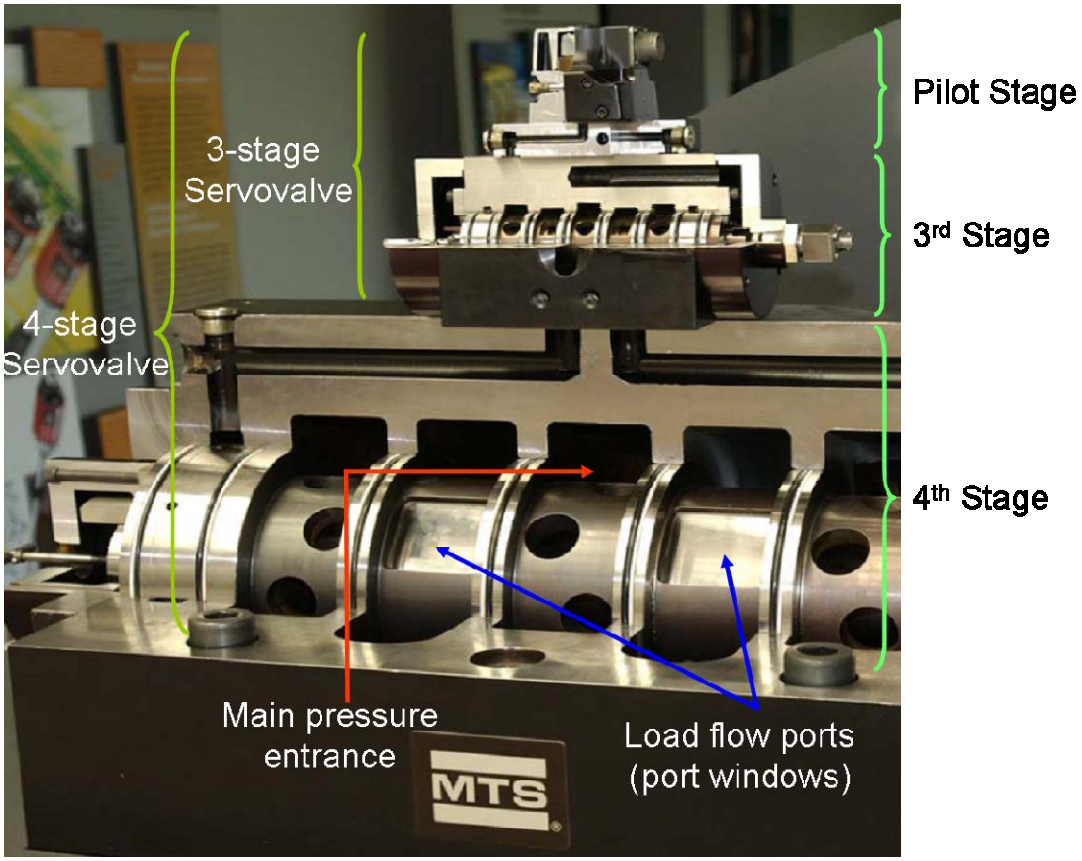

Figure 9.4: Four-stage valves similar to the ones used on LHPOST (Courtesy of MTS Systems Corporations, MN, USA).

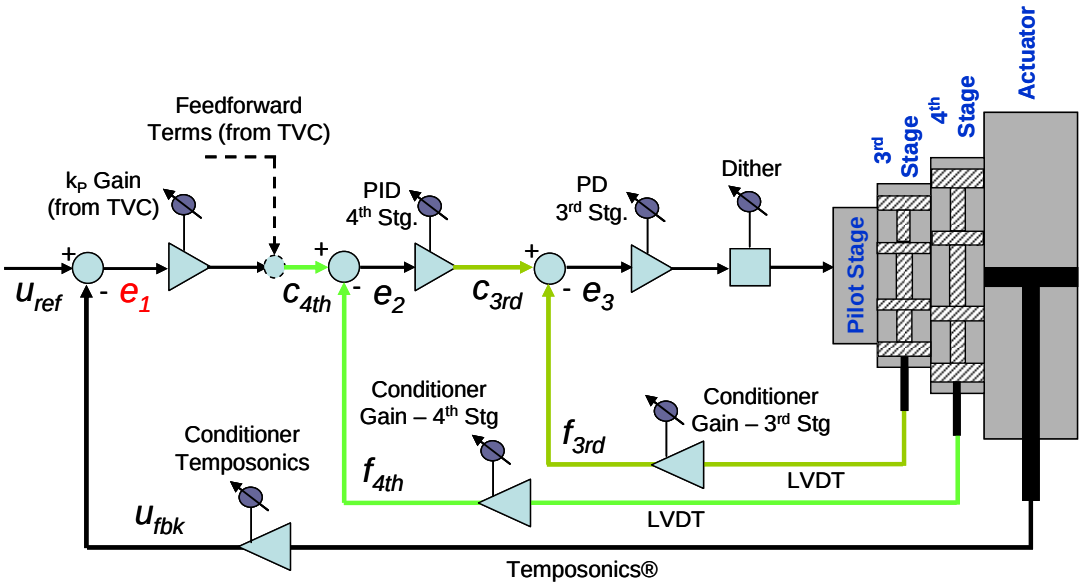

Figure 9.5: Schematics of the inner and outer control loops of LHPOST servovalve and actuator.

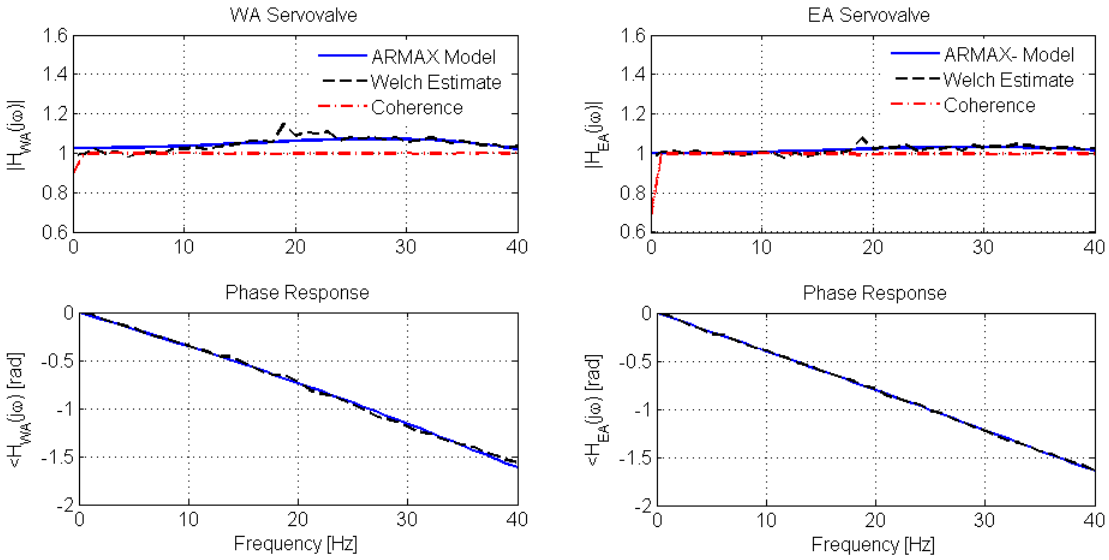

Figure 9.6: Bode plot comparisons of the ARMAX models and non-parametric transfer functions for the 4th stage spool dynamics estimated using a WN input (during the tests main hydraulics was off).

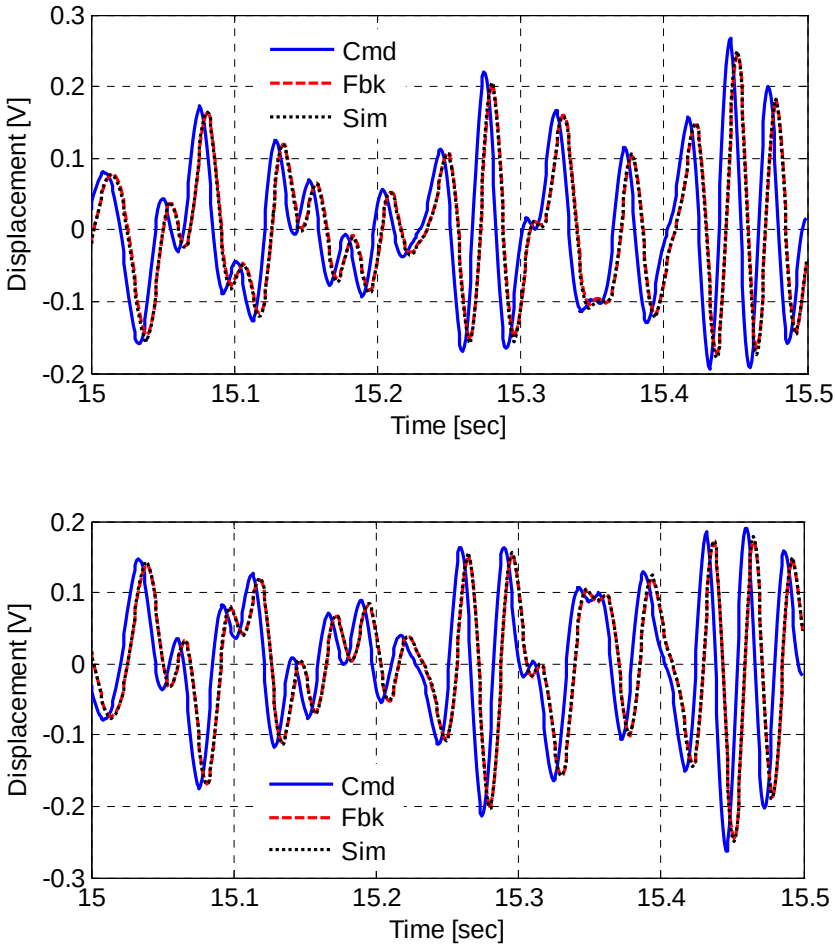

Figure 9.7: Time history comparison between simulated feedback displacement using the estimated parametric models and the recorded feedback displacement from a WN input (during the tests main hydraulics was off).

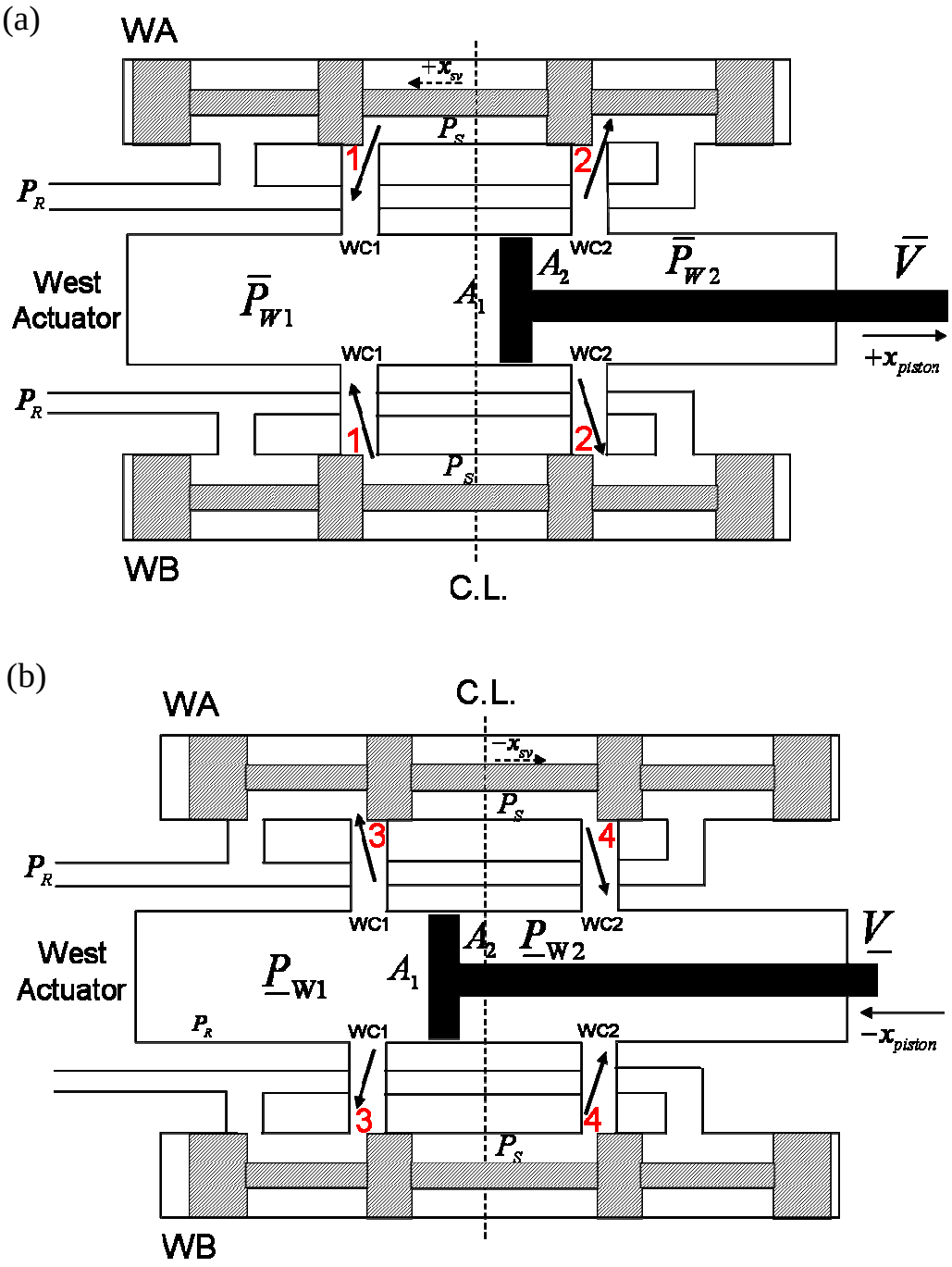

Figure 9.8: Sketch of the 4th stages of the WA and WB servovalves on the West single ended actuator: (a) extent direction; (b) retract direction. Also shown load-flow orifices 1-2 and 3-4 associated with extent and retract directions, respectively.

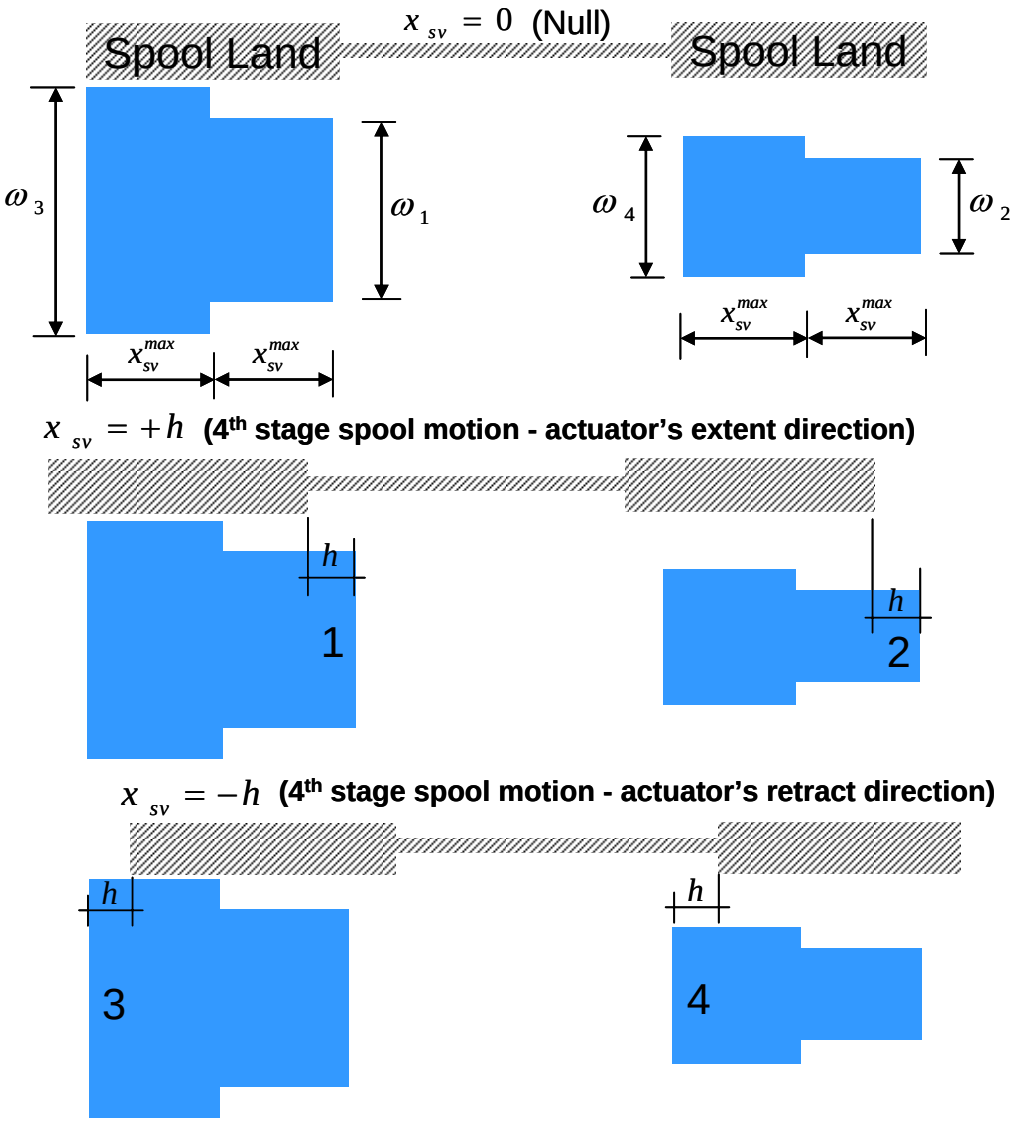

Figure 9.9: Port windows for one of the servovalves of LHPOST and active port areas (1, 2, 3, and 4) with associated 4th stage spool motions.

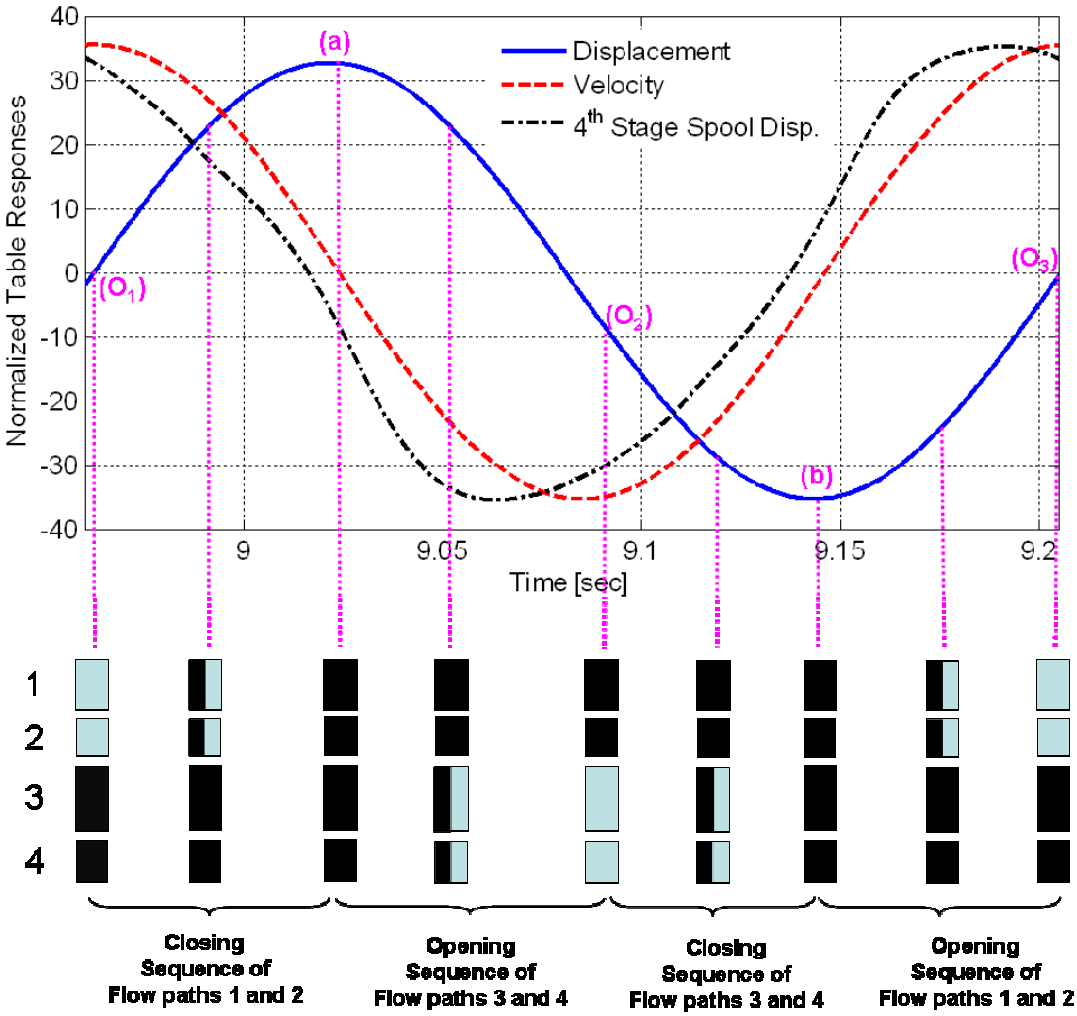

Figure 9.10: Normalized table responses from a harmonic test with 4.1 Hz frequency and 2.364g amplitude and 4th stage servovalve spool opening-closing sequence and corresponding flow paths.

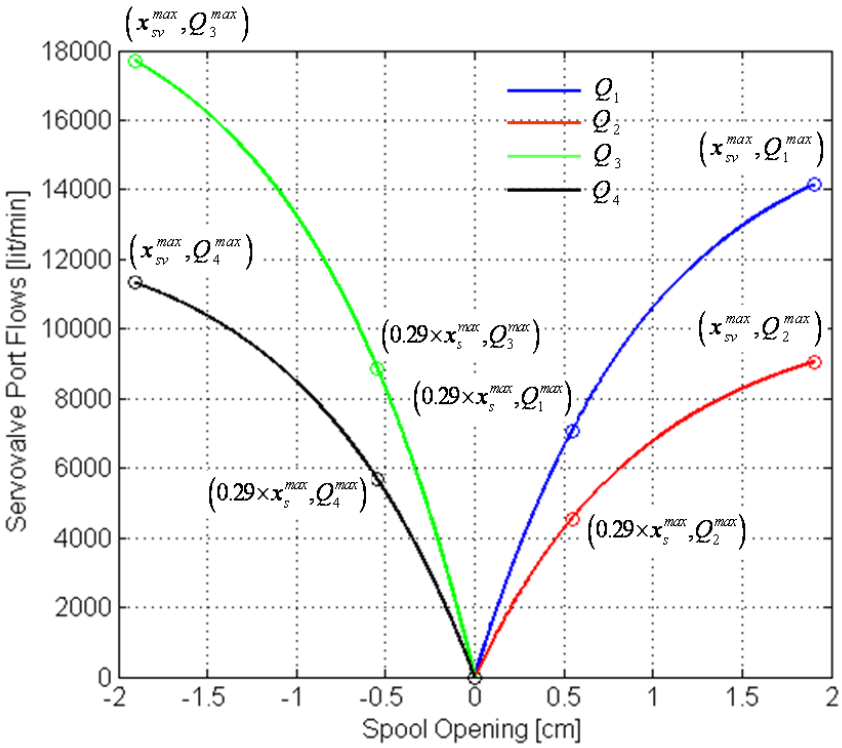

Figure 9.11: Servovalve's nonlinear flow curves used to model the nonlinear relation between flow vs. spool opening. This model is used for all four servovalves on the system.

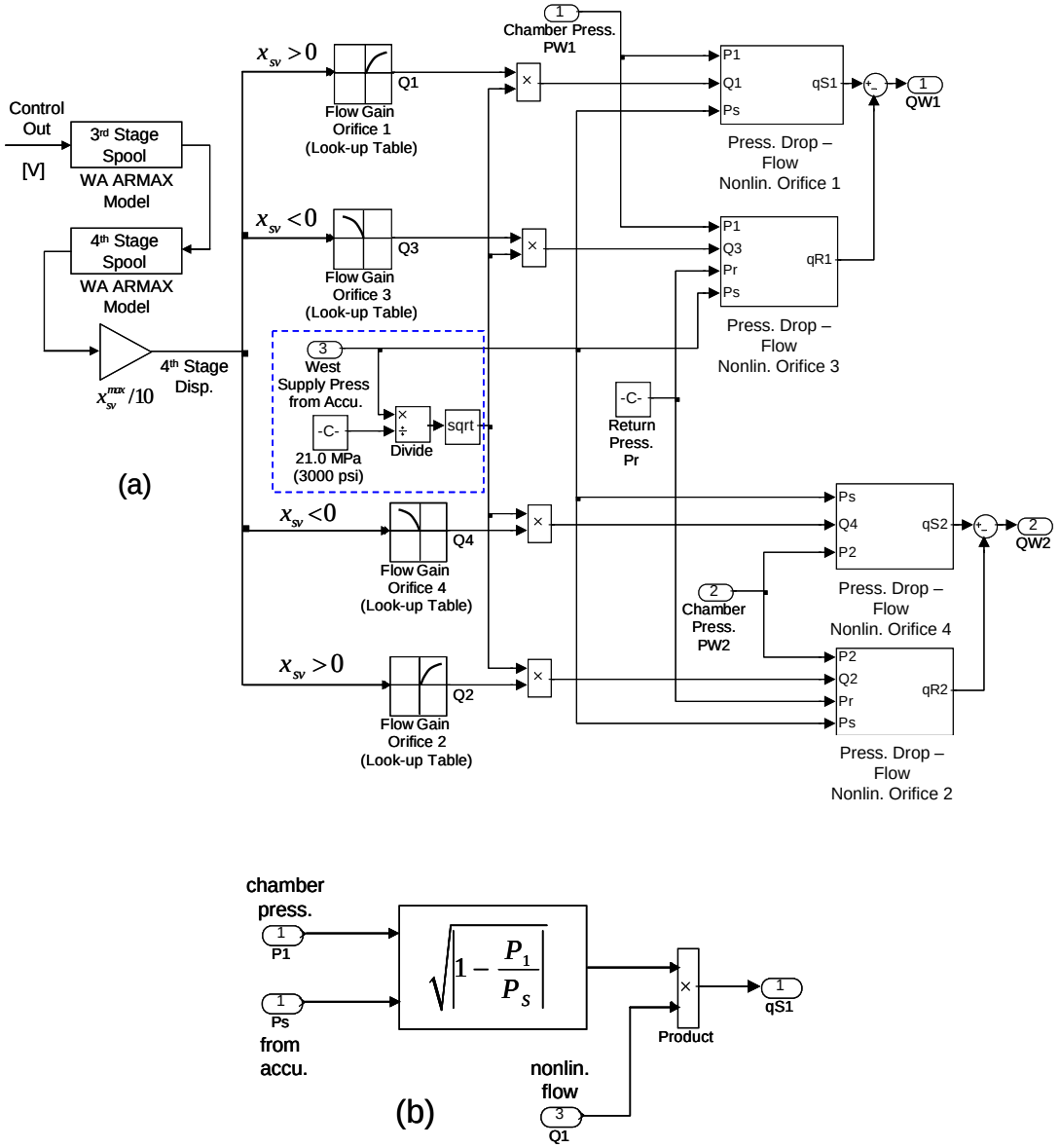

Figure 9.12: (a) Simulink model of the WA servovalve; (b) implementation details of Pressure Drop – Flow Nonlinearity Orifice 1 block.

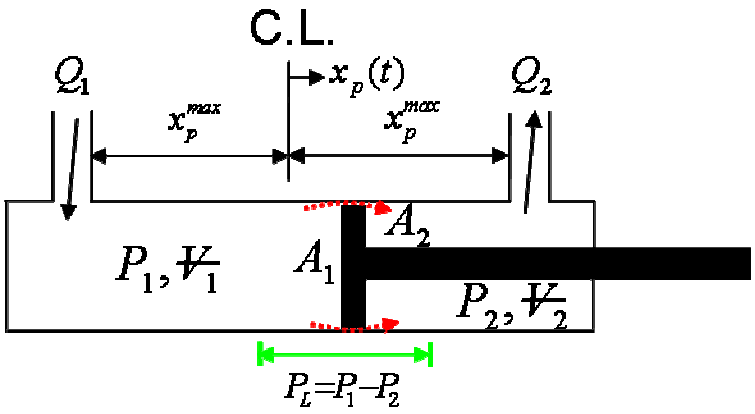

Figure 9.13: Sketch of a snapshot of a single-ended actuator.

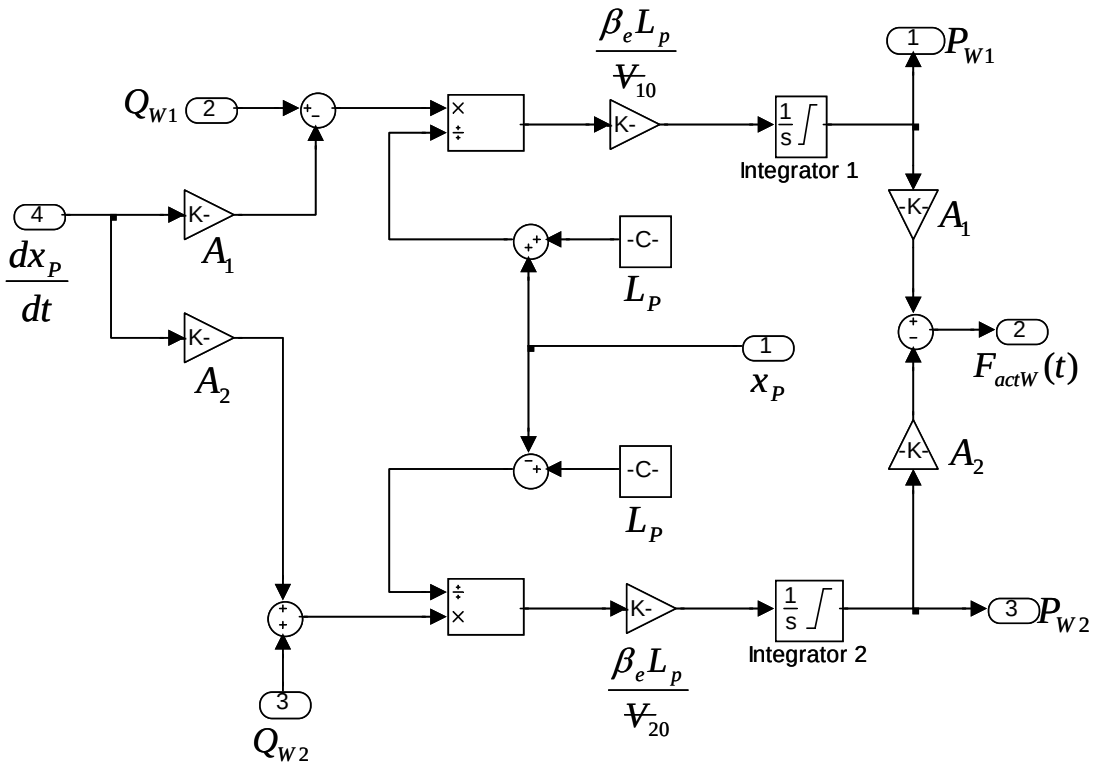

Figure 9.14: Simulink model of the West single-ended actuator.

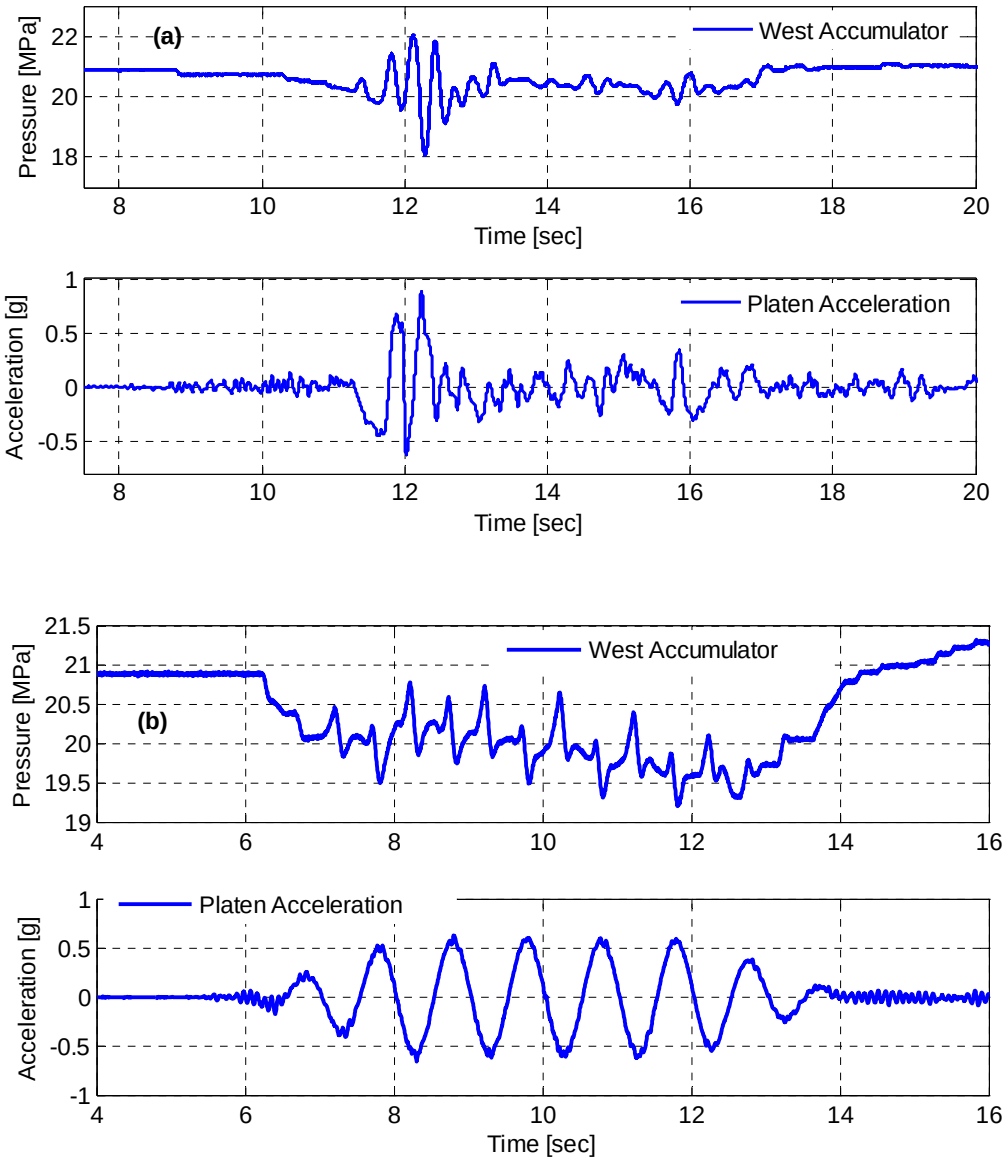

Figure 9.15: Platen accelerations and pressure recordings from the accumulator on the West actuator: (a) Sylmar earthquake test; (b) harmonic test with 1.0 Hz frequency and 0.577g amplitude.

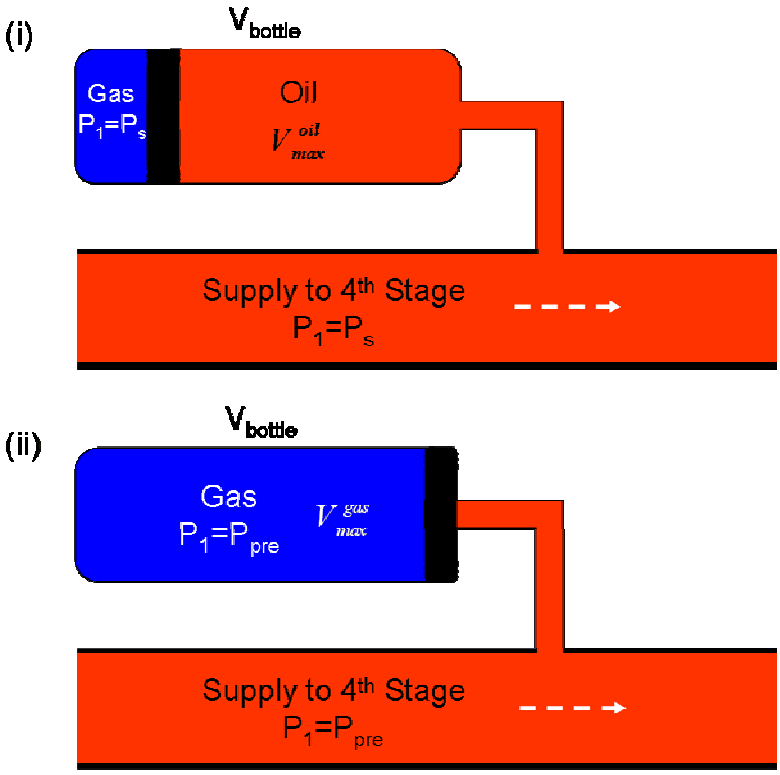

Figure 9.16: Sketch of a fictitious accumulator at two limit states: oil volume reaches to (i) its maximum level and (ii) its minimum level inside the accumulator tank.

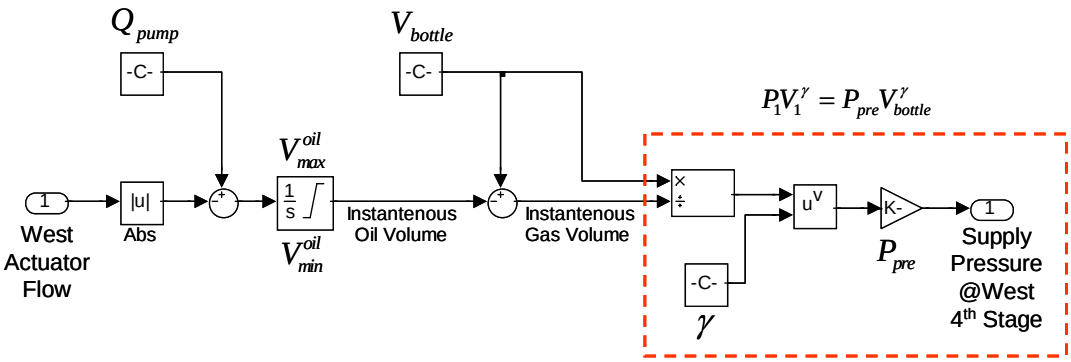

Figure 9.17: Simulink implementation of the fictitious accumulator model on the West actuator.

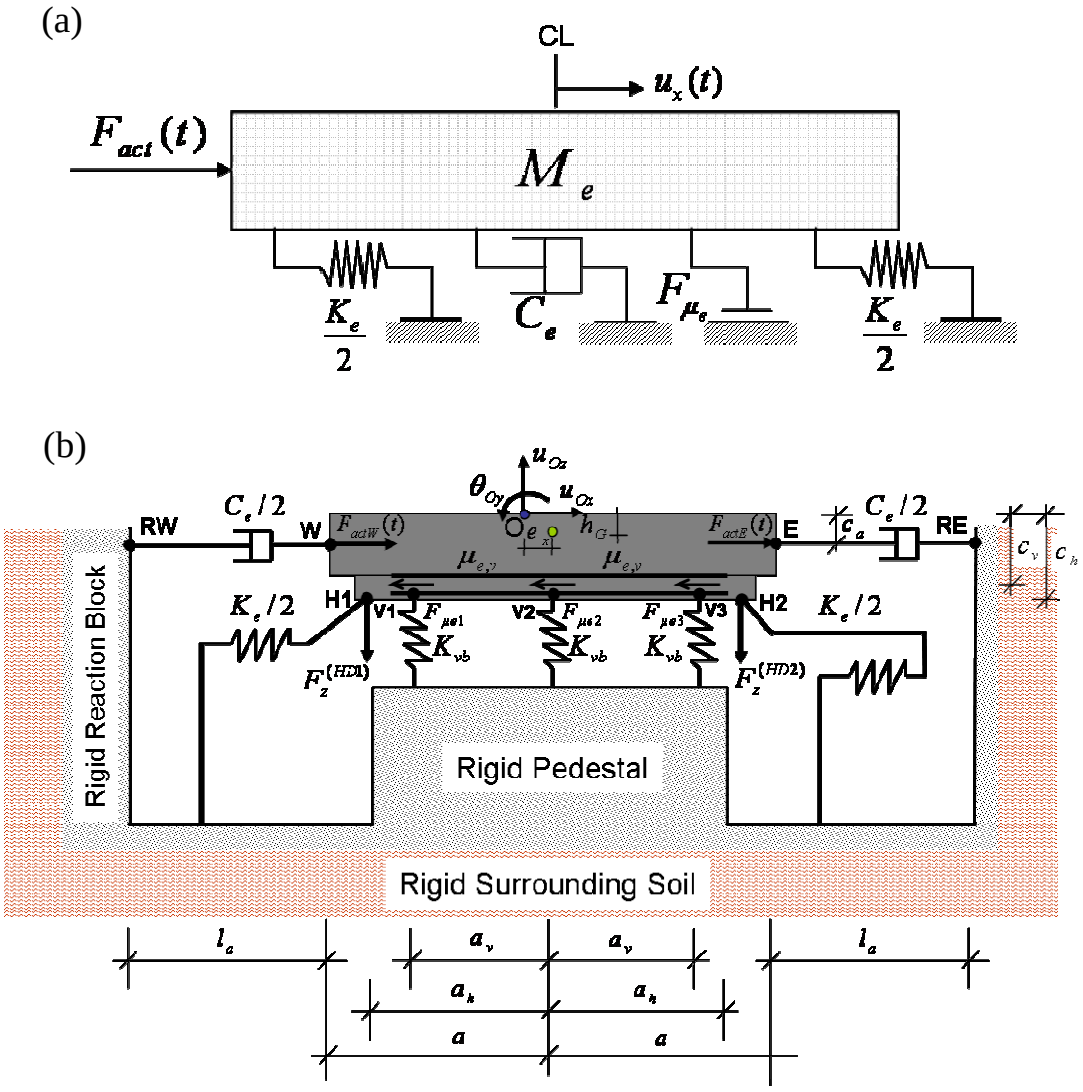

Figure 9.18: (a) Previously identified conceptual mechanical subsystem; (b) 2D mechanical subsystem with rigid reaction block and surrounding soil.

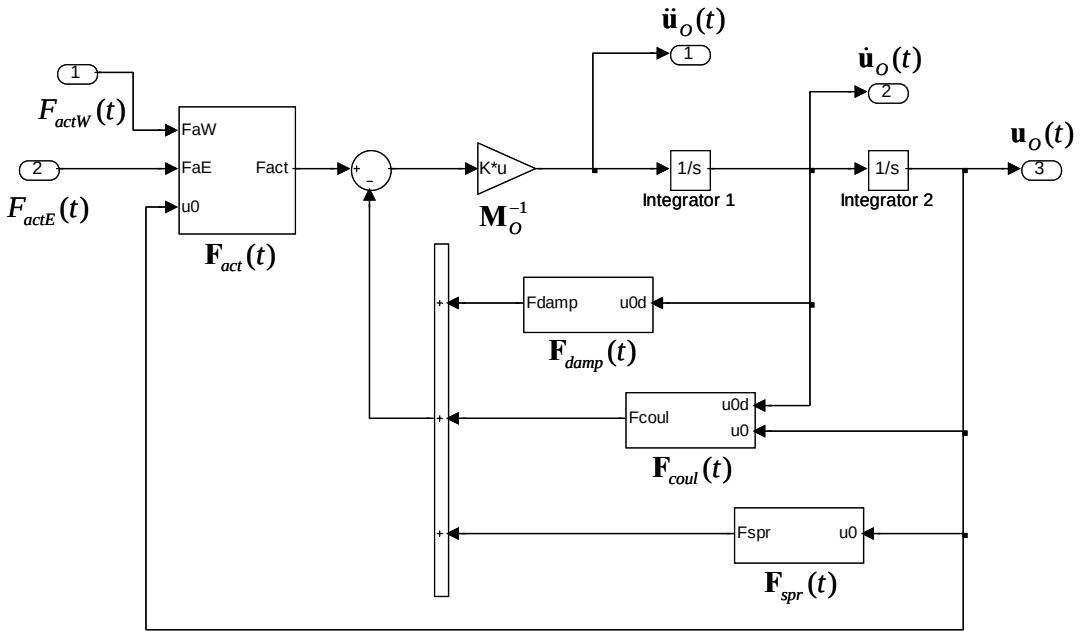

Figure 9.19: Simulink implementation of the 2D mechanical subsystem of LHPOST.

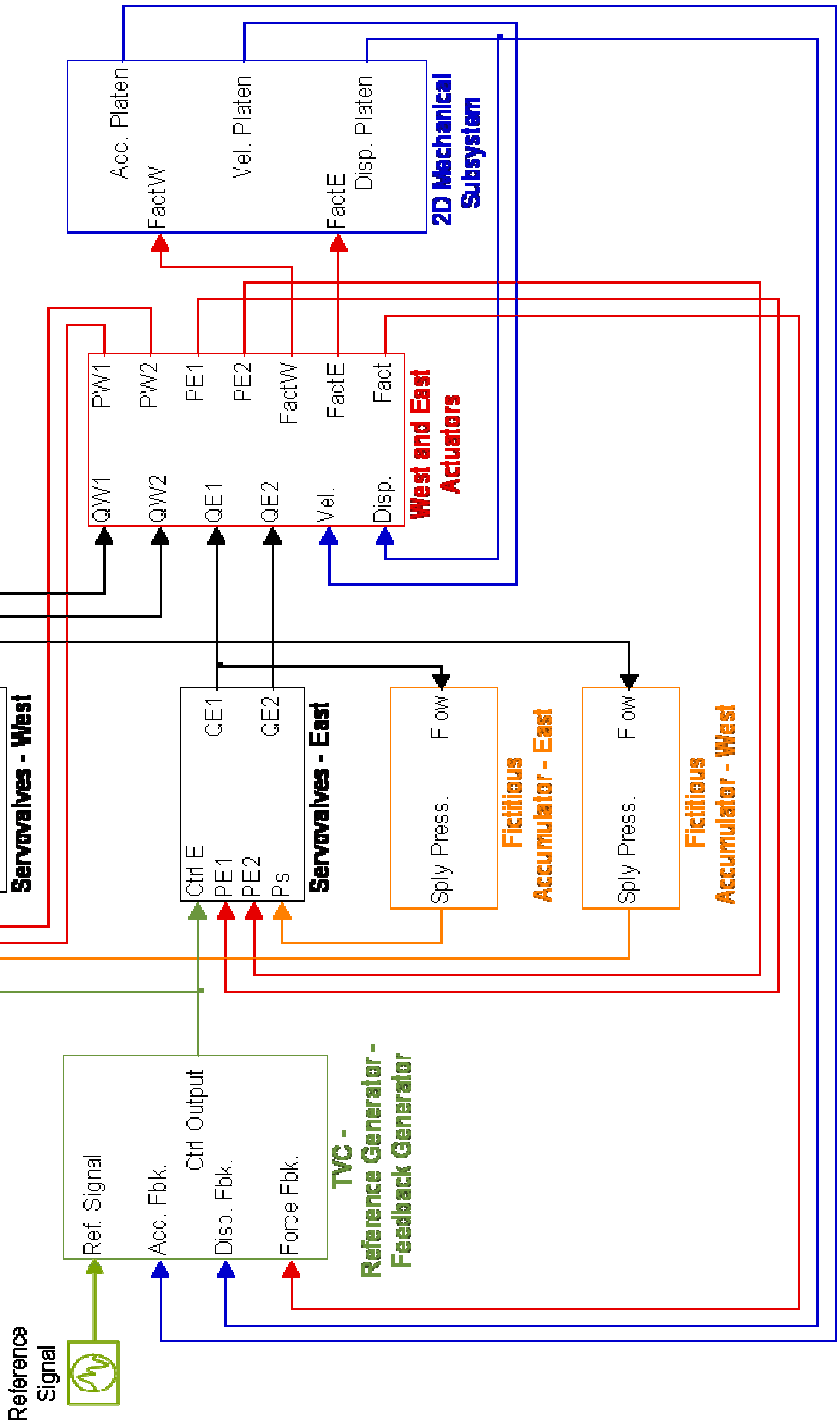

Figure 9.20: Simulink implementation of the complete virtual model of LHPOST under bare table conditions.

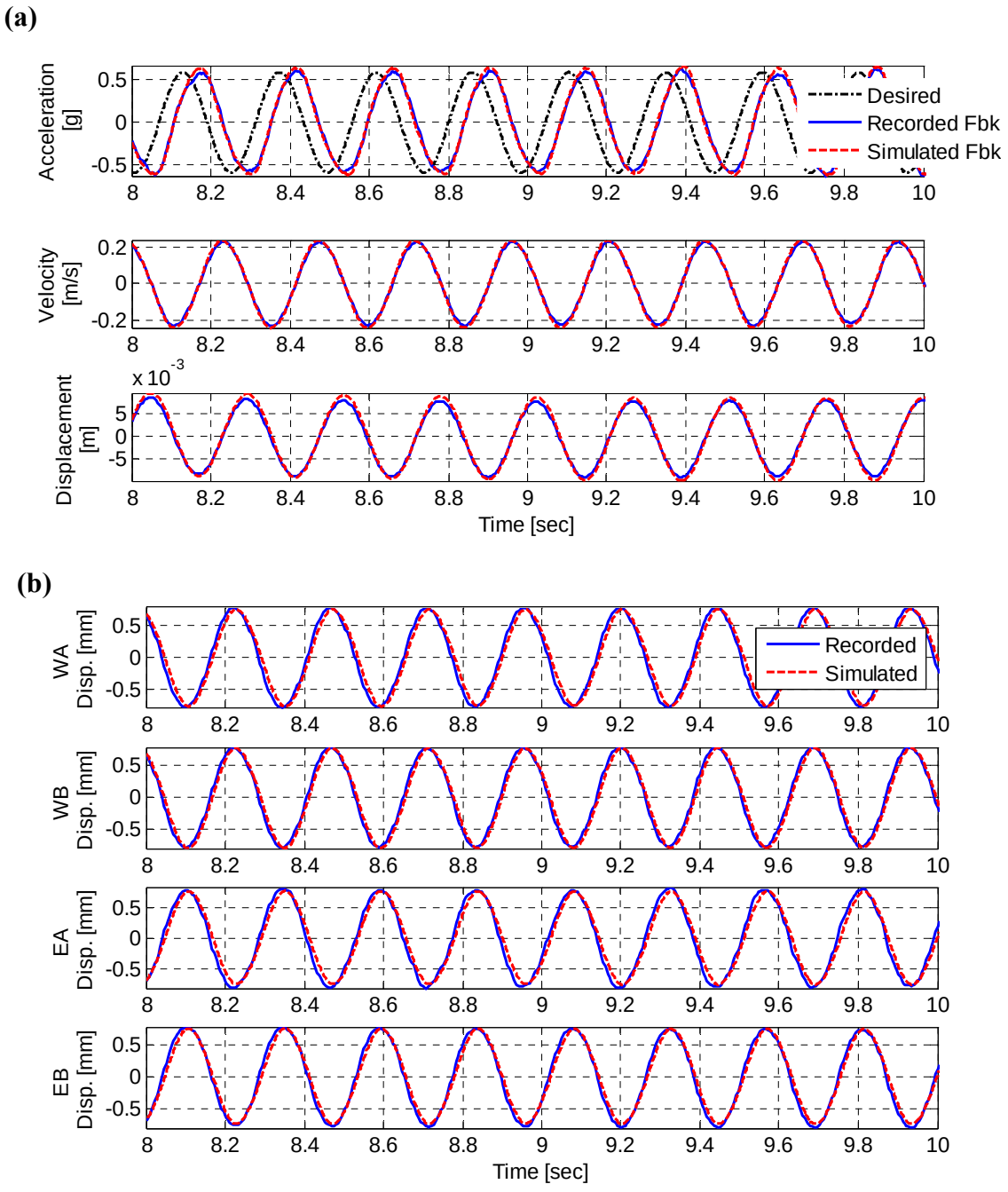

Figure 9.21: 4.1 Hz harmonic with 0.591g amplitude: comparisons of simulated and recorded (a) platen acceleration, velocity, and displacement; and (b) 4th stage spool displacements.

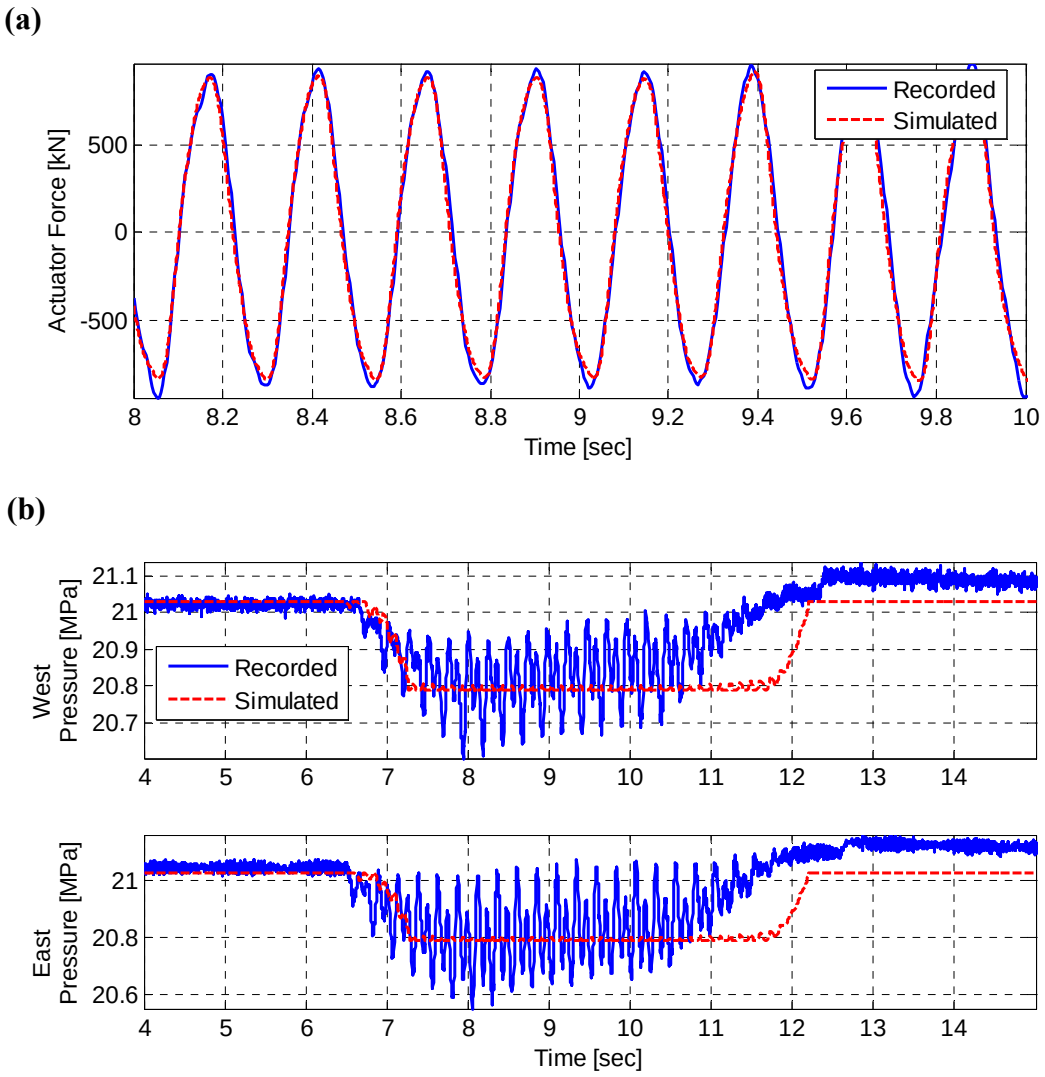

Figure 9.22: 4.1 Hz harmonic with 0.591g amplitude: comparisons of simulated and recorded (a) actuator driving force; and (b) closed coupled accumulator pressures.

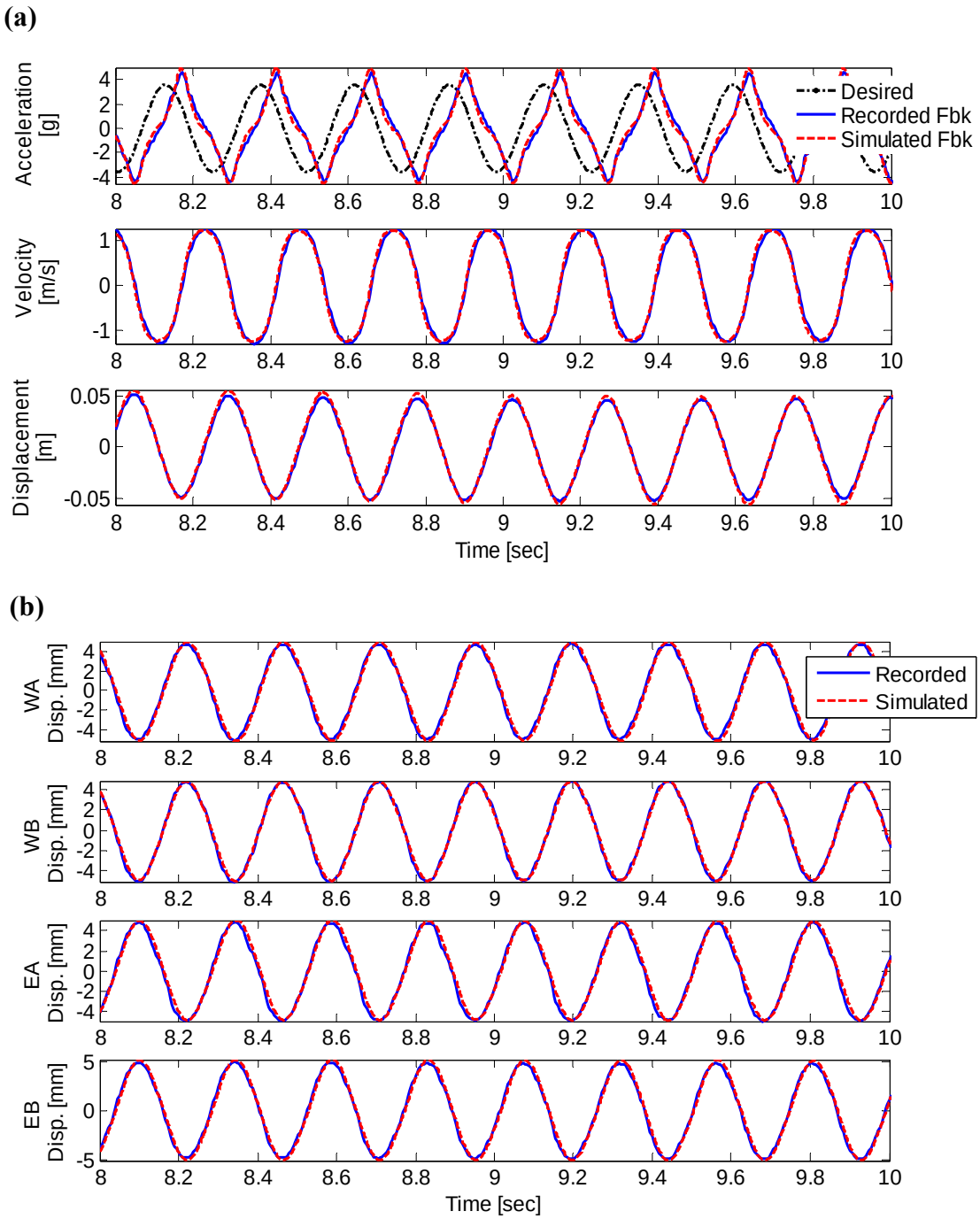

Figure 9.23: 4.1 Hz harmonic with 3.547g amplitude: comparisons of simulated and recorded (a) platen acceleration, velocity, and displacement; and (b) 4th stage spool displacements.

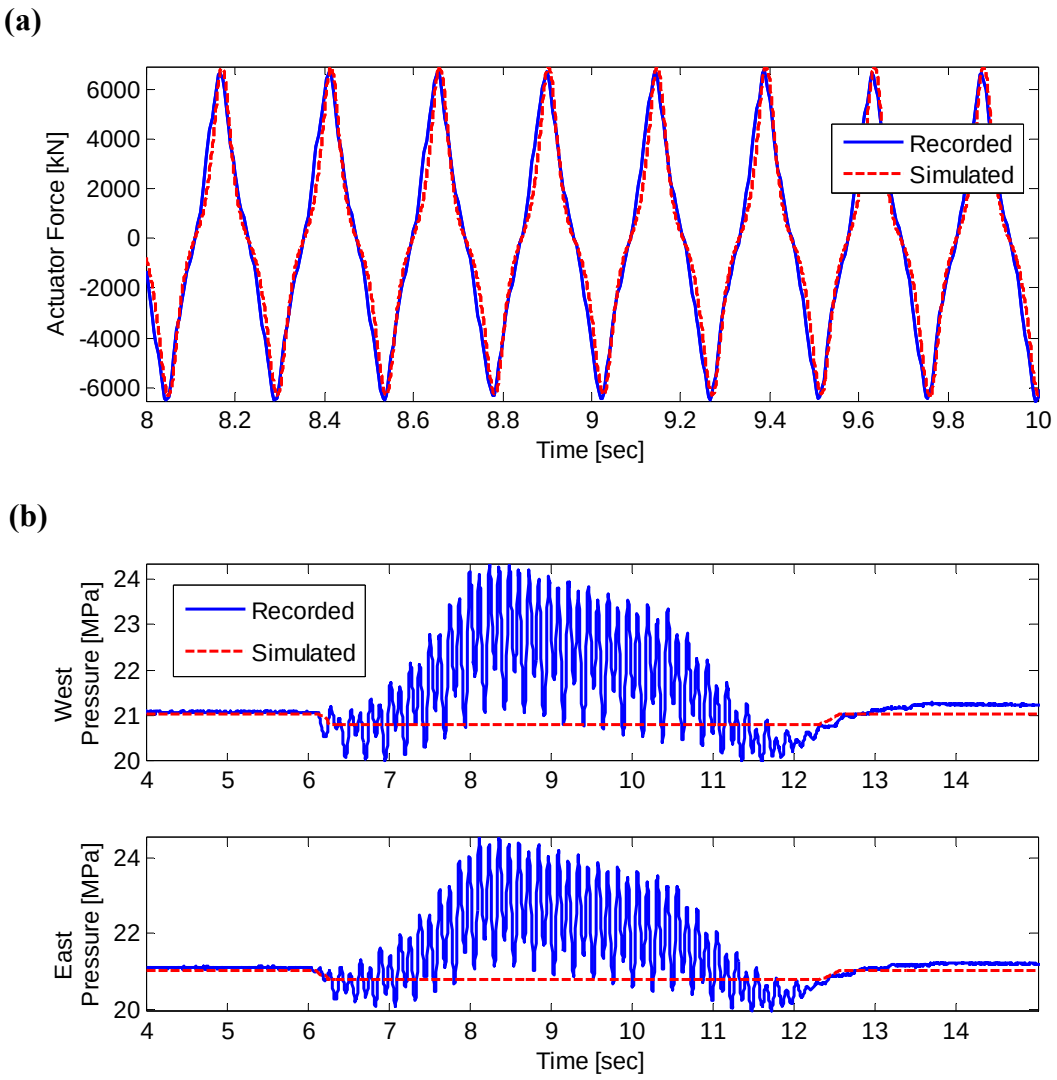

Figure 9.24: 4.1 Hz harmonic with 3.547g amplitude: comparisons of simulated and recorded (a) actuator driving force; and (b) closed coupled accumulator pressures.

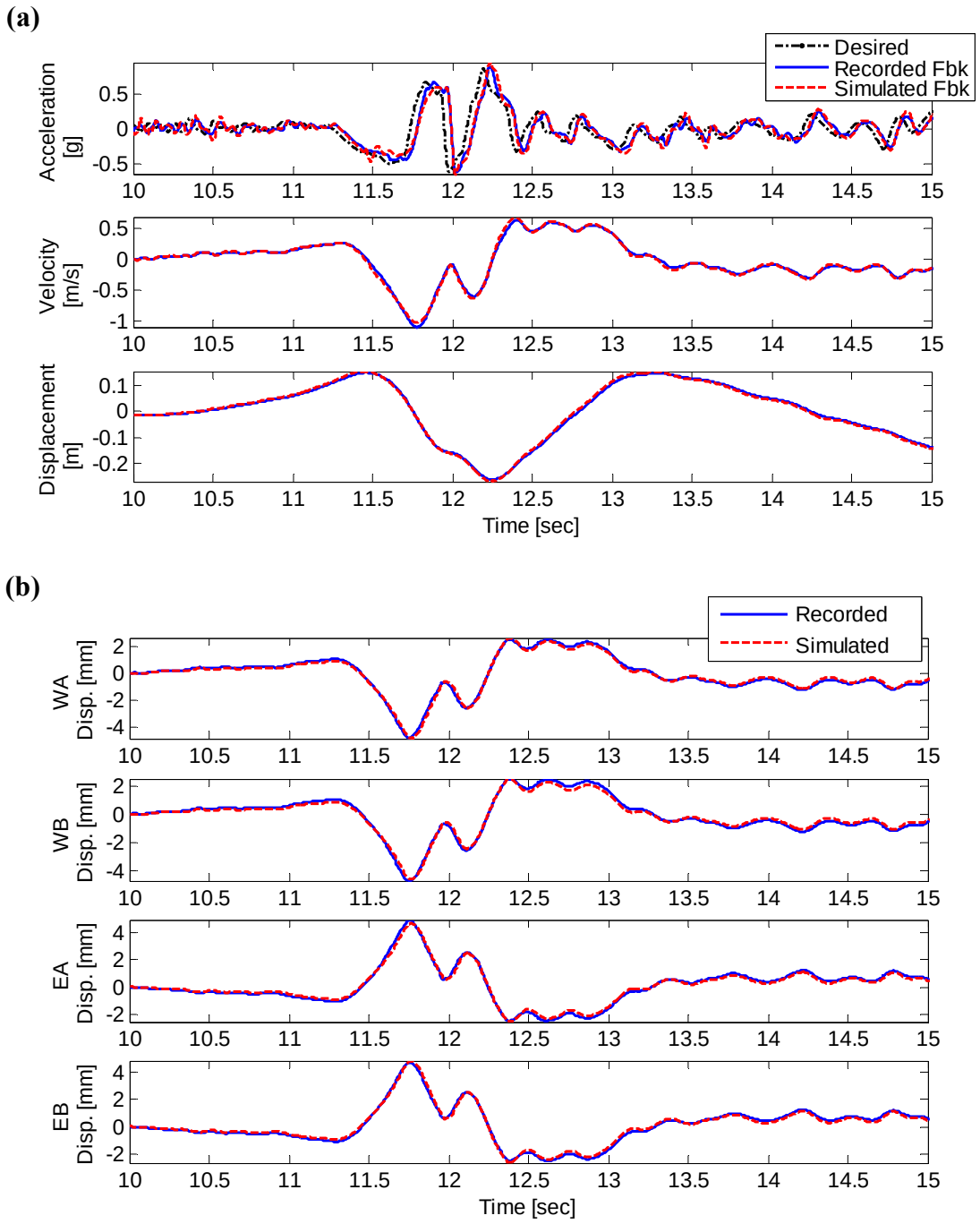

Figure 9.25: Sylmar record: comparisons of simulated and recorded (a) platen acceleration, velocity, and displacement; and (b) 4th stage spool displacements.

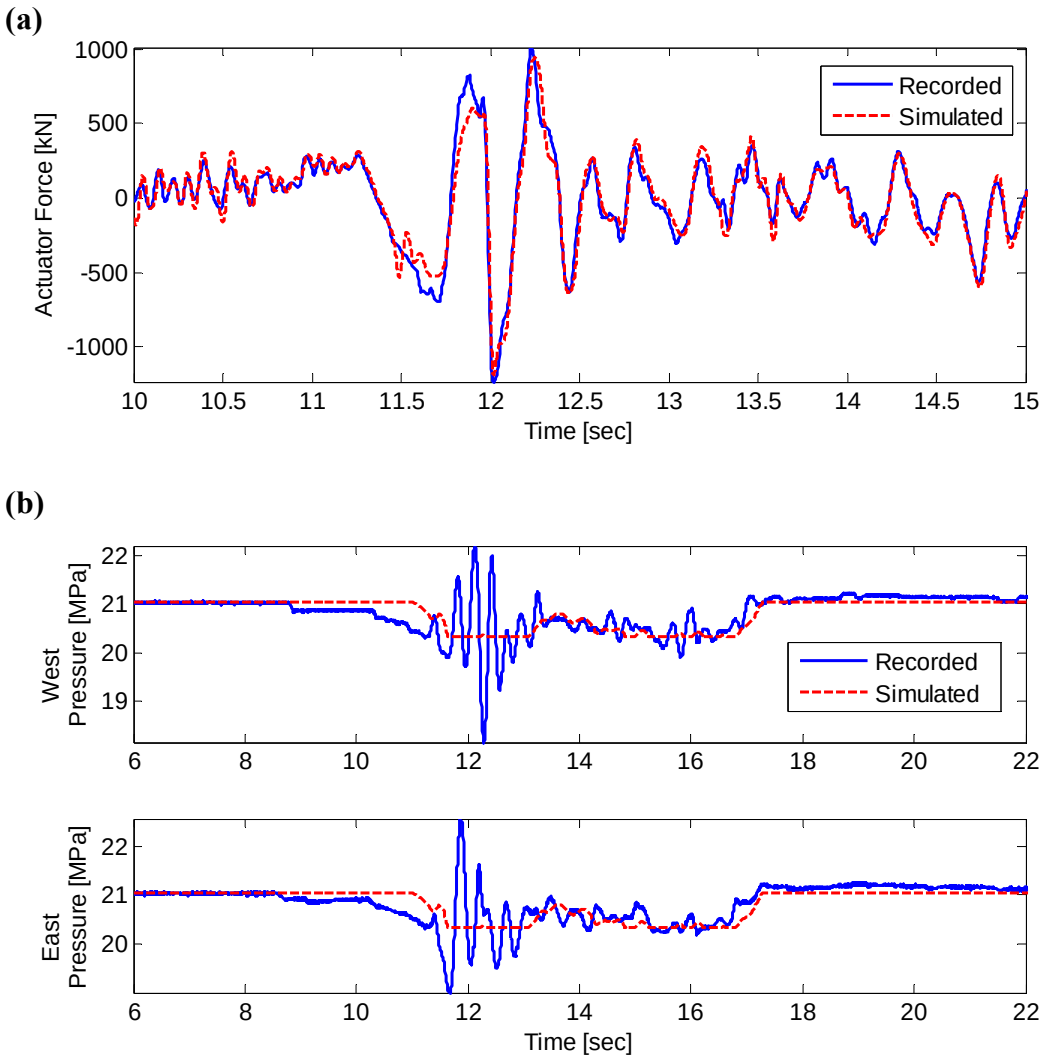

Figure 9.26: Sylmar record: comparisons of simulated and recorded (a) actuator driving force; and (b) closed-coupled accumulator pressures.

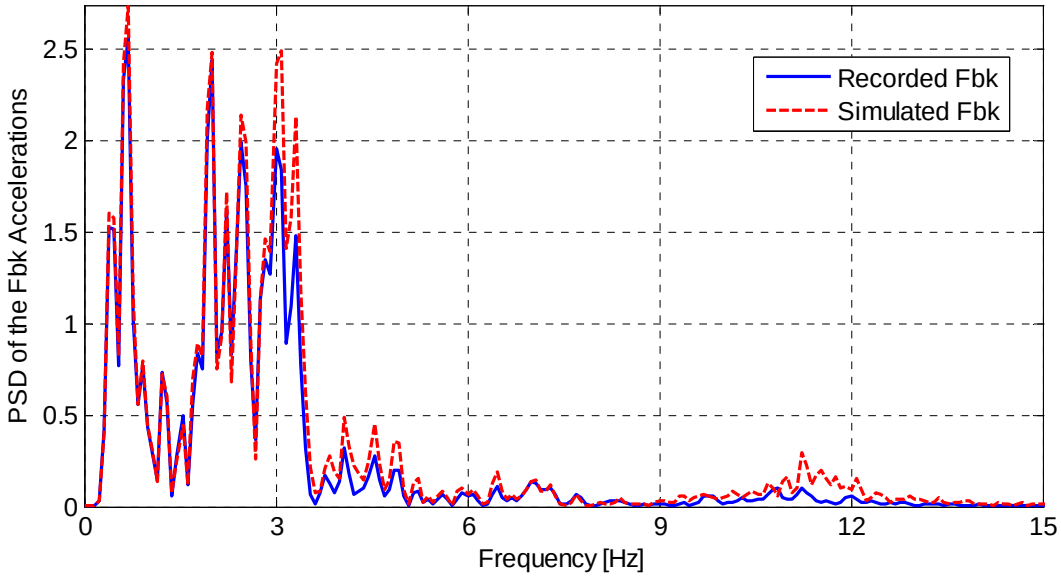

Figure 9.27: Comparison of power spectrum estimations of recorded and simulated acceleration feedback signals from Sylmar record.

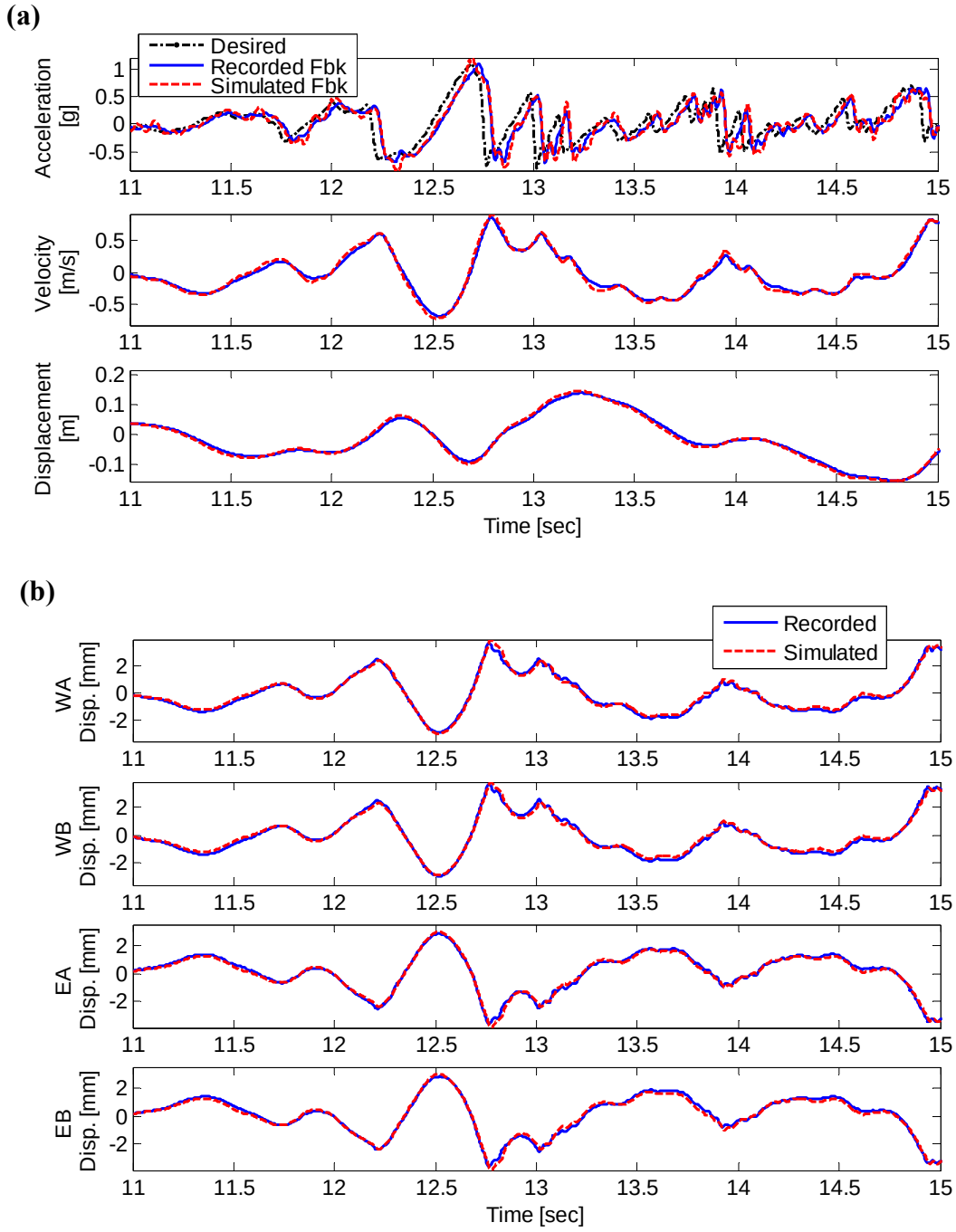

Figure 9.28: El Centro 300% record: comparisons of simulated and recorded (a) platen acceleration, velocity, and displacement; and (b) 4th stage spool displacements.

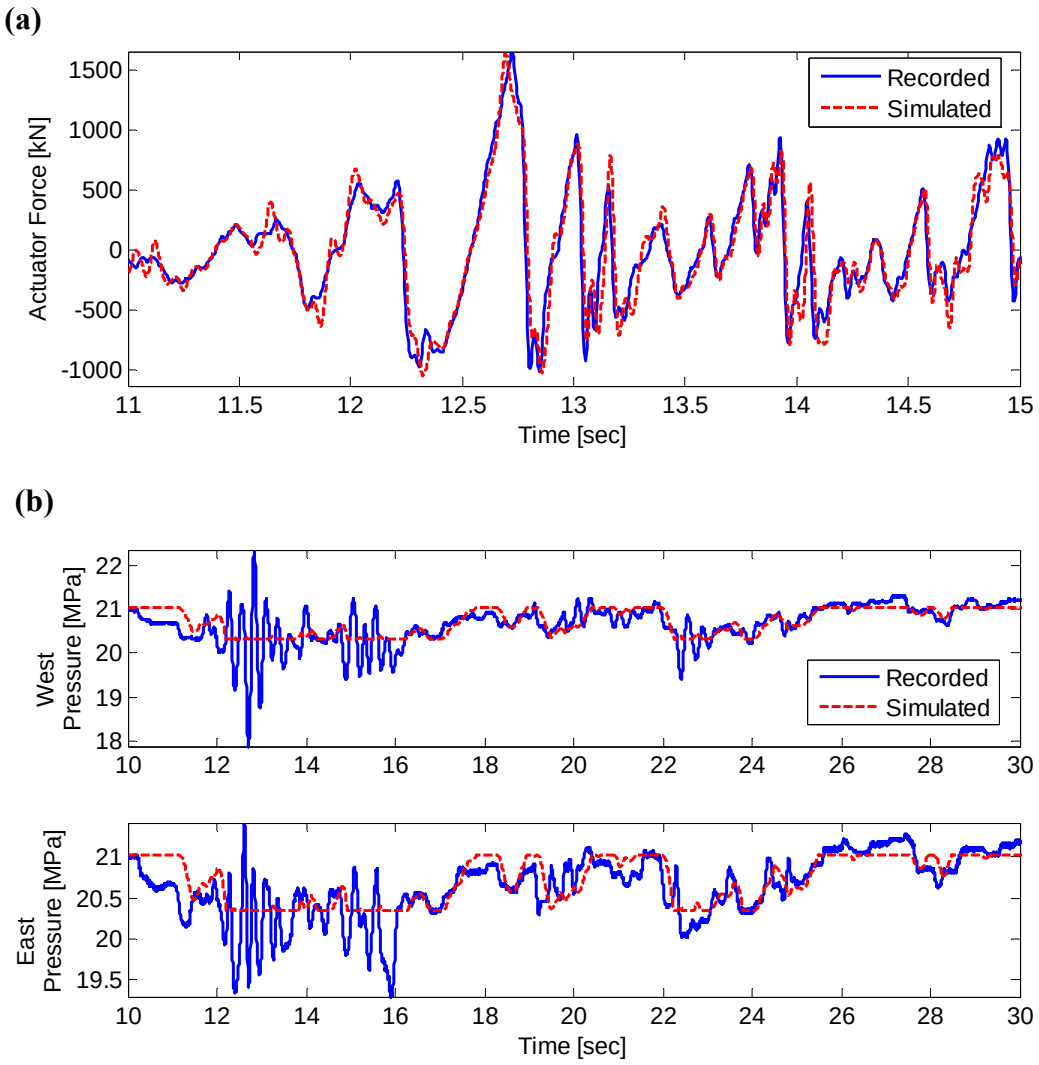

Figure 9.29: El Centro 300% record: comparisons of simulated and recorded (a) actuator driving force; and (b) closed coupled accumulator pressures.

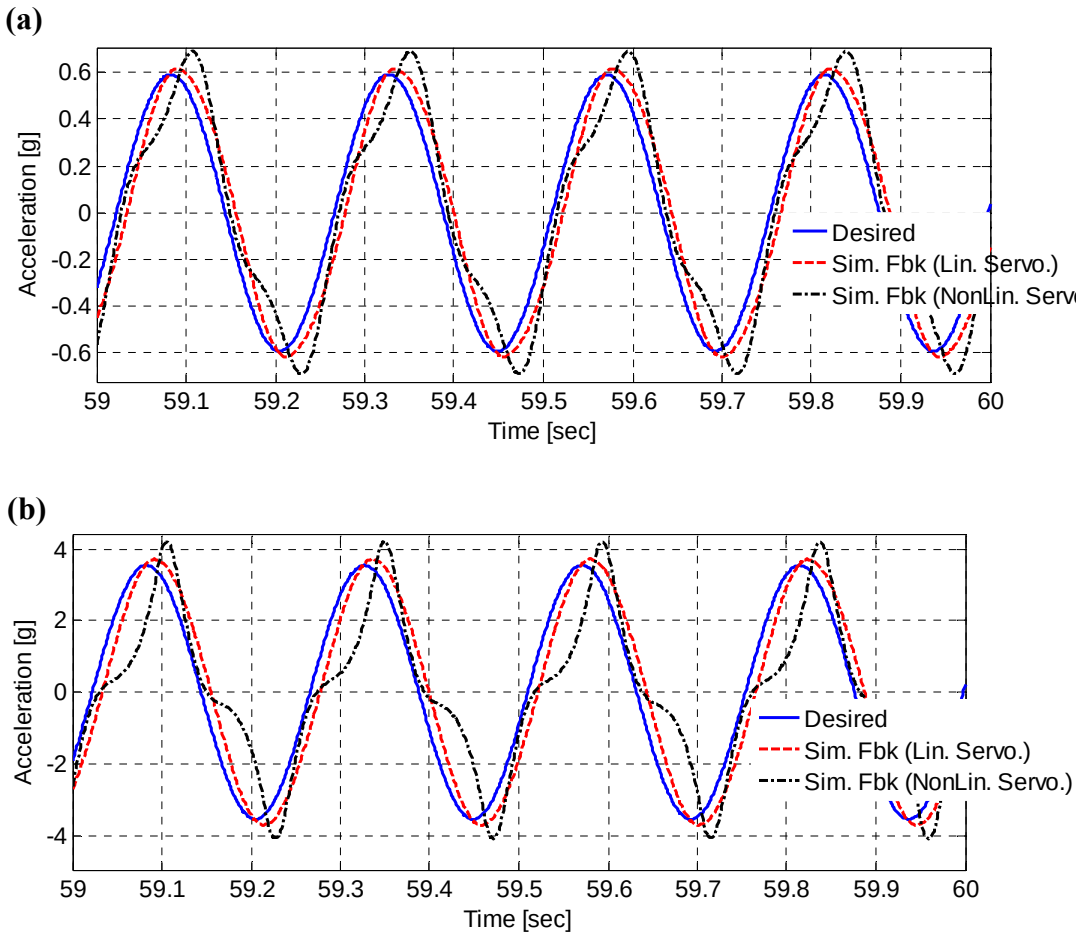

Figure 9.30: Shake table virtual model with linear and nonlinear servovalve models. Command signal is a harmonic signal with 4.1 Hz frequency and (a) 0.591g; and (b) 3.547g amplitudes.

(a)

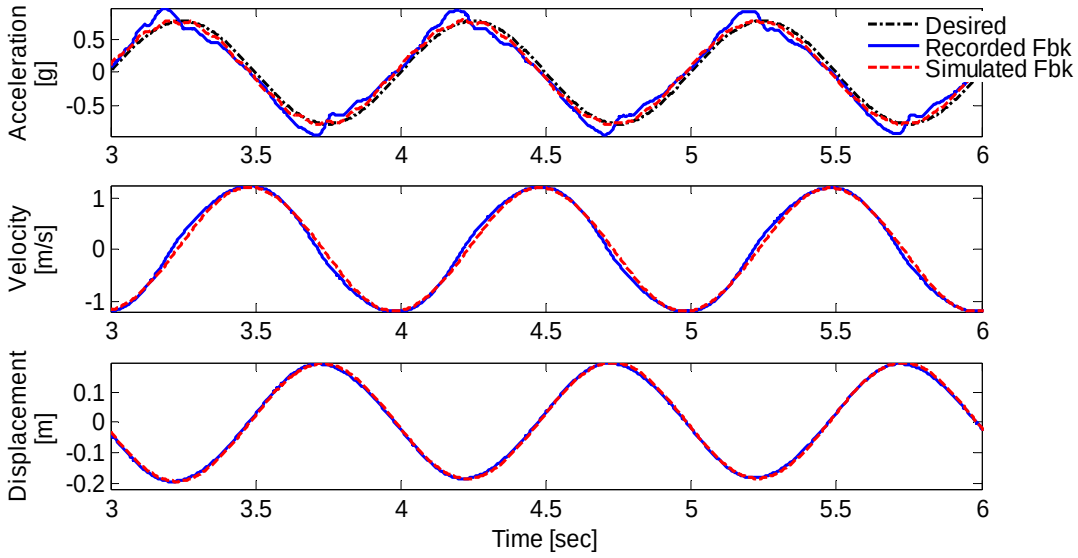

(b)

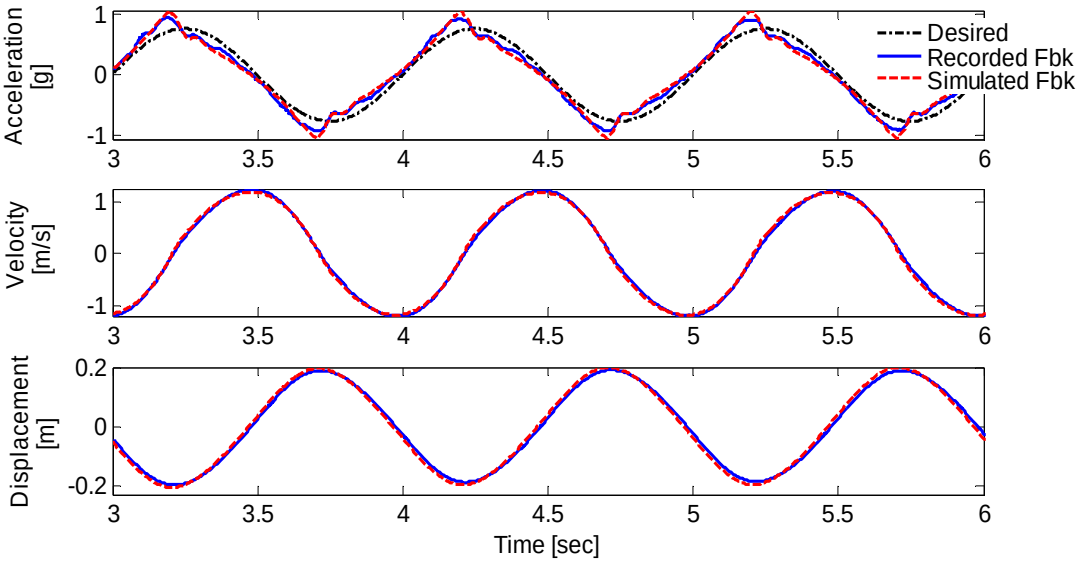

Figure 9.31: Comparison of the recorded platen acceleration, velocity, and displacement responses from an harmonic test with 1.0 Hz frequency with 0.769g amplitude with those of simulation responses using: (a) linear servovalve model; and (b) nonlinear servovalve model.

REFERENCES

Clark, A., Dynamic Characteristics of Large Multiple Degree of Freedom Shaking Tables. *Proc. 10th World Conf. on Earthquake Engineering*, Madrid, Spain, 2823-2828, 1992.

Clark, A.J. and Cross, D.J. (1984). "The effect of specimen resonances on accurate control of multiple defree-of-freedom servo-hydraulic shaking tables." *Proc. 8th World Conference on Earthquake Engineering*, San Francisco, California, U.S.A.

Clark, A.J. (1983). "Sinusoidal and Random Motion Analysis of Mass Loaded Actuators and Valves." *Proc. National. Conference Fluid Power*, Vol. 37: 168-171.

Crewe, A. J., Severn, R. T., The European Collaborative Program on Evaluating the Performance of Shaking Tables. *Phil. Trans. R. Soc. Lond. A*, 359, 1671-1696, 2001.

Crewe, A. J. (1998). "The characterization and optimization of earthquake shaking table performance." Ph.D. Thesis, University of Bristol.

Conte, J.P., and Trombetti, T.L. (2000). "Linear Dynamic Modeling of a Uni-axial Servo-Hydraulic Shaking Table System." *Earthquake Engineering and Structural Dynamics*, 29(9), 1375-1404.

Conte, J.P., Luco, J.E., Restrepo, J., Seible, F., and Van Den Einde, L., (2004). "UCSD-NEES Large High Performance Outdoor Shake Table.' *17th ASCE Engineering Mechanics Conference*, Newark, U.S.A, June 13-16, 2004.

Dyke, S. J., Spencer, B. J., Quast, P., and Sain, M. K. (1995). "Role of control-structure interaction in protective system design." *J. Eng. Mech., 121(2), 322-338.*

Dimig, J., Shield, C., French, C., Bailey, F., and Clark, A. (1999). "Effective force testing: a method of seismic simulation for structural testing." *J. Struct. Eng.*, 125(9), 1028-1037.

Gomez, G.E. (1999). "Application of the MCS algorithm to the control system of the Bristol shaking table." Ph.D. Thesis, University of Bristol.

Hwang, J. S., Chang, K. C., and Lee, G. C. (1987). "The System Characteristics and Performance of a Shaking Table." *NCEER Report No. 87-0004, National Center for Earthquake Engineering Research, State University of New York at Buffalo*, NY.

Kusner, D. A., Rood, J. D., and Burton, G. W., Signal Reproduction Fidelity of Servohydraulic Testing Equipment. *Proc. 10th World Conference on Earthquake Engineering*, Rotterdam, 2683-2688, 1992.

Luco, J.E., Conte, J.P., Ozcelik, O (2008). "Experimental study of the dynamic interaction between the foundation of the NEES-UCSD shake table and surrounding soil." *Under preparation for submission to Soil Dynamics and Earthquake Engineering*.

Luco, J.E., Ozcelik, O., and Conte, J.P. (2008). "Acceleration tracking performance of the NEES-UCSD shake table." *J. Struct. Eng.*, under review.

Larock, B.E., Jeppson, R.W., Watters, G.Z. (2000). *Hydraulics of pipeline systems*, CRC Press LLC, Boca Raton, Florida.Merritt, H.E. (1967). Hydraulic control systems, Wiley, New York.

Merrit E.H. (1967). *Hydraulic Control Systems*, John Wiley & Sons Inc, New York.

Rinawi, A. M., and Clough, R. W., Shaking Table-Structure Interaction. EERC Report No. 91/13, Earthquake Engineering Research Center, University of California at Berkeley, CA, 1991.

Thoen, B. K., and Laplace, P. N., Offline Tuning of Shaking Tables. *Proc. 13th World Conf. on Earthquake Engineering*, Vancouver, B.C., Canada, Aug. 1-6, 2004, Paper No. 960.

Thoen, B. K., 469D Seismic Digital Control Software. MTS Corporation, 2004.

Ozcelik, O., Luco, E. J., Conte, J. P., Trombetti, T. L., and Restrepo, J. I. (2008(1)). "Experimental characterization, modeling and identification of the UCSD-NEES shake table mechanical system." *Earthquake Eng. Struct. Dyn.*, 37:243-264.

Ozcelik, O., Luco, E.J., and Conte, J.P. (2008(2)). "Identification of the mechanical mubsystem of the NEES-UCSD shake table by a least-square approach." ASCE *J. Eng. Mech.*, 134(1), 23-34, doi: 10.1061/(ASCE)0733-9399(2008)134:1(23)

Stoten, D.P., Gomez, E. (2001). "Adaptive control of shaking tables using minimal control synthesis algorithm." *Phil. Trans. R. Soc. Lond. A*, 359, 1697-1723.

Streeter, V.L. and Wylie, E.B. (1975). *Fluid Mechanics*, McGraw Hill, New York.

Takahashi, Y., Fenves, G.L. (2005). "Software framework for distributed experimental-computational simulation of structural systems." *Earthquake Eng. Struct. Dyn.*, 35:267-291.

Trombetti, T.L., and Conte, J.P., Shaking Table Dynamics: Results from a Test Analysis Comparison Study. *Journal of Earthquake Engineering*, **6**(4), 513-551, 2002.

Thayer, W.J. (1965). "Transfer functions for Moog servovalves." *Technical Bulletin 103*, Moog Inc. controls division, East Aurora, N.Y.

Twitchell, B. S., and Symans, M. D., Analytical Modeling, System Identification, and Tracking Performance of Uniaxial Seismic Simulators. *Journal of Engineering Mechanics*, 129(12), 2003.

Van Den Einde, L., Restrepo, J., Conte, J. P., Luco, E., Seible, F., Filiatrault, A., Clark, A., Johnson, A., Gram, M., Kusner, D., and Thoen, B., Development of the George E. Brown Jr. Network for Earthquake Engineering Simulation (NEES) Large High Performance Outdoor Shake Table at the University of California, San Diego. *Proc. of 13-th World Conference on Earthquake Engineering*, Vancouver, BC Canada, August 1-6, 2004, Paper No. 3281.

Williams, D. M., Williams, M. S., and Blakeborough, A., Numerical Modeling of a Servohydraulic Testing System for Structures. *Journal of Engineering Mechanics, ASCE*, 127(8), 816-827, 2001.

Zhao, J., Shield, C., French, C., Posbergh, T., Nonlinear System Modeling and Velocity Feedback Compensation for Effective Force Testing. *Journal of Engineering Mechanics*, 131(3), 244-253, 2005.

Zhao, J., French, C., Shield, C., and Posbergh, T. (2006). "Comparison of Tests of a Nonlinear Structure Using a Shake Table and EFT Method." *J. Struct. Eng.*, 132(9), 1473-1481.

CHAPTER 10

COMPREHENSIVE MECHANICS-BASED VIRTUAL MODEL OF THE NEES-UCSD SHAKE TABLE (LOADED TABLE CONDITION)

10.1. Introduction

In this section of the study, the previously developed mechanics-based virtual model will be extended in order to incorporate linear/nonlinear specimen effects. The mechanics-based virtual shake table model will include the virtual replica of the controller, four servovalve models including servovalve spool dynamics and two independent servovalve flow nonlinearities, two single-ended actuators with variable internal volumes, two accumulators modeling the average supply pressure drop, two-dimensional mechanical subsystem model extended from the previously identified one-dimensional mechanical subsystem model, and finally linear/nonlinear specimen models.

10.2. A Tool Developed for Linking Simulink® with OpenSees

In this section, the details of a tool developed which combines the simulation capabilities of Matlab-Simulink® and OpenSees (Open System for Earthquake

Engineering Simulation) will be given. The tool will be used to investigate shake table linear/nonlinear specimen interaction problem.

Simulink provides an excellent platform to model entire shake table systems with linear structural systems with few degrees of freedom mounted on the platen. Since shake tables, in general, are used to test specimens under going large inertial forces, tested specimens are almost always forced to go into their nonlinear regimes. In order to investigate shake table - nonlinear specimen interaction problem, the simulation capabilities of Simulink has to be extended.

OpenSees and Simulink are both large software frameworks. Directly linking and compiling them together would require huge amount of effort if not totally impossible. One way to achieve this complicated task is to call OpenSees from Simulink at every time step, let OpenSees perform a one-step analysis and send the necessary results back to Simulink, save (e.g., export) the current states of the structural model in a file (e.g., database), turn itself off, and run itself again when Simulink needs it, retrieve the current states from the file (i.e., import the states from the database), and perform the next time step analysis. This importing-exporting process would continue until the end of the entire simulation. As it can be anticipated, “linking” OpenSees and Simulink this way would be inefficient due to the necessity of saving and retrieving the current states of a structural model at every time step from a file. The efficient communication between OpenSees and Simulink is a crucial problem for the entire simulation tool (i.e., Simulink and OpenSees) to solve large nonlinear problems.

An efficient but simple way to achieve this integration is to make Simulink the simulation coordinator by enabling it to call the FEA software whenever it is necessary while the FEA software and the structural model are still in the memory, in other words by letting OpenSees to be persistent in the memory so that the communication between Simulink and OpenSees becomes efficient (easily accessible).

10.3. Integration of OpenSees into Matlab-Simulink by Client-Server Technique

In the Client-Server (CS) technique, the finite element analysis (FEA) software OpenSees is set as a server and Simulink as a client. Setting OpenSees as a server enables OpenSees and the structural model to be persistent in the memory, and therefore the client (Simulink) can connect to the server and request from server to execute OpenSees analysis commands and retrieves the necessary structural responses in order to incorporate their effects into the simulation. The communication between the client and the server is enabled through the standard Internet protocol TCP/IP. Note that the model of the table and the model of the structure mounted on the table are in close loop.

OpenSees is an open source FEA software used for modeling structural systems and simulating their earthquake responses (McKenna et al., 2000). OpenSees' interface is based on a command-driven scripting language Tool Command Language (TCL) which allows OpenSees users to create more-versatile model and input files (Welch, 2000). Due to the flexibility provided by TCL, OpenSees does not need to be further programmed to act as server, therefore it remains intact. Instead a set of TCL

functions are used to achieve the communication between the server and the client through a simple TCL network communication channel (or socket) based on TCP network protocol. The client includes few short TCL commands.

The integration using CS technique is schematically described in Figure 10.1. At the server side, OpenSees creates the model in the memory. Then it stops and waits for commands to arrive from the client (Simulink) which will drive further actions. Once OpenSees receives commands and/or inputs (e.g., platen accelerations) for specific actions from the client, it performs the requested analysis and sends the required structural responses back to the client. For shake table application, these responses are base shear and overturning moment (e.g., base reaction forces). At the client side, at every time step an algorithm in Simulink will ask OpenSees to run an analysis with current platen accelerations as inputs. Then it will receive structural responses (e.g., resisting forces) from OpenSees and incorporates these responses to advance the simulation. To perform receiving action from an outside software (in this case OpenSees), a user-defined function in Simulink written in C++ is linked and compiled with a client written also in C++. User-defined functions in Simulink are called the S-functions. The client is a C++ object which persists in the memory therefore holding the connection with the server continuously and handling the communication with it.

Server Side. On the server side, the following TCL scripts are used to create the server

source model.tcl

socket -server accept 7200

vwait forever

where *model.tcl* is the finite element (FE) model of the specimen on the table, TCL command *source* will run the *model.tcl* to set up the model and to perform initial analysis if necessary (e.g., gravity loads). The second command *socket* creates the server socket with the port number 7200 (it can be any port number) and a callback procedure *accept* to execute commands whenever the client connects to this server socket. The third command *vwait* sets the server waiting for requests from the client. The callback procedure *accept* will accept commands from the client to perform time history analyses, get the responses from FE analysis, and send these responses back to the client through the same socket. Since the model is persistent in the memory, the procedure *accept* can visit any variable in the FE model directly from the memory and can perform certain actions on them and send them back to the client. More information on the TCL commands can be found in the literature (Welch, 2000).

Client Side. The client is a persistent C++ object called *OpenSeesHandler* which is linked to the user-defined S-function *OpenSimConn* in Simulink. To take advantage of TCL's library (e.g., TCP socket), *OpenSimConn* is also linked with it. For OpenSees to perform certain actions, within *OpenSeesHandler* necessary TCL commands are created and then are sent to the server. Detailed discussion about writing C++ S-functions in Simulink can be found in the literature (Dabney and Harman, 2004).

At the very beginning of the entire analysis, *OpenSeesHandler* is created inside the S-function. It will run the following TCL commands in its constructor function in order to set up and hold the connection with the server:

set s [socket localhost 7200]

fconfigure $s -buffering none

At every time step, Simulink will operate *OpenSeesHandler* client by calling the S-function, and it will form and run the following commands

puts $s "tryOpenSeesOneStep $currentTime $accel_i"

gets $s

where *puts $s* will pass the command to the server side. The command "*tryOpenSeesOneStep"* is a user defined macro written in TCL on the server side to run OpenSees at the time *currentTime* which is controlled by the client Simulink. Parameters $*accel_i* are the platen accelerations with respect to a generalized coordinates. In this version of the software longitudinal, vertical, and rocking accelerations are passed from Simulink to OpenSees. The TCL command "*gets $s"* gets the response from the server and saves them into variable "*s"* which will then be incorporated into simulation by Simulink to advance (continue) the simulation in time.

Advantages of the CS technique in general are as follows: (i) **It is efficient and flexible**. The users are allowed to update the FE model or loading parameters at any time step. The FE model and its state variables in the server side persist in the memory, therefore the server allows all state variables to be visited and updated by the client at any time step. Furthermore with commands like *tryOneStep*,

revertToLastStep, and *commitOneStep*, FE analysis software is able to work together with implicit (i.e., iterative type) as well as explicit (e.g., Runge-Kutta) solvers developed for solving initial value problems. Data transfer between the client and server can be implemented using TCP/IP or other protocols. The size of the data is usually very small and the speed and quality of this transfer are excellent; (ii) **it is robust**. The connection between the client and server is set up only once at the very beginning of the analysis and will be held at all time. This saves tremendous amount of time (20 times faster than exporting-importing method). Once connection is set up, a reliable communication method between the client and the server is established due to robustness of the Internet protocol; (iii) **it is easy to program and maintain**. In the client side a cheap component can be easily programmed and integrated into any higher-level software platforms (in this case Simulink). The client C++ object *OpenSeesHandler* is integrated into Simulink with very little programming work; therefore it is easy to change and maintain the integration software.

10.4. Simulink® Block Diagram Semantics

A Simulink block diagram model is a graphical representation of a mathematical model of a dynamic system. A mathematical model of a dynamic system is described by a set of equations. A classical block diagram model of a dynamic system graphically consists of blocks and lines (signals). A block within a block diagram defines a dynamic system itself. The relationships between each elementary dynamic system in a block diagram are illustrated by the use of signals connecting the blocks. Collectively the blocks and lines in a block diagram describe an overall

dynamic system and are called the “time-based block diagram”. Simulink block diagrams define time-based relationships between signals and state variables. The solution of a block diagram is obtained by evaluating these relationships over time. Each evaluation of these relationships is referred to as a time step.

As mentioned above, the relationships between signals and state variables are defined by a set of equations represented by blocks. Each block consists of a set of equations (block methods). These equations define a relationship between the input signals, output signals, and the state variables. Simulink® generates internal “systems” that are collections of block methods (equations) that are evaluated together. The semantics of time-based block diagrams does not require creation of these systems. Simulink creates these internal systems as a means to manage the execution of the model (Mathworks, 2008).

Each block within a Simulink block diagram represents multiple equations. These equations are represented as block methods within Simulink. These block methods are evaluated (executed) during the execution of a block diagram. The evaluation of these block methods is performed within a simulation loop, where each cycle through the simulation loop represents evaluation of the block diagram at a given point in time. Block method types relevant to this discussion are “Outputs” and “Derivative” methods. Outputs method computes the outputs of a block given its input at the current time step and its states at the previous time step. Derivatives method computes the derivatives of the block’s continuous states at the current time step, given the block’s inputs and the values of the states at the previous time step.

Typically the current values of some system outputs are functions of the previous values of temporal variables. Such variables are called states. Computing a model's outputs from a block diagram hence entails saving the value of states at the current time step for use in computing the outputs at a subsequent time step. There are two types of states in Simulink: discrete and continuous. A continuous state changes continuously. A discrete state is an approximation of a continuous state where the state is updated (recomputed) using finite intervals. The virtual model of the shake table is entirely modeled using continuous blocks. Therefore more on computing continuous states in Simulink will be given below.

Computing a continuous state entails knowing its rate of change or derivative. Since the rate of change of a continuous state typically itself changes continuously, computing the value of a continuous state at the current time step requires integration of its derivative from the start of a simulation. Thus modeling a continuous state entails representing the operation of integration and the process of computing the state's derivative at each point in time. Simulink block diagrams use Integrator blocks to indicate integration and a chain of blocks connected to an integrator block's input to represent the method for computing the state's derivative. In general, analytical methods do not exist for integrating the states of real-world dynamic systems represented by ordinary differential equations (ODEs). Therefore, integrating continuous states requires the use of numerical methods called ODE solvers (Mathworks, 2008).

Simulink simulates a dynamic system by computing its states at successive time steps using information provided by the model. The process of computing the successive states of a system from its model is known as solving the model. The continuous solvers use numerical integration to compute a model's continuous states at the current time step from the states at previous time steps and the state derivatives. Some continuous solvers (e.g., Runge-Kutta, Dormand-Prince etc.) subdivide the simulation time span into major and minor time steps where a minor time step represents a subdivision of the major time step. The solver uses results at the minor time steps to improve the accuracy of the result at the major time step. While solving a model, the Simulink engine invokes the continuous solver specified by the model. Depending on the solver, the solver either in turn calls the Derivative method of the model once or enters a sub-cycle of minor time steps where the solver repeatedly calls the model's Outputs methods and Derivatives methods (in this order) to compute the model's outputs and derivatives at successive intervals within the major time step.

10.4.1. 4th Order Runge-Kutta

The 4th order Runge-Kutta (RK) is used to advance in time the model of the shake table in Simulink. Runge-Kutta methods are often called as single-step or explicit methods due to requiring only the solution at the previous time step to advance the simulation in time. Here, a brief introduction on the 4th order Runge-Kutta (RK4) will be given; more on the subject can be found in the literature (Bewley, 2008; Lee, 2004; Moler, 2004).

Consider a first order, possibly nonlinear ordinary differential equation

$$\dot{y} = f(t, y), \quad y(t_0) = y_0 \tag{10.1}$$

where $y(t)$ is the response (state) to be determined for some $t > 0$, $f(t, y)$ is a function of time t and the solution itself y, and y_0 is the initial conditions. The fundamental Theorem of Calculus gives an important connection between differential equations and integrals

$$y(t + \Delta t) = y(t) + \int_t^{t+\Delta t} f(y(s), s)ds \tag{10.2}$$

Numerical quadrature can not be used directly to compute (10.2) since $y(s)$ is unknown so the integrand can not be evaluated. Nevertheless, the basic idea is to choose a sequence of values of Δt so that (10.2) can be used to generate numerical solution (approximation) $y_n \cong y(t_n)$, n=0,1,….

The 4th order Runge-Kutta method computes (or approximates) the integral given in (10.2) using four function evaluations per time step

$$\begin{aligned} k_1 &= f(t_n, y_n) \\ k_2 &= f(t_n + \frac{\Delta t}{2}, y_n + \frac{\Delta t}{2} k_1) \\ k_3 &= f(t_n + \frac{\Delta t}{2}, y_n + \frac{\Delta t}{2} k_2) \\ k_4 &= f(t_n + \Delta t, y_n + \Delta t k_3) \end{aligned} \tag{10.3}$$

There are four stages in RK4. Each stage computes a slope, k_i, by evaluating $f(t, y)$ for a particular value of t and a value of y obtained by taking linear combinations of the previous slopes (e.g. $y_n + \frac{\Delta t}{2} k_1$ etc). k_1, k_2, k_3, and k_4 are the slopes (or

derivatives) at time steps t_n, $t_n + \frac{\Delta t}{2}$, $t_n + \frac{\Delta t}{2}$, and $t_n + \Delta t$, respectively. Notice that y's (outputs or states) calculated at minor time steps (i.e., $t_n + \frac{\Delta t}{2}$, $t_n + \frac{\Delta t}{2}$, and $t_n + \Delta t$) are necessary to evaluate the slopes. Geometrical interpretation of RK4 is shown in Figure 10.2.

Using (10.3), numerical solution of (10.1) at time $n+1$ can be found

$$y(t_{n+1}) \cong y_{n+1} = y_n + \frac{\Delta t}{6}(k_1 + 2k_2 + 2k_3 + k_4) \tag{10.4}$$

where y_n is the last committed state (updated state) stored in the memory at time n.

By invoking RK4 solver, Simulink computes the value of a continuous state (e.g., y_{n+1} output of a Simulink Integral block) at the current time step by calling first the model Outputs methods to calculate the outputs of each block in the order specified by the Outputs method execution list; these are the outputs calculated at each minor time steps. Next by calling the Derivatives methods of each integral block or other blocks containing continuous states (e.g., Transfer Function block), it calculates the derivatives (slopes) given in (10.3); for each slopes given in (10.3) the solver repeatedly calls the Outputs and Derivatives methods. Once all the derivatives are calculated, Simulink finds the final results of the blocks' states using (10.4) at the major time step. Notice that the major time step for one step is the last minor time step for the previous step. Values found by (10.4) are used to update (commit) the states of each integral block which will in turn be stored in the memory in order to advance the simulation for the next time step.

10.4.2. OpenSees and Simulink® RK4 Solver

Simulink uses RK4 to solve (simulate) the shake table model. OpenSees is integrated into this model therefore it must take the same steps that the ODE solver takes to advance the simulation. In other words, OpenSees needs to act as a “built-in” Simulink block (e.g., Gain, Constant, Math Function blocks etc.) acting flawlessly with the Simulink software. More specifically, since OpenSees is a part of the whole simulation model, it has to provide the necessary inputs (e.g., reaction forces at the base of the structure) to Simulink while the RK4 solver calls the Outputs and Derivatives methods at successive intervals within the major time step in order to calculate the models’ continuous states (e.g., platen acceleration, velocity, displacement etc.). While providing these intermediate results to Simulink in minor time steps, the states of the structural model in OpenSees must not be updated (committed) since the final approximation of the platen acceleration at the current time has not been computed yet. OpenSees has to wait until the final values of the models’ states are computed and only then has to update the states of the structural model after performing one final analysis using final approximation of the platen acceleration. Reaction forces computed during the final analysis are returned to Simulink to be used for updating the models’ states. While the state updating stage, OpenSees waits for commands to arrive from Simulink which would advance the simulation to the next time step.

It is clear that Simulink needs to control OpenSees when to update and when not to update the states of the structural model. To do this, minor and major time steps

have to be tracked. This is done by using Simulink macros called *ssIsMinorTimeStep(S)* and *ssIsMajorTimeStep(S)*. These macros are used inside the S-Function *OpenSimConn* which works in conjunction with *OpenSeesHandler*. Once the simulation stages are known (i.e., minor and major time steps) OpenSees can be controlled based on this information. To control the committing sequence of OpenSees, two special commands have been created and embedded in OpenSees software: *tryOneStep* and *commitOneStep*. With *tryOneStep*, OpenSees performs intermediate analyses needed for RK4 method (Eq. (10.3)) and returns Simulink the base reaction forces by using the intermediate platen accelerations but does not update the states of the structural model. With *commitOneStep*, OpenSees performs one last analysis using the true platen accelerations and this time updates the states of the structural model. Note that the simulation time of OpenSees is also controlled by Simulink using the Simulink macro *ssGetT(S)*.

Simulink-OpenSees integration framework outlined above is checked by comparing the analytical transfer function between the reference input and actuator force of a linear shake table model with single-degree-of-freedom and multi-degree-of-freedom linear shear-type structures on its platen with the numerically estimated counterpart of the same shake table model where the same linear specimens are modeled with OpenSees. The match between the analytically and numerically obtained transfer functions is excellent. This check targets specifically the client-server framework set between OpenSees and Simulink, and OpenSees's ability to work with the continuous solver used in Simulink.

10.5. Incorporating Specimen Effects into the Mechanics-based Virtual Model of the Entire Shake Table Model

Models for the other constitutive parts of the mechanics-based shaking table model for the bare table conditions (i.e., table without specimen) have been presented in Chapter 10. Therefore, here only the model related to the specimen will be given.

Figure 10.3 shows the two-dimensional mechanical subsystem of LHPOST including a generic two-dimensional *N*-story one-bay specimen mounted on its platen. Specimen will be modeled using the finite element software OpenSees and it can be a linear or nonlinear model. OpenSees model of the specimen will be linked to the rest of the shake table model in Simulink using the framework presented above. The vector $\overline{\mathbf{u}}_i$ is the relative displacement vector of the i^{th} degree of freedom with respect to the platen and has the form:

$$\overline{\mathbf{u}}_i^T = \begin{pmatrix} u_x & u_z & u_{\theta y} \end{pmatrix}_i \tag{10.5}$$

In Figure 10.3, h_{spe} and a_{spe} are the story height and half the bay width of the specimen, respectively. Notice that the specimen is centered around *O*. Total displacement vector of the specimen $\mathbf{u}_t$ can be written as follows

$$\mathbf{u}_t = \overline{\mathbf{u}} + \boldsymbol{\alpha}\mathbf{u}_O \tag{10.6}$$

where $\boldsymbol{\alpha}$ is the $(3N \times 3)$ influence matrix composed of only geometric quantities, $\overline{\mathbf{u}}$ is the $(3N \times 1)$ relative displacement vector of the specimen, and $\mathbf{u}_O$ is the (3×1) displacement vector of the platen at point *O*. The influence matrix $\boldsymbol{\alpha}$ has the following form

$$\boldsymbol{\alpha}^T = \begin{bmatrix} \boldsymbol{\alpha}_1 & \dots & \boldsymbol{\alpha}_N \end{bmatrix} \tag{10.7}$$

where $\boldsymbol{\alpha}_i$ is the (3×3) transformation matrix which transforms the platen motion at point *O* to the rigid-body motion at the specimen degree-of-freedom *i*.

Effective forces acting on the specimen degrees-of-freedom due to the platen acceleration vector $\ddot{\mathbf{u}}_O$ can be calculated as follows

$$\mathbf{F}_{eff}(t) = -\mathbf{M}_{spe}\boldsymbol{\alpha}\ddot{\mathbf{u}}_0 \tag{10.8}$$

where $\mathbf{M}_{spe}$ is the mass matrix of the specimen, and $\ddot{\mathbf{u}}_0$ is the platen acceleration vector. Once the specimen responses are computed, the total reaction force acting on the platen at point *O* due to the specimen can be calculated using the absolute specimen accelerations

$$\mathbf{F}_{spe}(t) = \boldsymbol{\alpha}^T\mathbf{M}_{spe}\boldsymbol{\alpha}\ddot{\mathbf{u}}_0 + \boldsymbol{\alpha}^T\mathbf{M}_{spe}\ddot{\mathbf{u}} \tag{10.9}$$

The first term in (10.9) is the reaction forces at the base due to the rigid-body-motion of the specimen, and the second term is the reaction forces at the base due to flexibility of the specimen.

Equation of motion of the mechanical subsystem with respect to point *O* including the specimen effects can be written as follows

$$\ddot{\mathbf{u}}_O(t) = \mathbf{M}_O^{-1}\left\{\mathbf{F}_{act}(t) - \mathbf{F}_{spr}(t) - \mathbf{F}_{damp}(t) - \mathbf{F}_{coul}(t) - \mathbf{F}_{spe}(t)\right\} \tag{10.10}$$

where $\mathbf{M}_O$ is the mass matrix of the platen.

Simulink implementation of (10.10) is shown in Figure 10.4 where the connection between Simulink and OpenSees is represented by the double-ended dashed arrow. Equations (10.8) and (10.9) are computed at every time step by

getTotalResistingForce command which is a user defined macro in the server side written in TCL.

The complete virtual model of the NEES-UCSD shake table is shown in Figure 10.5 in which the 2D mechanical subsystem model including the specimen is modeled in OpenSees and linked to the rest of the virtual model using the client-server technique. Simulation work presented in the next section uses this final model of the table where the simulation parameters are the same as those used for the bare table model (Chapter 10).

10.6. Application Example: Nonlinear Shear-frames

In order to investigate the table-nonlinear specimen interaction problem, three different shear-frames are considered. Structures are chosen simple enough to allow comparisons with the analytical results for the linear shake table / linear specimen interaction problem yet realistic enough to gain insight into real test situations.

Shear-frames with three, five, and seven stories used for application examples are shown in Figure 10.6. Beams in all three frames are considered rigid to enforce a typical shear-building behavior; therefore only one horizontal degree-of-freedom is assigned to each floor. Columns are made of steel with a Young's modulus of 2.1×10^5 MPa. Story heights of all three frames are $h_{spe} = 2.75$ m. Floor masses are assumed to be lumped at floor levels and their values are taken from a full-scale specimen tested on the shake table in order to be representative of specimens that can be tested on the real table. The parameters k^i_{3stry}, k^i_{5stry}, and k^i_{7stry} are the initial story

stiffnesses of 3-story, 5-story, and 7-story frames, respectively. Physical characteristics of the shear-frames are summarized in Table 10.1. Natural frequencies, natural periods, effective modal mass ratios for the undamped structures are given in Table 10.2. Viscous damping in the form of Rayleigh damping is assumed with damping ratio $\xi = 0.03$ for the first and second modes of vibration.

The story shear force – interstory drift relation for the columns are modeled using Menegotto-Pinto (M-P) material constitutive model (Filippou et al., 1983). M-P model is used to describe the inelastic behavior of structural steel, and can be used for macroscopic modeling of hysteretic behavior of structures or substructures with an appropriate choice of modeling parameters (Barbato and Conte, 2006). The M-P material model available in OpenSees material library requires seven model parameters to be defined. These model parameters are initial yield strength f_{y0}; parameters R_0, a_1, a_2 for controlling the transition from elastic to plastic branches of hysteresis loops where a_1 and a_2 are experimentally determined; a_3 and a_4 are experimentally determined isotropic hardening parameters; and the post-yield stiffness to initial yield stiffness ratio b. Typical values used for the common structural steel are $R_0 = 20.0$, $a_1 = 18.5$, $a_2 = 0.15$, $a_3 = a_4 = 0.0$, and $b = 0.10$. Initial yield strength for each column element is determined from elastic design forces obtained from the design spectrum constructed for the Downtown Los Angeles area with $\xi = 0.05$ (Panagiotou et al., 2008). Peak modal story shear forces are found using square-root-of-sum-of-squares (SRSS) modal combination rule considering the first two modes. Elastic story shear forces obtained this way are reduced by force reduction factors of

$R2 = 2.0$ and $R4 = 4.0$ and assigned to each column element. Elastic story shear forces and reduced story yield strengths for the three shear-frames are given in Table 10.3

10.6.1. Simulations Results

In order investigate the table-nonlinear specimen interaction problem, simulation work is carried out using the virtual shake table model using two earthquake records: (i) 360 degree component of the 1994 Northridge earthquake record at Sylmar station modified with OLI; and (ii) the north-south component of 1940 Imperial Valley earthquake record at El Centro station scaled to 300%. The simulation model uses the same controller setting as the on the real system and its response is matched as close as possible to the real system (Chapter 10) for both earthquake records. Simulations are carried out using the bare table model as well as the table with specimens which have dynamic characteristics specified in the previous section. During simulations, bare table settings are kept fixed and only the specimens mounted on the table are changed in order to focus solely on the effects of specimens' responses on the table response.

Figure 10.7(a), (b), and (c) shows the 1st floor inter-story drift vs. 1st floor shear force relationships for the 3, 5, and 7-story shear-frames, respectively, under the Sylmar ground acceleration record (original record). It shows that all three specimens go into nonlinear regimes with R2 as well as R4 yield strengths.

Figure 10.8 through Figure 10.10 show the time history plots of: (a) feedback platen accelerations; (b) actuator driving forces; and (c) (actuator driving force)-(total

specimen shear force) = net platen forces simulated using the Sylmar record when the table has no specimen (Bare), and when there are specimens of 3, 5, and 7 stories on it with different yield strengths (i.e., R1 (linear), R2, and R4). It is apparent from the acceleration time history plots that the response of the table with specimens is different from the response of the table without specimen. Actuator driving force plots show that forces that the actuators exert on the platen are considerably different when there are specimens on the table and when there is no specimen on it. This shows clearly the interaction between the table and the specimen. As the yield strengths of the specimens get smaller (R4<R2<R1), interaction level between the specimen and the table reduces. The more the specimen exerts force on the table, the harder the actuator has to work in order to overcome the forces that the specimen exerts on it. For instance, in the case of table with the linear 3 story shear-frame (R1), actuator force is very different compare to the bare table case (Figure 10.8(b)). Also notice that, for the nonlinear specimen case with yield strength of R4, the actuator force is close to the actuator force under the bare table case since the resisting forces that the specimen can exert on the table is reduced (capped) due to the nonlinear behavior of the specimen. Net force (i.e., actuator force – specimen resisting shear force) that the actuator exerts on the platen (Figure 10.8(c), Figure 10.9(c), and Figure 10.10(c)) differs from the actuator force when there is no specimen on the platen (i.e., bare table). Based on the time history plots, it can be said that the interaction problem of table with specimen is complicated and it is a function of dynamic characteristics and nonlinearity level of

the specimen, as well as the characteristics of the acceleration record reproduced on the table.

In order to gain additional insight on the interaction problem, transfer functions for a fully linear system (i.e., linear table-linear specimens) will be considered. For more details on the linear table – linear specimen model refer to Chapter 7. Figure 10.11(a) and (b) shows the magnitude responses of the analytical table transfer function between the reference acceleration as input and the actuator force as output ($G_{fudd}(s)$), and of the analytical transfer function between the reference acceleration as input and feedback acceleration as output ($G_{audd}(s)$) with linear specimens with 3, 5, and 7 stories. TVC gain settings used are $k_P = 1.5$ V/V, $k_{VF} = 0.382$ V/V, $k_{AF} = 0.35$ V/V, $k_{AF} = 0.00469$ V/V, and $k_{DP} = -0.145$ V/V. The rest of the gains in TVC are set to zero including the notch filter settings. Notch gains are set to zero in order to see the interaction effects clearly around the oil-column frequency. The general pattern seen in both of the transfer functions is that there are peaks which are followed by troughs. These notch-trough pairs occur at the vicinity of the natural frequencies of the linear structures (Table 10.2). Peaks (poles) seen in the magnitude response of $G_{fudd}(s)$ coincide with the peaks seen in the magnitude response of $G_{audd}(s)$ whereas the troughs (zeros) in both of the transfer functions occur at different frequencies. A closer look at the troughs seen in $G_{fudd}(s)$ reveals that frequencies where these troughs occur are very close to the frequencies of the combined system of specimen and platen which can be estimated using the following expression

$$f_{T,i} = f_{S,i}\left(1+\frac{m_{s,i}^{eff}}{m_{pl}}\right)^{1/2} \tag{10.11}$$

where $f_{T,i}$ = frequency of the combined system for the i^{th} mode, $f_{S,i}$ = frequency of the i^{th} mode of the specimen, $m_{s,i}^{eff}$ = effective mass of the i^{th} mode of the specimen, and m_{pl} = mass of the platen. Table overshoots the frequencies below the vicinity of the natural frequencies of specimens and undershoots the frequencies above them. Also notice that the interaction at the oil column frequency of the system at around (~12.0 Hz) for the 5 and 7-story specimens. Based on the observations from the linear analysis, it can be said that shake tables exciting lightly damped structures have a limited ability to apply forces at the natural frequencies of the combined mechanical system. Similar observations have been done by various researchers for actuators which are directly attached to the specimens (Dyke et al., 1995; Dimig et al., 1999; Zhao et al., 2005).

Figure 10.12 through Figure 10.14 show estimations of the magnitude and phase response of $G_{audd}(s)$, and the magnitude response of $G_{fudd}(s)$ when the virtual model of the table is commanded a band-limited, [0.25 20] Hz, white noise (WN) acceleration input with 25%g RMS amplitude and 120 seconds long. The table is loaded with 3, 5, and 7-story linear (R1) and 3, 5, and 7-story nonlinear specimens with corresponding R4 yield strengths. RMS amplitude of the WN acceleration is chosen relatively high in order for specimens with R4 yield strengths to go into nonlinear regimes. Figure 10.12(a) and (b) are the magnitude and phase responses of

$G_{audd}(s)$, and (c) is the magnitude response of $G_{fudd}(s)$ when the table is loaded with the 3-story specimen; Figure 10.13(a) and (b) are the magnitude and phase responses of $G_{audd}(s)$, and (c) is the magnitude response of $G_{fudd}(s)$ when the table is loaded with the 5-story specimen; and finally Figure 10.14(a) and (b) are the magnitude and phase responses of $G_{audd}(s)$, and (c) is the magnitude response of $G_{fudd}(s)$ when the table is loaded with the 7-story specimen. It is clear from the magnitude response plots of $G_{audd}(s)$ and $G_{fudd}(s)$ that as the specimen becomes nonlinear the peak and notch pairs observed in the linear specimen cases (R1) get smoothened out, implying that the interaction between the table and the specimen becomes less severe. It should be noted that these simulations are carried out using the same controller settings as the ones used for the earthquake simulations (i.e., Sylmar and El Centro records) in Chapter 10. Notch filter parameters used for these simulations are $f_0 = 11.0\,\text{Hz}$, $bw = 22.0\,\text{Hz}$, and $depth = -0.95$.

Figure 10.15 through Figure 10.17 show the power spectrum density (PSD) estimations of the reproduced acceleration time histories of Sylmar record with 3, 5, and 7-story linear (R1) and nonlinear (R2 and R4) shear-frames along with the PSDs of the corresponding actuator driving forces. Figure 10.15(a) shows the PSD of the reproduced acceleration when there is the 3-story specimen on the table. The table overshoots (peak at ~2.0 Hz) the frequencies below the vicinity of the 1st natural frequency (2.51 Hz) of the specimen in the linear case (R1), whereas it undershoots the frequencies above the vicinity of the 1st natural frequency of the linear specimen

(trough at ~2.56 Hz). As the specimen gets nonlinear, the table in general undershoots the bare table response. Figure 10.15(b) shows the PSD of the actuator driving force; it is clear from the figure that although the actuator applies large forces at the vicinity of the natural 1st natural frequency of the specimen, it is not able to move the table as desired around this frequency. Again as the specimen gets nonlinear, actuator exerts smaller forces around the 1st natural frequency of the specimen (i.e., actuator force for R2 specimen > actuator force for R4 specimen).

Figure 10.16(a) shows the PSD of the reproduced acceleration when 5-story specimen is mounted on the table. The table slightly overshoots the frequencies below the vicinity of the 1st natural frequency (2.15 Hz) of the specimen in the linear case (R1), whereas it undershoots the frequencies above the vicinity of the 1st natural frequency of the linear specimen (trough at ~2.2 Hz). As the specimen gets nonlinear, the table undershoots the bare table response in general. Figure 10.16(b) shows the PSD estimation of the actuator driving force; similar observation holds for this case as seen in the 3-story specimen case.

Figure 10.17(a) shows the PSD of the reproduced acceleration when there is the 7-story specimen mounted on the table. The table overshoots the frequencies below the vicinity of the 1st natural frequency (1.59 Hz) of the specimen in the linear case (R1), and it undershoots the frequencies above the vicinity of the 1st natural frequency of the linear specimen (trough at ~1.65 Hz). As the specimen gets nonlinear, the table undershoots the bare table response in general. Figure 10.17 (b) shows the PSD estimation of the actuator driving force; similar observation holds for this case as

for the 3 and 5-story specimen cases. Note that for this case, the acceleration record has little energy in the vicinity of the 1st natural frequency of the specimen; therefore in the overall sense the reproduction of this particular acceleration record with 7-story specimen was less challenging than with 3 and 5-story specimens. Figure 10.18 makes this observation clearer. It shows the PSD estimations of the error between the bare table acceleration response and the table acceleration responses with 3, 5, and 7-story specimens with strengths of R1 (linear), R2, and R4. As it is expected, the error in acceleration reproduction is clustered around the natural frequencies of the linear specimens with decreasing errors as the specimen gets more nonlinear. For this particular acceleration record, the largest error occurs with the 5-story specimen, and the smallest error occurs with the 7-story specimen.

Figure 10.19 through Figure 10.21 show the power spectrum density (PSD) estimations of the reproduced acceleration time histories of El Centro record with 3, 5, and 7-story linear (R1) and nonlinear (R2 and R4) shear-frames along with the PSDs of the corresponding actuator driving forces. Similar trends can be seen for the El Centro case as for the Sylmar case. Figure 10.22 shows the PSD estimations of the error between the bare table acceleration response and the table acceleration responses with 3, 5, and 7-story specimens with strengths of R1 (linear), R2, and R4 under the El Centro record. In this case, the largest error occurs with the 7-story specimen on the table, and the smallest error occurs with the 3-story specimen on the table.

10.7. Conclusions

A mechanics-based virtual model of the NEES-UCSD Shake Table including models for: (i) the controller; (ii) four servovalves; (iii) two single-ended actuators; (iv) two accumulators; and (v) two-dimensional mechanical subsystem is extended for loaded-table conditions. A tool based on a client-server technique is developed in order to link Simulink® with the generic finite element analysis software OpenSees. With this tool, it is possible to investigate the effects of nonlinear specimens on the response of shake tables.

Shear-frames whit 3, 5, and 7-storeys are used to investigate the table-nonlinear specimen interaction problem when the columns of the specimens ere modeled using the M-P nonlinear material model. Simulation work carried out using the shear-frames revealed that: (i) interaction between the specimen and the table is more pronounced when the specimen on the table remains linear. As the specimen becomes nonlinear the interaction effects are reduced; (ii) actuator driving force time history plots show that actuator forces increase significantly when the table is loaded with a linear specimen. When a nonlinear specimen is on the table, the actuator forces are smaller than in this case of a linear specimen; this is due to reduced specimen resisting forces acting on the platen due to specimen's nonlinear behavior; (iii) table-specimen interaction takes place at the vicinity of the natural frequency of the specimens and shows itself on the magnitude response plots of transfer functions between the reference acceleration (input) and actuator force (output), and the reference acceleration (input) and feedback acceleration (output) as peak-and-trough

pairs. Again, as the specimen becomes nonlinear peak-and-trough pairs get smoothened out and becomes less significant; (iv) PSDs of the reproduced acceleration time histories show that for the linear specimen case, the table overshoots the bare table response at frequencies below the vicinity of the 1st natural frequency and undershoots it above that frequency. For the nonlinear specimen cases, the table undershoots the table response in general; (v) PSDs of the error between the bare table acceleration response and the table acceleration responses with 3, 5, and 7-story specimens show that the error is clustered around the natural frequencies of the linear specimens with decreasing errors as the specimen gets more nonlinear; (vi) error in acceleration reproduction is a function of specimen's dynamic characteristics as well as the input acceleration record.

LIST OF TABLES

Table 10.1: Characteristics of the shear-frames.

3-Story shear-frame			
	Mass [kg]	k^{i}_{3stry} [MN/m]	Story height [m]
1st Story	65,000	76.3636	2.75
2nd Story	59,760	61.0909	2.75
3rd Story	49,540	61.0909	2.75
Total	174,300	N/A	8.25
5-Story shear-frame			
	Mass [kg]	k^{i}_{5stry} [MN/m]	Story height [m]
1st Story	65,000	133.6364	2.75
2nd Story	59,760	133.6364	2.75
3rd Story	59,660	114.5455	2.75
4th Story	59,600	114.5455	2.75
5th Story	49,540	114.5455	2.75
Total	293,560	N/A	13.75

Table 10.1 (Contd.): Characteristics of the one-bay shear-frames.

7-Story shear-frame			
	Mass [kg]	k^{i}_{7stry} [MN/m]	Story height [m]
1st Story	65,000	152.7273	2.75
2nd Story	59,760	152.7273	2.75
3rd Story	59,660	114.5455	2.75
4th Story	59,600	114.5455	2.75
5th Story	59,600	114.5455	2.75
6th Story	61,060	114.5455	2.75
7th Story	49,540	114.5455	2.75
Total	414,220	N/A	19.25

Table 10.2: Modal analysis results for the linear elastic undamped one-bay shear-frames.

3-Story shear-frame			
Mode #	Natural frequency [Hz]	Natural period [sec]	Effective modal mass ratio [%]
1	2.51	0.40	89.00
2	6.67	0.15	9.57
3	9.26	0.11	1.43
5-Story shear-frame			
Mode #	Natural frequency [Hz]	Natural period [sec]	Effective modal mass ratio [%]
1	2.15	0.47	86.19
2	6.05	0.17	10.31
3	9.40	0.11	2.51
4	12.12	0.08	0.71
5	13.64	0.07	0.27

Table 10.2 (Contd.): Modal analysis results for the linear elastic undamped one-bay shear-frames.

7-Story shear-frame			
Mode #	Natural frequency [Hz]	Natural period [sec]	Effective modal mass ratio [%]
1	1.59	0.63	82.76
2	4.60	0.22	11.06
3	7.26	0.14	3.89
4	9.65	0.10	1.28
5	11.69	0.09	0.46
6	13.19	0.08	0.22
7	14.07	0.07	0.34

Table 10.3: Elastic and reduced story shear forces for the three shear-frames.

3-Story shear-frame			
Story #	R1 (Linear) [kN]	R2 [kN]	R4 [kN]
1	2040.2	1020.1	510.0
2	1602.5	801.3	400.6
3	844.3	422.2	211.1
5-Story shear-frame			
Story #	R1 (Linear) [kN]	R2 [kN]	R4 [kN]
1	3332.4	1666.2	833.1
2	3017.4	1508.7	754.3
3	2508.2	1254.1	627.0
4	1788.0	894.0	447.0
5	869.7	434.8	217.4

Table 10.3 (Contd.): Elastic and reduced story shear forces for the three shear-frames.

7-Story shear-frame			
Story #	R1 (Linear) [kN]	R2 [kN]	R4 [kN]
1	4522.9	2261.4	1130.7
2	4309.7	2154.8	1077.4
3	3949.8	1974.9	987.4
4	3413.2	1706.6	853.3
5	2725.1	1362.6	681.3
6	1884.6	942.3	471.1
7	880.3	440.1	220.1

LIST OF FIGURES

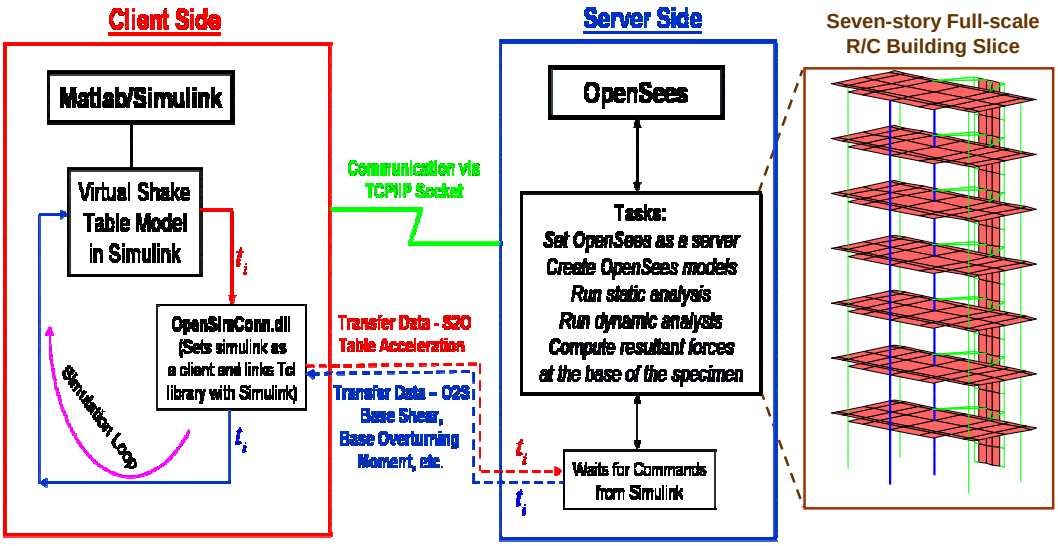

Figure 10.1: Simulink and OpenSees integration via client-server technique using TCP/IP socket.

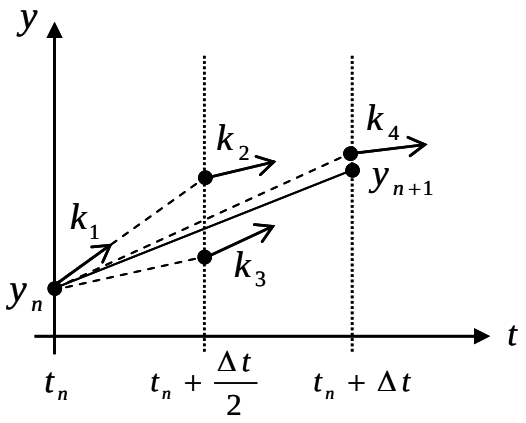

Figure 10.2: Geometric interpretation of the 4th order Runge-Kutta method. Average of four slopes is used to advance (march) y_n to y_{n+1}.

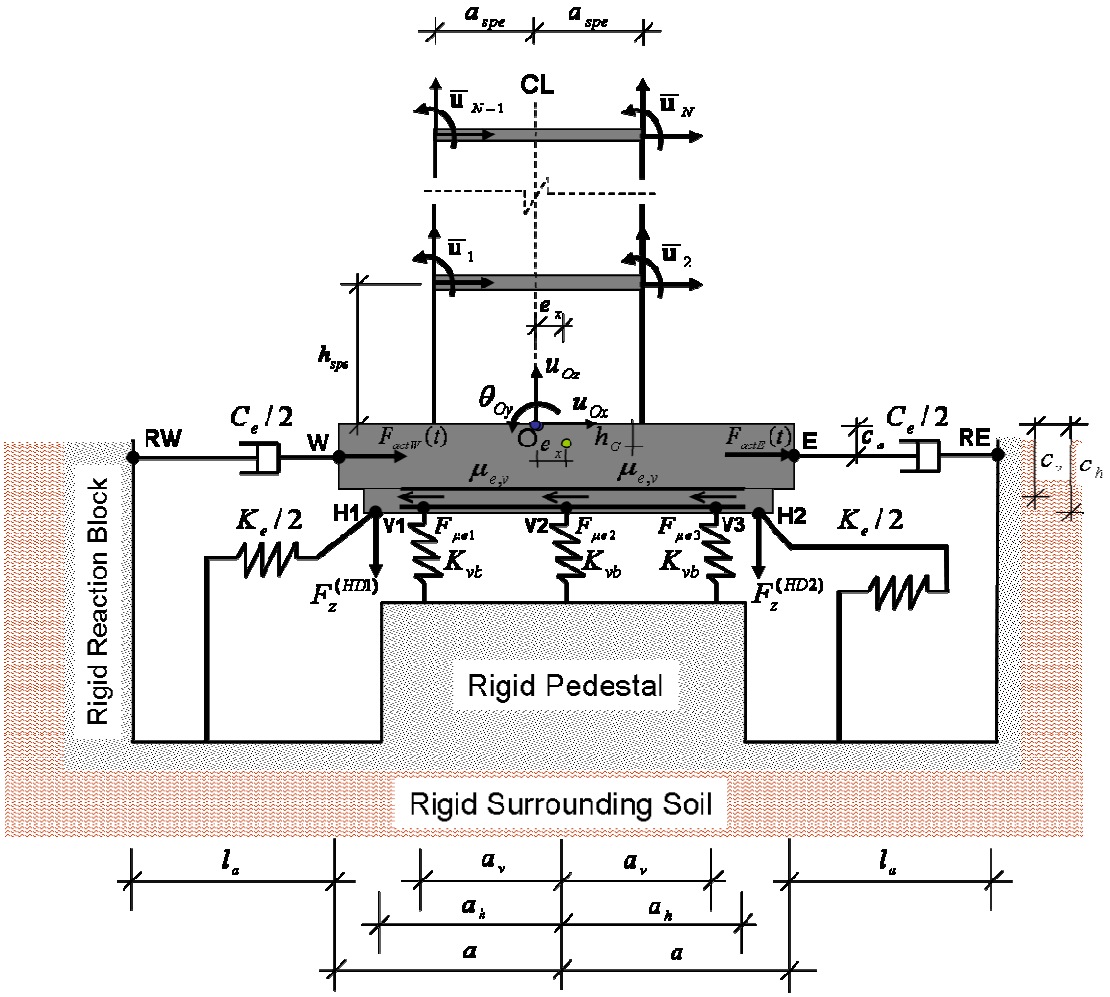

Figure 10.3: Two-dimensional mechanical subsystem model of LHPOST with a generic specimen mounted on its platen.

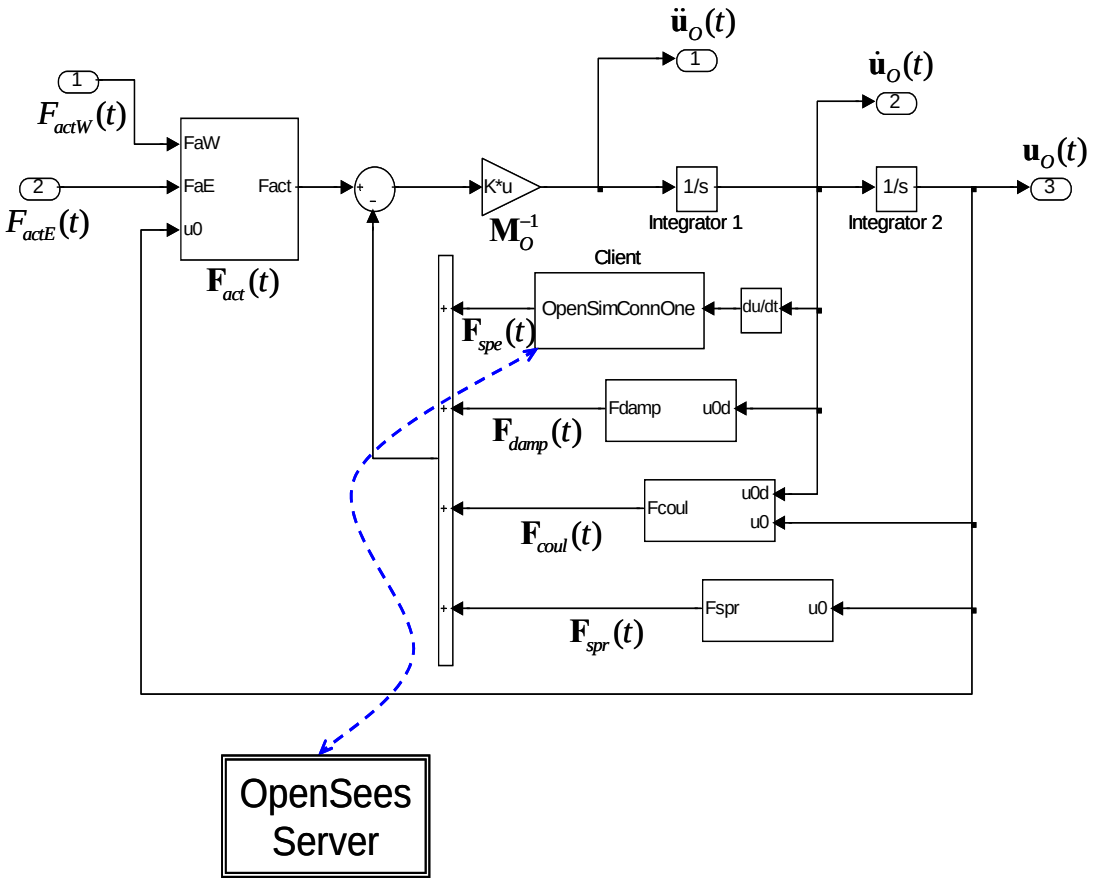

Figure 10.4: Simulink implementation of the equation of motion of the mechanical subsystem with specimen effects where the latter is modeled within OpenSees using the client-server framework.

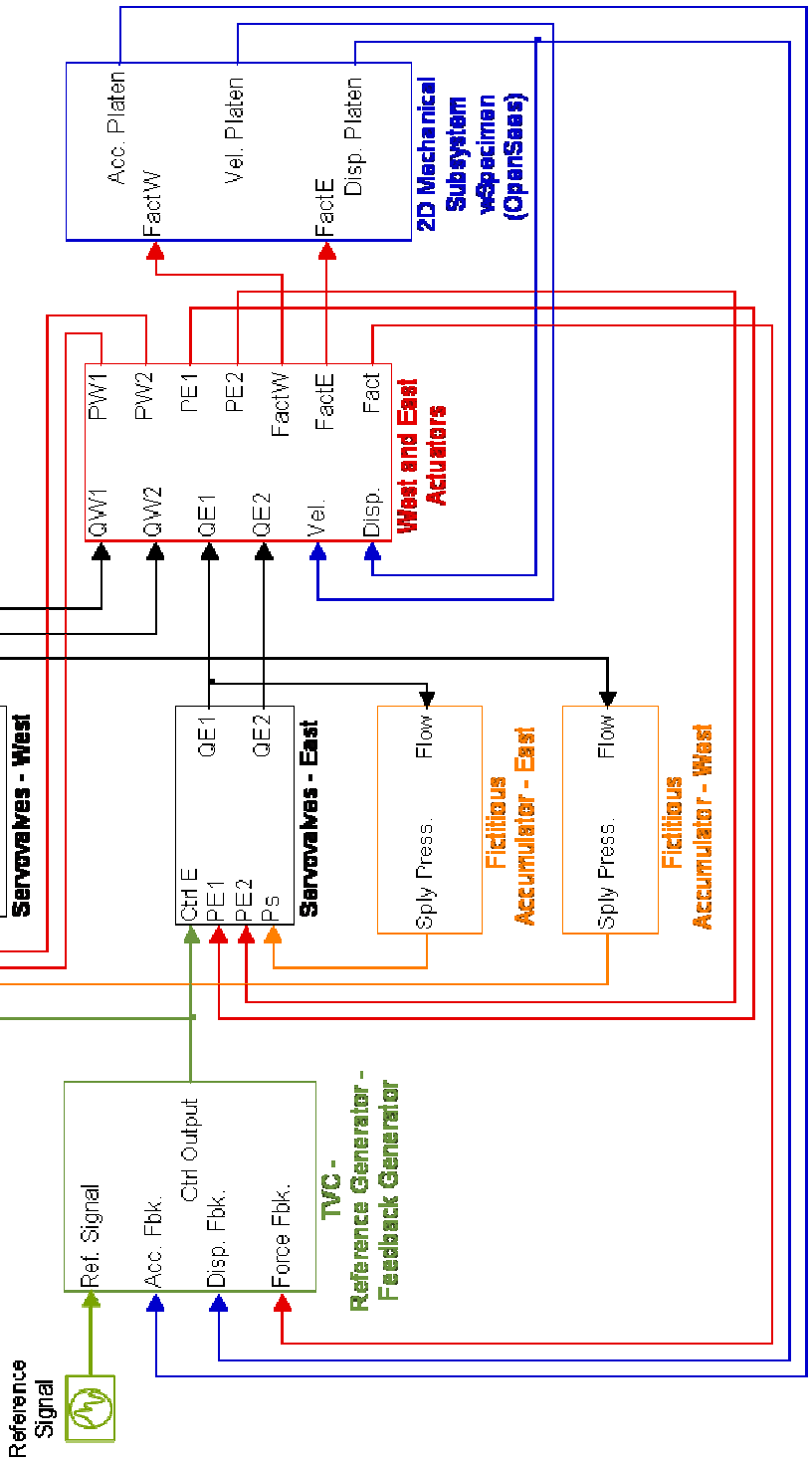

Figure 10.5: Simulink implementation of the complete virtual model of LHPOST under loaded-table conditions.

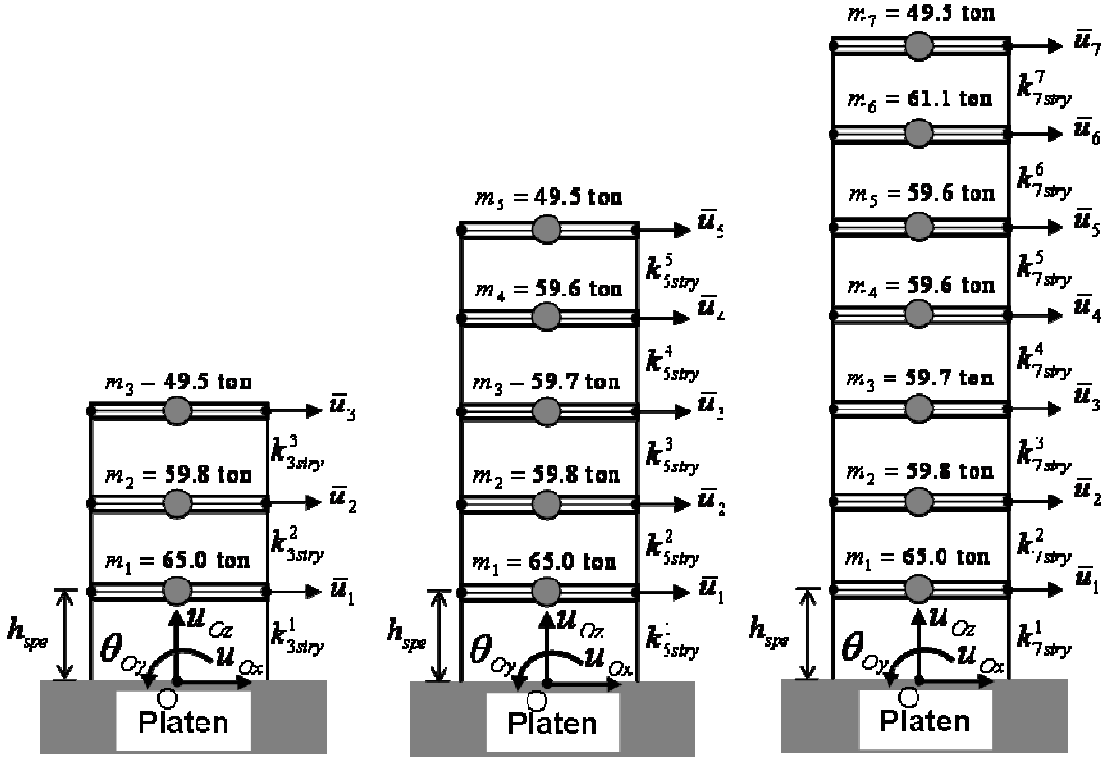

Figure 10.6: Three, five, and seven story shear-frames mounted on the table platen.

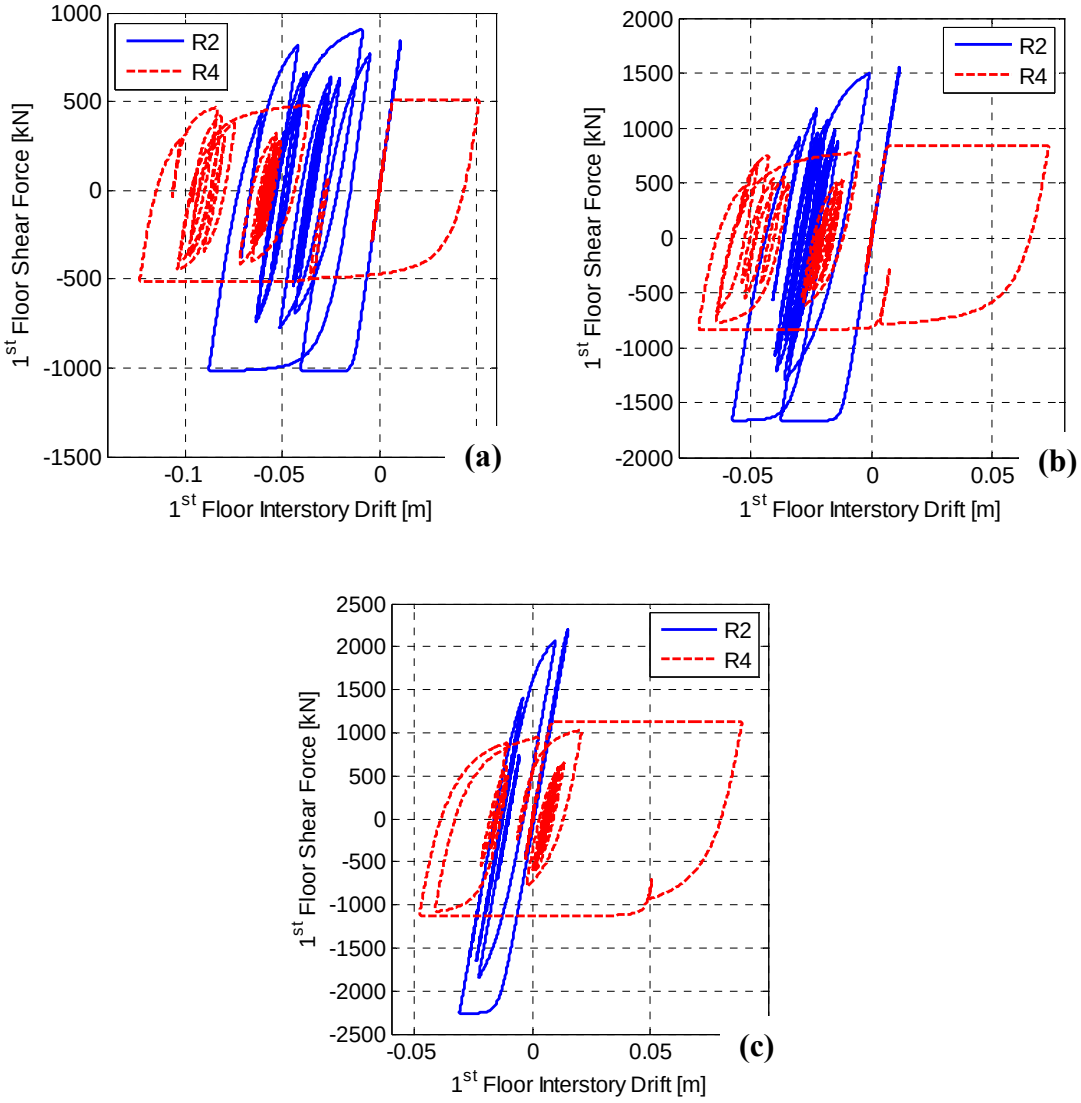

Figure 10.7: 1st floor inter-story drift vs. 1st floor shear force relationships under reproduced Sylmar record: (a) 3-story shear frame; (b) 5-story shear frame; and (c) 7-story shear frame.

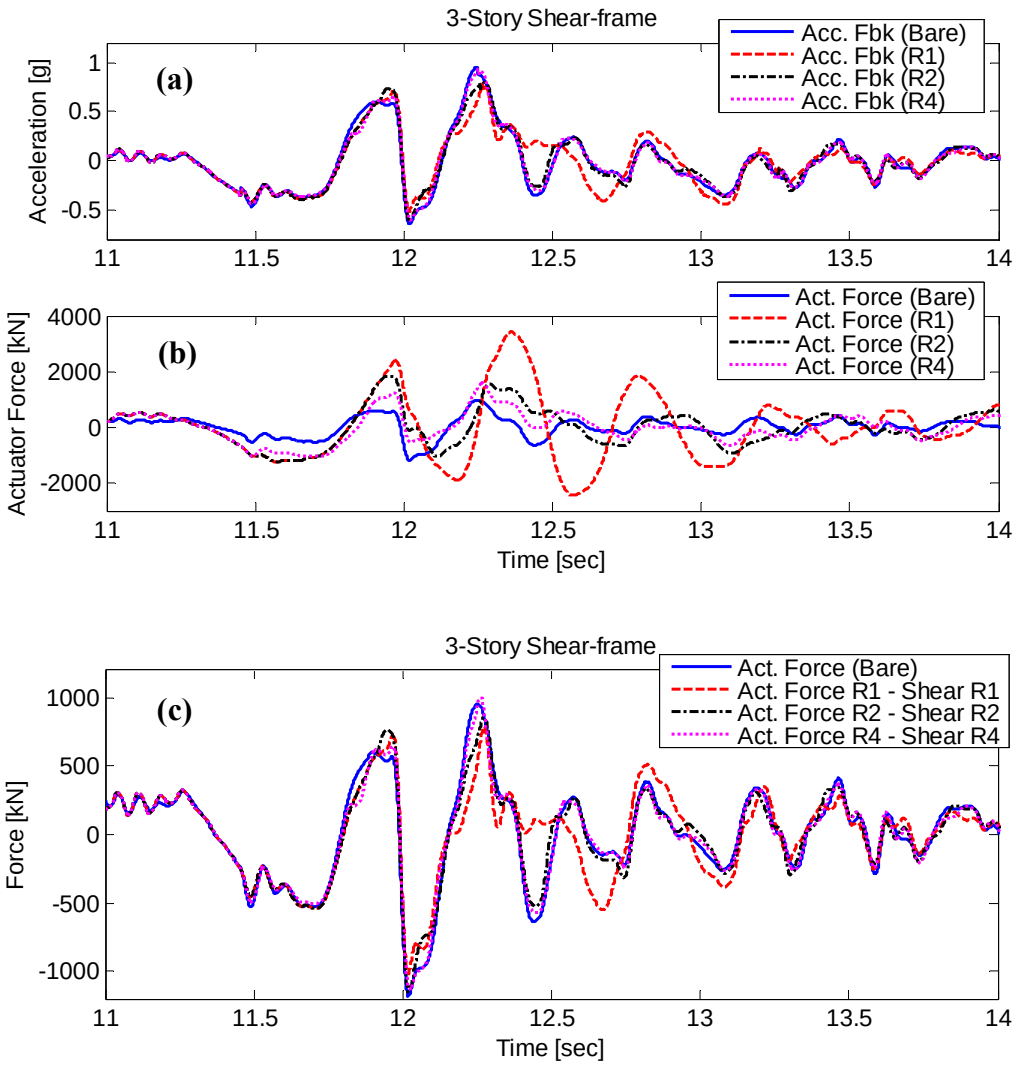

Figure 10.8: Simulation results using Sylmar earthquake record reproduced under bare table condition and table with 3 story shear-frame modeled linearly (R1), and with M-P models of yield strengths R2 and R4: (a) acceleration; (b) actuator force; and (c) actuator force minus the total specimen shear force.

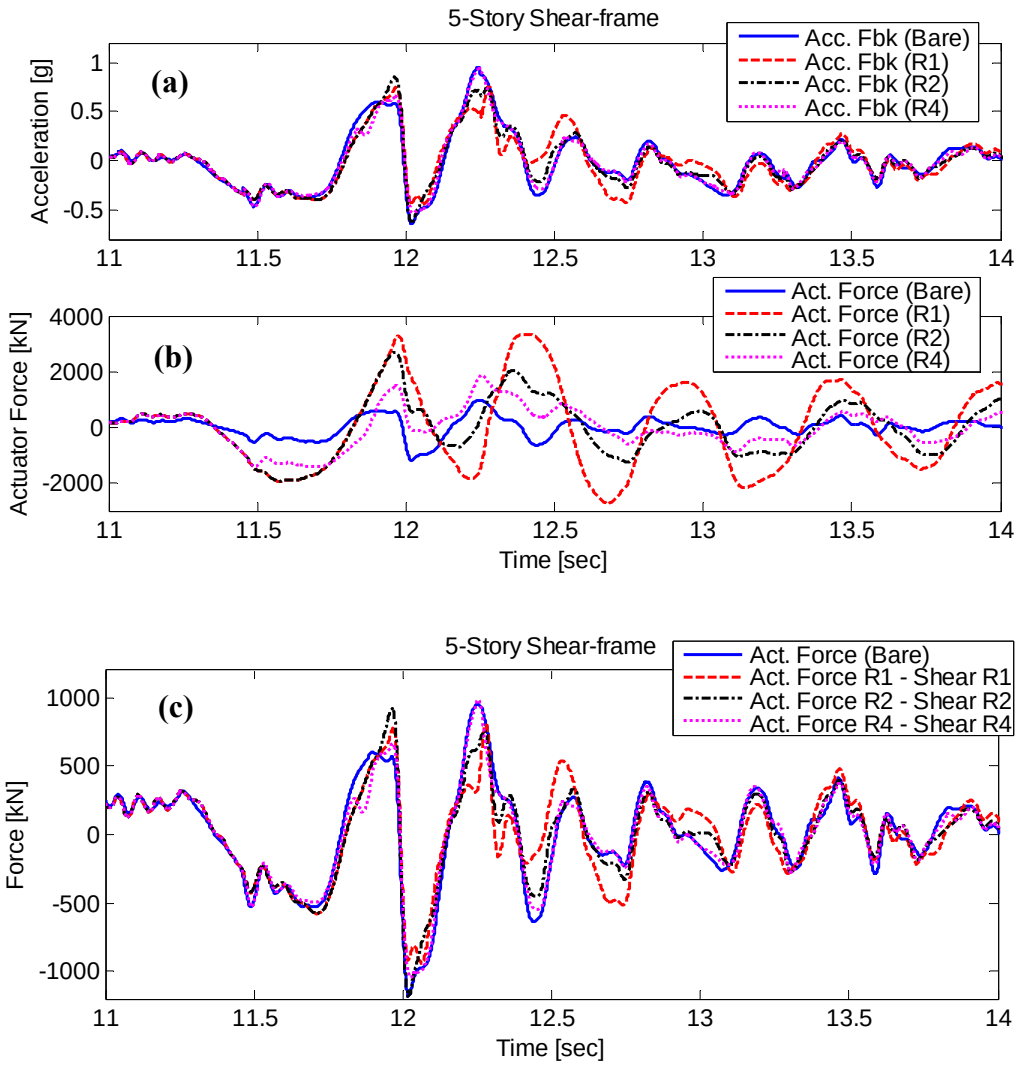

Figure 10.9: Simulation results using Sylmar earthquake record reproduced under bare table condition and table with 5 story shear-frame modeled linearly (R1), with M-P models of yield strengths R2 and R4: (a) acceleration; (b) actuator force; and (c) actuator force minus the total specimen shear force.

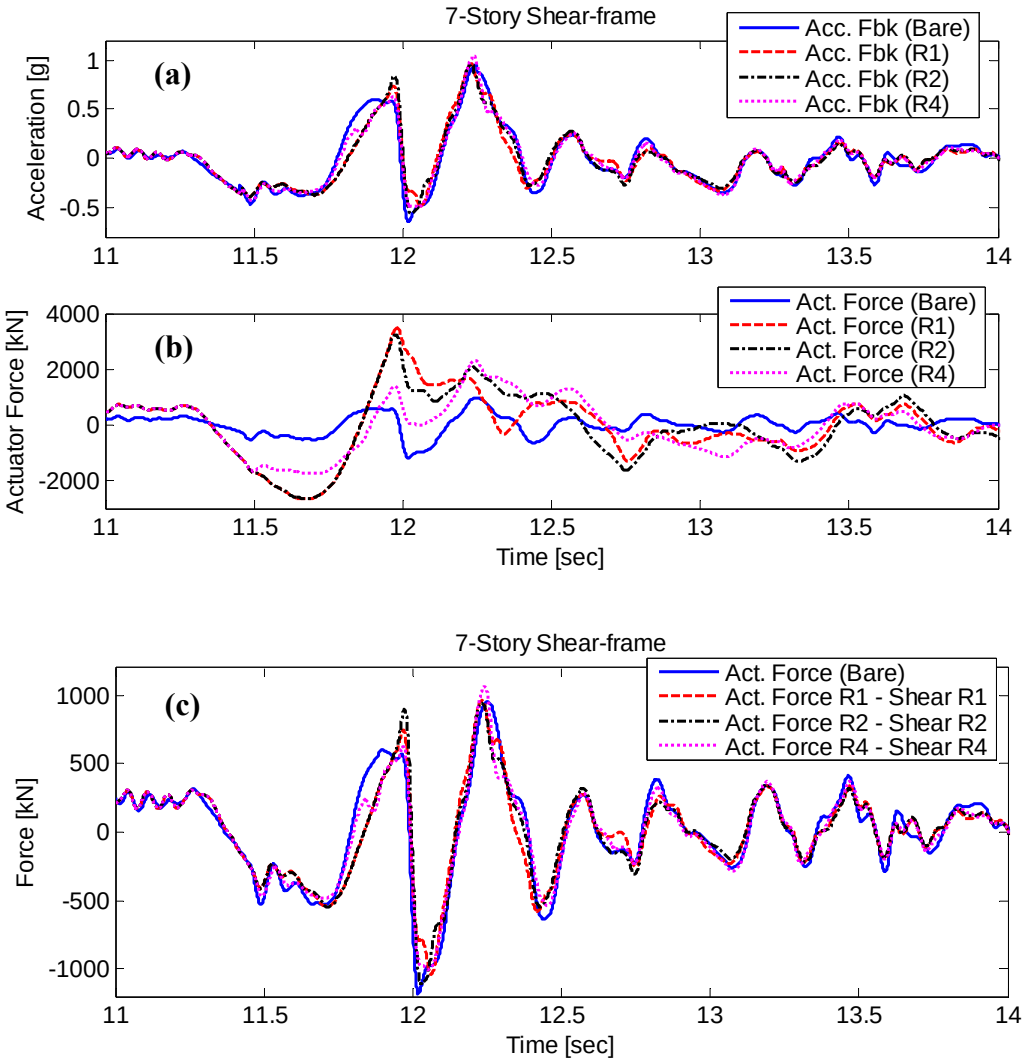

Figure 10.10: Simulation results using Sylmar earthquake record reproduced under bare table condition and table with 7 story shear-frame modeled linearly (R1), with M-P models of yield strengths R2 and R4: (a) acceleration; (b) actuator force; and (c) actuator force minus the total specimen shear force.

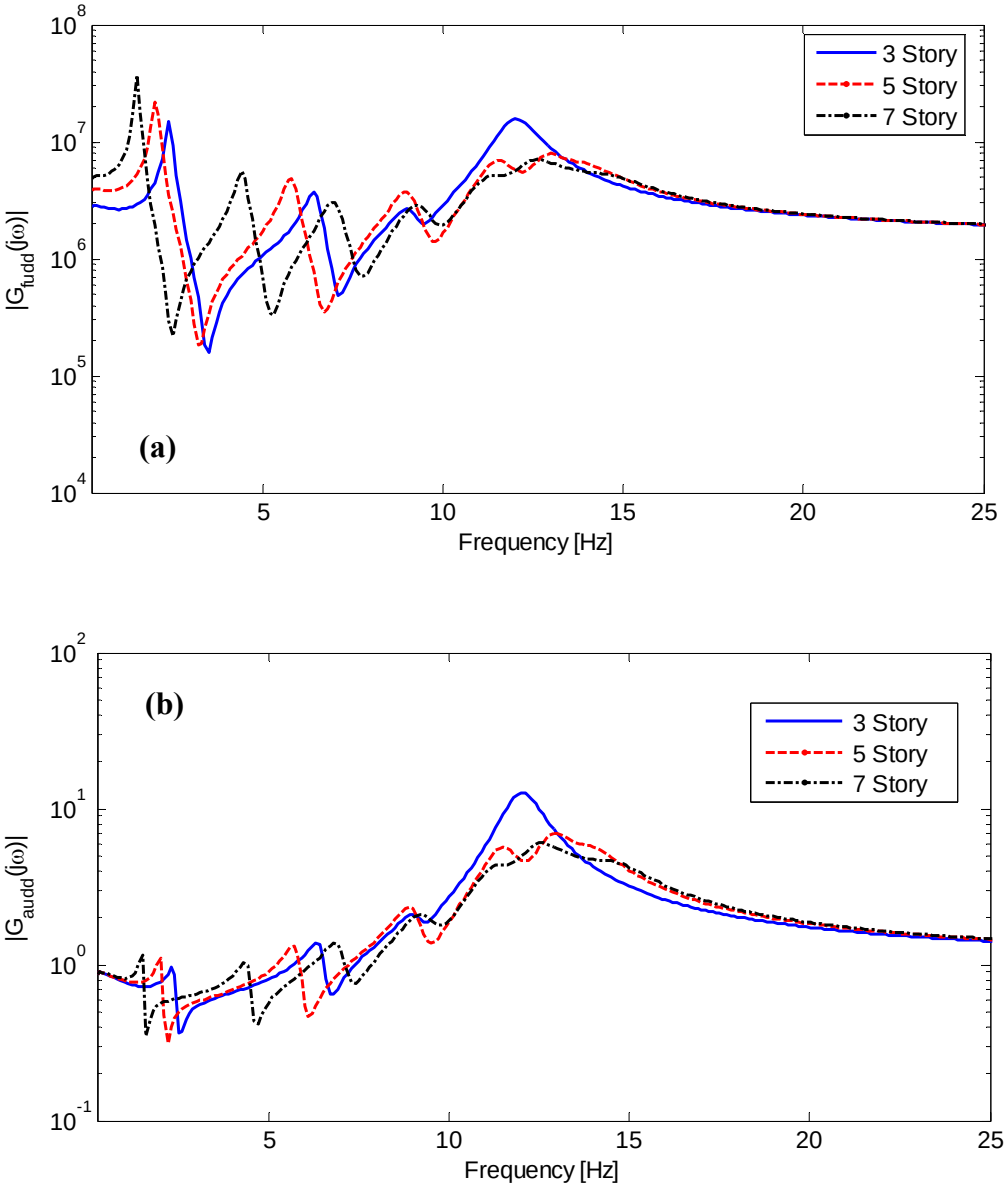

Figure 10.11: Magnitude responses of analytical transfer functions of the linear table-linear shear frames with 3, 5, and 7 stories: (a) $G_{fudd}(s)$; and (b) $G_{audd}(s)$.

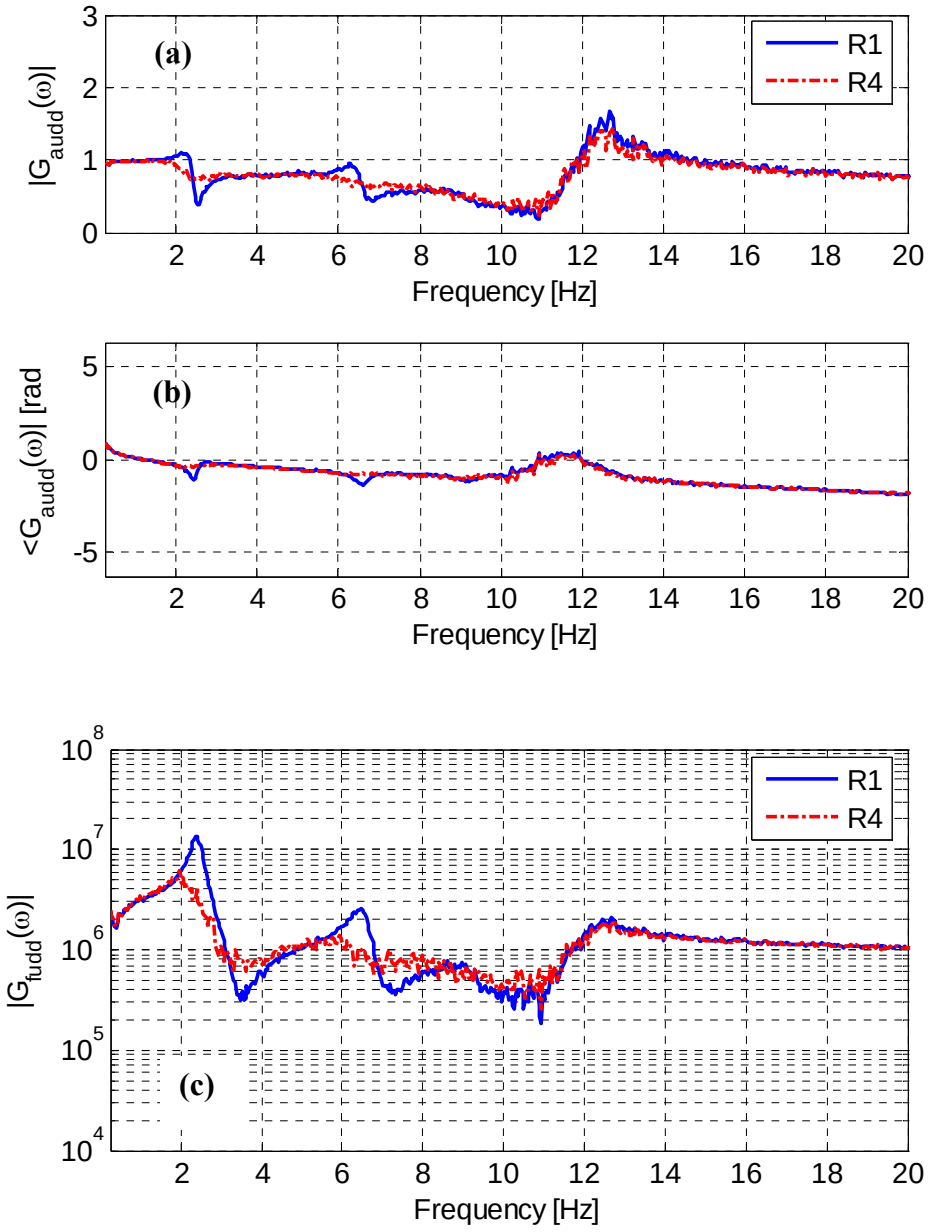

Figure 10.12: Numerical transfer function estimations under white noise input with 3-story linear (R1), and nonlinear shear-frame (R4) models: (a) $\left|G_{audd}(s)\right|$; (b) $< G_{audd}(s)$; (c) $\left|G_{fudd}(s)\right|$.

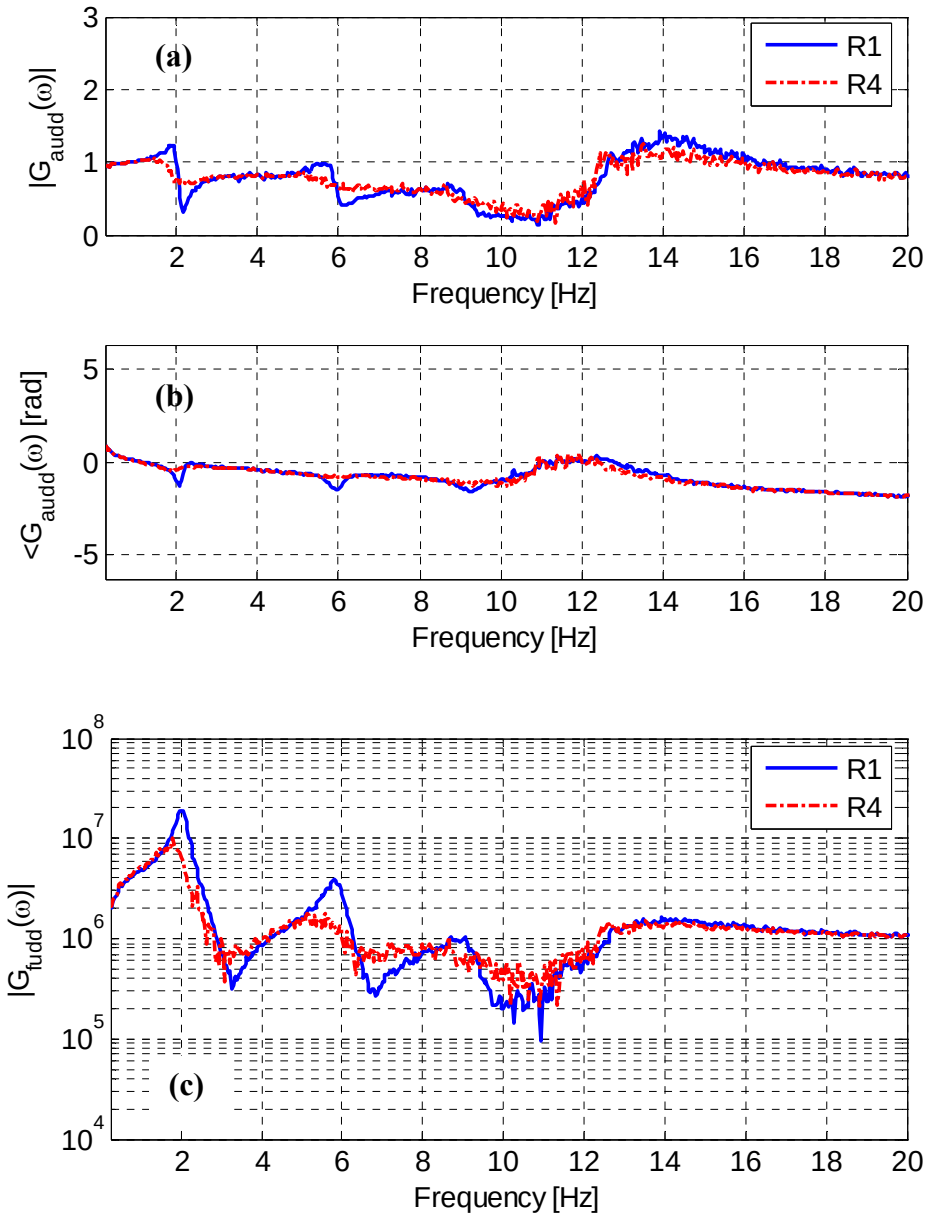

Figure 10.13: Numerical transfer function estimations under white noise input with 5-story linear (R1), and nonlinear shear-frame (R4) models: (a) $\left|G_{audd}(s)\right|$; (b) $< G_{audd}(s)$; (c) $\left|G_{fudd}(s)\right|$.

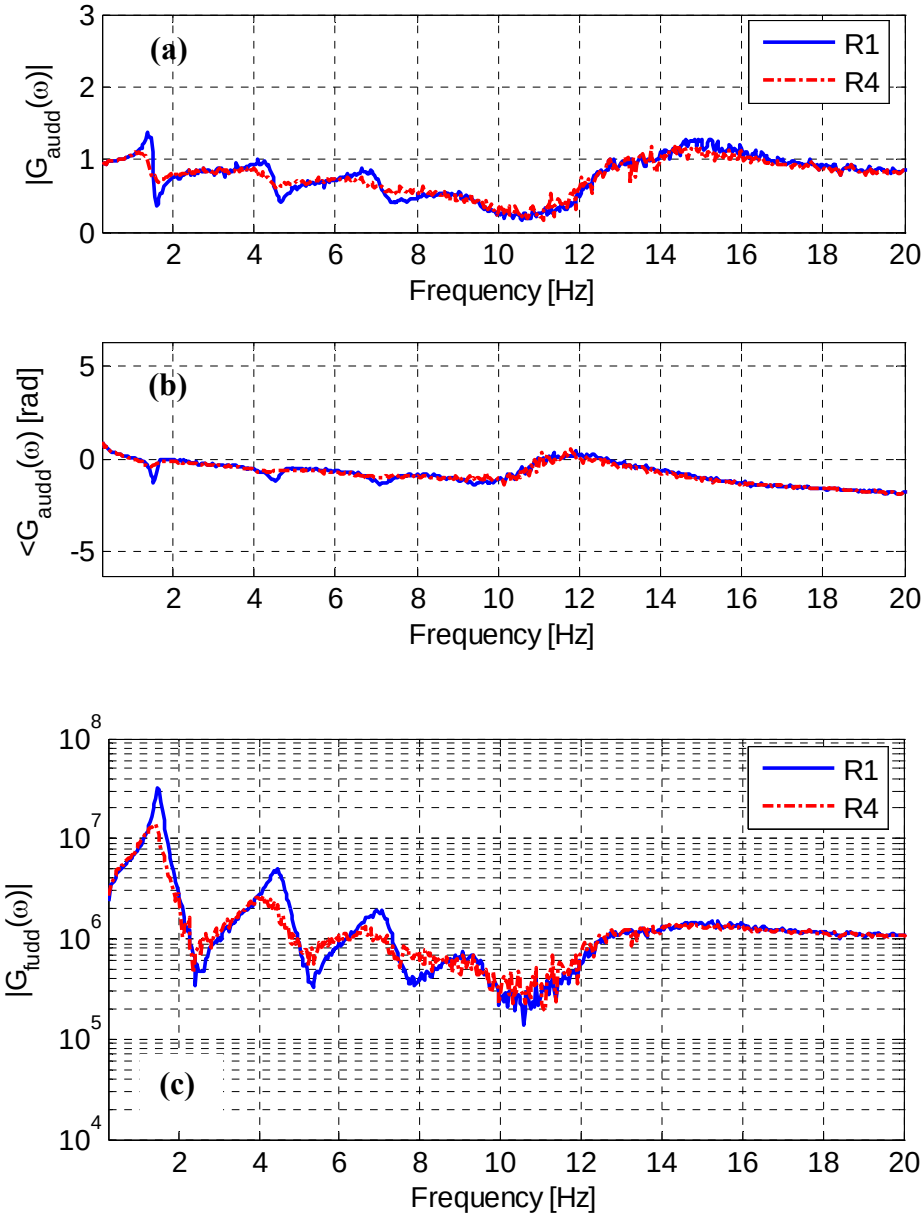

Figure 10.14: Numerical transfer function estimations under white noise input with 7-story linear (R1) and nonlinear shear-frame (R4) models: (a) $\left|G_{audd}(s)\right|$; (b) $< G_{audd}(s)$; (c) $\left|G_{fudd}(s)\right|$.

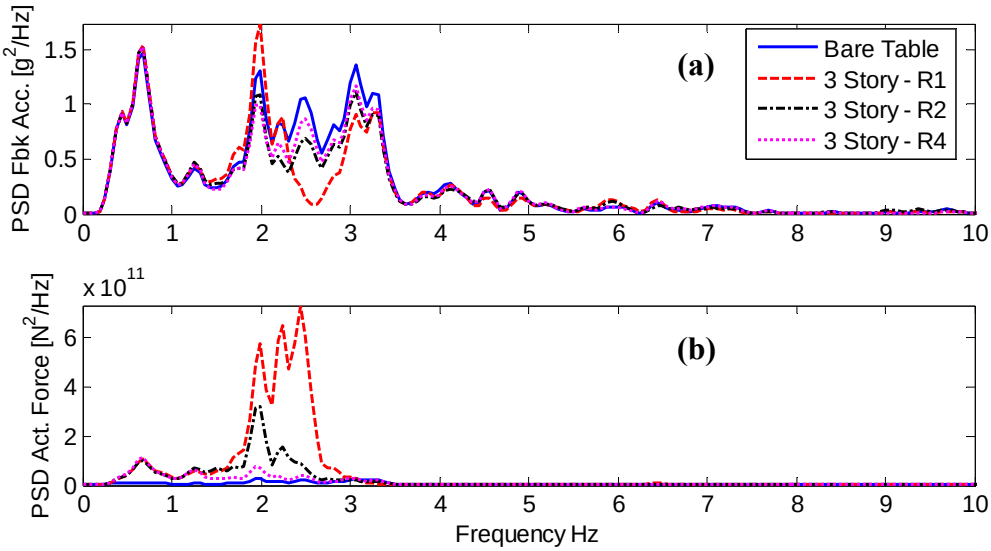

Figure 10.15: Power spectra of reproduced Sylmar acceleration record under bare and loaded table conditions with 3-story shear-frame modeled linearly (R1), and with M-P model of yield strengths R2 and R4: (a) acceleration; and (b) force feedbacks.

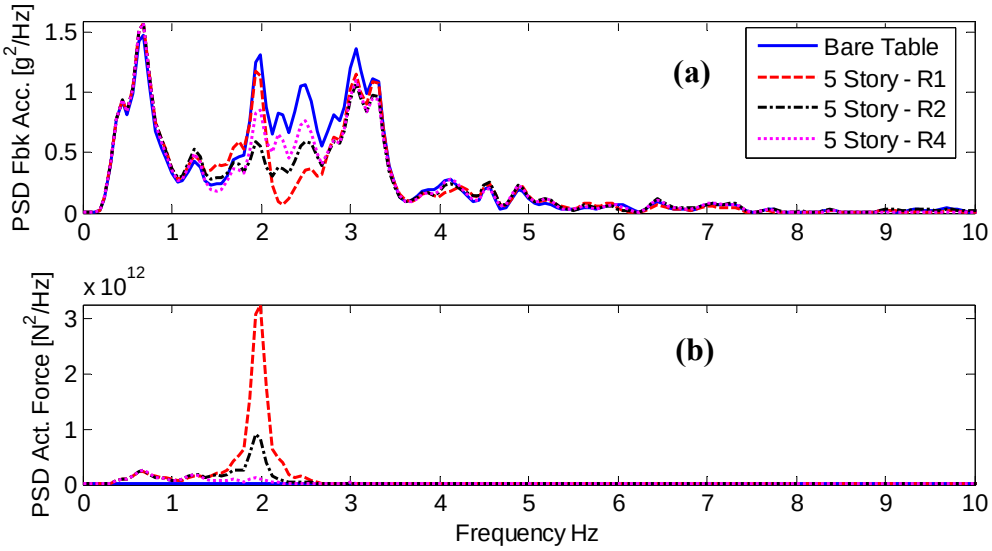

Figure 10.16: Power spectra of reproduced Sylmar acceleration record under bare and loaded table conditions with 5-story shear-frame modeled linearly (R1), and with M-P model of yield strengths R2 and R4: (a) acceleration; and (b) force feedbacks.

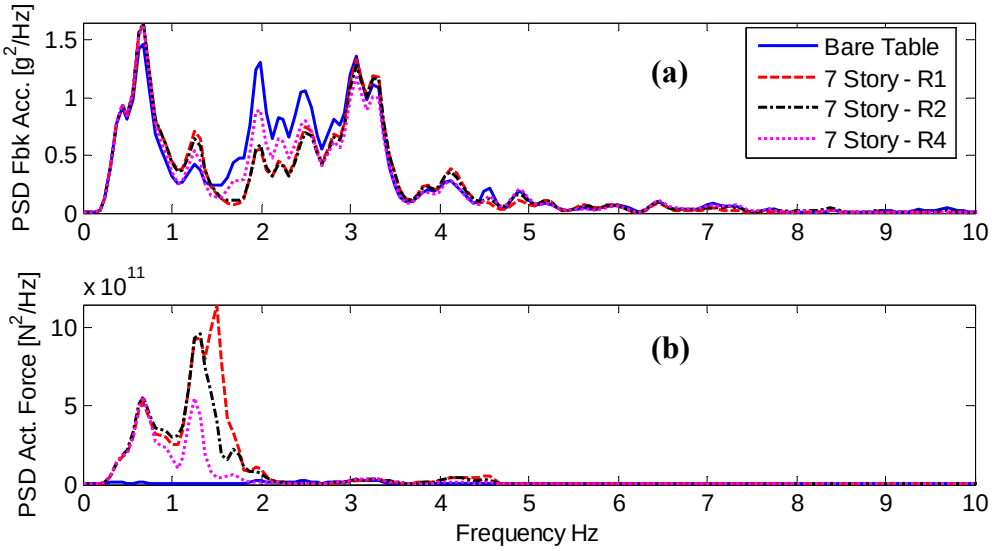

Figure 10.17: Power spectra of reproduced Sylmar acceleration record under bare and loaded table conditions with 7-story shear-frame modeled linearly (R1), and with M-P model of yield strengths R2 and R4: (a) acceleration; and (b) force feedbacks.

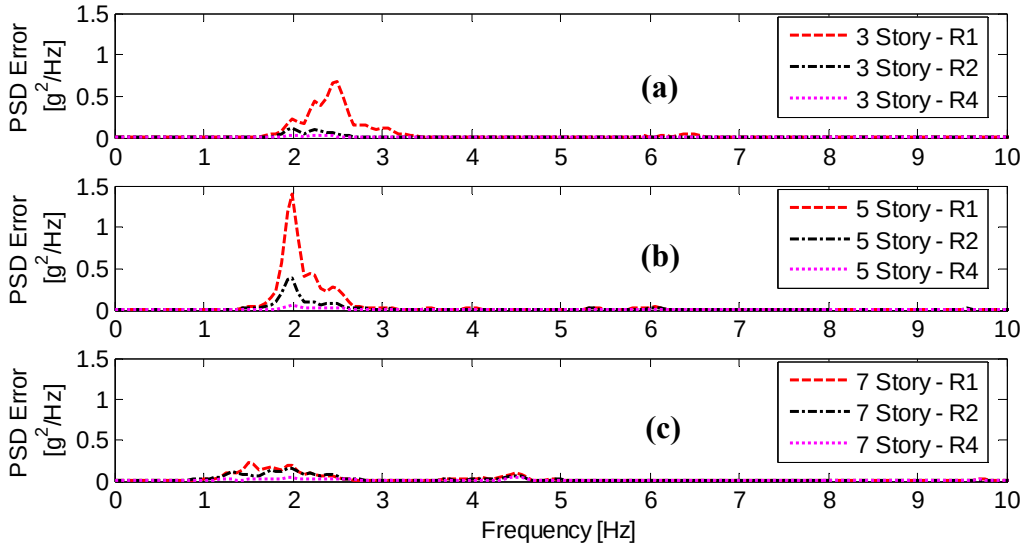

Figure 10.18: Power spectra of the error between reproduced Sylmar acceleration record under bare table and loaded table conditions with shear frames modeled linearly (R1), and with M-P models of yield strengths R2 and R4: (a) 3-story; (b) 5-story; and (c) 7-story.

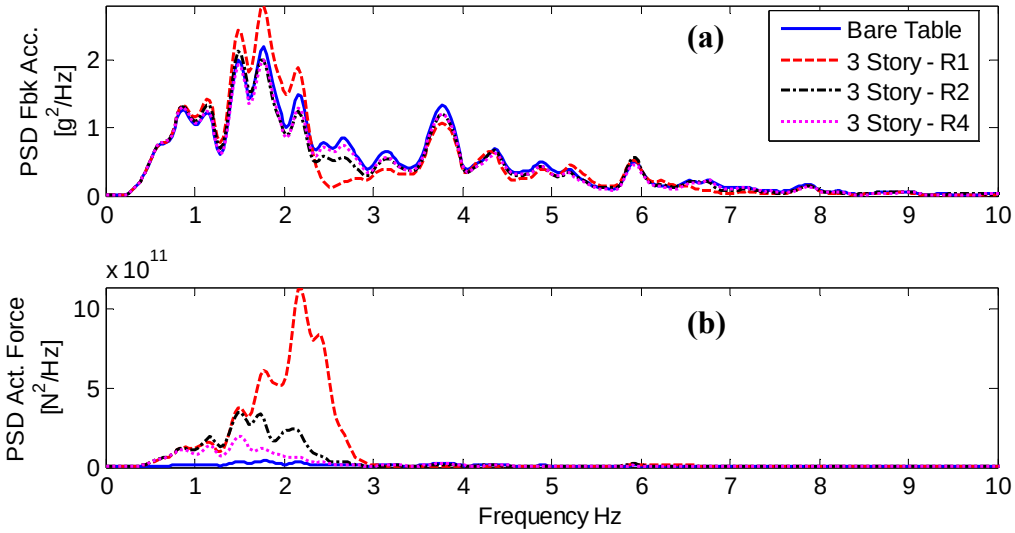

Figure 10.19: Power spectra of reproduced El Centro acceleration record under bare and loaded table conditions with 3-story shear-frame modeled linearly (R1), and with M-P model of yield strengths R2 and R4: (a) acceleration; and (b) force feedbacks.

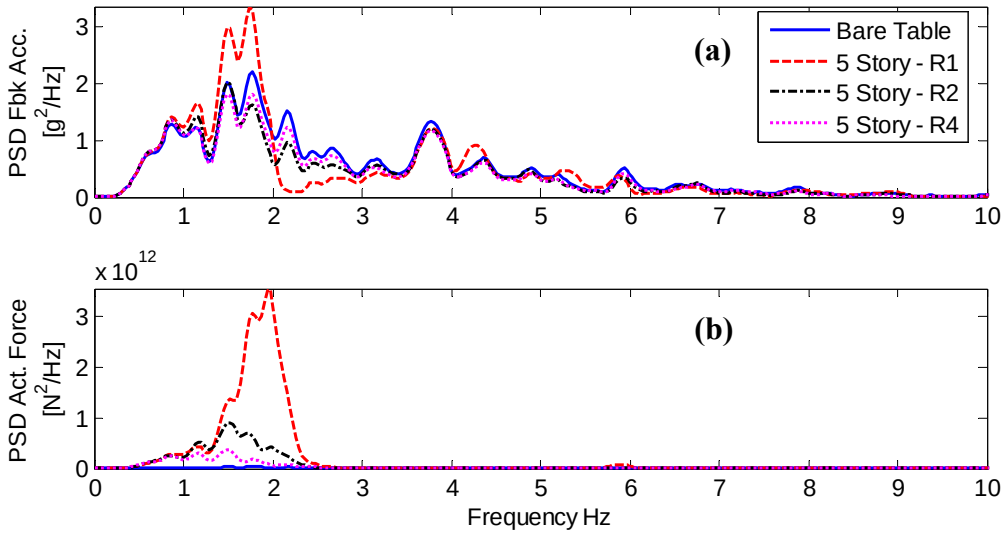

Figure 10.20: Power spectra of reproduced El Centro acceleration record under bare and loaded table conditions with 5-story shear-frame modeled linearly (R1), and with M-P model of yield strengths R2 and R4: (a) acceleration; and (b) force feedbacks.

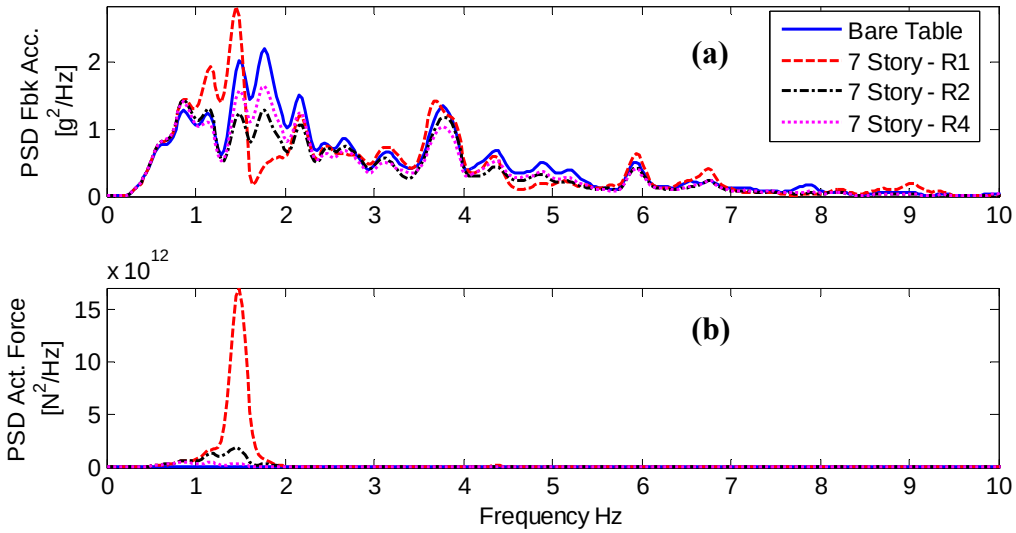

Figure 10.21: Power spectra of reproduced El Centro acceleration record under bare and loaded table conditions with 7-story shear-frame modeled linearly (R1), and with M-P model of yield strengths R2 and R4: (a) acceleration; and (b) force feedbacks.

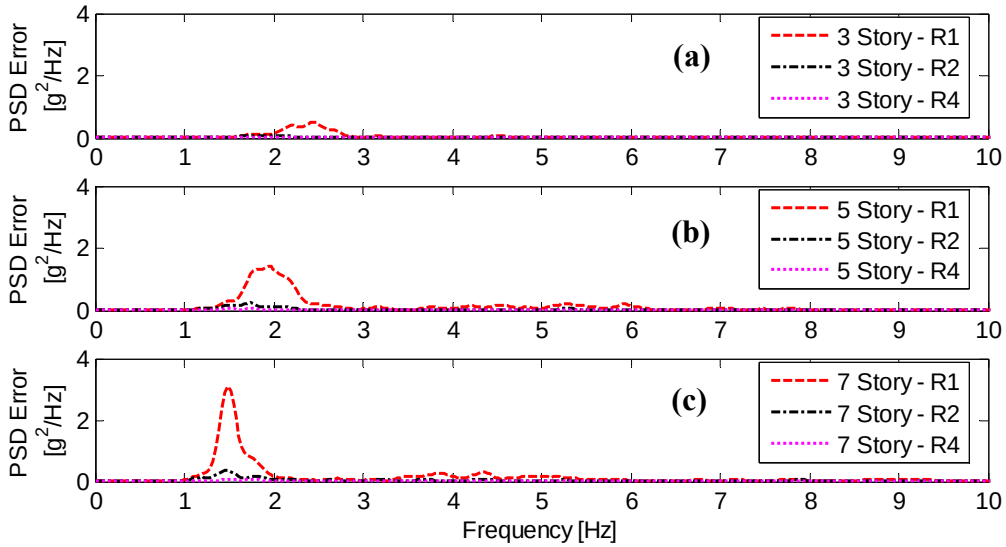

Figure 10.22: Power spectra of the error between reproduced El Centro acceleration record under bare and loaded table conditions with shear frames modeled linearly (R1), and with M-P models of yield strengths R2 and R4: (a) 3-story; (b) 5-story; and (c) 7-story.

REFERENCES

Barbato, M. and Conte J.P., (2006). "Finite element structural response sensitivity and reliability analyses using smooth versus non-smooth material constitutive models." *Int. J. Reliability and Safety*, Vol. 1: 3-39.

Bewley, T. (2008). *Numerical Renaissance,* Renaissance Press, San Diego.

Dabney, J. and Harman, T. L. (2004). *Mastering Simulink*, Pearson/Prentice Hall, Upper Saddle River, New Jersey.

Dyke, S. J., Spencer, B. J., Quast, P., and Sain, M. K. (1995). "Role of control-structure interaction in protective system design." *J. Eng. Mech.*, 121(2), 322-338.

Filippou, F.C., Popov E.P. and Bertero, V.V. (1983). "Effects of bond deterioration on hysteretic behavior of reinforced concrete joints." *Report EERC 83-19*, Earthquake Engineering Research Center, University of California, Berkeley.

Lee, S. (2004). Ordinary and Partial Differential Equation Routines in C, C++, Fortran, Java, Maple, and Matlab, Chapman and Hall/CRC, New York.

McKenna, F., Fenves, G. L., and Scott, M. H. (2000). "Open system for earthquake engineering simulation", http://opensees.berkeley.edu.

Moler, C. (2004). *Numerical Computing with Matlab*, SIAM, Philadelphia, PA.

Panagiotou, M.P. and Restrepo, J. (2007). "Computational Model for the UCSD 7-STORY Structural Wall Building Slice." *Report SSRP-07/09*, University of California, San Diego.

Welch, B.B. (2000). *Practical Programming in Tcl and Tk*, 3rd Edition, Prentice-Hall, Inc., Upper Saddle River, New Jersey.

CHAPTER 11

CONCLUSIONS

11.1. Summary of Contributions and Major Findings

A comprehensive mechanics-based virtual model of the large NEES-UCSD shake table under bare and loaded table conditions is developed. The model includes the virtual replica of the actual controller, four servovalve models accounting for servovalve spool dynamics and two independent servovalve flow nonlinearities, two single-ended actuators with variable internal chamber volumes, two effective accumulators capturing the average fluctuation of the supply pressure at the 4^{th} stage of the servovalves, a two-dimensional mechanical subsystem model accounting for the effective mass of the platen, the nitrogen-filled hold-down struts, and various viscous and Coulomb type dissipative mechanisms, and linear/nonlinear specimens modelled using the OpenSees finite element analysis framework. An efficient TCP/IP-based client-server technique is developed and implemented to integrate the simulation platform OpenSees used for the specimen and the Matlab-Simulink® simulation platform used for the rest of the system.

Results of the forced vibration tests conducted on the foundation block show that the deformations of the foundation block and of the surrounding soil are very

small. Therefore, they are neglected in the virtual system model which assumes the foundation block and the surrounding soil to be rigid.

A mathematical model for the mechanical components of the NEES-UCSD shake table is developed. It is shown that several nonlinear terms arising from the significant displacements and rotations of the hold-down struts remain small, and that a simplified model including an effective horizontal mass, an effective horizontal stiffness due to the pre-charge pressure in the hold-down struts, and dissipative force terms composed of classical Coulomb friction and nonlinear viscous damping elements is sufficient to simulate the response of the subsystem with reasonable accuracy.

An extensive set of 74 shake table tests composed of harmonic and earthquake acceleration records were performed on the NEES-UCSD shake table to assess its signal reproduction fidelity after tuning the table with the tools available, namely the fixed-gain controller (Three-Variable-Controller) and an iterative time history matching technique (Online Iteration). These tests were designed to quantify the effects of the amplitude of the signal used for tuning the table on the signal reproduction fidelity. A number of comparisons and measures were used to evaluate the signal reproduction capability of the shake table. Based on these comparisons, it was found that the level of fidelity in signal reproduction achieved for a specific amplitude of the commanded signal under the corresponding optimum tuning of the table cannot be maintained when reproducing the same signal at different amplitudes. This is a clear indication that shake tables are highly nonlinear systems and the current

state-of-the-art controller and tuning techniques fall short of compensating accurately for these inherent system nonlinearities. Especially, difficulties encountered with tuning at low signal amplitudes and testing at much higher signal amplitudes indicate the need for an accurate virtual tuning of the table based on a detailed mechanics-based model of the complete system. A set of Table Performance Curves were generated based on the results of these extensive shake table tests. These curves provide the shake table user with a quantitative guide to decide on the level of calibration PGA amplitude that should be used to obtain a desired level of signal fidelity for a given test PGA amplitude.

Analytical work using a linear model of a servo-hydraulic shake table system with single- and multi-degree-of-freedom specimens mounted on its platen showed that shake tables exciting lightly damped structures (e.g., civil structures) have limited ability to apply forces at the vicinity of the natural frequencies of these structures modeled as linear. Furthermore, the open-loop transfer function between the servovalve command signal and the actuator force show that the numerator of this transfer function contains the 1^{st}, 2^{nd}, and 3^{th} derivatives of the command signal. This observation is valuable in the sense that in order for the actuator to move the table at higher frequency range, any feedforward control signal added onto the valve command signal must be proportional with the velocity, acceleration, and the jerk (3^{rd} derivative) of the displacement reference signal; this justifies the motivation of using feedforward control signals in TVC. A parametric study investigating the effects of the TVC control gains on the transfer function between the acceleration reference signal

and the actuator force indicates that: (i) the proportional (feedback) gain, k_P, can be used to change effectively the system gains (i.e, magnitude transfer function between reference acceleration and actuator force) in the low frequency range (i.e., DC up to ~2.0 Hz); (ii) the velocity feedforward gain, k_{VF}, is effective mostly in modifying the system gains in the low-to-medium frequency range (i.e., from ~2.0 Hz up to the oil column frequency of the system at ~11.0Hz); (iii) the acceleration feedforward gain, k_{AF}, affects the system gain around the oil-column frequency (~11.0 Hz); (iv) the jerk feedforward term, k_{JF}, affects the system gains effectively above the oil-column frequency (i.e., ~11.0 Hz and onward); and (v) the force feedback gain, k_{DP}, damps out the oil-column resonance of the system as its value increases.

Under narrow and broadband inputs, the virtual shake table model with bare table condition is able to reproduce accurately the actual (achieved) platen motion (e.g., displacement, velocity, and acceleration) using the same controller settings as on the actual system. Moreover, the 4th stage spool displacements of the four servovalves and the total actuator driving force from the actual tests are also reproduced accurately by the virtual shake table model. Supply pressure fluctuations measured during the actual tests at the 4th stage of the servovalves are captured in the average sense by the effective accumulator models used. It is observed that the two flow nonlinearities in the servovalves are the most significant sources of signal distortion in servo-hydraulic shake table systems. The virtual shake table model with the servovalves assumed linear (linearized) is not capable of replicating the observed signal distortions. Both the pressure drop - flow nonlinearity (square-root nonlinearity) and the flow gain

nonlinearity need to be incorporated in the servovalve model in order to match the actual platen motion with the simulated one. Based on the test-simulation correlation studies performed, it is observed that the simulation results are sensitive to the flow gain nonlinearity (i.e., flow vs. spool displacement nonlinearity). Therefore, experimental determination of these curves for each orifice on the four servovalves is deemed necessary in order to further improve the calibration, accuracy and reliability of the virtual shake table model developed and use it safely for simulation-based offline tuning purposes.

In order to investigate the shake table - linear/nonlinear specimen interaction problem, an analytical study was performed using 3, 5, and 7-story shear frames in which the relation between the interstory drift and story shear force is modeled using the Menegotto-Pinto nonlinear constitutive model. The simulation results of this study, specific to shear-frames, revealed that: (i) The dynamic interaction between the specimen and the table gets more pronounced when the specimen on the table remains linear. The degree of interaction decreases with increasing level of nonlinearity in the specimen response. (ii) The actuator force time history plots show that the actuator force increases proportionally with the specimen reaction force. The actuator force decreases with increasing level of nonlinearity in the specimen response. This is due to the reduction of the specimen reaction force due to yielding of the material. (iii) The table-specimen dynamic interaction takes place at the vicinity of the natural frequencies of the specimen (linear specimen), and manifests itself in the form of peak-and-trough pairs in the magnitude response plots of the transfer functions

between (a) the reference acceleration and the actuator force, and (b) the reference acceleration and feedback (achieved) acceleration. These two transfer functions have the same poles (peaks) but different zeros (troughs). As the specimen becomes increasingly nonlinear, these peak-and-trough pairs are smoothened out and become less significant. (iv) Power spectral density (PSD) estimations of the simulated table acceleration response histories show that for the linear specimen case, the table overshoots the bare table response at frequencies below the vicinity of the 1st natural frequency and undershoots it above that frequency under fixed table control setting. For the nonlinear specimen case, the table undershoots the bare table response throughout the frequency range of operation and especially at frequencies in the vicinity of the zeros of the transfer function between the reference acceleration and actuator force. (v) PSDs of the error between the simulated bare table acceleration response and the simulated table acceleration responses with a 3, 5, or 7-story specimen mounted on the table show that the error is clustered around the natural frequencies of the linear specimens and decreases with increasing level of specimen nonlinearity. (vi) The error seen in the acceleration reproduction is a function of the specimen's dynamic characteristics, level of nonlinearity, as well as the characteristics of the input acceleration record.

11.2. Recommendations for Future Work

Future work on the subject should focus on the following topics: (i) Conducting shake table tests with a dummy linear and/or nonlinear specimen on the table in order to generate Seismic Performance Curves for loaded table conditions.

Although these curves will be specific to the dummy specimens used, it will still give invaluable information about the effects of the specimen on the table seismic performance curves. (ii) Conducting targeted tests for identifying the nonlinear flow vs. spool displacement curves for the four orifices on each servovalve. These experimentally determined curves would replace the prototype curves currently used in the virtual model and would increase the reliability to the model. (iii) More complete and detailed mechanics-based model of the hydraulic system should be developed, including mathematical models for the pumps, accumulator bank, blow-down valves and their controllers (blow-down controller), in-line and close-coupled accumulators and transient flow conditions in the hydraulic power lines. (iv) More realistic nonlinear specimens should be modeled using the finite element analysis framework OpenSees (this task is under progress). The realistic specimen model can be coupled easily to the rest of the nonlinear shake table model using the TCP/IP-based client-server tool developed in this study. (v) Flexibility of the platen should be considered for heavy specimens on the platen as well as the moving vertical support conditions of the platen (as the platen slides over the pressure-balanced bearings). (vi) The detailed mechanics-based virtual shake table model developed in this study can be used to develop and test more advanced controllers (e.g., nonlinear, adaptive) which can then be implemented on both existing and future shake table systems.